Dissertation

Structural Motifs in the Lithium (Oxo/Imido)nitridophosphate System

Stefanie Schneider

München 2023

Dissertation zur Erlangung des Doktorgrades
der Fakultät für Chemie und Pharmazie
der Ludwig-Maximilians-Universität München

Structural Motifs in the Lithium (Oxo/Imido)nitridophosphate System

Stefanie Schneider

aus

Crailsheim, Deutschland

2023

Erklärung

Diese Dissertation wurde im Sinne von §7 der Promotionsordnung vom 28. November 2011 von Herrn Prof. Dr. Wolfgang Schnick betreut.

Eidesstattliche Versicherung

Diese Dissertation wurde eigenständig und ohne unerlaubte Hilfe erarbeitet.

München, 21.12.2023

Stefanie Schneider

Dissertation eingereicht am:	03. November 2023
1. Gutachter:	Prof. Dr. Wolfgang Schnick
2. Gutachter:	Prof. Dr. Oliver Oeckler
Mündliche Prüfung am:	06. Dezember 2023

Danksagung

Wie jede wissenschaftliche Publikation wäre auch diese Doktorarbeit nicht ohne das Zutun und die Hilfe vieler weiterer Menschen möglich gewesen.

Zunächst möchte ich Herrn Prof.,Dr. Wolfgang Schnick für die Möglichkeit danken, meine Promotion in seinem Arbeitskreis durchführen zu dürfen.

Ich danke Prof. Dr. Oliver Oeckler für die Übernahme der Zweitkorrektur und seine wertvollen Anmerkungen bei der gemeinsamen Publikation.

Des Weiteren danke ich Prof. Dr. Hubert Huppertz, der sofort freudig zur Prüfung zugesagt hat, bei Prof. Dr. Joost Wintterlin, der extra ein Praktikum umgeplant hat, um als Prüfer zugegen sein zu können, bei Prof. Dr. Konstantin Karaghiosoff, der sich immer Zeit nimmt und selbst im Ruhestand die Studis beim Namen kennt, und bei Prof. Dr. Bettina Lotsch, die bei all unseren gemeinsamen Publikationen tolle, konstruktive Anmerkungen beigetragen hat.

Außerdem möchte ich allen meinen Coautor*innen für ihre Anteile an den Publikationen danken: Lucas Balzat, Anna-Katharina Hatz, Sandra Kreiner, Sebastian Klenk, Simon Kloß, Markus Nentwig, Voloydymyr Baran und Thomas Bräuniger. Vielen Dank auch an diejenigen, die diverse Spektren und Analytik für mich aufgenommen haben: Christian Minke am NMR und EDX, Lisa Gamperl am EDX, Sandra Albrecht am ICP-OES, Susanne Ebert am CHNS und Achim Schulz vom MPI in Stuttgart für Ramanmessungen.

Dank geht auch an den gesamten AK Schnick, insbesondere an meine alten und neuen Laborkollegen, vor allem an Eva-Maria Wendinger, die mir das Handwerk beigebracht hat, das ich für diese Doktorarbeit gebraucht habe und für die Startpunkte, die sie mir gegeben hat.

Schließlich möchte ich mich noch bei all den großartigen Menschen bedanken, die mir immer helfen, meine Balance zu finden: meiner Familie, die mich immer darin unterstützt, meinen eigenen Weg zu gehen, und meinen Freunden aus ganz unterschiedlichen Freundeskreisen: von daheim, aus der Fachschaft, dem P4P, dem KaR, und viele andere. Danke, dass ihr mich vor dem Wahnsinn bewahrt.

Mein allergrößter Dank geht dabei an Frank, ohne den es diese Dissertation niemals gegeben hätte.

It's dangerous to go alone! Take this.
–Old man *The Legend of Zelda*

Contents

List of Figures

List of Tables

1. Introduction

When Johan August Arfvedson discovered lithium in 1817, he could not possibly have conceived the importance this element would attain in the 21st century. He discovered the element in petalite ($LiAl[Si_4O_{10}]$), a silicate mineral that had been discovered by José Bonifacio de Andrada e Silva several years before.[1–3] The name *lithium* originates from the Greek word λίθος (líthos = stone). Berzelius, Arfvedson's teacher, had suggested this name, since lithium could be found in the "mineral kingdom", in contrast to the other alkali metals sodium and potassium, which were discovered in the "vegetable kingdom".[2,4,5] One year later, Humphry Davy was able to obtain the pure metal by electrolysis from Li_2O. After that, it took over one hundred years until commercial production of Li was started in 1923.[6,7] Another hundred years later, Li has become one of the most sought-after elements in technology.

In the year 2022 alone, 130 400 t of lithium have been mined, mainly in the form of Li_2CO_3 and LiOH, the main producing countries being Australia (61 000 t), Chile (39 000 t), and China (19 000 t) (Figure 1.1a). At an annual growth rate of 21 % in 2022 production, Li_2CO_3 prices rose about 335 % compared to 2021.[8,9]

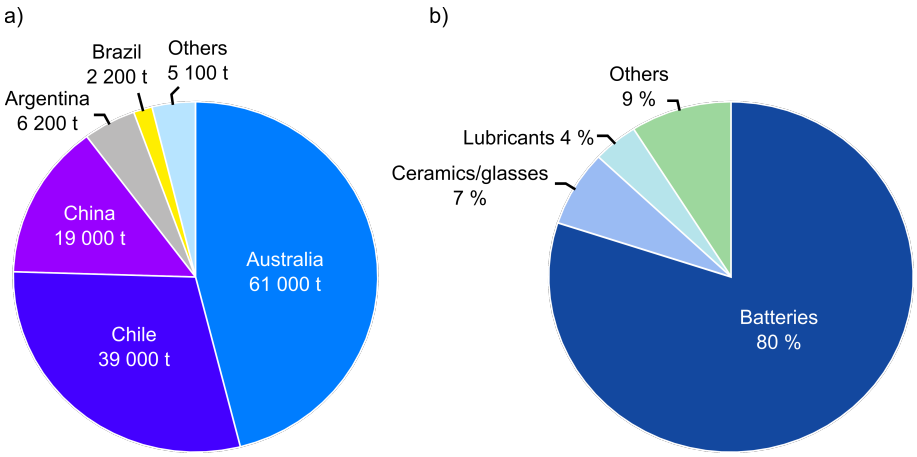

Figure 1.1.: a) Main Li-producing countries in 2022. b) Main end-usage of Li in 2022.[8,9]

Over the years, lithium compounds have seen a wide variety of uses. For example, lithium and its salts were used as admixture in food products like lemonade or as substitute for table salt for salt-reduced diets in the US, a use which was rather short-lived. Since intake of larger amounts of lithium has severe health effects,[10] only medical application for the treatment of bipolar disorder persisted.[11] Some of the main uses between 1950 and 1975 were in metallurgical processes, ceramic

glazing, and high-temperature greases. In the US, military applications comprised a large part of lithium use. For example, lithium hydride was utilized as hydrogen carrier for inflation of naval balloons during the Second World War and ^{6}LiD was used for thermonuclear weapons during the Cold War. Use of lithium hydroxide in alkaline batteries started around 1935. Over the years, a steady low percentage of lithium persisted to be used for battery applications, until the demand for rechargeable batteries has made this percentage spike sharply around the turn of the century.[12]
Today, batteries are *the* main end-usage of lithium (Figure 1.1b). In 2022, 80 % of lithium went into battery production and the demand for lithium is expected to still rise with the market for electric vehicles (EV) growing and being subsidized by governments.[13] Lithium ion batteries (LIBs), like all batteries, comprise an anode and a cathode with a separator and electrolyte between them (Figure 1.2a). Current collectors contacting these electrodes are used to make the electric energy accessible and casings allow portability and safety. After decades of research, intercalation materials for both cathode and anode have proven most viable. Cathode materials are usually lithium transition metal oxides with layered structures, like $LiCoO_2$,[13,14] or $LiNi_xM_{1-x}O_2$ ($x \geq 0.6$, M = Co, Al, Mn),[15,16] but also phosphates like $LiFePO_4$.[17] During discharge of the battery, C_6Li is oxidized at the anode. Lithium ions are intercalated into the cathode structure and the transition metal in the cathode is reduced (Equation (1.1)). Charging of the battery reverses the reaction, the transition metal is oxidized, Li^+ is extracted from the oxide and intercalated into the graphite and they form C_6Li.[18,19]

$$C_6Li + Fe^{[III]}PO_4 \rightleftharpoons 6\,C + LiFe^{[II]}PO_4 \tag{1.1}$$

Various anode materials, among others lithium alloys with silicon, tin, or antimony, polymers, or transition metal oxides, have been proposed, all of which pose significant problems like reactivity against the electrolyte, or volume expansion upon charge. The typical anode material in LIBs on the market is graphite, in which lithium is intercalated upon charging of the battery.[20] This intercalation anode itself raises safety concerns due to its reactivity that almost matches that of lithium at the additional price of lower capacity.[20] As anode, metallic lithium would offer the highest energy density. However, several problems arise when elemental lithium is used as anode material like short circuiting caused by dendrite formation and subsequent pressure buildup.[21] If the built-up pressure is too high, the cell can burst and the electrolyte and lithium ignite in the subsequent contact with air.[18] Commonly used electrolytes mainly consist of a lithium salt like $LiPF_6$ dissolved in a (mixture of) polar organic liquid, often ethylene carbonate, in combination with additives that regulate specific properties like operation temperature.[18]
However, these mixtures of liquid electrolyte also pose major challenges. Since requirements vary with the application area, anode and cathode material, different electrolyte mixtures have to be used. Electrolytes should be stable against both the highly reductive environment of the anode, and the highly oxidative environment of the cathode. However, due to the high electrochemical potential in LIBs, reaction can hardly be prevented, leading to formation of solid passivating products on the anode surface that reduce reaction with the electrolyte, but can hamper battery capacity (solid electrolyte interphase, SEI).[18,22–25]

Furthermore, liquid organic electrolyte bear the intrinsic hazard of leaking and pose a higher risk of fire.[26,27]

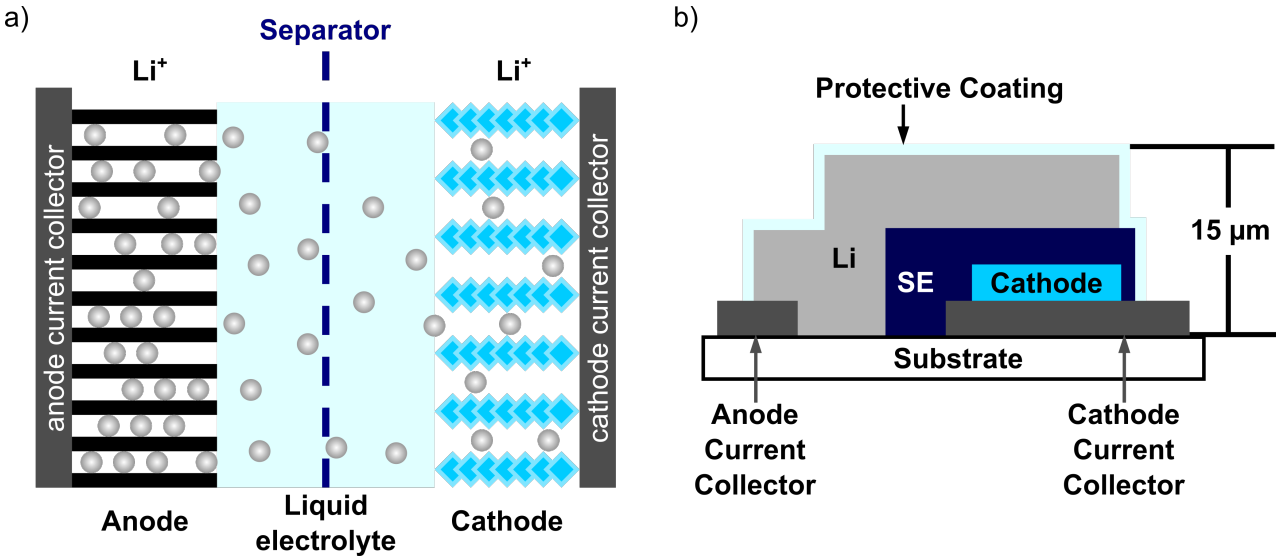

Figure 1.2.: a) Commercially available LIB with graphite as the anode, layered lithium transition metal oxide as cathode and a liquid electrolyte. b) Lithium metal thin film battery.

One possible solution for some of these problems are solid electrolytes (SE). Safety concerns can be largely eliminated, since solid electrolytes do not contain volatile compounds. They have a larger thermal stability window, which makes them usable at higher temperatures and diminishes the risk of bursting battery cells. The risk of leaking is eliminated since no liquid components are used, making all-solid state batteries (ASSBs) an interesting alternative in medical devices like pacemakers. Weight can be reduced in battery packaging, since components like separators can be removed entirely.[28–30] Furthermore, SEs allow a considerable increase in energy density. Battery size can be reduced significantly, since ASSBs can be deposited directly onto a substrate. This enables batteries only several µm thin and additionally allows for high flexibility in shape and size (Figure 1.2b). Finally, since SEs are solid inorganic materials, they can be a mechanical impediment for dendrite formation during lithium deposition, enabling safer use of elemental lithium as anode.[31]

Since no separator is present in the cell, solid electrolytes are required to be electrical insulators with a high ionic conductivity (above $10^{-4}\,\mathrm{S\,cm^{-1}}$) and to have a wide electrochemical stability window of about 5 V.

Depending on the reaction of the SE with the lithium anode, three types of interfaces are possible (Figure 1.3). (1) If there is no reaction, a thermodynamically stable interface results, which applies for binary compounds like Li_3N, Li_3P, Li_2O, or Li_2S.

If the interface is thermodynamically unstable, reaction between lithium and the electrolyte takes place. (2) Is the formed product both an electronic and ionic, i.e. mixed conductor, the reaction can be maintained throughout the SE layer and self-discharge of the battery results. A mixed ionic-electronic conducting interphase (MCI) forms. (3) The third type of interface, a kinetically stabilized SEI, results when the reaction products show negligible electronic conductivity and is comparable to

SEIs in LIBs with liquid electrolytes.[32–34] Battery performance then depends on the conductivity of this SEI.

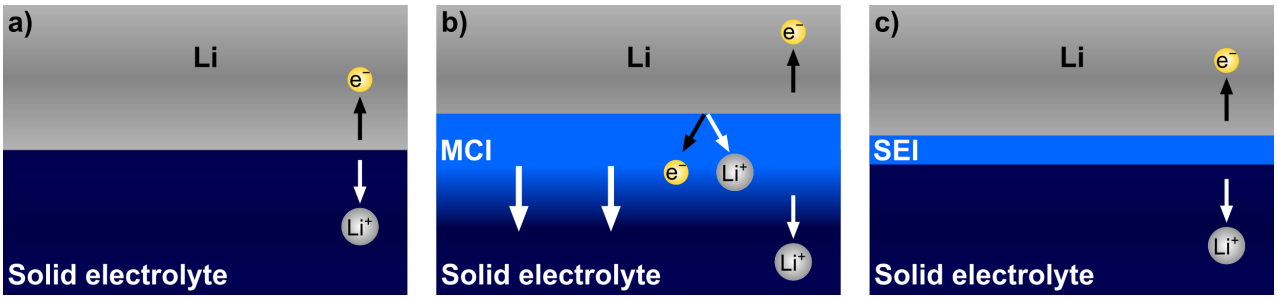

Figure 1.3.: Three different types of interfaces. a) Thermodynamically stable interface, electrons do not pass into the solid electrolyte (SE). b) Formation of mixed conducting interphase (MCI), depleting both Li and SE, leading to short circuiting. c) Kinetically stabilized stable interphase formation (SEI).

Therefore, SEIs and SEI formation have become a major focus for the tuning of batteries.[35] There have been approaches to apply artificial SEIs from the binary compounds Li_3N and Li_3P onto lithium anodes in order to prevent reaction with SEs. However, these deposited layers tend to be relatively thick, brittle, and to have poor interconnection.[36] Thus, tuning of SEs to form suitable SEIs upon reaction with the lithium anode is preferable.

One SE used mainly in thin film batteries is the amorphous lithium phosphorus oxynitride (a-LiPON).[37–39] a-LiPON is a SE with the chemical composition $Li_xPO_yN_z$. While a-LiPON exhibits relatively moderate ionic conductivity in comparison to other solid electrolytes, it is very hard and can possibly suppress dendrite formation at lithium/LiPON interface due to its high shear modulus.[31,40] Its rather moderate ionic conductivity in the region of $10^{-6}\,\mathrm{S\,cm^{-1}}$ is heavily dependent on the nitrogen content and the thickness of the applied film.[29,39,41,42]

Preparation of a-LiPON thin films can be accomplished by radio frequency (RF) magnetron sputtering of lithium phosphate,[43–45] pulsed laser deposition (PLD),[46,47] metal-organic chemical vapor deposition (MOCVD),[48,49] or by atomic layer deposition (ALD).[42,50] Due to the relatively easy deposition and controllable thickness of a-LiPON thin films, thin film batteries with thicknesses of only 15 µm and flexible geometries can be built. These miniaturized batteries can be built with lithium metal anodes, enabling high potentials and large capacities. They can be used in medical applications like pacemakers, implantable defibrillators, sensors, or neural stimulators.[28,38] A schematic cross-section of a thin-film lithium battery is shown in Figure 1.2.[37,38] a-LiPON was long thought to be thermodynamically stable against the lithium anode.[51,52] However, upon contact with metallic lithium, formation of decomposition products like Li_3PO_4, Li_3P, Li_3N, and Li_2O have been observed. These decomposition products' ionic conductivity is high enough to provide battery function, while insulating electronically, leading to a SEI.[53,54]

Although—or even because—it is amorphous, the structure of a-LiPON has been investigated extensively in order to better simulate degradation and conductivity processes.[55–61] Many simulations depend on crystalline model structures.[60] The structural motifs found in amorphous LiPON are single $P(O,N)_4$ tetrahedra with apical N atoms (N_a) and tetrahedra that are connected by a bridging

nitrogen atom (N_b). The formerly postulated threefold coordinated nitrogen atom (N_t) was not confirmed in subsequent studies.[56–58]

Beside a wide variety of stoichiometries in amorphous LiPON, there are only four crystalline lithium oxonitridophosphates known so far: $Li_{2.88}PO_{3.73}N_{0.14}$, Li_2PO_2N, $Li_{14}(PON_3)_2O$, and $Li_{3.6}PO_{3.4}N_{0.6}$. $Li_{2.88}PO_{3.73}N_{0.14}$, $Li_{14}(PON_3)_2O$, and $Li_{3.6}PO_{3.4}N_{0.6}$ only comprise $P(O,N)_4$ tetrahedra occurring as $[PO_3N]^{4-}$, $[PO_2N_2]^{5-}$, and $[PON_3]^{6-}$.[62–65] In addition to tetrahedra, oxide anions are found in $Li_{14}(PON_3)_2O$, making this the first reported lithium oxonitridophosphate oxide. In Li_2PO_2N, the anionic structure consists of infinite chains of corner-sharing tetrahedra with a P–N–P backbone and apical O atoms (Figure 1.4).[62–65]

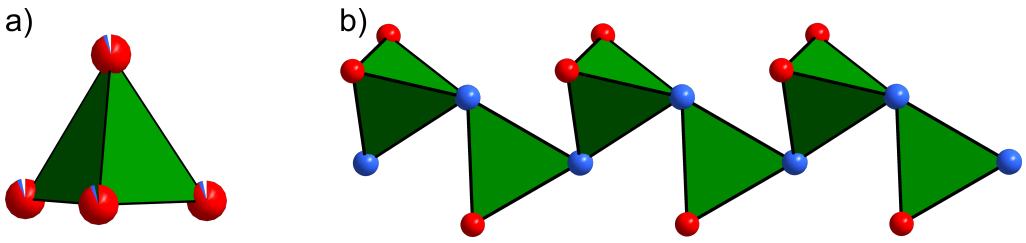

Figure 1.4.: Structural motifs in lithium oxonitridophosphates. O atoms are shown in red, N atoms in blue. a) Non-condensed tetrahedra (here with mixed occupancy of vertices). b) infinite chains of tetrahedra with P–N–P backbone.

In phosphates, description of structures by the degree of condensation κ is a common method to visualize the connectivity of a phase consisting of tetrahedra (Equation (1.2)).[66]

$$\kappa = \frac{number\ of\ central\ atoms\ (P)}{number\ of\ vertices\ (O/N)} \tag{1.2}$$

In lithium oxonitridophosphates, only two degrees of condensation are known so far, which are $\kappa = 1/4$ for the non-condensed tetrahedra, and $\kappa = 1/3$ for infinite chains of tetrahedra. With non-condensed tetrahedra and infinite chains of tetrahedra the only known structural motifs in crystalline lithium oxonitridophosphates, the range of model structures is still narrow (Figure 1.4). Since condensation of tetrahedra caused by incorporation of nitrogen was found to be beneficial for conductivity in a-LiPON,[57] explorative synthesis of crystalline lithium oxonitridophosphates with hitherto not investigated composition seems beneficial.

Finally, due to their relation to a-LiPON, crystalline lithium oxonitridophosphates might themselves exhibit ionic conductivities interesting for solid electrolytes or as sputtering target for the production of thin solid films. So far, only the ionic conductivities of $Li_{2.88}PO_{3.73}N_{0.14}$, Li_2PO_2N, and $Li_{3.6}PO_{3.4}N_{0.6}$ are known. Li_2PO_2N has been used as sputtering target for the synthesis of a-LiPON thin films.[42,47] It has also been used as model structure for simulation of LiPON degradation in contact with lithium anodes.[60]

For all these reasons, explorative synthesis of crystalline lithium oxonitridophosphates is a worthwhile research objective. There have been several different synthesis methods so far. With $LiPO_3$ and Li_3N as starting materials in a flowing N_2 atmosphere, $Li_{2.88}PO_{3.73}N_{0.14}$ can be obtained after

24 hours at 600 °C.[62] Li_2PO_2N is synthesized by solid-state reaction of Li_2O, P_2O_5, and P_3N_5 at 950 °C.[63] $Li_{14}(PON_3)_2O$ can be prepared by reaction of the molecular precursors phosphoric triamide $PO(NH_2)_3$ and $LiNH_2$ at 550 °C in evacuated fused silica ampoules.[64] $Li_{3.6}PO_{3.4}N_{0.6}$ is the latest reported crystalline lithium oxonitridophosphate and can be obtained by simple ball-milling of $LiPO_3$ and Li_3N for 20 min.[65] All of these synthesis strategies yield microcrystalline powders, complicating structural analysis. Thus, development of synthesis strategies that yield larger single-crystals is important for acceleration of structural characterization.

A field directly adjacent to that of lithium oxonitridophosphates is that of lithium nitridophosphates and it might offer a solution for synthesis of larger single-crystals. In lithium nitridophosphates, this problem was solved by application of an excess of Li_3N in the solid-state reactions. This resulted in phase-pure compounds and the formation of a self-flux, which stimulates the formation of larger single-crystals.[67–69]

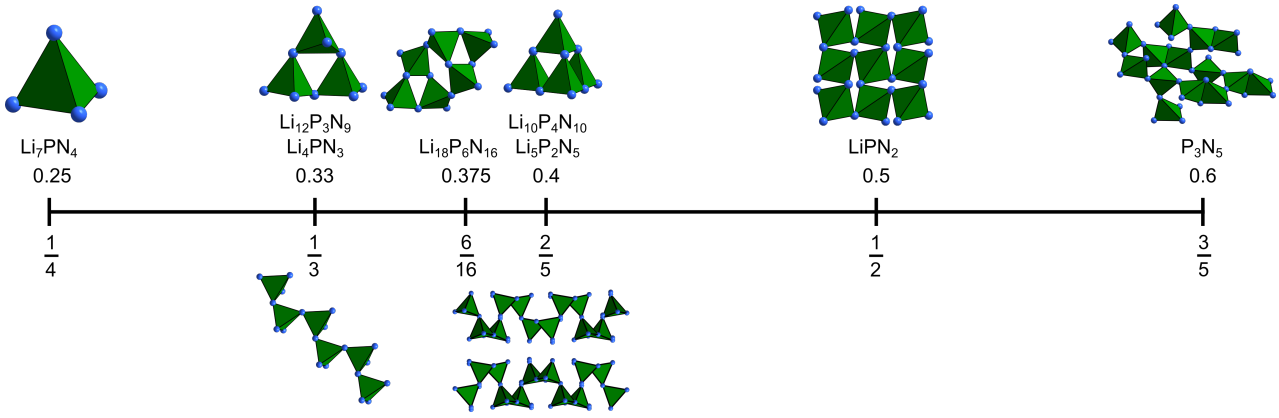

Figure 1.5.: Known structural motifs of PN_4-tetrahedra observed in lithium nitridophosphates before the start of this work.[70–75] N atoms are shown in blue.

The structural chemistry of these materials is diverse, with various structural motifs in different degrees of condensation κ. In the range of $0.25 \leq \kappa \leq 0.5$ there are five different degrees of condensation known with seven different structures exhibiting different structural motifs. Besides the structural diversity, ionic conductivity can also be observed in lithium nitridophosphates. Li_7PN_4 ($\kappa = 1/4$), the lithium nitridophosphate with the highest lithium content, consists of non-condensed tetrahedra, was first synthesized in 1971 and exhibits a conductivity of $\sigma_{400\,K} = 1.7 \times 10^{-5}\,S\,cm^{-1}$.[70,76] The lithium nitridophosphate with the largest connectivity is $LiPN_2$ ($\kappa = 0.5$). First synthesized in 1960, it is the oldest known and most stable lithium nitridophosphate. It exhibits an ionic conductivity of $\sigma_{400\,K} = 6.9 \times 10^{-7}\,S\,cm^{-1}$. The structure consists of a network of all-side corner-sharing PN_4 tetrahedra with lithium in tetrahedral coordination spheres.[68,77] Within this range of condensation, there are $Li_{12}P_3N_9$, Li_4PN_3 (both $\kappa = 1/3$), $Li_{18}P_6N_{16}$ ($\kappa = 6/16$), α-$Li_{10}P_4N_{10}$, and $Li_5P_2N_5$ (both $\kappa = 2/5$). The structural motifs are *dreier*-rings, infinite chains of corner-sharing tetrahedra, six tetrahedra that form a *vierer*-ring with two connected *dreier*-rings, a T2 supertetrahedron, and layers of tetrahedra, respectively (Figure 1.5).[68,71–75]

This structural diversity is remarkable, however, possibly incomplete. So far, only lithium nitridophosphates with high lithium content—thus, low connectivity—have been investigated. Since there are other alkali- and alkaline earth nitridophosphates known with $0.5 \leq \kappa < 0.6$ (with κ limited by the binary compound P_3N_5), there might be additional lithium nitridophosphates to be found in this area of the phase diagram.[78–82]

1.1. References

[1] J. A. Arfvedson, *Ann. Chim. Phys.* **1819**, 82–107.

[2] M. E. Weeks, *J. Chem. Educ.* **1932**, *9*, 223–227, DOI 10.1021/ed009p3.

[3] M. E. Weeks, *J. Chem. Educ.* **1932**, *9*, 1035–1045, DOI 10.1021/ed009p1035.

[4] M. E. Weeks, M. E. Larson, *J. Chem. Educ.* **1937**, 403–407, DOI 10.1021/ed014p403.

[5] U. Ocken, *Die Entdeckung der Chemischen Elemente und die Etymologie ihrer Namen – Von der Antike über die Alchemie bis zum Atomzeitalter*, BoD – Books on Demand, Achim-Baden, **2017**, pp. 193–194.

[6] M. Bertau, W. Voigt, A. Schneider, G. Martin, *Chemie Ing. Tech.* **2017**, *89*, 64–81, DOI 10.1002/cite.201600101.

[7] P. Kausch, M. Bertau, J. Gutzmer, J. Matschullat, *Strategische Rohstoffe — Risikovorsorge*, (Ed.: P. Kausch), Springer Spektrum, Berlin, Heidelberg, **2014**, DOI 10.1007/978-3-642-39704-2.

[8] B. W. Jaskula, *United States Geol. Surv.* **2023**, 2022–2023.

[9] BP PLC, *BP Energy Outlook 2023* **2023**, *70*, 8–20.

[10] S. A. Hedya, A. Avula, H. D. Swoboda, *Lithium Toxicity*, StatPearls Publishing, Treasure Island (FL), **2022**.

[11] G. Ayano, *Austin J. Psychiatry Behav. Sci.* **2016**, *3*, 1053, DOI 10.4172/2472-1077.1000109.

[12] A. Miatto, B. K. Reck, J. West, T. E. Graedel, *Resour. Conserv. Recycl.* **2020**, *162*, 105034, DOI 10.1016/j.resconrec.2020.105034.

[13] F. Maisel, C. Neef, F. Marscheider-Weidemann, N. F. Nissen, *Resour. Conserv. Recycl.* **2023**, *192*, 106920, DOI 10.1016/j.resconrec.2023.106920.

[14] B. L. Rinkel, D. S. Hall, I. Temprano, C. P. Grey, *J. Am. Chem. Soc.* **2020**, *142*, 15058–15074, DOI 10.1021/jacs.0c06363.

[15] K. Zhou, Q. Xie, B. Li, A. Manthiram, *Energy Storage Mater.* **2021**, *34*, 229–240, DOI 10.1016/j.ensm.2020.09.015.

[16] F. Wang, J. Bai, *Batter. & Supercaps* **2022**, *5*, e202100174, DOI https://doi.org/10.1002/batt.202100174.

[17] B. Ramasubramanian, S. Sundarrajan, V. Chellappan, M. V. Reddy, S. Ramakrishna, K. Zaghib, *Batteries* **2022**, *8*, 1–25, DOI 10.3390/batteries8100133.

[18] G. Wittstock, *Lehrbuch der Elektrochemie*, Wiley VCH GmbH, Weinheim, Germany, **2023**, pp. 834–852.

[19] J. M. Tarascon, D. Guyomard, *Electrochim. Acta* **1993**, *38*, 1221–1231, DOI 10.1016/0013-4686(93)80053-3.

[20] P. U. Nzereogu, A. D. Omah, F. I. Ezema, E. I. Iwuoha, A. C. Nwanya, *Appl. Surf. Sci. Adv.* **2022**, *9*, 100233, DOI 10.1016/j.apsadv.2022.100233.

[21] W. Xu, J. Wang, F. Ding, X. Chen, E. Nasybulin, Y. Zhang, J. G. Zhang, *Energy Environ. Sci.* **2014**, *7*, 513–537, DOI 10.1039/c3ee40795k.

[22] M. Li, J. Lu, Z. Chen, K. Amine, *Adv. Mater.* **2018**, *30*, 1–24, DOI 10.1002/adma.201800561.

[23] J. O. Besenhard, H. P. Fritz, *J. Electroanal. Chem.* **1974**, *53*, 329–333, DOI 10.1016/S0022-0728(74)80146-4.

[24] G. Eichinger, *J. Electroanal. Chem.* **1976**, *74*, 183–193, DOI 10.1016/S0022-0728(76)80234-3.

[25] M. Arakawa, J. I. Yamaki, *J. Electroanal. Chem.* **1987**, *219*, 273–280, DOI 10.1016/0022-0728(87)85045-3.

[26] Y. Chen, Y. Kang, Y. Zhao, L. Wang, J. Liu, Y. Li, Z. Liang, X. He, X. Li, N. Tavajohi, B. Li, *J. Energy Chem.* **2021**, *59*, 83–99, DOI 10.1016/j.jechem.2020.10.017.

[27] M. Kaliaperumal, M. S. Dharanendrakumar, S. Prasanna, K. V. Abhishek, R. K. Chidambaram, S. Adams, K. Zaghib, M. V. Reddy, *Materials* **2021**, *14*, 5676, DOI 10.3390/ma14195676.

[28] B. Owens, B. Scrosati, P. Reale in *Encyclopedia of Electrochemical Power Sources*, 1964, Elsevier, Amsterdam, **2009**, pp. 120–128, DOI 10.1016/B978-044452745-5.00118-0.

[29] F. Zheng, M. Kotobuki, S. Song, M. O. Lai, L. Lu, *J. Power Sources* **2018**, *389*, 198–213, DOI 10.1016/j.jpowsour.2018.04.022.

[30] J. F. Oudenhoven, L. Baggetto, P. H. Notten, *Adv. Energy Mater.* **2011**, *1*, 10–33, DOI 10.1002/aenm.201000002.

[31] E. G. Herbert, W. E. Tenhaeff, N. J. Dudney, G. M. Pharr, *Thin Solid Films* **2011**, *520*, 413–418, DOI 10.1016/j.tsf.2011.07.068.

[32] P. Hartmann, T. Leichtweiss, M. R. Busche, M. Schneider, M. Reich, J. Sann, P. Adelhelm, J. Janek, *J. Phys. Chem. C* **2013**, *117*, 21064–21074, DOI 10.1021/jp4051275.

[33] S. Wenzel, T. Leichtweiss, D. Krüger, J. Sann, J. Janek, *Solid State Ionics* **2015**, *278*, 98–105, DOI 10.1016/j.ssi.2015.06.001.

[34] S. Wenzel, S. Randau, T. Leichtweiß, D. A. Weber, J. Sann, W. G. Zeier, J. Janek, *Chem. Mater.* **2016**, *28*, 2400–2407, DOI 10.1021/acs.chemmater.6b00610.

[35] Y. Zhu, X. He, Y. Mo, *J. Mater. Chem. A* **2016**, *4*, 3253–3266, DOI 10.1039/c5ta08574h.

[36] V. Jabbari, V. Yurkiv, M. G. Rasul, A. H. Phakatkar, F. Mashayek, R. Shahbazian-Yassar, *Energy Storage Mater.* **2023**, *57*, 1–13.

[37] J. B. Bates, G. R. Gruzalski, N. J. Dudney, C. F. Luck, X. Yu, *Solid State Ionics* **1994**, *70–71*, 619–628, DOI 10.1016/0167-2738(94)90383-2.

[38] N. J. Dudney, B. J. Neudecker, *Current Opinion in Solid State and Materials Science* **1999**, *4*, 479–482, DOI 10.1016/S1359-0286(99)00052-2.

[39] J. D. LaCoste, A. Zakutayev, L. Fei, *J. Phys. Chem. C* **2021**, *125*, 3651–3667, DOI 10.1021/acs.jpcc.0c10001.

[40] C. Monroe, J. Newman, *J. Electrochem. Soc.* **2005**, *152*, A396–A404, DOI 10.1149/1.1850854.

[41] C. H. Choi, W. I. Cho, B. W. Cho, H. S. Kim, Y. S. Yoon, Y. S. Tak, *Electrochem. Solid-State Lett.* **2002**, *5*, 13–17, DOI 10.1149/1.1420926.

[42] A. C. Kozen, A. J. Pearse, C. F. Lin, M. Noked, G. W. Rubloff, *Chem. Mater.* **2015**, *27*, 5324–5331, DOI 10.1021/acs.chemmater.5b01654.

[43] J. B. Bates, N. J. Dudney, G. R. Gruzalski, R. A. Zuhr, A. Choudhury, C. F. Luck, J. D. Robertson, *J. Power Sources* **1993**, *43*, 103–110, DOI 10.1016/0378-7753(93)80106-Y.

[44] Y. Su, J. Falgenhauer, A. Polity, T. Leichtweiß, A. Kronenberger, J. Obel, S. Zhou, D. Schlettwein, J. Janek, B. K. Meyer, *Solid State Ionics* **2015**, *282*, 63–69, DOI 10.1016/j.ssi.2015.09.022.

[45] L. Le Van-Jodin, A. Claudel, C. Secouard, F. Sabary, J. P. Barnes, S. Martin, *Electrochim. Acta* **2018**, *259*, 742–751, DOI 10.1016/j.electacta.2017.11.021.

[46] S. Zhao, Z. Fu, Q. Qin, *Thin Solid Films* **2002**, *415*, 108–113, DOI 10.1016/S0040-6090(02)00543-6.

[47] W. C. West, Z. D. Hood, S. P. Adhikari, C. Liang, A. Lachgar, M. Motoyama, Y. Iriyama, *J. Power Sources* **2016**, *312*, 116–122, DOI 10.1016/j.jpowsour.2016.02.034.

[48] H. T. Kim, T. Mun, C. Park, S. W. Jin, H. Y. Park, *J. Power Sources* **2013**, *244*, 641–645, DOI 10.1016/j.jpowsour.2012.12.109.

[49] L. Meda, E. E. Maxie, *Thin Solid Films* **2012**, *520*, 1799–1803, DOI 10.1016/j.tsf.2011.08.091.

[50] M. Nisula, Y. Shindo, H. Koga, M. Karppinen, *Chem. Mater.* **2015**, *27*, 6987–6993, DOI 10.1021/acs.chemmater.5b02199.

[51] J. B. Bates, N. J. Dudney, G. R. Gruzalski, R. A. Zuhr, A. Choudhury, C. F. Luck, J. D. Robertson, *Solid State Ionics* **1992**, *53–56*, 647–654, DOI 10.1016/0167-2738(92)90442-R.

[52] X. Yu, J. B. Bates, G. E. Jellison Jr., F. X. Hart, *J. Electrochem. Soc.* **1997**, *144*, 524–532, DOI 10.1149/1.1837443.

[53] A. Schwöbel, R. Hausbrand, W. Jaegermann, *Solid State Ionics* **2015**, *273*, 51–54, DOI 10.1016/j.ssi.2014.10.017.

[54] D. Cheng, T. A. Wynn, X. Wang, S. Wang, M. Zhang, R. Shimizu, S. Bai, H. Nguyen, C. Fang, M.-c. Kim, W. Li, B. Lu, S. J. Kim, Y. S. Meng, *Joule* **2020**, *4*, 2484–2500, DOI 10.1016/j.joule.2020.08.013.

[55] B. Fleutot, B. Pecquenard, H. Martinez, M. Letellier, A. Levasseur, *Solid State Ionics* **2011**, *186*, 29–36, DOI 10.1016/j.ssi.2011.01.006.

[56] N. Mascaraque, A. Durán, F. Muñoz, G. Tricot, *Int. J. Appl. Glas. Sci.* **2016**, *7*, 69–79, DOI 10.1111/ijag.12120.

[57] V. Lacivita, N. Artrith, G. Ceder, *Chem. Mater.* **2018**, *30*, 7077–7090, DOI 10.1021/acs.chemmater.8b02812.

[58] V. Lacivita, A. S. Westover, A. Kercher, N. D. Phillip, G. Yang, G. Veith, G. Ceder, N. J. Dudney, *J. Am. Chem. Soc.* **2018**, *140*, 11029–11038, DOI 10.1021/jacs.8b05192.

[59] F. Munõz, J. Ren, L. Van Wüllen, T. Zhao, H. Kirchhain, U. Rehfuß, T. Uesbeck, *J. Phys. Chem. C* **2021**, *125*, 4077–4085, DOI 10.1021/acs.jpcc.0c10427.

[60] K. Leung, A. J. Pearse, A. A. Talin, E. J. Fuller, G. W. Rubloff, N. A. Modine, *ChemSusChem* **2018**, *11*, 1956–1969, DOI 10.1002/cssc.201800027.

[61] J. Li, W. Lai, *Solid State Ionics* **2020**, *351*, 115329, DOI 10.1016/j.ssi.2020.115329.

[62] B. Wang, B. C. Chakoumakos, B. C. Sales, B. S. Kwak, J. B. Bates, *J. Solid State Chem.* **1995**, *115*, 313–323, DOI 10.1006/jssc.1995.1140.

[63] K. Senevirathne, C. S. Day, M. D. Gross, A. Lachgar, N. A. Holzwarth, *Solid State Ionics* **2013**, *233*, 95–101, DOI 10.1016/j.ssi.2012.12.013.

[64] D. Baumann, W. Schnick, *Eur. J. Inorg. Chem.* **2015**, 617–621, DOI 10.1002/ejic.201403125.

[65] P. López-Aranguren, M. Reynaud, P. Głuchowski, A. Bustinza, M. Galceran, J. M. López Del Amo, M. Armand, M. Casas-Cabanas, *ACS Energy Lett.* **2021**, *6*, 445–450, DOI 10.1021/acsenergylett.0c02336.

[66] F. Liebau, *Structural chemistry of silicates*, Springer, Berlin, Heidelberg, **1985**, DOI 10.1016/0025-5408(86)90097-8.

[67] W. Schnick, J. Luecke, *J. Solid State Chem.* **1990**, *87*, 101–106, DOI 10.1016/0022-4596(90)90070-E.

[68] W. Schnick, J. Lücke, *Z. Anorg. Allg. Chem.* **1990**, *588*, 19–25, DOI 10.1002/zaac.19905880103.

[69] E.-M. Bertschler, PhD thesis, Ludwig-Maximilians-University Munich, München, **2017**.

[70] W. Schnick, J. Luecke, *Solid State Ionics* **1990**, *38*, 271–273, DOI 10.1016/0167-2738(90)90432-Q.

[71] E.-M. Bertschler, R. Niklaus, W. Schnick, *Chem. Eur. J.* **2017**, *23*, 9592–9599, DOI 10.1002/chem.201700979.

[72] E.-M. Bertschler, C. Dietrich, J. Janek, W. Schnick, *Chem. Eur. J.* **2017**, *23*, 2185–2191, DOI 10.1002/chem.201605316.

[73] W. Schnick, U. Berger, *Angew. Chem. Int. Ed.* **1991**, *30*, 830–831, *Angew. Chem.* **1991**, *103*, 857–858, DOI 10.1002/anie.199108301.

[74] E.-M. Bertschler, C. Dietrich, T. Leichtweiß, J. Janek, W. Schnick, *Chem. Eur. J.* **2018**, *24*, 196–205, DOI 10.1002/chem.201704305.

[75] E.-M. Bertschler, R. Niklaus, W. Schnick, *Chem. Eur. J.* **2018**, *24*, 736–742, DOI 10.1002/chem.201704975.

[76] J. F. Brice, J. P. Motte, A. Maslout, J. Aubry, *C.R. Acad. Sci. Paris C* **1971**, *273*, 744–746.

[77] P. Eckerlin, C. Langereis, I. Maak, A. Rabenau, *Angew. Chem.* **1960**, *7*, 19561.

[78] A. A. Vitola, J. Ronis, T. Millers, *B. Acad. Sci. USSR. Ch.* **1990**, *1*, 35–39.

[79] K. Landskron, E. Irran, W. Schnick, *Chem. Eur. J.* **1999**, *5*, 2548–2553, DOI 10.1002/(sici)1521-3765(19990903)5:9<2548::aid-chem2548>3.3.co;2-n.

[80] J. Ronis, B. Bondars, A. A. Vitola, T. Millers, *Latv. PSR Zinat. Akad. Kim. Serija1* **1990**, *3*, 299–301.

[81] H. Jacobs, R. Nymwegen, *Z. Anorg. Allg. Chem.* **1997**, *623*, 429–433, DOI 10.1002/zaac.19976230168.

[82] K. Landskron, W. Schnick, *J. Solid State Chem.* **2001**, *156*, 390–393, DOI 10.1006/jssc.2000.9010.

2. Aims and Scope

The main objective of this work is the explorative synthesis of lithium oxonitridophosphates, their structural characterization and contextualization of their ionic conductivity. Since non-condensed $P(O,N)_4$ tetrahedra and infinite chains of corner-sharing tetrahedra are the only known structural motifs in lihtium oxonitridophosphates, expansion of structural diversity is one main goal of this work. As starting point, bulk synthesis of $Li_{27-x}[P_4O_{7+x}N_{9-x}]O_3$ was chosen. A single-crystal of this phase was obtained earlier during synthesis of β-$Li_{10}P_4N_{10}$ from P_3N_5 and Li_3N.[1] Thus, in addition to the compounds mentioned, Li_2O was chosen as defined oxygen source. By application of flux conditions through an excess of Li_3N,[2] formation of larger crystals was envisaged, since lithium oxonitridophosphates are known to form microcrystalline powders, thus expanding this method to the Li–P–O–N system.[3–6]

The so-obtained lithium oxonitridophosphates are subject to structural investigation with X-ray and neutron diffraction methods. Nuclear magnetic resonance spectroscopy is employed to corroborate the structures and to establish differentiation between $P(O,N)_4$ tetrahedra with differing O and N content. To exclude presence of H and other elements, Fourier transform infrared (FTIR) spectra, as well as elemental analyses energy dispersive X-ray (EDX) spectroscopy, inductively coupled plasma optical emission spectroscopy (ICP-OES), and CHNS combustion analysis is performed. All of the examined structures can only be solved by synopsis of some or all of these methods. For thermal stability measurements, variable-temperature XRD is used. Lithium ion conductivity is obtained from electrochemical impedance spectroscopy.

Many of the starting points and parameters for the synthesis of lithium oxonitridophosphates are derived from litihum nitridophosphate synthesis. However, with the typical combination of starting materials $LiPN_2$ and Li_7PN_4, no compound with $\kappa > 0.5$ can be produced. Thus, another aim for this work was establishment of a synthesis strategy for highly condensed lihtium nitridophosphates. Since only P_3N_5 can be used to increase the degree of condensation further, it was combined with $LiPN_2$ as starting material. The use of Li_3N was avoided, since it is prone to side reactions. High pressure was used for the synthesis, since it has been observed that higher degrees of condensation require elevated temperatures, at which decomposition of the starting materials would occur if no external pressure was applied.[7] Characterization of the thus obtained lithium nitridophosphates was approached with the same methods as for lithium oxonitridophosphates.

2.1. References

[1] E.-M. Bertschler, PhD thesis, Ludwig-Maximilians-University Munich, München, **2017**.

[2] E.-M. Bertschler, C. Dietrich, T. Leichtweiß, J. Janek, W. Schnick, *Chem. Eur. J.* **2018**, *24*, 196–205, DOI 10.1002/chem.201704305.

[3] B. Wang, B. C. Chakoumakos, B. C. Sales, B. S. Kwak, J. B. Bates, *J. Solid State Chem.* **1995**, *115*, 313–323, DOI 10.1006/jssc.1995.1140.

[4] K. Senevirathne, C. S. Day, M. D. Gross, A. Lachgar, N. A. Holzwarth, *Solid State Ionics* **2013**, *233*, 95–101, DOI 10.1016/j.ssi.2012.12.013.

[5] D. Baumann, W. Schnick, *Eur. J. Inorg. Chem.* **2015**, 617–621, DOI 10.1002/ejic.201403125.

[6] P. López-Aranguren, M. Reynaud, P. Głuchowski, A. Bustinza, M. Galceran, J. M. López Del Amo, M. Armand, M. Casas-Cabanas, *ACS Energy Lett.* **2021**, *6*, 445–450, DOI 10.1021/acsenergylett.0c02336.

[7] S. D. Kloß, W. Schnick, *Angew. Chem. Int. Ed.* **2019**, *58*, 7933–7944, *Angew. Chem.* **2019**, *131*, 8015–8027, DOI 10.1002/anie.201812791.

3. Structure Determination of the Crystalline LiPON Model Structure $Li_{5+x}P_2O_{6-x}N_{1+x}$ with $x \approx 0.9$

Stefanie Schneider, Lucas G. Balzat, Bettina V. Lotsch, and Wolfgang Schnick

Chem. Eur. J. **2023**, *29*, e202202984.
https://doi.org/10.1002/chem.202202984
DOI: 10.1002/chem.202202984

Reprinted (adapted) with permission from Chemistry – European Journal. Copyright 2022

$Li_{5+x}P_2O_{6-x}N_{1+x}$ ($x \approx 0.9$) is a crystalline compound suitable as model compound for the understanding of structural traits within amorphous LiPON materials. A plethora of analytical methods, including diffraction methods, NMR, vibration spectroscopy and elemental analyses, was employed for elucidation of structure and composition of this substance. Ionic conductivity was measured using impedance spectroscopy.

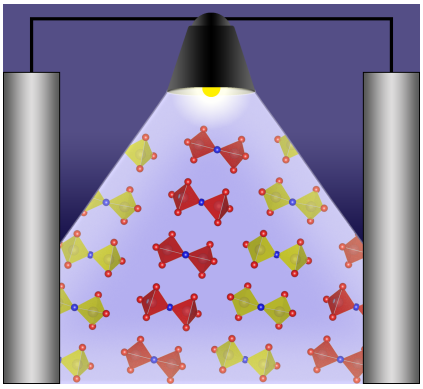

3.1. Abstract

Non-crystalline lithium oxonitridophosphate (LiPON) is used as solid electrolyte in all-solid-state batteries. Crystalline lithium oxonitridophosphates are important model structures to retrieve analytical information that can be used to understand amorphous phases better. The new crystalline lithium oxonitridophosphate $Li_{5+x}P_2O_{6-x}N_{1+x}$ was synthesized as off-white powder by ampoule synthesis at 700–800 °C under Ar atmosphere. It crystallizes in the monoclinic space group $P2_1/c$ with $a = 15.130\,87(11)$ Å, $b = 9.706\,82(9)$ Å, $c = 8.886\,81(7)$ Å, and $\beta = 106.8653(8)°$. Two $P(O,N)_4$ tetrahedra connected by an N atom form the structural motif $[P_2O_{6-x}N_{1+x}]^{(5+x)-}$. The structure was elucidated from X-ray diffraction data and the model corroborated by NMR and infrared spectroscopy, and elemental analyses. Measurements of ionic conductivity show a total ionic conductivity of 6.8×10^{-7} S cm^{-1} at 75 °C with an activation energy of 0.52(1) eV.

3.2. Introduction

Lithium oxonitridophosphates (LiPON) have gained attention over the past 30 years due to their Li^+ ion conductivity.[1–4] They develop stable solid electrolyte interfaces (SEI) in contact with Li[5,6] and therefore have found application as solid electrolytes (SE) within thin film all-solid-state batteries (SSBs).[7,8] Conceptually, SSBs provide the possibility of min iaturization of energy carriers with higher energy densities and better safety features than can be achieved with batteries based on liquid electrolytes.[6,9–12] In particular, the electrolytes used in SSBs are not flammable in contrast to the organic liquids conventionally used,[13,14] making them an excellent choice for application in medical devices like pacemakers.[15]

For miniaturization, solid electrolytes have to be applied in thin films, which is mostly achieved by sputtering lithium phosphate species in N_2-atmosphere onto a substrate.[1,2,4,16,17] The amorphous thin films obtained in this way have the advantage of mitigating grain boundary effects and enabling a high conductivity due to short diffusion pathways.[18]

However, structural analysis of amorphous materials – thin films or bulk – is always challenging. Absence of long-range order prevents classical diffraction methods like single-crystal X-ray diffraction or neutron powder diffraction. Instead, solid-state nuclear magnetic resonance (ssNMR) is a highly powerful tool to analyze local structure and especially the phosphate species present.[19,20] The anion sublattice plays a major role in Li^+ ion conductivity, as the Coulomb attraction towards Li^+ can be varied by the connectivity of the anionic species. Whereas non-condensed PO_4-tetrahedra exhibit strong Coulomb attraction towards Li^+, the net charge of one-dimensionally condensed chains (PO_3) is reduced, lowering attraction towards Li^+. Substitution of N for O in phosphate networks promotes condensation of $P(O,N)_4$-tetrahedra, leading to increased conductivity. Nitrogen atoms are versatile and can take doubly or triply bridging or even terminal positions. Whereas bridging N increase conductivity by the aforementioned mechanism, terminal N can hamper conductivity due to the higher charge Li^+ ions are exposed to.[21]

Whereas the search for amorphous LiPON materials with high ionic conductivities is important for their practical application as solid electrolyte materials, crystalline LiPON can help understand the intricacies of this system.[21–23] This can facilitate the development of the former. To date, only four crystalline phases in the quaternary system Li–P–O–N have been characterized crystallographically, namely $Li_{2.88}PO_{3.73}N_{0.14}$, Li_2PO_2N, $Li_{14}(PON_3)_2O$, and $Li_{3.6}PO_{3.4}N_{0.6}$.[20,24–26]
$Li_{2.88}PO_{3.73}N_{0.14}$ crystallizes isotypically to the three-dimensionally connected γ-Li_3PO_4 with both $P(O,N)_4$ and $Li(O,N)_4$ tetrahedra and is synthesized by heating Li_3N with $LiPO_3$ in N_2 gas flow. $P(O,N)_4$ tetrahedra are completely surrounded by $Li(O,N)_4$ tetrahedra.[24] Li_2PO_2N is prepared from Li_2O, P_2O_5, and P_3N_5 at 950 °C. Its structure comprises corner-sharing tetrahedra forming chains that are separated by Li^+ ions.[25] $Li_{3.6}PO_{3.4}N_{0.6}$ is obtained from $LiPO_3$ and Li_3N through mechanical milling for 20 min under Ar. Its structure consists of non-condensed, statistically disordered $[PO_2N_2]^{5-}$, $[PO_3N]^{4-}$, and $[PO_4]^{3-}$ tetrahedra.[20]
$Li_{14}(PON_3)_2O$, synthesized from $PO(NH_2)_3$ and $LiNH_2$, was the first oxonitridophosphate comprising non-condensed PON3 tetrahedra. It also contains O^{2-} ions, making it a lithium oxonitridophosphate oxide.[26] Impedance measurements have not been carried out for this material as yet.

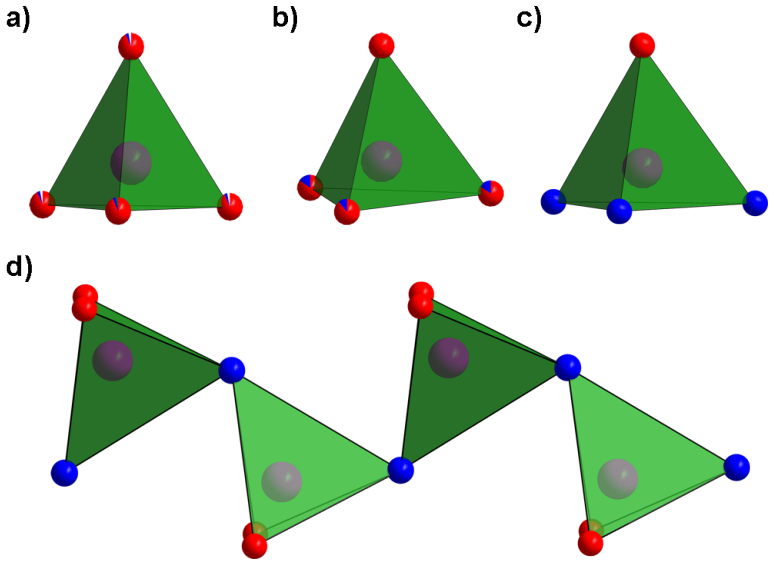

Figure 3.1.: Structural motifs in known crystalline lithium oxonitridophosphates. P atoms are displayed in pink, O and N are displayed in red and blue, respectively. a)–c): isolated tetrahedra with mixed and full occupations of O/N positions.[20,24,26] d): chain of tetrahedra.[25]

As can be seen in Figure 3.1, the existing structural motifs are limited to isolated tetrahedra and one-dimensional chains of corner-sharing tetrahedra. Thus, ab-initio calculations for the diffusion of Li^+ in a hypothetical crystalline LiPON material are often carried out using lithium phosphates as starting point. Besides non-condensed Li_3PO_4 phases, $Li_4P_2O_7$, which contains diphosphate anions, has been considered, in which bridging O were substituted by N. This results in the sum formula $Li_5P_2O_6N$, which was assumed to crystallize in $P\bar{1}$ as $Li_4P_2O_7$ does.[19,27]
In this work, we present the synthesis and thorough characterization of a new crystalline lithium oxonitridophosphate, namely $Li_{5+x}P_2O_{6-x}N_{1+x}$. This compound contains $[P_2O_{6-x}N_{1+x}]^{(5+x)-}$ oxoni-

tridodiphosphate anions, a motif that has not been reported in lithium oxonitridophosphates so far. With the spectroscopic and diffraction information collected from this compound, structural models for ab initio calculations on conductivity and NMR spectroscopic data of amorphous films can be improved.

3.3. Results and Discussion

3.3.1. Synthesis

$Li_{5+x}P_2O_{6-x}N_{1+x}$ was prepared from P_3N_5, Li_3N, and Li_2O in a 4 : 7 : 20 molar ratio under Ar atmosphere in an open Ta crucible that was placed in a sealed silica ampoule. The mixture was heated at $300\,K\,h^{-1}$, held at 760 °C for 90 h and cooled with a rate of $300\,K\,h^{-1}$. The reaction is very sensitive to changes in reaction conditions and side phases like $Li_{10}P_4N_{10}$ can occur.[28] As in lithium nitridophosphate syntheses, Li_3P is a common byproduct, especially at long reaction times and higher temperatures.[28–32] Large amounts of Li_2O remained in all samples. Stoichiometric amounts of starting materials as stated in the idealized balanced reaction Equation (3.1) did not yield the title compound in a phase pure state.

$$2\ P_3N_5 + (18-3x)\ Li_2O \longrightarrow 3\ Li_{5+x}P_2O_{6-x}N_{1+x} + (7-3x)\ Li_3N \tag{3.1}$$

Instead, Li_3N had to be introduced as starting material. This is in accordance with lithium nitridophosphate synthesis, in which an excess of Li_3N had to be used to achieve a Li_3N self-flux.[28–31] Furthermore, additional incorporation of N into the structure necessitates larger amounts of Li_3N as nitrogen source. Figure 3.2 shows the Rietveld-refinement for a sample with Li_2O (15 %) and small amounts of $Li_{10}P_4N_{10}$ (< 1 %) and Li_3P (< 1 %) as byproducts. Li_3P can largely be removed by washing the sample with dry ethanol. Soaking in dry ethanol additionally reduces Li_2O content, but also slowly decomposes $Li_{5+x}P_2O_{6-x}N_{1+x}$.

3.3.2. Crystal structure

The crystal structure was solved using both single-crystal and powder X-ray diffraction data. Due to small crystal sizes, only data sets of poor quality were collected with single-crystal X-ray diffraction. However, cell parameters and the space group were determined and subsequently used to solve the structure from X ray powder diffraction data. For additional crystallographic data, see Table 3.1 and Tables A.1–A.3.

$Li_{5+x}P_2O_{6-x}N_{1+x}$ crystallizes in the monoclinic space group $P2_1/c$ (no. 14) with lattice parameters $a = 15.130\,87(11)$ Å, $b = 9.706\,82(9)$ Å, $c = 8.886\,81(7)$ Å, and $\beta = 106.8653(8)°$. The structure comprises pairs of corner-sharing $P(O,N)_4$ tetrahedra connected by N. Two crystallographically different $[P_2O_{6-x}N_{1+x}]^{(5+x)-}$ diphosphate anions occur with altogether four crystallographically different P positions. The bridging atoms are assumed to be N, as substitution of bridging atoms by N is energetically favorable in contrast to bridging O-atoms (Figure 3.3).[21,27,33] Due to the very simi-

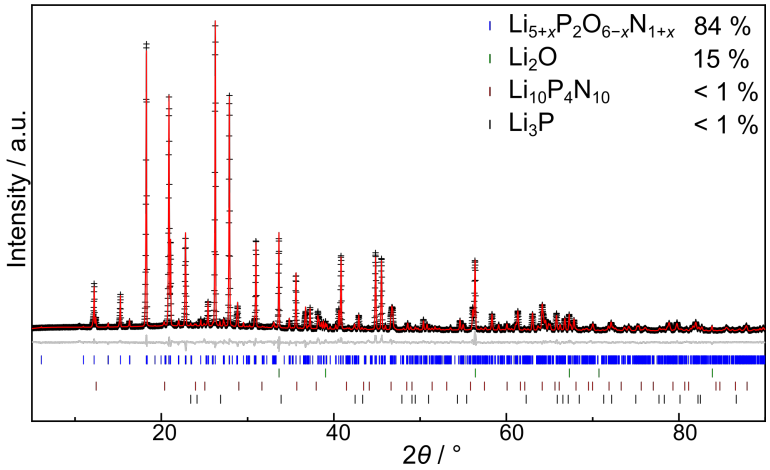

Figure 3.2.: Rietveld refinement for $Li_{5+x}P_2O_{6-x}N_{1+x}$ with observed (black crosses) and calculated (red line) intensities, and difference (gray line). Positions of possible Bragg reflections of $Li_{5+x}P_2O_{6-x}N_{1+x}$, Li_2O, $Li_{10}P_4N_{10}$, and Li_3P are shown with blue, green, brown, and black tick marks, respectively. Fractions of the respective phases are given in wt-%.

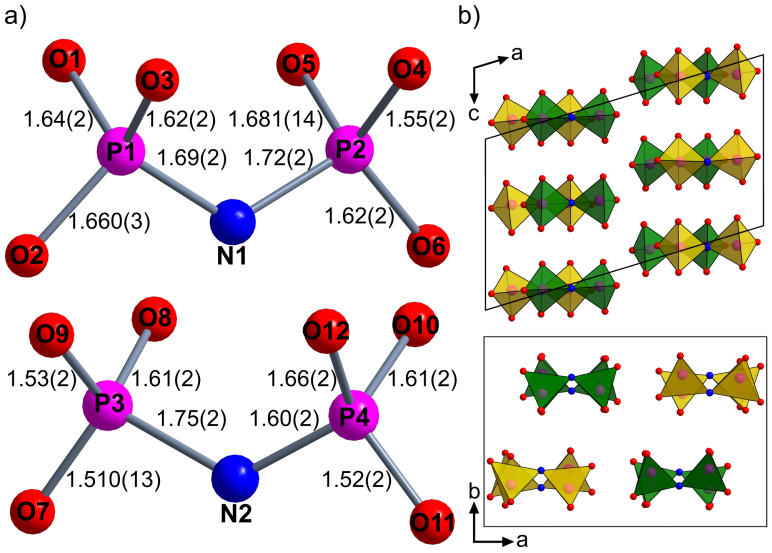

Figure 3.3.: Structural motifs in $Li_{5+x}P_2O_{6-x}N_{1+x}$. a) Vertex-sharing pairs of PO_3N-tetrahedra with bond lengths in Å. O-positions can also have mixed occupation with N. b) Unit cells with the two crystallographically different $[P_2O_{6-x}N_{1+x}]^{(5+x)-}$ motifs in yellow and green.

lar atomic form factors of O and N, the atom types cannot be determined unequivocally by X-ray diffraction. Mixed occupancy of additional O positions would lead to a higher negative charge of the structural motif and could be balanced by partial or full occupation of additional Li^+ positions. This issue can be considered with the sum formula $Li_{5+x}P_2O_{6-x}N_{1+x}$.

P–N bond lengths vary between 1.60(2)–1.75(2) Å, P–O bond lengths between 1.510(13) Å and 1.681(14) Å. These values are within the normal range for known P–N/O distances in reported crystalline LiPON phases.[20,24–26]

Table 3.1.: Crystallographic details on $Li_{5+x}P_2O_{6-x}N_{1+x}$. Standard deviations are given in parentheses.

formula	$Li_{5+x}P_2O_{6-x}N_{1+x}$
formula mass / g mol^{-1}	206.66
crystal system/ space group type	monoclinic $P2_1/c$ (no. 14)
lattice parameters / Å, °	$a = 15.13087(11)$
	$b = 9.70682(9)$
	$c = 8.88681(7)$
	$\beta = 106.8653(8)$
cell volume / Å^3	1249.091(18)
formula units per cell Z	8
X-ray density / g cm^2	2.198(1)
Absorption coefficient / cm^{-1}	62.63
radiation	Cu-K$_{\alpha 1}$ ($\lambda = 1.540\,596$ Å)
monochromator	Ge(111)
diffractometer	Stoe StadiP
detector	Mythen 1K linear PSD
2θ range / °	5–101
temperature / K	297(2)
data points	6432
number of observed reflections	1337
number of parameters	119
program used	TOPAS 6
structure refinement	Rietveld method
profile function	fundamental parameters
background function	shifted Chebychev
terms (backgr. function)	12
R_{wp}	0.064
R_{exp}	0.023
R_{p}	0.046
R_{Bragg}	0.032
χ^2	2.793

3.3.3. Nuclear magnetic resonance spectroscopy

^{31}P, ^{6}Li and ^{7}Li NMR measurements were performed. If no mixed occupation O/N is assumed, four distinct P positions can be expected to result in four signals with shifts around 14.2 ppm. Two distinct signals at 21.4 and 14.2 ppm are visible (Figure 3.4). For two PO_3N tetrahedra bridged by N, measurements in amorphous LiPON showed an isotropic shift $\delta_{iso}(^{31}\mathrm{P}) = 14.6$ ppm, while ab initio molecular dynamics (AIMD) simulations predict a shift of $\delta_{iso} = 12.77$ ppm.[19] This corresponds well with the observed $\delta = 14.2$ ppm. Furthermore, the deconvolution of NMR signals of amorphous LiPON shows a difference in shifts of about 10 ppm upon substituting the bridging O by N. In non-condensed phases, a shift difference of about 10 ppm is seen for each O substituted by N in the respective tetrahedron.[19] Thus, the second signal at 21.4 ppm is expected to be the result of

additional incorporation of one N at an O atomic position, PO_2N_2. The breadth of the signals is probably a result of statistically distributed incorporation of N into the anionic motifs and of the two crystallographically different dimers being present. As there are only two signals at 14.2 and 21.4 ppm, the environment of P is assumed to hold a maximum of two N atoms. This would result in $Li_{5+x}P_2O_{6-x}N_{1+x}$ with $0 \leq x \leq 2$. Deconvolution of the two signals yielded a 53(2) : 47(2) ratio of the signals at 14.2 and 21.4 ppm, which corresponds to the presence of 94(4) % $[P_2O_5N_2]^{6-}$ and 6(4) % $[P_2O_6N]^{5-}$. This means that in 94(4) % of the dimers one additional N is inserted, leading to $0.90 \leq x \leq 0.98$. However, as this error margin is possibly an underestimation of the actual error, the more rough value of $x \approx 0.9$ will be used. More precise values could be obtained by additional O/N-sensitive analytical methods like neutron diffraction.

^{6}Li and ^{7}Li NMR spectra show one broad signal at 1.15 and 2.9 ppm, respectively, indicating only very low mobility of Li^+ (Figures A.2 and A.3).[34,35] To extract information on Li dynamics, variable temperature measurements would be necessary.[34,36,37]

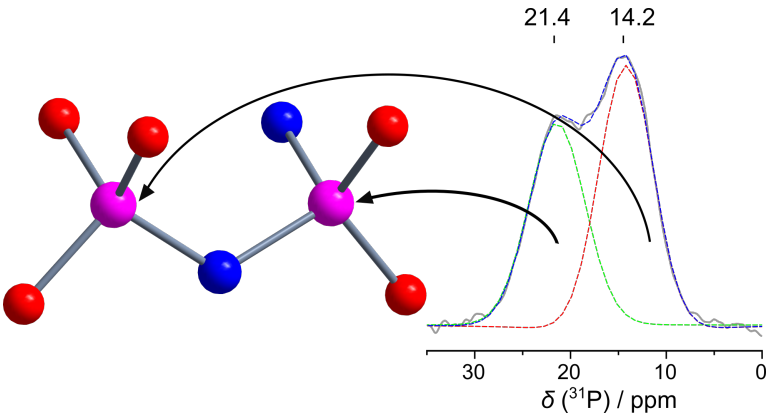

Figure 3.4.: ^{31}P NMR spectrum of $Li_{5+x}P_2O_{6-x}N_{1+x}$ with corresponding tetrahedra. Signals were fitted with pseudo-Voigt functions.[38] P, O, and N are shown in pink, red, and blue, respectively.

3.3.4. FTIR and thermal stability measurements

Infrared (IR) spectroscopic measurements were conducted in order to rule out the presence of hydrogen in the structure. O–H or N–H vibrational bands should be visible in the area of 2800–3200 and 3000–3500 cm^{-1}, if hydrogen is present in the structure. However, no peaks are visible in this area (Figure 3.5).[39–41] The fingerprint area between 400–1200 cm^{-1} contains six distinct signals. Possibly, some modes are superimposed and cannot be resolved. Modes in the area of 900–1100 cm^{-1} correspond to stretching vibrations of P–N, P–O and P–N–P, whereas those in the area of 500–550 cm^{-1} result from bending modes of P–N–P and O–P–O.[39–42] The sharp signal at 785 cm^{-1} might be caused by asymmetric stretching modes of P–N–P, as was proposed for short chains within lithium oxonitridophosphates.[43] Furthermore, the width of the signals at ca. 500 cm^{-1} might also result from underlying Li–O/N vibrations.[43,44]

$Li_{5+x}P_2O_{6-x}N_{1+x}$ is thermally stable up to 620 °C. At 640 °C, incipient decomposition of $Li_{5+x}P_2O_{6-x}N_{1+x}$ to Li_3P is visible in temperature-dependent PXRD (Figure 3.6). Reflections of

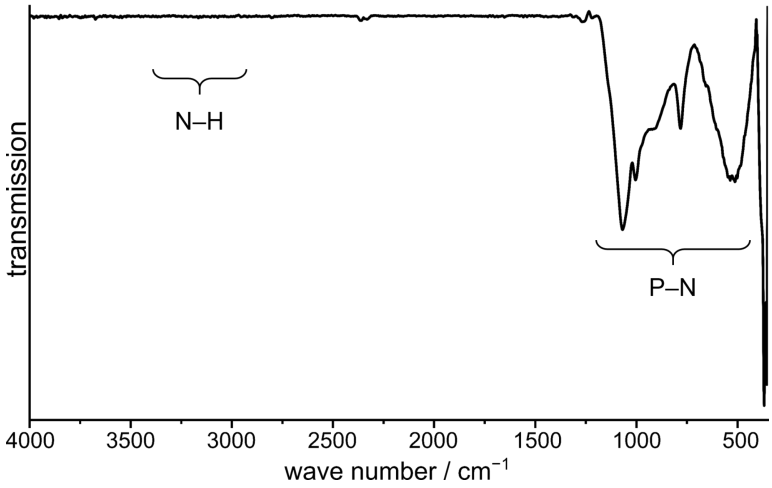

Figure 3.5.: Infrared spectrum of $Li_{5+x}P_2O_{6-x}N_{1+x}$ measured with an ATR unit. No O–H or N–H peaks are visible. Small signals at 2366 cm^{-1} can be explained by partial hydrolysis of the sample surface.

$Li_{5+x}P_2O_{6-x}N_{1+x}$ are visible up to 800 °C, above which only Li_3P is visible. This is in good agreement with other lithium nitridophosphates[28–31] and with the observation of Li_3P as side phase at syntheses with higher reaction temperature. Upon cooling, only Li_3P remains in the sample.

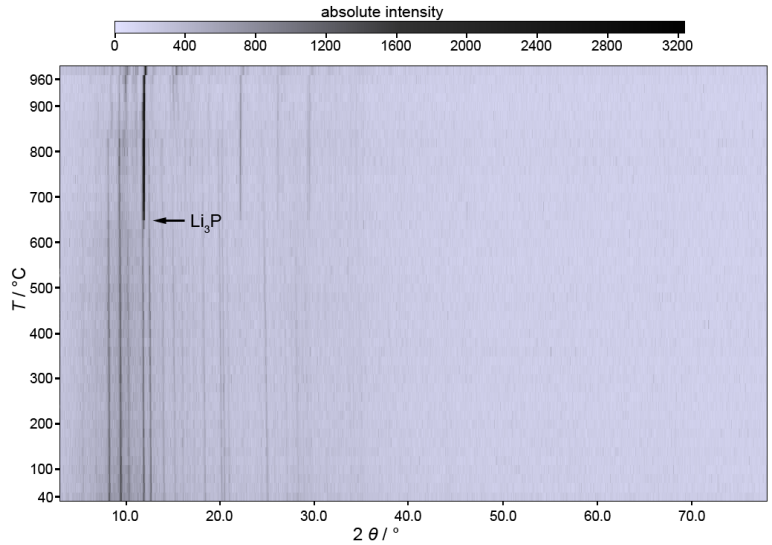

Figure 3.6.: Temperature-dependent X-ray powder diffraction (Mo $K_{\alpha 1}$ $\lambda = 0.709\,30$ Å) data shows $Li_{5+x}P_2O_{6-x}N_{1+x}$ up to 900 °C, with decomposition towards Li_3P beginning at 640 °C.

Elemental analysis is hindered by the compound's composition, side phases and sensitivity to hydrolysis. Electrondispersive X-ray spectroscopy (EDX), inductively-coupled plasma optical emission spectroscopy (ICP-OES), and combustion analysis (CHNS) was performed. However, light elements are not (Li) or not reliably (O,N) detected by EDX. ICP-OES can only detect Li and P, which is confounded by Li-containing side phases (mainly Li_2O, and residues of $Li_{10}P_4N_{10}$). CHNS can only give absolute values for N, but due to hydrolysis during the weighing process, these results are also

falsified. Thus, elemental analysis (EDX) was only deployed to confirm that no other elements are present in the sample.

3.3.5. Determination of the ionic conductivity

The ionic conductivity of $Li_{5+x}P_2O_{6-x}N_{1+x}$ was determined through electrochemical impedance spectroscopy (EIS). All measured samples contained Li_2O and $Li_{10}P_4N_{10}$ as side phases. EIS data of $Li_{5+x}P_2O_{6-x}N_{1+x}$ measured at 75 °C are shown in a Nyquist plot in Figure 3.7. All temperature-dependent EIS spectra are shown in Figure A.4. The data were fitted with an equivalent circuit containing two circuits in series, containing each a resistor and a constant phase element (CPE) in parallel. Polarization was modeled with an additional CPE in series. CPEs were chosen to account for non-ideal sample behavior.[45] The capacities of CPE1 and CPE2 were calculated using the Brug formula.[46] The capacities at 75 °C of CPE1 and CPE2 are 2.9×10^{-11} F and 1.1×10^{-10} F, respectively. Therefore, the first process modeled by R1/CPE1 was assigned to the bulk ionic conductivity of $Li_{5+x}P_2O_{6-x}N_{1+x}$.[47] The bulk ionic conductivity was calculated using the resistance R1 and is 2.2×10^{-7} S cm^{-1} at 25 °C and 1.4×10^{-6} S cm^{-1} at 75 °C. The second semi-circle modeled by R2/CPE2 could stem from grain boundaries or ionic contributions from the impurity side phase $Li_{10}P_4N_{10}$, but an unambiguous assignment was not possible.[28,47] The total ionic conductivity of $Li_{5+x}P_2O_{6-x}N_{1+x}$ was calculated from the total resistance (R1+R2) and amounts to 4.6×10^{-8} S cm^{-1} at 25 °C and 6.8×10^{-7} S cm^{-1} at 75 °C.

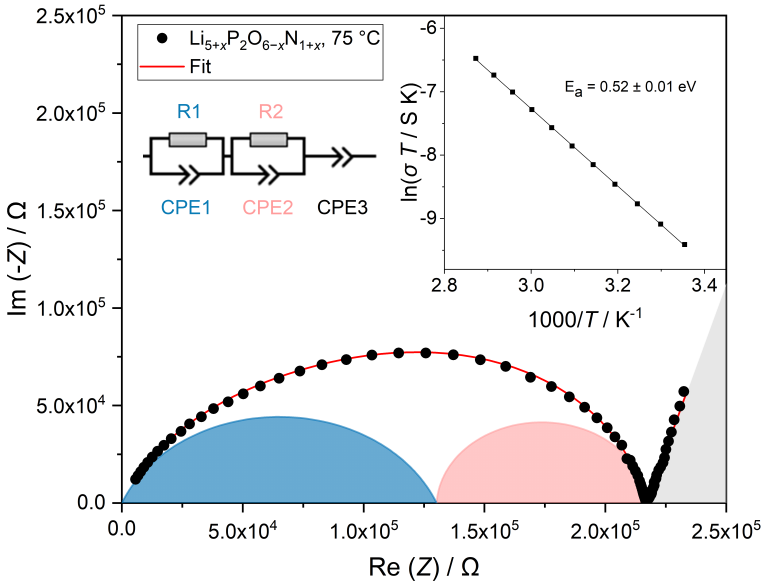

Figure 3.7.: Nyquist plot of $Li_{5+x}P_2O_{6-x}N_{1+x}$ at 75 °C. The data were modelled using an R1/CPE1-R2/CPE2-CPE3 model. The contributions of the different circuit elements have been highlighted. The inset shows an Arrhenius plot obtained from temperature-dependent EIS measurements resulting in an activation energy of 0.52(1) eV for $Li_{5+x}P_2O_{6-x}N_{1+x}$. This is a corrected version of the figure according to a submitted corrigendum.

The total activation energy of $Li_{5+x}P_2O_{6-x}N_{1+x}$ was obtained by fitting temperature-dependent EIS data to a linear Arrheniustype behavior. The corresponding Arrhenius plot is shown in the inset in Figure 3.7. The total activation energy for $Li_{5+x}P_2O_{6-x}N_{1+x}$ is 0.52(1) eV. Both the ionic conductivity and activation energy lie well in the expected range for LiPON materials (e. g.: LiPON, 1.6×10^{-6} S cm^{-1}, 0.58 eV; $Li_{3.6}PO_{3.4}N_{0.6}$, 5.6×10^{-8} S cm^{-1}, 0.55 eV; all values at 25 °C).[20,22,24,25,48] Since no completely phase-pure samples of $Li_{5+x}P_2O_{6-x}N_{1+x}$ were obtained, several samples were measured to confirm the obtained ionic conductivity and activation energy. All samples gave similar values for ionic conductivity and activation energy. The EIS data for two different samples of $Li_{5+x}P_2O_{6-x}N_{1+x}$ are shown in the Supporting Information as representative examples (Figures A.4–A.6, Tables A.7–A.9).

3.4. Conclusion

The lithium oxonitridophosphate $Li_{5+x}P_2O_{6-x}N_{1+x}$ was prepared from ampoule synthesis. It crystallizes in space group $P21/c$ with a = 15.130 87(11) Å, b = 9.706 82(9) Å, c = 8.886 81(7) Å, and β = 106.8653(8)°. The structure consists of corner-sharing tetrahedra, similar to $Li_4P_2O_7$.[49–53] N does not only occupy bridging positions, but also terminal ones. Stoichiometric use of starting materials does not produce $Li_{5+x}P_2O_{6-x}N_{1+x}$ ($x = 0$). Instead, Li_3N had to be used to obtain the phase, but also results in $x \approx 0.93$ due to the additional N source material. The total ionic conductivity of 4.6×10^{-8} S cm^{-1} at 25 °C puts $Li_{5+x}P_2O_{6-x}N_{1+x}$ into a range comparable to that of amorphous LiPON.[3,48] Grain boundary effects restrict Li^+ movement, reducing applicability in all-solid-state batteries.[18,54] Nonetheless, with the structural and spectroscopic information obtained from $Li_{5+x}P_2O_{6-x}N_{1+x}$, structural models for amorphous LiPON films can be improved in their accuracy. Furthermore, analytics of LiPON thin films – especially NMR – can benefit from this, as local structure observed by NMR in amorphous materials can be cross-checked with crystalline references. Finally, this compound might be employed as a model structure for the computational investigation of conduction pathways. In the future, neutron diffraction experiments should be conducted for more detailed information on O/N occupation.

3.5. Acknowledgements

The authors thank Lisa Gamperl, Christian Minke, Valentin Bockmaier, and Sandra Albrecht for EDX, NMR, FTIR, and ICPOES measurements, respectively (all at Department of Chemistry, LMU Munich). The authors acknowledge funding support from the Deutsche Forschungsgemeinschaft (DFG, German Research Foundation) under Germany's Excellence Strategy-EXC 2089/1-390776260 (e-conversion). L.G.B. and B.V.L. acknowledge financial support by the German Federal Ministry of Research and Education (BMBF), project 03XP0177B (FestBatt). Open Access funding enabled and organized by Projekt DEAL.

3.6. References

[1] J. B. Bates, N. J. Dudney, G. R. Gruzalski, R. A. Zuhr, A. Choudhury, C. F. Luck, J. D. Robertson, *Solid State Ionics* **1992**, *53–56*, 647–654, DOI 10.1016/0167-2738(92)90442-R.

[2] J. B. Bates, N. J. Dudney, G. R. Gruzalski, R. A. Zuhr, A. Choudhury, C. F. Luck, J. D. Robertson, *J. Power Sources* **1993**, *43*, 103–110, DOI 10.1016/0378-7753(93)80106-Y.

[3] X. Yu, J. B. Bates, G. E. Jellison Jr., F. X. Hart, *J. Electrochem. Soc.* **1997**, *144*, 524–532, DOI 10.1149/1.1837443.

[4] J. B. Bates, N. J. Dudney, B. Neudecker, A. Ueda, C. D. Evans, *Solid State Ionics* **2000**, *135*, 33–45, DOI 10.1016/S0167-2738(00)00327-1.

[5] J. Janek, W. G. Zeier, *Nat. Energy* **2016**, *1*, 1–4, DOI 10.1038/nenergy.2016.141.

[6] J. Schnell, T. Günther, T. Knoche, C. Vieider, L. Köhler, A. Just, M. Keller, S. Passerini, G. Reinhart, *J. Power Sources* **2018**, *382*, 160–175, DOI 10.1016/j.jpowsour.2018.02.062.

[7] F. Zheng, M. Kotobuki, S. Song, M. O. Lai, L. Lu, *J. Power Sources* **2018**, *389*, 198–213, DOI 10.1016/j.jpowsour.2018.04.022.

[8] J. D. LaCoste, A. Zakutayev, L. Fei, *J. Phys. Chem. C* **2021**, *125*, 3651–3667, DOI 10.1021/acs.jpcc.0c10001.

[9] J. G. Kim, B. Son, S. Mukherjee, N. Schuppert, A. Bates, O. Kwon, M. J. Choi, H. Y. Chung, S. Park, *J. Power Sources* **2015**, *282*, 299–322, DOI 10.1016/j.jpowsour.2015.02.054.

[10] W. Weppner in *Encyclopedia of Electrochemical Power Sources*, Elsevier B.V, Amsterdam, **2009**, pp. 162–168, DOI 10.1016/B978-044452745-5.00210-0.

[11] Y. Su, J. Falgenhauer, A. Polity, T. Leichtweiß, A. Kronenberger, J. Obel, S. Zhou, D. Schlettwein, J. Janek, B. K. Meyer, *Solid State Ionics* **2015**, *282*, 63–69, DOI 10.1016/j.ssi.2015.09.022.

[12] R. Chen, W. Qu, X. Guo, L. Li, F. Wu, *Mater. Horiz.* **2016**, *3*, 487–516, DOI 10.1039/C6MH00218H.

[13] E. P. Roth, C. J. Orendorff, *Electrochem. Soc. Interface* **2012**, *21*, 45–49, DOI 10.1149/2.F04122if.

[14] Y. C. Jung, S. K. Kim, M. S. Kim, J. H. Lee, M. S. Han, D. H. Kim, W. C. Shin, M. Ue, D. W. Kim, *J. Power Sources* **2015**, *293*, 675–683, DOI 10.1016/j.jpowsour.2015.06.001.

[15] B. Owens, B. Scrosati, P. Reale in *Encyclopedia of Electrochemical Power Sources*, 1964, Elsevier, Amsterdam, **2009**, pp. 120–128, DOI 10.1016/B978-044452745-5.00118-0.

[16] H. Y. Park, S. C. Nam, Y. C. Lim, K. G. Choi, K. C. Lee, G. B. Park, S. R. Lee, H. P. Kim, S. B. Cho, *J. Electroceram.* **2006**, *17*, 1023–1030, DOI 10.1007/s10832-006-8976-3.

[17] P. Birke, W. F. Chu, W. Weppner, *Solid State Ionics* **1996**, *93*, 1–15, DOI 10.1016/s0167-2738(96)00489-4.

[18] J. A. Dawson, P. Canepa, T. Famprikis, C. Masquelier, M. S. Islam, *J. Am. Chem. Soc.* **2018**, *140*, 362–368, DOI 10.1021/jacs.7b10593.

[19] M. A. T. Marple, T. A. Wynn, D. Cheng, R. Shimizu, H. E. Mason, Y. S. Meng, *Angew. Chem. Int. Ed.* **2020**, *59*, 22185–22193, *Angew. Chem.* **2020**, *132*, 22369–22377, DOI 10.1002/anie.202009501.

[20] P. López-Aranguren, M. Reynaud, P. Głuchowski, A. Bustinza, M. Galceran, J. M. López Del Amo, M. Armand, M. Casas-Cabanas, *ACS Energy Lett.* **2021**, *6*, 445–450, DOI 10.1021/acsenergylett.0c02336.

[21] V. Lacivita, N. Artrith, G. Ceder, *Chem. Mater.* **2018**, *30*, 7077–7090, DOI 10.1021/acs.chemmater.8b02812.

[22] A. Al-Qawasmeh, N. A. Holzwarth, *J. Power Sources* **2017**, *364*, 410–419, DOI 10.1016/j.jpowsour.2017.08.025.

[23] P. Henkel, D. Mollenhauer, *J. Comput. Chem.* **2021**, *42*, 1283–1295, DOI 10.1002/jcc.26546.

[24] B. Wang, B. C. Chakoumakos, B. C. Sales, B. S. Kwak, J. B. Bates, *J. Solid State Chem.* **1995**, *115*, 313–323, DOI 10.1006/jssc.1995.1140.

[25] K. Senevirathne, C. S. Day, M. D. Gross, A. Lachgar, N. A. Holzwarth, *Solid State Ionics* **2013**, *233*, 95–101, DOI 10.1016/j.ssi.2012.12.013.

[26] D. Baumann, W. Schnick, *Eur. J. Inorg. Chem.* **2015**, 617–621, DOI 10.1002/ejic.201403125.

[27] Y. A. Du, N. A. Holzwarth, *Phys. Rev. B* **2010**, *81*, 1–15, DOI 10.1103/PhysRevB.81.184106.

[28] E.-M. Bertschler, C. Dietrich, T. Leichtweiß, J. Janek, W. Schnick, *Chem. Eur. J.* **2018**, *24*, 196–205, DOI 10.1002/chem.201704305.

[29] E.-M. Bertschler, C. Dietrich, J. Janek, W. Schnick, *Chem. Eur. J.* **2017**, *23*, 2185–2191, DOI 10.1002/chem.201605316.

[30] E.-M. Bertschler, R. Niklaus, W. Schnick, *Chem. Eur. J.* **2017**, *23*, 9592–9599, DOI 10.1002/chem.201700979.

[31] E.-M. Bertschler, R. Niklaus, W. Schnick, *Chem. Eur. J.* **2018**, *24*, 736–742, DOI 10.1002/chem.201704975.

[32] E.-M. Bertschler, T. Bräuniger, C. Dietrich, J. Janek, W. Schnick, *Angew. Chem. Int. Ed.* **2017**, *56*, 4806–4809, *Angew. Chem.* **2017**, *129*, 4884–4887, DOI 10.1002/anie.201701084.

[33] Y. A. Du, N. A. Holzwarth, *Phys. Rev. B* **2008**, *78*, 1–13, DOI 10.1103/PhysRevB.78.174301.

[34] R. Böhmer, K. R. Jeffrey, M. Vogel, *Prog. Nucl. Magn. Reson. Spectrosc.* **2007**, *50*, 87–174, DOI 10.1016/j.pnmrs.2006.12.001.

[35] A. Kuhn, V. Duppel, B. V. Lotsch, *Energy Environ. Sci.* **2013**, *6*, 3548–3552, DOI 10.1039/c3ee41728j.

[36] A. Kuhn, M. Kunze, P. Sreeraj, H. D. Wiemhöfer, V. Thangadurai, M. Wilkening, P. Heitjans, *Solid State Nucl. Mag.* **2012**, *42*, 2–8, DOI 10.1016/j.ssnmr.2012.02.001.

[37] A. Haffner, T. Bräuniger, D. Johrendt, *Angew. Chem. Int. Ed.* **2016**, *55*, 13585–13588, *Angew. Chem.* **2016**, *128*, 13783–13786, DOI 10.1002/anie.201607074.

[38] *Origin Pro 2018G*, Origin Lab Corporation, Northampton, USA, **2018**.

[39] W. Schnick, J. Lücke, *Z. Anorg. Allg. Chem.* **1992**, *610*, 121–126, DOI 10.1002/zaac.19926100120.

[40] S. Horstmann, E. Irran, W. Schnick, *Z. Anorg. Allg. Chem.* **1998**, *624*, 620–628, DOI 10.1002/(SICI)1521-3749(199804)624:4<620::AID-ZAAC620>3.0.CO;2-K.

[41] D. Baumann, W. Schnick, *Inorg. Chem.* **2014**, *53*, 7977–7982, DOI 10.1021/ic500767f.

[42] K. Nakamoto, *Infrared and Raman Spectra of Inorganic and Coordination Compounds: Part A: Theory and Applications in Inorg. Chem.: Sixth Edition*, 6th ed., John Wiley & Sons, Inc., Hoboken, NJ, **2008**, DOI 10.1002/9780470405840.

[43] M. A. Carrillo Solano, M. Dussauze, P. Vinatier, L. Croguennec, E. I. Kamitsos, R. Hausbrand, W. Jaegermann, *Ionics* **2016**, *22*, 471–481, DOI 10.1007/s11581-015-1573-1.

[44] E. I. Kamitsos, G. D. Chryssikos, *Solid State Ionics* **1998**, *105*, 75–85, DOI 10.1016/s0167-2738(97)00451-7.

[45] J. R. Macdonald, W. B. Johnson in *Impedance Spectroscopy: Theory, Experiment, and Applications, Second Edition*, John Wiley & Sons, Inc., Hoboken, NJ, **2005**, pp. 1–26.

[46] G. J. Brug, A. L. van den Eeden, M. Sluyters-Rehbach, J. H. Sluyters, *J. Electroanal. Chem.* **1984**, *176*, 275–295, DOI 10.1016/S0022-0728(84)80324-1.

[47] J. T. S. Irvine, D. C. Sinclair, A. R. West, *Adv. Mater.* **1990**, *2*, 132–138, DOI 10.1002/adma.19900020304.

[48] S. Zhao, Z. Fu, Q. Qin, *Thin Solid Films* **2002**, *415*, 108–113, DOI 10.1016/S0040-6090(02)00543-6.

[49] O. Yakubovich, O. Mel'nikov, *Kristallografiya* **1994**, *39*, 815–820.

[50] A. Daidouh, M. L. Veiga, C. Pico, M. Martinez-Ripoll, *Acta Crystallogr. C* **1997**, *53*, 167–169, DOI 10.1107/S0108270196011869.

[51] M. S. Song, Y. M. Kang, Y. I. Kim, K. S. Park, H. S. Kwon, *Inorg. Chem.* **2009**, *48*, 8271–8275, DOI 10.1021/ic9009114.

[52] V. I. Voronin, E. A. Sherstobitova, V. A. Blatov, G. S. Shekhtman, *J. Solid State Chem.* **2014**, *211*, 170–175, DOI 10.1016/j.jssc.2013.12.015.

[53] B. Raguž, K. Wittich, R. Glaum, *Eur. J. Inorg. Chem.* **2019**, *2019*, 1688–1696, DOI 10.1002/ejic.201801100.

[54] Z. A. Grady, C. J. Wilkinson, C. A. Randall, J. C. Mauro, *Front. Energy Res.* **2020**, *8*, 1–23, DOI 10.3389/fenrg.2020.00218.

4. Comprehensive Investigation of Anion Species in Crystalline Li^+ ion Conductor $Li_{27-x}[P_4O_{7+x}N_{9-x}]O_3$ ($x \approx 1.9(3)$)

Stefanie Schneider, Eva-Maria Wendinger, Volodymyr Baran, Anna-Katharina Hatz, Bettina V. Lotsch, Markus Nentwig, Oliver Oeckler, Thomas Bräuniger, and Wolfgang Schnick

Chem. Eur. J. **2023**, *29*, e202300174.
https://doi.org/10.1002/chem.202300174
DOI: 10.1002/chem.202300174

Reprinted (adapted) with permission from Chemistry – European Journal. Copyright 2023

The structure of the crystalline lithium oxonitridophosphate $Li_{27-x}[P_4O_{7+x}N_{9-x}]O_3$ contains three different anions, namely $[PO_2N_2]^{5-}$, $[PO_3N]^{4-}$, and O^{2-}. It was comprehensively investigated by single-crystal and powder X-ray diffraction, neutron powder diffraction, NMR spectroscopy and elemental analysis. A total ionic conductivity of $6.6 \times 10^{-8}\,S\,cm^{-1}$, which is similar to that of amorphous a LiPON, was determined with impedance spectroscopy.

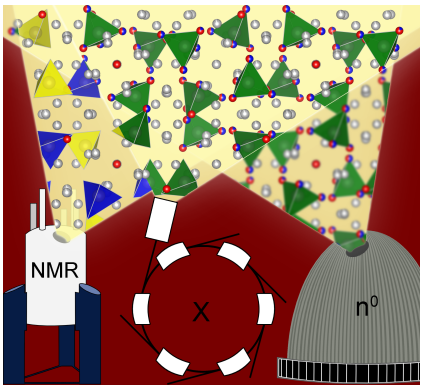

4.1. Abstract

The Li^+ ion conductor $Li_{27-x}[P_4O_{7+x}N_{9-x}]O_3$ ($x \approx 1.9(3)$) has been synthesized from P_3N_5, Li_3N and Li_2O in a Ta ampoule at 800 °C under Ar atmosphere. The cubic compound crystallizes in space group $I\bar{4}3d$ with $a = 12.0106(14)$ Å and $Z = 4$. It contains both non-condensed $[PO_2N_2]^{5-}$ and $[PO_3N]^{4-}$ tetrahedra as well as O^{2-} ions, surrounded by Li^+ ions. Charge neutrality is achieved by partial occupancy of Li positions, which was refined with neutron powder diffraction data. Measurements of the partial ionic and electronic conductivity show a total ionic conductivity of $6.6 \times 10^{-8}\,S\,cm^{-1}$ with an activation energy of 0.46(2) eV and a bulk ionic conductivity of $4 \times 10^{-6}\,S\,cm^{-1}$ at 25 °C, which is close to the ionic conductivity of amorphous lithium nitridophosphate. This makes $Li_{27-x}[P_4O_{7+x}N_{9-x}]O_3$ an interesting candidate for investigation of structural factors affecting ionic conductivity in lithium oxonitridophosphates.

4.2. Introduction

Introduction of nitrogen into oxide glasses was found to affect materials properties significantly.[1] Therefore, oxonitrides became the subject of thorough investigations.[2–6] Especially oxonitridophosphates showed promising alterations of their properties compared to oxosilicate and oxophosphate glasses.[4,6,7] The initial focus on materials properties such as chemical durability, softening temperature, refractive index, or thermal expansion[4,8] has more recently been shifted toward electronic properties such as ionic or electronic conductivity.[9–11] Amorphous lithium phosphorus oxonitride (LiPON) materials with a composition of $Li_xPO_yN_z$ have become a hot topic due to their relatively high Li^+ ion conductivity, paired with high electrochemical inertness.[12] Although these materials have been thoroughly investigated focusing on application as solid electrolytes, the underlying conduction mechanism is largely unknown. Structural investigation on glasses, such as amorphous LiPON, is difficult with standard techniques such as X-ray diffraction (XRD). However, applying analytical tools for local order such as solid-state NMR (ssNMR) allows the assessment of structural features such as the N content and N positions as well as the degree of condensation of $P(O,N)_4$ tetrahedra that have a significant influence on the conductivity and other materials properties.[8,13–18] ssNMR enables characterization of both amorphous and crystalline materials and ^{31}P ssNMR proved to be a suitable tool to detect the composition of PO_yN_{4-y} tetrahedra, since the chemical shift is highly dependent on the O/N ratio.[14–17,19]

In addition, modelling of ionic diffusion pathways is also challenging and requires complex structural models based on crystalline frameworks.[20] These crystalline model structures help to understand the influence of certain structural features on Li^+ conductivity, as they provide an ordered environment in which various influences can be observed.

To date, only few crystalline lithium oxonitridophosphates are known and thus the number of model structures is limited. They show a high anionic structural diversity including noncondensed PO_yN_{4-y} with $1 \leq y \leq 4$ tetrahedra and one-dimensionally connected chains of tetrahedra. Recently, $Li_{5+x}P_2O_{6-x}N_{1+x}$ with pairs of corner-sharing tetrahedra $[P_2O_6N]^{5-}$ with a bridging N atom

has been reported.[21] Crystalline lithium oxonitridophosphates are lithium ion conductors and their conductivities range from 1×10^{-13} to $6 \times 10^{-8}\,\mathrm{S\,cm^{-1}}$(Table 3).[22–26]
In this work, we report on synthesis, structural characteristics and Li^+ ion conductivity of $Li_{27-x}[P_4O_{7+x}N_{9-x}]O_3$. Similar to $Li_{14}(PON_3)_2$, $Li_{27-x}[P_4O_{7+x}N_{9-x}]O_3$ is composed of non-condensed $P(O,N)_4$ tetrahedra and O^{2-} ions.[24] The range of anionic species in this compound make it a valuable model system for the investigation of the impact of structural features on Li^+ ion conductivity in LiPON compounds.

4.3. Results and Discussion

4.3.1. Synthesis

The title compound was initially observed in a heterogeneous sample of partially hydrolyzed $Li_{10}P_4N_{10}$. Targeted synthesis was subsequently accomplished from Li_3N, P_3N_5, and Li_2O. Stoichiometric mixtures of starting materials as shown in the idealized reaction Equation (4.1) did not yield $Li_{27-x}[P_4O_{7+x}N_{9-x}]O_3$, but $Li_{5+x}P_2O_{6-x}N_{1+x}$.[21] Instead, Li_3N had to be used in excess to form a Li_3N flux, a method previously reported for synthesis of lithium nitridophosphates.[27–31] The reaction mixture was heated to 800 °C for 90 h under Ar atmosphere in an open Ta crucible placed in a fused silica ampoule.

$$(7-3x)\ Li_3N + 4\ P_3N_5 + (30+x)\ Li_2O \longrightarrow 3\ Li_{27-x}[P_4O_{7+x}N_{9-x}]O_3 \tag{4.1}$$

Despite comprehensive variation of the stoichiometry of starting materials and reaction conditions, a phase-pure product could not be achieved so far. Similar to the synthesis of lithium nitridophosphates, Li_3P is formed as a side product.[31] Other identified side phases include $Li_{10}P_4N_{10}$, $Li_5P_2O_6N$, and Li_2O.[21,30] Whereas the quantity of these side phases could be lowered by prolonged reaction times, a small amount of Li_2O remained in all samples. In contrast, the Li_3P content increased upon prolonged reaction times and higher temperatures, but this byproduct was removed with dry EtOH. Longer treatment of the sample with EtOH also decreases the amount of Li_2O. A moisture- and air-sensitive, colorless, microcrystalline powder was obtained. Subsequently, analytical data were collected on a sample with 11 wt-% Li_2O as side phase, as determined by Rietveld refinement (measurements were taken with Cu $K_{\alpha 1}$ radiation, Figure 4.1).
By ampoule synthesis, only relatively small amounts of the product could be synthesized (batches up to 200 mg). Experiments in a hot isostatic press (HIP) could enable larger batch sizes, however, no phase pure synthesis could be achieved with this method, either.

4.3.2. Crystal structure determination

X-ray diffraction

The structure model of $Li_{27-x}[P_4O_{7+x}N_{9-x}]O_3$ was determined by single-crystal X-ray diffraction, applying direct methods. Due to small crystallite sizes of less than 10 µm, diffraction data were

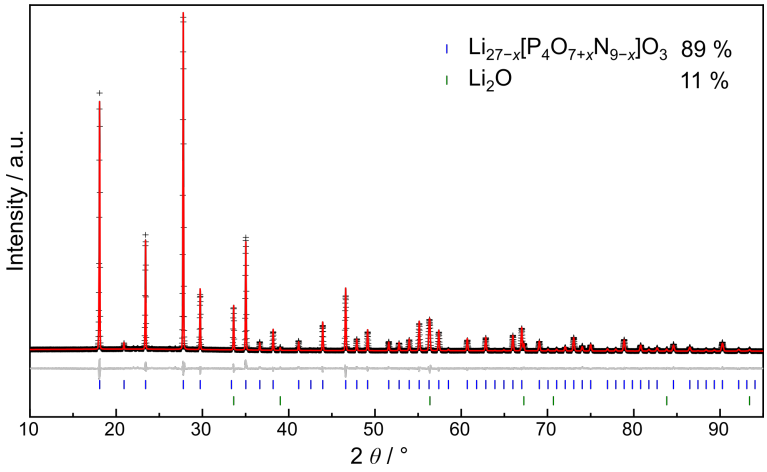

Figure 4.1.: Observed (black crosses, Cu $K_{\alpha 1}$ radiation) and calculated (red line) powder diffraction pattern of $Li_{27-x}[P_4O_{7+x}N_{9-x}]O_3$. Calculated Bragg reflections for $Li_{27-x}[P_4O_{7+x}N_{9-x}]O_3$ and Li_2O are shown with blue and green markers, respectively.

collected at the ESRF beamline ID11 in Grenoble. The title compound crystallizes in cubic space group $I\bar{4}3d$ with $a = 12.0106(14)$ Å and $Z = 4$. The analysis showed that the structure consists of anionic P(O,N)4 tetrahedra with only one crystallographically independent P site. Additional O^{2-} and Li^+ make this compound a lithium oxonitridophosphate oxide (Figure 3).
Assuming all Li and oxide positions being fully occupied and a mixed occupancy of O and N positions in $P(O,N)_4$ tetrahedra leads to the charge-neutral sum formula of $Li_{27}[P_4O_7N_9]O_3$. Written in brackets is the composition of tetrahedra, O from oxide positions is given outside of the brackets. As deduced from ssNMR data, there are both $[PO_3N]^{4-}$ and $[PO_2N_2]^{5-}$ tetrahedra present in the structure. Due to the similar electron counts, O and N lack X-ray scattering contrast so that ordering of O and N atoms cannot be assessed. The charge neutral sum formula mentioned above seems not fully consistent with these types of tetrahedra. With the mixed occupancy observed in neutron diffraction, charge neutrality can only be reached with Li vacancies, resulting in the sum formula $Li_{27-x}[P_4O_{7+x}N_{9-x}]O_3$ (see below).

Solid-state magic angle spinning NMR spectroscopy

In principle, five different $[PO_yN_{4-y}]^{(7-y)-}$ (y = 0–4) tetrahedra are possible. To find out which particular tetrahedral anions are present, ^{31}P solid-state magic angle spinning (MAS) NMR was performed. Although there is only one crystallographic P site in the average structure, ^{31}P MAS NMR (Figure 2) shows two signals with a ratio of 72 to 28 % at chemical shifts of 33.0 and 19.6 ppm, respectively, suggesting two different atomic environments for P. At 44 ppm, the intensity is raised slightly above the background, which might indicate presence of a small amount of another different chemical environment around P. However, the intensity of the signal was too small for integration, so no ratio could be obtained. A ^{31}P–^{31}P 2D double-quantum single-quantum correlation MAS NMR spectrum confirms that both signals are from the same phase Figure B.7 in Supporting Information).

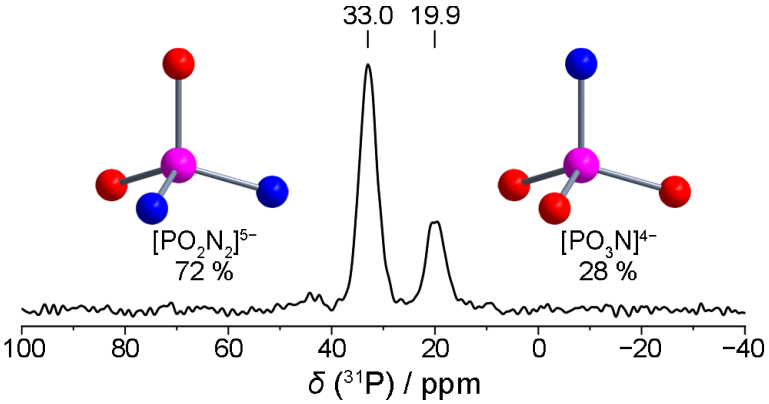

Figure 4.2.: ^{31}P NMR spectrum of $Li_{27-x}[P_4O_{7+x}N_{9-x}]O_3$ at a MAS rate of 25 kHz. Two signals are visible at 33.0 and 19.6 ppm, which belong to the P1 atomic position in the $[PO_2N_2]^{5-}$ and the $[PO_3N]^{4-}$ environment, respectively (P: pink, O: red, N: blue).

Table 4.1.: Overview of ^{31}P MAS NMR shifts for non-condensed lithium phosphates.

$[PO_yN_{4-y}]^{(7-y)-}$	Compound	δ / ppm
$[PN_4]^{7-}$	Li_7PN_4	49.2, 54.6[28]
$[PON_3]^{6-}$	$Li_{14}(PON_3)_2O$	44.3[24]
$[PO_2N_2]^{5-}$	$Li_{3.6}PO_{3.4}N_{0.6}$	31.3[25]
$[PO_3N]^{4-}$	$Li_{3.6}PO_{3.4}N_{0.6}$, a-LiPON[a]	19.8[25], 19.4[16]
$[PO_4]^{3-}$	$Li_{3.6}PO_{3.4}N_{0.6}$, a-LiPON[a] , Li_3PO_4	10.3[25], 9.3[16], 8.9[32]

[a] amorphous LiPON with 2.6 at − % N.

Previous NMR studies on LiPON materials have shown a shift in the positions of ^{31}P MAS NMR signals of approximately +10 ppm for each O atom that is replaced by N within noncondensed $P(O,N)_4$ tetrahedra.[16] Table 4.1 shows ^{31}P MAS NMR shifts for lithium oxonitridophophates with discrete $P(O,N)_4$ tetrahedra. The two signals of the title compound are in good agreement with literature data of $[PO_2N_2]^{5-}$ (31.3 ppm)[25] and $[PO_3N]^4$ tetrahedra (19.8 and 19.4 ppm)[16,25] (Figure 4.2). However, the presence of $[PO_2N_2]^{5-}$ and $[PO_3N]^{4-}$ in a 72 : 28 ratio would not meet the number of negative charges required for a charge-neutral sum formula with the Li positions found with X-ray diffraction fully occupied (−5.25 per P atom, balancing 27 positive charges from Li^+ and six negative charges from O^{2-}). Charge neutrality with a partial sum formula of $4 \times [(PO_2N_2)_{0.72}(PO_3N)_{0.28}]^{4.72-}$, as derived from NMR would result in too few negative charges to balance the charges from fully occupied Li positions. To achieve charge neutrality, there are two options. One possibility is a mixed occupancy of the oxide position with N, so a higher negative charge would result. The second possibility are Li vacancies, which would lower the amount of positive charges and then result in $x = 2.12$. Furthermore, the weak resonance at 44 ppm might indicate the presence of $[PON_3]^{6-}$ (Figures B.3 and B.4). This would further reduce the value of x. The $[PO_2N_2]^{5-}$ and $[PO_3N]^{4-}$ tetrahedra may be distributed randomly. Alternatively, some form of ordering might decrease the symmetry to the

space groups $R3c$ or $I\bar{4}2d$. No splitting of reflections is observed in either X-ray or neutron powder diffraction. Refinement was attempted in other space groups, but did not yield indication towards lowering of symmetry.
^{6}Li ($\delta = 1.9$ ppm) and ^{7}Li ($\delta = 2.8$ ppm) MAS NMR both show only one signal, which is probably due to significant Li^+ ion mobility (Figures B.5 and B.6) and the three crystallographically independent sites cannot be distinguished. However, the signals exhibit shoulders due to slightly different local environments. The chemical shift is in good agreement with known shifts of lithium, which range from 4.9 to 1.6 ppm in lithium (oxo)nitridophosphates.[24,27,28,30,31]

Neutron powder diffraction

Ordering of O and N atoms and thus $[PO_2N_2]^{5-}$ and $[PO_3N]^{4-}$ might result in reduced space group symmetry. Charge neutrality could be achieved by Li vacancies or mixed occupancy of the O3 position with N. To address these questions, neutron diffraction data were obtained Figure B.2. Since only small amounts of the product could be obtained in one batch and with respect to the large amount of sample needed for neutron diffraction, a combined sample with Li_2O (16 %) and $Li_{5+x}P_2O_{6-x}N_{1+x}$ (9 %) as side phases was used. The data in Figure B.2 show no split reflections and thus no indication of a decrease in symmetry towards subgroups of $I\bar{4}3d$ by ordering of the O/N positions. Neutron data suggest statistically occupied O/N positions in tetrahedra. The O1/N1 position is predominantly occupied by oxygen (81(3) %), whereas the O2/N2 position shows no preferred occupancy (53(3) % N). The O3 position is fully occupied with O as expected for a position that is not part of a phosphate ion (Figure 4.3). The resulting Li site occupancy of 92.9(12) % leads to the sum formula $Li_{27-x}[P_4O_{7+x}N_{9-x}]O_3$ with $x \approx 1.9(3)$, which is close to the value derived from NMR ($x = 2.12$), if only $[PO_3N]^{4-}$ and $[PO_2N_2]^{5-}$ are assumed. As mentioned before, the value obtained from NMR might be lower, if $[PON_3]^{6-}$ is indeed present. Within the margin of error, the values are congruent. Thus, $x \approx .1.9(3)$, as obtained from neutron diffraction, will be used for further considerations.

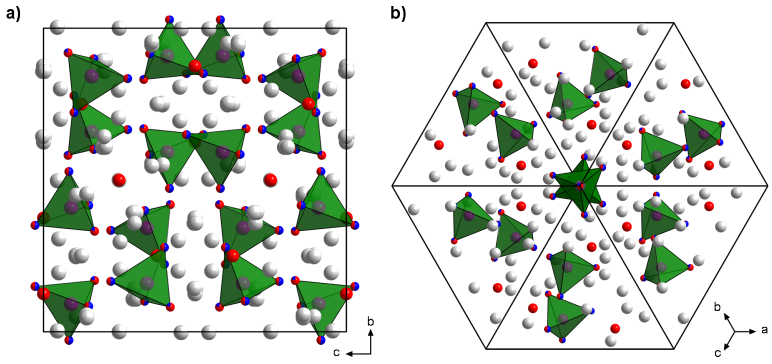

Figure 4.3.: Unit cell of $Li_{27-x}[P_4O_{7+x}N_{9-x}]O_3$ along [100] (a) and [111] (b) (P: pink, O: red, N: blue, Li: light gray.

Combined structure model

Analytical data are consistent with the space group $I\bar{4}3d$ for $Li_{27-x}[P_4O_{7+x}N_{9-x}]O_3$ ($x \approx 1.9(3)$); crystallographic data are summarized in Table 4.2. Atomic coordinates and anisotropic displacement parameters as well as selected interatomic distances and angles are listed in Tables B.1–B.4 The unit cell is shown in Figure 4.3.

Table 4.2.: Crystallographic data of $Li_{27-x}[P_4O_{7+x}N_{9-x}]O_3$ ($x \approx 1.9(3)$) from single-crystal X-ray diffraction data.

Crystal size / mm	$0.01 \times 0.01 \times 0.03$
Formula	$Li_{27-x}[P_4O_{7+x}N_{9-x}]O_3$
Formula weight / $g\,mol^{-1}$	587.78
Crystal system	cubic
Space group	$I\bar{4}3d$ (no. 220)
Lattice parameter a / Å	12.0106(14)
Cell volume / $Å^3$	1732.6(6)
Formula units per unit cell	4
Density / $g\,cm^{-3}$	2.253
μ / mm^{-1}	0.071
Radiation / λ/Å	Synchrotron, $\lambda = 0.294\,70$ Å
θ-range / °	$1.7 \leq \theta \leq 13.7$
Total no. of reflections	17851
Independent reflections	691, thereof 687 with $F^2 > 2\sigma(F^2)$
Refined parameters	38
R_{int}; R_σ	0.0607; 0.0182
$R1$ (all data); $R1$ ($F^2 > 2\sigma(F^2)$)	0.0197; 0.0194
$wR2$ (all data); $wR2$ ($F^2 > 2\sigma(F^2)$)	0.0512; 0.0511
Goodness of fit (χ^2)	1.177
$\Delta\rho_{max}; \Delta\rho_{min}$ / $e/Å^3$	0.212; −0.151

There is one crystallographic P position which is tetrahedrally coordinated by one O1/N1 position and three symmetry equivalent O2/N2 positions with O/N disorder on both positions according to neutron diffraction. Thus, $[PO_2N_2]^{5-}$ and $[PO_3N]^{4-}$, as confirmed by NMR are statistically distributed. The final structure model is based on SCXRD but uses site occupancies from neutron powder diffraction without further refinement. P–O/N bond lengths in lithium oxonitridophosphates are assumed to be longer than pure P–O bonds and shorter than pure P–N bonds, due to the larger ionic radius of N^{3-} in contrast to O^{2-} and stronger covalency of the P–N bond.[22,33,34] Despite the mixed occupancy bond lengths in $Li_{27-x}[P_4O_{7+x}N_{9-x}]O_3$ can be best compared to lithium ortho-oxonitridophosphates, Li_7PN_4, or Li_3PO_4. Comparison to $Li_{14}(PON_3)_2O$ proves useful, since it also contains oxide ions.[22,24,25,35,36] P–O bond lengths in Li_3PO_4 range from 1.53 to 1.58 Å,[36] whereas P–N bond lengths in Li_7PN_4 are within a range of 1.69 to 1.73 Å.[35] Thus, P–O/N bond lengths in $Li_{27-x}[P_4O_{7+x}N_{9-x}]O_3$ with 1.6114(10) Å (P1–O1/N1) and 1.5951(10) Å (P1–O2/N2) are in good

agreement with other lithium (nitrido-)phosphates.[22–25,27,28,30,31,35,36]
The oxide ion O^{2-} (O3 position) shows a distorted cubic coordination by eight Li^+ positions (Li2 and Li3). Two of the three Li positions are tetrahedrally coordinated by O/N atoms. Li3 is located in a distorted tetragonal pyramid (Figure 4.4). Neutron data shows Li vacancies (92 % occupancy) Pure Li–O distances are in the range of 1.996(4) to 2.029(3) Å, whereas Li–O/N distances range from 1.9595(12) to 2.299(6) Å, which is in good agreement with known Li–O and Li–N distances.[27–31,36–39] All Li-centered polyhedra share edges with other Li-centered polyhedra, which decreases the Li–Li distances, enabling potentially higher conductivity as discussed below.

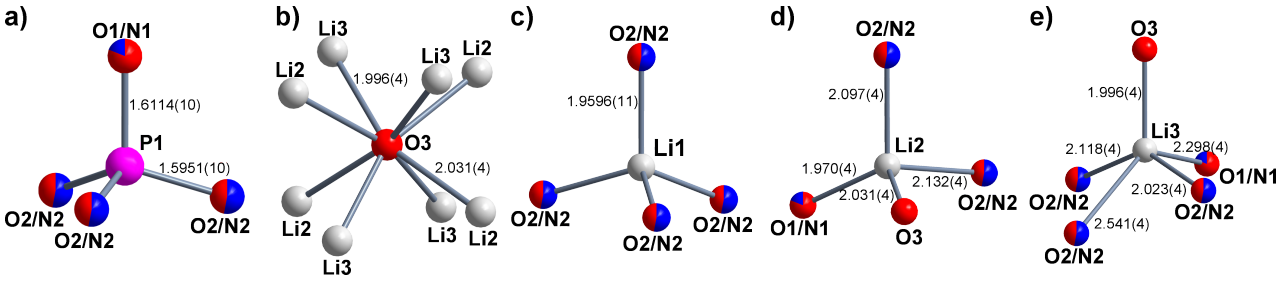

Figure 4.4.: Coordination of different atomic positions with bond lengths in Å (P: pink, O: red, N: blue, Li: light gray).

4.3.3. FTIR and chemical analysis

The infrared spectrum shows no vibrational modes of O–H and N–H bonds in the range of 2800–3200 and 3000–3500 cm^{-1}, respectively (Figure 4.5). Thus, no N–H or O–H bonds are present in the structure. The five distinct signals at 1050, 1000, 940, 835 and 785 cm^{-1} may be attributed to P–O stretching modes that are typically found between 900 and 1200 cm^{-1}, whereas O–P–O bending modes occur around 650–300 cm^{-1}.[40] The broad signal around 400 cm^{-1} might be caused by Li cation vibrations.[41]
Elemental analysis is complicated by the fact that the samples are prone to hydrolysis and the presence of side phases. Energy-dispersive X-ray (EDX) spectroscopy cannot precisely quantify light elements, especially Li. Thus, elemental analyses only indicated that no other elements are present (Tables B.8 and B.9).

4.3.4. Thermal stability

The thermal stability of $Li_{27-x}[P_4O_{7+x}N_{9-x}]O_3$ was investigated using a sample with 11 % Li_2O for temperature-dependent X-ray powder diffraction. Up to 620 °C, the reflections of $Li_{27-x}[P_4O_{7+x}N_{9-x}]O_3$ only show the expected thermal shift. At 640 °C, possibly as a result of a reaction between $Li_{27-x}[P_4O_{7+x}N_{9-x}]O_3$ and the present impurity Li_2O, $Li_{5+x}P_2O_{6-x}N_{1+x}$ is formed. At 860 °C, reflections of Li_3PO_4 indicate decomposition. Above 880 °C, full decomposition has taken place and reflections of neither $Li_{5+x}P_2O_{6-x}N_{1+x}$ nor $Li_{27-x}[P_4O_{7+x}N_{9-x}]O_3$ are detectable (Figure B.8).

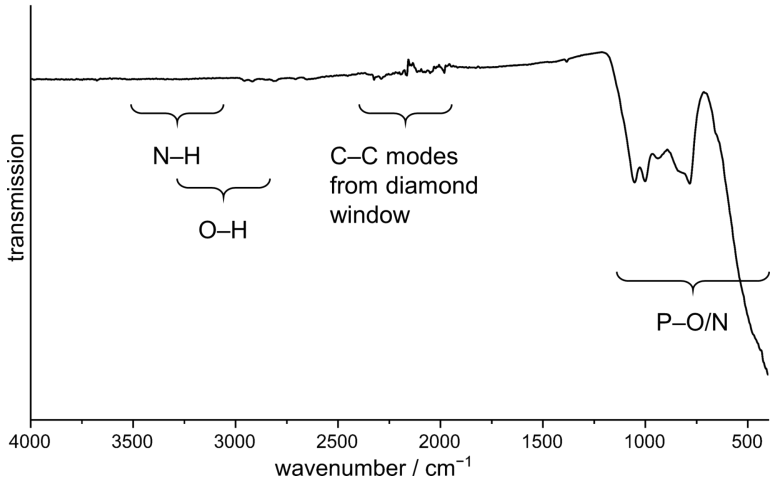

Figure 4.5.: IR spectrum of $Li_{27-x}[P_4O_{7+x}N_{9-x}]O_3$. No signals are visible in the area of 3000–3500 cm^{-1}. Thus, no N–H or O–H bonds are present in the structure. Increased background in the area 2300–2000 cm^{-1} is due to C–C bonds in the diamond window of the ATR unit.

4.3.5. Ionic and electronic partial conductivities

For a cold pressed pellet of $Li_{27-x}[P_4O_{7+x}N_{9-x}]O_3$ with 11 % of Li_2O as side phase, a total ionic conductivity of 6.6×10^{-8} S cm^{-1} at 25 °C with an activation energy of 0.46(2) eV (extrapolated to 3.8×10^{-6} S cm^{-1} at 127 °C) and a bulk ionic conductivity of 4×10^{-6} S cm^{-1} were measured by electrochemical impedance spectroscopy. The impedance spectrum in 4.6 consists of three contributions: one high frequency and one low frequency semicircle and a spike at low frequencies. The semicircles are modelled by a resistor R and a constant phase element (CPE) in parallel denoted as R1-CPE1 and R2-CPE2, respectively.

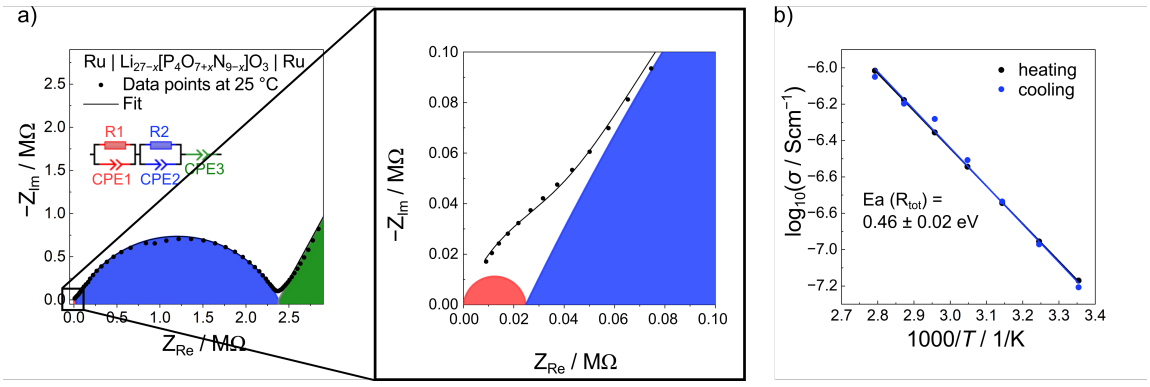

Figure 4.6.: a) Impedance spectrum of $Li_{27-x}[P_4O_{7+x}N_{9-x}]O_3$ with 11 % Li_2O as side phase, showing two semicircles of the bulk (R1-CPE1) and grain boundary process (R2-CPE2), respectively. The activation energy of the total ionic conductivity from heating and cooling the sample determined in b) is 0.46(2) eV and is dominated by the grain boundary process.

The low frequency spike stems from the polarization of Li^+ ions at the blocking electrode and is modelled by a CPE (CPE3) in series. The total ionic conductivity is calculated by $\sigma = d/AR_{tot}$ with d being the thickness of the pellet, A the surface area and R_{tot} the sum of R1 and R2 that

were obtained from the fit of the spectrum. Considering the effective capacitances (C_{eff}) of the two processes of 24 pF for the high frequency semicircle and 0.1 nF for the low frequency semicircle, they are assigned to bulk and grain boundary contributions, respectively.[42] The C_{eff} is calculated by $C_{\text{eff}} = (Q/(R^{\alpha-1})^{1/\alpha}$ with Q being CPE's admittance value, R the respective resistance in parallel to the CPE and α a fitting parameter with a value between 0.5 and 1, modelling the deviation from an ideal capacitor. An activation energy E_a of 0.46(2) eV is derived from the total conductivity by $\sigma = (\sigma_0/T) \cdot e^{-E_A/RT}$ from heating and cooling the sample as plotted in 4.6b. This activation energy represents an overlapped value of the two processes, which is dominated by the more resistive grain boundary process. The issue of reproducibility is discussed in the Supporting Information (Figure B.9 and Table B.10).

The average activation energy is lower with 0.39(3) eV being consistent with the less pronounced influence of the resistive grain boundaries in this sample (Table B.10). An electronic conductivity of 9×10^{-10} S cm^{-1} of $Li_{27-x}[P_4O_{7+x}N_{9-x}]O_3$ was obtained by potentiostatic polarization measurements as depicted in Figure B.9, leading to a transference number $\tau_i = \sigma_{\text{ion}}/(\sigma_{\text{ion}} + \sigma_{\text{eon}})$ of 0.991, rendering $Li_{27-x}[P_4O_{7+x}N_{9-x}]O_3$ a predominantly ionic conductor.

The total ionic conductivity of $Li_{27-x}[P_4O_{7+x}N_{9-x}]O_3$ at 80 °C (Table 4.3) is comparable to Li_2PO_2N, but is lower than that of amorphous a-LiPON with 2.5 at-% of N at room temperature. Li_2O is contained in the sample as side phase (11 %) and is considered to exist side by side to the title phase. As Li_2O exhibits a Li^+ ion conductivity well below that of $Li_{27-x}[P_4O_{7+x}N_{9-x}]O_3$ (10^{-12} S cm^{-1}),[43] its effect on the total conductivity should only be negative. The effect should be comparable to that of a lower relative density of the pellet, resulting in a larger total resistance. Nevertheless, the bulk ionic conductivity of 4×10^{-6} S cm^{-1} is very similar to amorphous a-LiPON.

Table 4.3.: Ionic conductivity and activation energy of lithium oxonitridophosphates.

Compound	σ at 25 °C / S cm^{-1}	σ at 80 °C / S cm^{-1}	σ at 127 °C / S cm^{-1}	E_a / eV	Ref
$Li_{27-x}[P_4O_{7+x}N_{9-x}]O_3$ (best sample)	$\sigma_{\text{tot}} = 6.6 \times 10^{-8}$	7.9×10^{-7}	3.8×10^{-6} [a]	0.46	This work
$Li_{27-x}[P_4O_{7+x}N_{9-x}]O_3$	$\sigma_{\text{tot}} = 1.4 \times 10^{-7}$	1.3×10^{-6}	5.6×10^{-6} [a]	0.39	This work
a-LiPON	1.6×10^{-6}			0.58	[44]
$Li_{2.88}PO_{3.73}N_{0.14}$	1×10^{-13}			0.97	[22]
Li_2PO_2N		8.8×10^{-7}		0.57	[23]
$Li_{14}(PON_3)_2O$					[24]
$Li_{3.6}PO_{3.4}N_{0.6}$	5.6×10^{-8}			0.55	[25]
$Li_{5+x}P_2O_{6-x}N_{1+x}$	$\sigma_{\text{tot}} = 4.6 \times 10^{-8}$			0.52	[21]

[a] Extrapolated values.

Lacivita et al. have performed diffusivity simulations on amorphous model systems to investigate structural features that are beneficial or detrimental for ionic conductivity.[18] At first glance, the

conductivity of $Li_{27-x}[P_4O_{7+x}N_{9-x}]O_3$ might seem high, considering that there are several features present in the structure that have been associated with reduced ionic conductivity.

For example, the presence of connected $P(O,N)_4$ tetrahedra that share a bridging N (N_d) would be advantageous in comparison to the non-connected P(O,N)4 tetrahedra found in the structure. This is due to the overall reduced anion charge of $[P_2O_6N]^{5-}$ in comparison to two $[PO_4]^{3-}$ that exerts smaller coulombic attraction on Li^+ and thereby enables higher Li^+ mobility. Instead of these beneficial double tetrahedra, the structure contains even more highly charged $[PO_3N]^{4-}$ and $[PO_2N_2]^{5-}$, as well as isolated O^{2-} that was also shown to decrease Li^+ ion mobility due to larger electrostatic interaction.[18,45]

Additionally, edge-sharing between $Li(O,N)_4$ and $P(O,N)_4$ improves conductivity, as the close proximity between Li and P destabilizes Li sites. In $Li_{27-x}[P_4O_{7+x}N_{9-x}]O_3$ however, $Li(O,N)_4$ and $P(O,N)_4$ tetrahedra only share corners. Only the polyhedron around Li3 shares edges with two $P(O,N)_4$ tetrahedra. As no other coordination geometry than tetrahedra are discussed for this substance class in literature, the influence of other polyhedra is not known. However, as the effect is based on coulombic repulsion between P and Li, and larger polyhedra cause larger distances between the two atoms, no or only slight destabilization of Li sites by the proximity to P might be present.

Finally, amorphization of structures is known to increase Li^+ mobility significantly. As the presence of defects flatten the energy landscape around Li, amorphous compounds often have higher conductivities than crystalline materials.[18,45–47] Thus, a lower conductivity of crystalline LiPON in comparison to amorphous a-LiPON is expected.

Summarizing, several structural features seem to be detrimental for the Li^+ ion conductivity in $Li_{27-x}[P_4O_{7+x}N_{9-x}]O_3$ at first glance. However, on a second look, there are several structural features that could be beneficial for the Li^+ ion conductivity.

Firstly, partial occupancy of Li sites opens migration pathways. In a fully occupied crystal with no defects, no mobility is possible. Holzwarth et al. have calculated for Li_3PO_4 that the activation energy consists to a large part of the formation of interstitial and site defects, whereas migration barriers play only a minor role. Thus, the observed vacancies might be essential for Li^+ mobility.[46] Additionally, the density of Li^+ in the structure is very high, which might result in coulombic repulsion and thus destabilization of Li positions by neighboring Li. Whereas no edge-sharing is observed with $P(O,N)_4$ tetrahedra, which would destabilize Li positions, there are many $Li(O,N)_4$ sharing edges with other $Li(O,N)_4$ polyhedra. Lacivita et al. stated that a high number of short-range Li–Li interactions might lead to higher conductivity due to raised Li site energies. Around each Li position are a minimum of six edge-sharing $Li(O,N)_4$ polyhedra. This is also represented in the number of next Li neighbors with a distance of 3 Å around each Li site, which is 8 (Li1), 8 (Li2), and 6 (Li3). This is a very large number of direct Li–Li neighbors, which might also be a factor for the observed high conductivity.[18]

Furthermore, as mentioned before, amorphization – or a higher degree of disorder in the system – is very beneficial for conductivity. Although $Li_{27-x}[P_4O_{7+x}N_{9-x}]O_3$ is undoubtedly a crystalline compound, there is a significant degree of disorder. Firstly, Li sites are only partially occupied, which means that around 93 % of Li positions are occupied in a statistical way. Moreover, both the

distribution and orientation of $[PO_3N]^{4-}$ and $[PO_2N_2]^{5-}$ are statistical. This statistical occupation of five out of seven atom sites might lead to a smoothening of the overall energy landscape around Li similar to the situation in amorphous structures, allowing higher Li^+ mobility.
Overall, there are several structural factors that are indeed benign for the ionic conductivity. Overall, our findings point us to a lack of understanding of the complex interplay of all of these structural features in LiPON materials.

4.4. Conclusion

The new lithium oxonitridophosphate oxide $Li_{27-x}[P_4O_{7+x}N_{9-x}]O_3$ with $x \approx 1.9(3)$ was synthesized from Li_3N, P_3N_5 and Li_2O. The crystal structure consisting of statistically distributed $[PO_2N_2]^{5-}$ and $[PO_3N]^{4-}$ tetrahedra as well as oxide ions has been elucidated by employing a multitude of analytical methods (scXRD,PXRD, MAS NMR, 2D MAS NMR, neutron powder diffraction). The ionic conductivity of $6.6 \times 10^{-8}\,S\,cm^{-1}$ at 25 °C was obtained from impedance spectroscopy and is comparable to that of amorphous a-LiPON.
With various anion species ($[PO_3N]^{4-}$ and $[PO_2N_2]^{5-}$), as well as a partial occupancy of Li positions and mixed occupancy of O/N positions, $Li_{27-x}[P_4O_{7+x}N_{9-x}]O_3$ contains a complex mixture of structural features that influence the ionic conductivity. However, the impact of those various features on the conductivity is not fully understood yet. With further investigation of the conduction mechanism in $Li_{27-x}[P_4O_{7+x}N_{9-x}]O_3$, Li^+ ion conduction processes in LiPON materials might be understood better.

4.5. Acknowledgements

The authors thank Dr. Lisa Gamperl, Christian Minke, and Sandra Albrecht for EDX, NMR, and ICP measurements (all at Department of Chemistry, LMU Munich). Financial support by the DFG under Germany's Excellence Strategy - EXC 2089/1-390776260 (e-conversion) and as part of the grant OE530/6-1 is gratefully acknowledged. A.H. and B.V.L. acknowledge financial support by the German Federal Ministry of Research and Education (BMBF), project 03XP0177B (FestBatt). We thank the ESRF (Grenoble, France) for granting beamtime (experiment CH-6412); Dr. Vadim Dyadkin, Dr. Peter Schultz, Dr. Stefan Schwarzmüller and Dr. Frank Heinke are acknowledged for support during the beamtime. We also thank the FRM II (Munich, Germany) for rapid access beamtime (proposal no.16528). Open Access funding enabled and organized by Projekt DEAL.

4.6. References

[1] H.-O. Mulfinger, *J. Am. Ceram. Soc.* **1966**, *49*, 462–467.

[2] R. E. Loehman, *J. Non. Cryst. Solids* **1980**, *42*, 433–445, DOI 10.1016/0022-3093(80)90042-3.

[3] R. E. Loehman, *J. Non. Cryst. Solids* **1983**, *56*, 123–134, DOI 10.1016/0022-3093(83)90457-X.

[4] M. R. Reidmeyer, D. E. Day, *J. Am. Ceram. Soc.* **1985**, *68*, C188–C190, DOI 10.1111/j.1151-2916.1985.tb10177.x.

[5] T. Holmes, G. Leatherman, T. El-Korchi, *J. Mater. Res.* **1991**, *6*, 152–158, DOI 10.1557/JMR.1991.0152.

[6] M. R. Reidmeyer, D. E. Day, *J. Non. Cryst. Solids* **1995**, *181*, 201–214, DOI 10.1016/S0022-3093(94)00511-7.

[7] R. Marchand, *J. Non. Cryst. Solids* **1983**, *56*, 173–178, DOI 10.1016/0022-3093(83)90464-7.

[8] R. W. Larson, D. E. Day, *J. Non. Cryst. Solids* **1986**, *88*, 97–113, DOI 10.1016/S0022-3093(86)80091-6.

[9] J. B. Bates, N. J. Dudney, G. R. Gruzalski, R. A. Zuhr, A. Choudhury, C. F. Luck, J. D. Robertson, *Solid State Ionics* **1992**, *53–56*, 647–654, DOI 10.1016/0167-2738(92)90442-R.

[10] S. D. Jones, J. R. Akridge, F. K. Shokoohi, *Solid State Ionics* **1994**, *69*, 357–368, DOI 10.1016/0167-2738(94)90423-5.

[11] J. B. Bates, N. J. Dudney, B. Neudecker, A. Ueda, C. D. Evans, *Solid State Ionics* **2000**, *135*, 33–45, DOI 10.1016/S0167-2738(00)00327-1.

[12] J. F. Ribeiro, R. Sousa, J. P. Carmo, L. M. Gonçalves, M. F. Silva, M. M. Silva, J. H. Correia, *Thin Solid Films* **2012**, *522*, 85–89, DOI 10.1016/j.tsf.2012.09.007.

[13] B. C. Bunker, D. R. Tallant, C. A. Balfe, R. J. Kirkpatrick, G. L. Turner, M. R. Reidmeyer, *J. Am. Ceram. Soc.* **1987**, *70*, 675–681, DOI 10.1111/j.1151-2916.1987.tb05738.x.

[14] D. E. Day, *J. Non. Cryst. Solids* **1989**, *112*, 7–14, DOI 10.1016/0022-3093(89)90488-2.

[15] N. Mascaraque, A. Durán, F. Muñoz, G. Tricot, *Int. J. Appl. Glas. Sci.* **2016**, *7*, 69–79, DOI 10.1111/ijag.12120.

[16] M. A. T. Marple, T. A. Wynn, D. Cheng, R. Shimizu, H. E. Mason, Y. S. Meng, *Angew. Chem. Int. Ed.* **2020**, *59*, 22185–22193, *Angew. Chem.* **2020**, *132*, 22369–22377, DOI 10.1002/anie.202009501.

[17] F. Munõz, J. Ren, L. Van Wüllen, T. Zhao, H. Kirchhain, U. Rehfuß, T. Uesbeck, *J. Phys. Chem. C* **2021**, *125*, 4077–4085, DOI 10.1021/acs.jpcc.0c10427.

[18] V. Lacivita, N. Artrith, G. Ceder, *Chem. Mater.* **2018**, *30*, 7077–7090, DOI 10.1021/acs.chemmater.8b02812.

[19] A. L. Sauze, L. Montagne, G. Palavit, F. Fayon, R. Marchand, *J. Non. Cryst. Solids* **2000**, *263-264*, 139–145, DOI 10.1016/s0022-3093(99)00630-4.

[20] C. Dietrich, M. Sadowski, S. Sicolo, D. A. Weber, S. J. Sedlmaier, K. S. Weldert, S. Indris, K. Albe, J. Janek, W. G. Zeier, *Chem. Mater.* **2016**, *28*, 8764–8773, DOI 10.1021/acs.chemmater.6b04175.

[21] S. Schneider, L. G. Balzat, B. V. Lotsch, W. Schnick, *Chem. Eur. J.* **2023**, *29*, e202202984, DOI 10.1002/chem.202202984.

[22] B. Wang, B. C. Chakoumakos, B. C. Sales, B. S. Kwak, J. B. Bates, *J. Solid State Chem.* **1995**, *115*, 313–323, DOI 10.1006/jssc.1995.1140.

[23] K. Senevirathne, C. S. Day, M. D. Gross, A. Lachgar, N. A. Holzwarth, *Solid State Ionics* **2013**, *233*, 95–101, DOI 10.1016/j.ssi.2012.12.013.

[24] D. Baumann, W. Schnick, *Eur. J. Inorg. Chem.* **2015**, 617–621, DOI 10.1002/ejic.201403125.

[25] P. López-Aranguren, M. Reynaud, P. Głuchowski, A. Bustinza, M. Galceran, J. M. López Del Amo, M. Armand, M. Casas-Cabanas, *ACS Energy Lett.* **2021**, *6*, 445–450, DOI 10.1021/acsenergylett.0c02336.

[26] A. Al-Qawasmeh, N. A. Holzwarth, *J. Power Sources* **2017**, *364*, 410–419, DOI 10.1016/j.jpowsour.2017.08.025.

[27] E.-M. Bertschler, C. Dietrich, J. Janek, W. Schnick, *Chem. Eur. J.* **2017**, *23*, 2185–2191, DOI 10.1002/chem.201605316.

[28] E.-M. Bertschler, R. Niklaus, W. Schnick, *Chem. Eur. J.* **2017**, *23*, 9592–9599, DOI 10.1002/chem.201700979.

[29] E.-M. Bertschler, T. Bräuniger, C. Dietrich, J. Janek, W. Schnick, *Angew. Chem. Int. Ed.* **2017**, *56*, 4806–4809, *Angew. Chem.* **2017**, *129*, 4884–4887, DOI 10.1002/anie.201701084.

[30] E.-M. Bertschler, R. Niklaus, W. Schnick, *Chem. Eur. J.* **2018**, *24*, 736–742, DOI 10.1002/chem.201704975.

[31] E.-M. Bertschler, C. Dietrich, T. Leichtweiß, J. Janek, W. Schnick, *Chem. Eur. J.* **2018**, *24*, 196–205, DOI 10.1002/chem.201704305.

[32] Y. Deng, C. Eames, J. N. Chotard, F. Laleìre, V. Seznec, S. Emge, O. Pecher, C. P. Grey, C. Masquelier, M. S. Islam, *J. Am. Chem. Soc.* **2015**, *137*, 9136–9145, DOI 10.1021/jacs.5b04444.

[33] R. D. Shannon, *Acta Crystallogr.* **1976**, *A32*, 751–767, DOI 10.1023/A:1018927109487.

[34] S. D. Kloß, O. Janka, T. Block, R. Pöttgen, R. Glaum, W. Schnick, *Angew. Chem. Int. Ed.* **2019**, *58*, 4685–4689, *Angew. Chem.* **2019**, *131*, 4733–4737, DOI 10.1002/anie.201809146.

[35] W. Schnick, J. Luecke, *J. Solid State Chem.* **1990**, *87*, 101–106, DOI 10.1016/0022-4596(90)90070-E.

[36] N. I. Ayu, E. Kartini, L. D. Prayogi, M. Faisal, Supardi, *Ionics* **2016**, *22*, 1051–1057, DOI 10.1007/s11581-016-1643-z.

[37] T. Ben-Chaabane, L. Smiri-Dogguy, Y. Laligant, A. Le Bail, *Eur. J. Solid State Inorg. Chem.* **1998**, *35*, 255–264, DOI 10.1016/S0992-4361(98)80006-4.

[38] E. V. Murashova, N. N. Chudinova, *Crystallogr. Reports* **2001**, *46*, 942–947, DOI 10.1134/1.1420823.

[39] V. I. Voronin, E. A. Sherstobitova, V. A. Blatov, G. S. Shekhtman, *J. Solid State Chem.* **2014**, *211*, 170–175, DOI 10.1016/j.jssc.2013.12.015.

[40] K. Nakamoto, *Infrared and Raman Spectra of Inorganic and Coordination Compounds: Part A: Theory and Applications in Inorg. Chem.: Sixth Edition*, 6th ed., John Wiley & Sons, Inc., Hoboken, NJ, **2008**, DOI 10.1002/9780470405840.

[41] M. A. Carrillo Solano, M. Dussauze, P. Vinatier, L. Croguennec, E. I. Kamitsos, R. Hausbrand, W. Jaegermann, *Ionics* **2016**, *22*, 471–481, DOI 10.1007/s11581-015-1573-1.

[42] J. T. S. Irvine, D. C. Sinclair, A. R. West, *Adv. Mater.* **1990**, *2*, 132–138, DOI 10.1002/adma.19900020304.

[43] S. Lorger, R. Usiskin, J. Maier, *J. Electrochem. Soc.* **2019**, *166*, A2215–A2220, DOI 10.1149/2.1121910jes.

[44] S. Zhao, Z. Fu, Q. Qin, *Thin Solid Films* **2002**, *415*, 108–113, DOI 10.1016/S0040-6090(02)00543-6.

[45] J. Li, W. Lai, *Solid State Ionics* **2020**, *351*, 115329, DOI 10.1016/j.ssi.2020.115329.

[46] Y. A. Du, N. A. W. Holzwarth, *Phys. Rev. B* **2007**, *76*, 174302, DOI 10.1103/PhysRevB.76.174302.

[47] H. Rabaâ, R. Hoffmann, N. Cruz Hernández, J. Fernandez Sanz, *J. Solid State Chem.* **2001**, *161*, 73–79, DOI 10.1006/jssc.2001.9269.

5. Finding Order in Disorder – The Highly Disordered Lithium Oxonitridophosphate Double Salt $Li_{8+x}P_3O_{10-x}N_{1+x}$ ($x = 1.4(5)$)

Stefanie Schneider, Sandra T. Kreiner, Lucas G. Balzat, Bettina V. Lotsch, and Wolfgang Schnick

Chem. Eur. J. **2023**, *29*, e202301986.
https://doi.org/10.1002/chem.202301986
DOI: 10.1002/chem.202301986

Reprinted (adapted) with permission from Chemistry – European Journal. Copyright 2023

$Li_{8+x}P_3O_{10-x}N_{1+x}$ is a lithium oxonitridophosphate double salt synthesized from P_3N_5 and Li_2O in ampoule synthesis. The structure consists of phosphate and diphosphate motifs and exhibits a severe disorder in the diphosphate unit. NMR and vibrational spectroscopy give additional information concerning the composition with oxygen and nitrogen. $Li_{8+x}P_3O_{10-x}N_{1+x}$ is a Li^+ ion conductor with a total ionic conductivity of $1.2 \times 10^{-7}\,S\,cm^{-1}$.

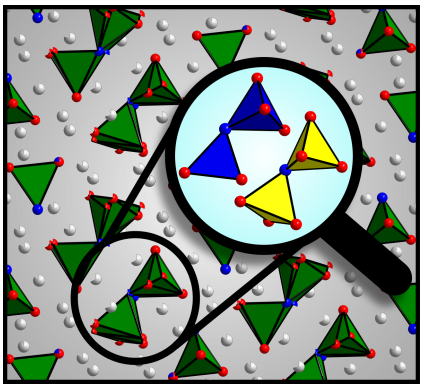

5.1. Abstract

The crystalline lithium oxonitridophosphate $Li_{8+x}P_3O_{10-x}N_{1+x}$, was obtained in an ampoule synthesis from P_3N_5 and Li_2O. The compound crystallizes in the triclinic space group $P\bar{1}$ with $a = 5.125(2)$, $b = 9.888(5)$, $c = 10.217(5)$ Å, $\alpha = 70.30(2)$, $\beta = 76.65(2)$, $\gamma = 77.89(2)°$. $Li_{8+x}P_3O_{10-x}N_{1+x}$ a double salt, the structure of which contains distinctive complex anion species, namely non-condensed $P(O,N)_4$ tetrahedra, and $P(O,N)_7$ double tetrahedra connected by one N atom. Additionally, there is mixed occupation of O/N positions, which enables further anionic species by variation of O/N occupancies. To characterize these motifs in detail, complementary analytical methods were applied. The double tetrahedron exhibits significant disorder in single-crystal X-ray diffraction. Furthermore, the title compound is a Li^+ ion conductor with a total ionic conductivity of $1.2 \times 10^{-7}\,S\,cm^{-1}$ at 25 °C, and a corresponding total activation energy of 0.47(2) eV.

5.2. Introduction

Lithium oxonitridophosphate (LiPON) glasses have been subject of extensive research since their discovery as Li^+ ion conductors in the 1990s.[1–5] Amorphous LiPON layers are deposited by sputtering Li_3PO_4 in a defined nitrogen-containing atmosphere.[1,2,6,7] Their electrochemical stability and ionic conductivity are much larger than that of the starting material and depend strongly on N-content and the atomic ratio of N/P.[6–9]

As solid state electrolyte, their mechanical stability enables the use of pure Li anodes, as dendrite formation during cycling is prevented.[10] Due to these properties and the easy formation of thin layers from inexpensive starting materials, amorphous LiPON has been used in thin film batteries of only several µm thickness.[2–5,11]

In spite of the comprehensive investigation of LiPON with spectroscopic methods, its missing long-range order made investigation of its structural intricacies impossible over a long period of time.[2,12–14] However, structural information is highly desirable in order to determine the correlation of structural with materials properties like ionic conductivity. Since common diffraction methods cannot be applied to amorphous materials, structural information must be obtained from short-range sensitive methods such as XPS, IR, or NMR.[2,14–16] However, owing to the sparse local structure information available, the structural traits of LiPON-type materials still remained largely speculative. The first crystalline lithium oxonitridophosphate $Li_{2.88}PO_{3.73}N_{0.14}$ enabled the complementary use of diffraction with short-range sensitive methods.[12,17] Thus, signals obtained from XPS and IR could be assigned to apical (Na) or bridging (Nb) nitrogen atoms with the help of overall structural information from diffraction data. Since then, several further crystalline lithium oxonitridophosphates have been found that add to the pool of information on short-range sensitive data supported by long-range diffraction methods.[18–22] Additionally, *in-silico* methods like *ab-initio* molecular dynamics (AIMD) simulations were employed to further characterize the structure of amorphous LiPON and its influence on conductivity.[9,12,23–25] It was observed that a high degree of disorder within the structure is beneficial for increased ionic conductivity due to flattened energy landscapes around Li^+

positions.[9,25]
Sharing various chemical and physical properties like chemical stability and physical hardness with amorphous LiPON, crystalline lithium oxonitridophosphates have also attracted notice as potential solid electrolytes to be used in all-solid-state batteries.[20] Furthermore, their structures exhibit significant disorder. Whereas in Li_2PO_2N and $Li_{14}(PON_3)_2O$ full occupancy of O and N positions can be observed, $Li_{2.88}PO_{3.73}N_{0.14}$, $Li_{3.6}PO_{3.4}N_{0.6}$, $Li_{5+x}P_2O_{6-x}N_{1+x}$, and $Li_{27-x}[P_4O_{7+x}N_{9-x}]O_3$ exhibit mixed or partial occupancy of O and N positions.[17–22] This can lead to a significant degree of disorder and various different environments around Li. In these crystalline lithium oxonitridophosphates, different complex anions present in the structure are a result of mixed or statistical occupancy of O/N positions.[17,20,21] For example, mixed occupancy of O and N in $P(O,N)_4$ tetrahedra could result in PO_4, PO_3N, PO_2N_2, PON_3, and PN_4 motifs in the structure. In contrast, the structure of $Li_{8+x}P_3O_{10-x}N_{1+x}$ shows two different structural motifs, which are non-condensed tetrahedra and pairs of corner-sharing tetrahedra, both of which can have mixed occupancy of O/N positions. Since the distinction between O and N is difficult with X-ray diffraction, other analytical methods have to be employed. Solid-state magic-angle spinning (MAS) NMR spectroscopy is a powerful tool for the analysis of both crystalline and amorphous materials, as only the local environment is observed.[13,20,26–28] The different possible non-condensed $P(O,N)_4$ tetrahedra can be clearly distinguished, since the substitution of each O for N results in an additional shift of about +10 ppm.[13,20] Therefore, the structures of lithium oxonitridophosphates can only be distinguished by a combination of complementary analytical methods. In the case of $Li_{8+x}P_3O_{10-x}N_{1+x}$, the crystal structure was investigated by single-crystal X-ray diffraction, which allows the analysis of atomic positions, and by NMR, which allows the assignment of O and N occupancies to these sites in more detail. The characterization is complemented with IR and elemental analysis, thermal stability measurements, and the examination of ionic and electronic conductivity by impedance spectroscopy.

5.3. Results and Discussion

5.3.1. Synthesis

$Li_{8+x}P_3O_{10-x}N_{1+x}$ was obtained over a wide range in stoichiometry and reaction duration, by reaction of P_3N_5 with Li_2O in an open Ta crucible sealed under Ar into a silica ampoule. P_3N_5 and Li_2O in a molar ratio of 1 : 6 to 1 : 11 were heated to 800 °C with heating and cooling rates of 5 K min^{-1} and held for 30–90 h. Equation (5.1) shows the idealized reaction equation. An excess of Li_2O is beneficial for the formation of $Li_{8+x}P_3O_{10-x}N_{1+x}$ with as little $Li_{5+x}P_2O_{6-x}N_{1+x}$ side phase as possible. This corresponds well with other known lithium nitridophosphate and lithium oxonitridophosphate syntheses, in which an excess of lithium-containing starting material had to be used to acquire targeted compounds.[29–32] The formal formation of Li_3N has not been observed, possibly due to further reactions. Instead, small amounts of Li3P were formed at elevated temperatures as has been observed in other lithium (oxo)nitridophosphate syntheses.[21,22,29–32] Li_3P was washed out with dry ethanol.

$$P_3N_5 + (10 - x)\ Li_2O \longrightarrow Li_{8+x}P_3O_{10-x}N_{1+x} + (4 - x)\ Li_3N \tag{5.1}$$

$Li_{8+x}P_3O_{10-x}N_{1+x}$ was obtained as colorless, microcrystalline powder sensitive to air and moisture. No phase pure synthesis could be achieved. Various amounts of Li_2O were present in all synthesis conditions and could not be avoided by variation of the amount of Li_2O as starting material. $Li_{5+x}P_2O_{6-x}N_{1+x}$ was another regularly observed side phase. Figure 5.1 shows the Rietveld refinement of a sample with the highest content of the targeted phase.

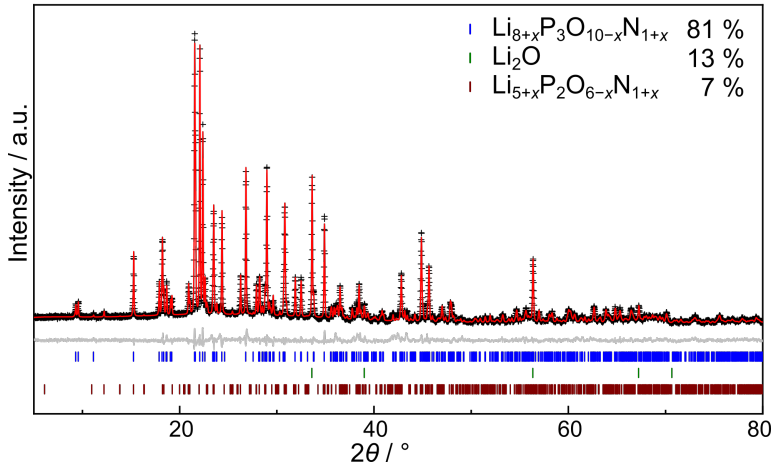

Figure 5.1.: Rietveld Refinement for a sample of $Li_{8+x}P_3O_{10-x}N_{1+x}$ with measured (black crosses) and calculated (red) intensities and their difference (gray). The positions of reflections of $Li_{8+x}P_3O_{10-x}N_{1+x}$, Li_2O, and $Li_{5+x}P_2O_{6-x}N_{1+x}$ are shown with blue, green, and brown markers, respectively.

5.3.2. Crystal structure

The crystal structure of $Li_{8+x}P_3O_{10-x}N_{1+x}$ was determined by single-crystal X-ray diffraction. The structure crystallizes in the triclinic space group $P\bar{1}$ with $a = 5.125(2)$, $b = 9.888(5)$, $c = 10.217(5)$ Å, $\alpha = 70.30(2)$, $\beta = 76.65(2)$, $\gamma = 77.89(2)°$. Additional crystallographic details are listed in Table 5.1 and Tables C.1, C.2 and C.5 and **??**.

The structure consists of $P(O,N)_4$ tetrahedra and pairs of tetrahedra $P_2(O,N)_7$ connected by one N atom, resulting in an oxonitridophosphate oxonitridodiphosphate (Figure 5.2a). NMR data suggest that P is coordinated by at least one N in both the non-condensed tetrahedron and the diphosphate motif. Due to the small X-ray scattering contrast and the large degree of disorder within this structure, exact positions of O and N cannot be assigned unequivocally. However, the obtained NMR data indicate occupation of bridging positions with N. As N atoms have been shown to be energetically favorable in contrast to O in bridging positions, this is considered accurate.[9,33,34] In the phosphate unit, N was placed according to ssNMR results and in positions that yielded a stable refinement and the best figures of merit. For a conclusive answer to the occupancy of O and N atoms, neutron diffraction would be required.

Table 5.1.: Crystallographic data on $Li_{8+x}P_3O_{10-x}N_{1+x}$.

Formula	$Li_{9.23}P_3O_{8.77}N_{2.23}$
Formula weight / g mol^{-1}	328.54
Crystal system	triclinic
Space group	$P\bar{1}$ (no. 2)
Lattice parameters / Å, °	$a = 5.125(2)$
	$b = 9.888(5)$
	$c = 10.217(5)$
	$\alpha = 70.30(2)$
	$\beta = 76.65(2)$
	$\gamma = 77.89(2)$
Cell volume / Å^3	469.3(4)
Formula units per unit cell	2
Density / g cm^{-3}	2.325
μ / mm^{-1}	0.673
Crystal size / mm	$0.04 \times 0.04 \times 0.03$
Radiation λ	Mo-K$_\alpha$ $\lambda = 0.710\,73$ Å
θ-range / °	$3.522 \leq \theta \leq 18.995$
Total no. of reflections	12246
Independent reflections	3792, thereof 2748 with $F^2 > 2\sigma(F^2)$
Refined parameters	303
R_{int}; R_σ	0.0716; 0.0795
$R1$ (all data); $R1$ ($F^2 > 2\sigma(F^2)$)	0.0864; 0.0586
$wR2$ (all data); $wR2$ ($F^2 > 2\sigma(F^2)$)	0.1547; 0.1407
Goodness of fit (χ^2)	1.049
$\Delta\rho_{max}$; $\Delta\rho_{min}$ / e Å^{-3}	0.878; −0.992

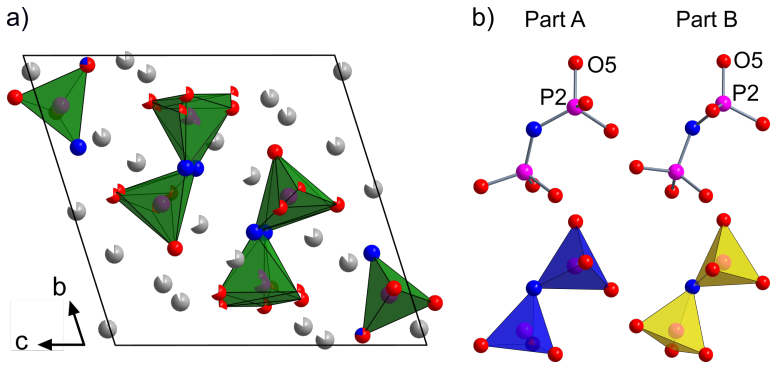

Figure 5.2.: Structure of $Li_{8+x}P_3O_{10-x}N_{1+x}$. P and Li are shown in pink and gray, O and N in red and blue, respectively. a) Unit cell of $Li_{8+x}P_3O_{10-x}N_{1+x}$ along a with superimposed diphosphate motifs and their partial occupancies. Li positions were refined with an occupational restraint for charge neutrality. b) Side-by-side view of disordered diphosphate motifs as ball-and-stick representation (top) and as polyhedra (bottom). Rotation around the P2–O5 bond and tilting of the connected tetrahedron can project Part A onto Part B.

The non-condensed tetrahedron is slightly distorted. P–O/N bond lengths of 1.572(2)–1.592(3) Å are well within the range of known P–O and P–N distances in lithium phosphates[35–38] and (oxo)nitridophosphates.[17–22,29–32] Angles within this tetrahedron range from 107.13(14)–114.84(14)°.
The diphosphate motif is highly disordered and can be explained with two orientations (Part A and Part B) that are twisted against each other around the P2–O5 bond and tilted in the bridging atom (Figure 5.2b). 31.5(8) % of O/N atoms occupy sites in Part A, whereas sites in Part B have an occupancy of 68.5(8) %. P–O/N distances in the diphosphate motif have a wider range compared to the non-condensed phosphate motif (1.568(3)–1.634(7) Å in Part A, 1.537(4)–1.688(4) Å in Part B), which are, however, also well within the range of known P–O/N distances.[17–22,29–32,35–38] The P–N–P angle around P002–N08A–P03A is with 130.5(11)° distinctly larger than that around P002–N08B–P03B (124.3(3)°) (Figure 5.2b). Presence of O or N at specific positions might influence preference of either Part A or Part B and influence occupancy of Li positions or vice versa.
There are eleven Li^+ positions found in the structure, all of which are not fully occupied when refined freely. Since free refinement does not yield charge neutrality, an occupancy restraint was used to match the anion charge and to produce a charge-neutral sum-formula. The Li positions exhibit very diverse, distorted coordination polyhedra (Figure C.1). Neutron diffraction would provide more reliable data on the occupancy of Li positions.

5.3.3. Nuclear magnetic resonance (NMR) spectroscopy

Magic angle spinning (MAS) NMR spectra were obtained for ^{31}P, ^{6}Li, and ^{7}Li. The ^{31}P MAS-NMR spectrum shows signals at 33.7, 21.8 and 16.3 ppm, with the signals at 21.8 and 16.3 ppm overlapping partly (Figure 5.3). From single-crystal X-ray diffraction the $P(O,N)_4$ and $P_2(O,N)_7$ motifs are expected in a 1 : 1 ratio. Thus, one third of the total area of the signals must result from non-condensed tetrahedra, whereas two thirds result from double-tetrahedra. The chemical shift of non-condensed $P(O,N)_4$ tetrahedra is well investigated and increases by about 10 ppm for each O that is substituted by N.[13,19,20,22,39] The signal at $\delta_{iso} = 33.7$ ppm can be assigned to $[PO_2N_2]^{5-}$, which is in good accordance with literature data (31.3 and 33.0 ppm).[20,22] The signal at 16.3 ppm is partly overlapped by the signal at 21.8 ppm, which results in a slight downfield-shift of the maximum upon comparison of the added signals with the deconvoluted signals. Deconvolution of the signals results in a maximum at 16.2 ppm. Overall, the chemical shift is in good agreement with $[P_2O_6N]^{5-}$ motifs in literature (14.6 and 14.2 ppm).[13,21] The signal resulting in a shoulder with a chemical shift of 21.8 ppm can be attributed either to $[PO_3N]^{4-}$ (19.4, 19.8 and 19.6 ppm in literature)[13,20,22] or to $[P_2O_5N_2]^{6-}$ (21.4 ppm in literature)[21]. Deconvolution of the signals shows a 10.4(7) : 26.2(13) : 63(2) ratio. Since the signal at 33.8 ppm (10.4(7) % of the total area) can be assigned to $[PO_2N_2]^{5-}$ and one third of the overall signal area must result from non-condensed tetrahedra, another 22.9(7) % must result from $[PO_3N]^{4-}$, which is a large portion of the signal at 21.8 ppm. From this signal, which constitutes 26.2(13) % of the total area, 3.3(8) % remain. These 3.3(8) % of the total area result from the P coordinated by two N atoms within $[P_2O_5N_2]^{6-}$. As the bridging atom is assumed to be N, the diphosphate $[P_2O_6N_2]^{6-}$ must constitute the same amount from the remaining signal at 16.4 ppm. This signal

at 16.4 ppm with 63(2) % of the total area results from singly N-coordinated P in both $[P_2O_6N]^{5-}$ (60(3) %) and $[P_2O_5N_2]^{6-}$ (3.3(8) %). In summary, the signal at 33.8 ppm stems from $[PO_2N_2]^{5-}$, the signal at 16.3 ppm is from the singly N-coordinated P within both diphosphate species ($[P_2O_5N_2]^{6-}$ and $[P_2O_6N]^{5-}$), and the signal at 21.8 ppm results from both $[PO_3N]^{4-}$ and the doubly N-coordinated P in $[P_2O_5N_2]^{6-}$. With this assignment of motifs, a sum formula of $Li_{9.4(14)}P_3O_{8.6(5)}N_{2.4(2)}$ results. Thus, the general sum formula $Li_{8+x}P_3O_{10-x}N_{1+x}$ can be obtained with $x = 1.4(5)$.

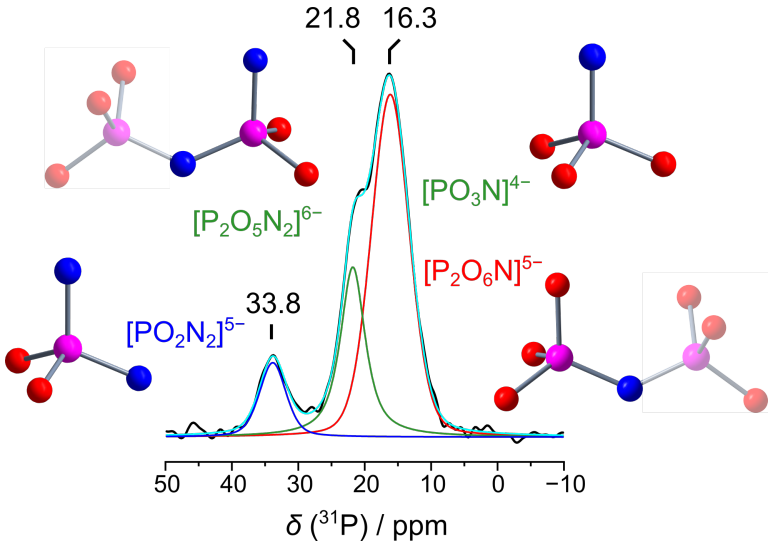

Figure 5.3.: ^{31}P NMR spectrum with structural motifs corresponding to the respective signals. The signal at 33.8 ppm can be attributed to $[PO_2N_2]^{5-}$ (blue), the signal at 21.8 ppm is constituted from $[PO_3N]^{4-}$ and the doubly by N coordinated P in $[P_2O_5N_2]^{6-}$ (green), and the signal at 16.3 ppm results from the singly by N coordinated P in both $[P_2O_5N_2]^{6-}$ and $[P_2O_6N]^{5-}$ (red).

The ^6Li and ^7Li spectra each show one signal that cannot be deconvoluted (Figure 5.3). The width of the signal can be explained by the presence of eleven partly occupied Li positions, which are all slightly different. Due to the disorder in the diphosphate motif, coordination spheres around each Li position vary again, depending on which orientation of the diphosphate motif is coordinated. Only Li10 is coordinated solely by O and N from the phosphate motif, which does not exhibit disorder. Thus, Li10 exhibits only one coordination sphere (Figure C.3).

5.3.4. Thermal stability measurements and FTIR spectroscopy

Variable-temperature powder X-ray diffraction of a sample with Li_2O as side phase showed additional reflections of $Li_{5+x}P_2O_{6-x}N_{1+x}$ and Li_3PO_4 above 720 °C due to decomposition of the title compound. Above 840 °C, mostly Li_3P remains (Figure 5.4).

Presence of hydrogen in the structure can be identified with infrared (IR) spectroscopy. O–H or N–H vibrations would be visible at around 2800–3200 or 3000–3500 cm^{-1}, respectively.[40–42] As no such signal is present in these areas, the presence of H in the structure can be excluded (Figure 5.5). P–O

and P–N vibrational bands are visible in the fingerprint area between 400–1200 cm^{-1}. However, the signals are superimposed and cannot be resolved and assigned to distinct vibrations.

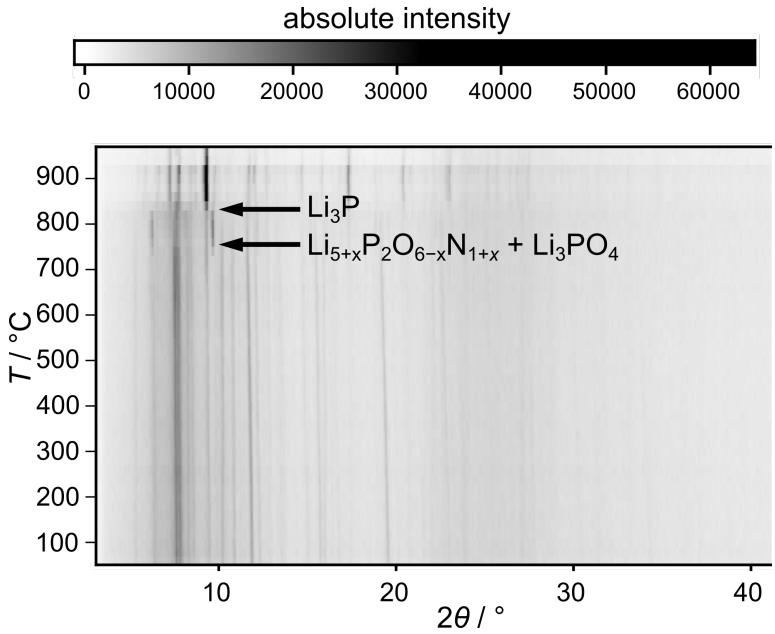

Figure 5.4.: Variable-temperature powder X-ray diffraction measurement of $Li_{8+x}P_3O_{10-x}N_{1+x}$ from 60–960 °C.

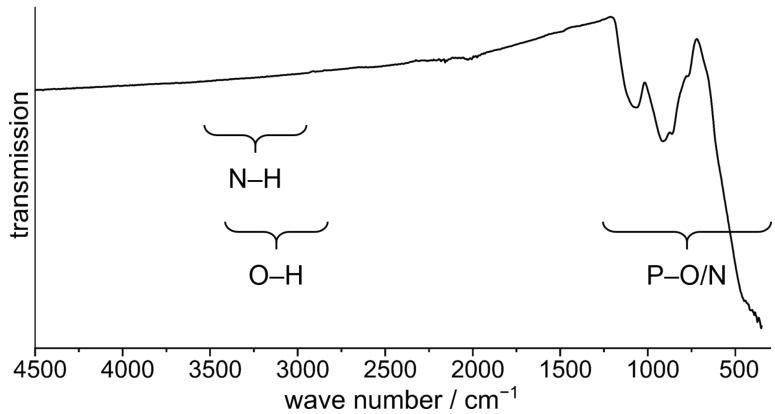

Figure 5.5.: Infrared transmission spectrum of $Li_{8+x}P_3O_{10-x}N_{1+x}$ measured under Ar with an ATR unit with diamond window.

5.3.5. Elemental analysis

Energy-dispersive X-ray spectroscopy showed a very large deviation from calculated values as obtained from NMR ($x = 1.4$). Instead, EDX suggests a stoichiometry of $Li_{11}P_3O_7N_4$ ($x = 3$) (C.7). However, the uncertainties of these values are very large due to the presence of light atoms. The sum formula derived from EDX would be $Li_{11(8)}P_{3.0(13)}O_{7(5)}N_{4(2)}$.

The N content measured with CHNS is slightly larger than expected for $Li_{8+x}P_3O_{10-x}N_{1+x}$. The side phase $Li_{5+x}P_2O_{6-x}N_{1+x}$ was considered in the calculations with an average value of $x = 0.9$. However, as this phase is not stoichiometrically precise, the deviation of the measured from the expected value might be increased by the coexistence of this side phase.

5.3.6. Ionic and electronic conductivity measurements

The ionic conductivity of $Li_{8+x}P_3O_{10-x}N_{1+x}$ was determined by electrochemical impedance spectroscopy (EIS). Figure 5.6 shows EIS data gathered from a pellet containing 70 wt-% $Li_{8+x}P_3O_{10-x}N_{1+x}$, 24 wt-% Li_2O and 6 wt-% $Li_{5+x}P_2O_{6-x}N_{1+x}$ (phase composition determined from Rietveld refinement). Three processes are visible, indicated as two semicircles and one spike in the low-frequency range. The semicircles were modeled with a serial connection of a resistor (R) and a constant phase element (CPE) in parallel, while the low-frequency polarization spike was modeled with an additional CPE in series. CPEs were chosen to account for non-ideal sample behavior.[43] To assign processes to the semicircles, the capacities of CPE1 and CPE2 were calculated using the Brug formula.[44] At 25 °C the first and second semicircle exhibit capacities of 1.7×10^{-11} Fand 3.8×10^{-11} farad, respectively. Because the capacities are very similar it is not possible to assign bulk and grain boundary contributions to the individual semicircles.[45] Therefore, in the following only the total conductivity and total activation energy are reported.

Using R1+R2 the total ionic conductivity is found to be $1.2 \times 10^{-7}\,S\,cm^{-1}$ at 25 °C. The total activation energy of $Li_{8+x}P_3O_{10-x}N_{1+x}$ was determined by fitting temperature dependent EIS data to a linear Arrhenius-type behavior, resulting in a total activation energy of 0.47(2) eV (see inset Figure 5.6). The electronic conductivity of $Li_{8+x}P_3O_{10-x}N_{1+x}$ was determined via potentiostatic polarization measurements. An exemplary U-I curve is displayed in C.5. $Li_{8+x}P_3O_{10-x}N_{1+x}$ shows an electronic conductivity of $2.3 \times 10^{-9}\,S\,cm^{-1}$ at 25 °C, about two orders of magnitude lower than its ionic conductivity. With an ionic transference number $\tau_i = \sigma_{ion}/(\sigma_{ion} + \sigma_{eon})$ of 0.981, $Li_{8+x}P_3O_{10-x}N_{1+x}$ can thus be classified as a predominantly ionic conductor with a small, yet significant electronic conductivity.

Since only multi-phase samples of $Li_{8+x}P_3O_{10-x}N_{1+x}$ in small quantities were available, several EIS measurements using two samples with different compositions were carried out to ensure reproducibility (see SI and Figure S4 for a discussion on reproducibility). Generally, the total conductivities of the two measured samples vary slightly ($1.2 \times 10^{-7}\,S\,cm^{-1}$ and $3.4 \times 10^{-8}\,S\,cm^{-1}$, 25 °C), which is likely due to differing phase compositions, while the total activation energies are in good agreement. The ionic conductivity of $Li_{8+x}P_3O_{10-x}N_{1+x}$ is comparable to that of other known lithium oxonitridophosphates, which range from $1 \times 10^{-13}\,S\,cm^{-1}$ ($Li_{2.88}PO_{3.73}N_{0.14}$) to $1.6 \times 10^{-6}\,S\,cm^{-1}$ (amorphous LiPON) at room temperature.[17,18,20–22,46]

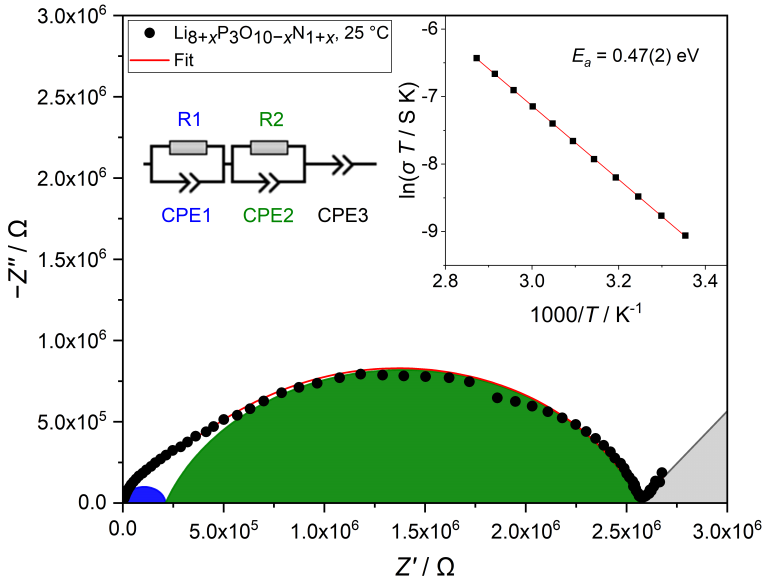

Figure 5.6.: Nyquist plot of impedance data of $Li_{8+x}P_3O_{10-x}N_{1+x}$ gathered at 25 °C. The contributions of the first (R1/CPE1; blue) and second semicircle (R2/CPE2, green) are are highlighted, respectively. The inset shows an Arrhenius plot of temperature-dependent EIS data, resulting in a total activation energy of $E_a = 0.47(2)$ eV. This is a corrected version of the figure according to a submitted corrigendum.

5.4. Conclusion

With $Li_{8+x}P_3O_{10-x}N_{1+x}$, a new crystalline lithium oxonitridophosphate was synthesized from ampoule synthesis. It is a double salt containing both phosphate and diphosphate motifs. With mixed occupancies, as shown by NMR spectroscopy, the following structural motifs could be identified: PO_2N_2, PO_3N, P_2O_6N, and $P_2O_5N_2$. Furthermore, the diphosphate motif exhibits severe disorder. For further characterization and more detailed information on both O/N and Li occupancy, neutron diffraction would be indispensable. Impedance spectroscopy showed a total Li^+ conductivity of 1.2×10^{-7} S cm^{-1} at 25 °C, with a total activation energy of 0.47(2) eV, which is within the range of other crystalline lithium oxonitridophosphates.[17,18,20–22,46] The significant disorder in the structure might be beneficial for the system's conductivity. Density functional theory (DFT) calculations could be employed to give further insights to the mechanisms of conductivity in lithium oxonitridophosphates in general and in $Li_{8+x}P_3O_{10-x}N_{1+x}$ specifically.

If applied as thin film, the conductivity of $Li_{8+x}P_3O_{10-x}N_{1+x}$ might be sufficient for use in thin film batteries. Thus, its applicability as electrolyte against suitable electrode materials should be investigated, as the electrochemical stability window, stability against reaction with Li, and cycle stability are not yet known. Considering the immense structural diversity of lithium nitridophosphates and the few hitherto known lithium oxonitridophosphates, lithium oxonitridophosphates harbor the potential of a large amount of complex crystal structures, some of which might exhibit much larger ionic conductivities than the known representatives.

5.5. Acknowledgements

The authors thank Dr. Lisa Gamperl, Christian Minke, and Sandra Albrecht (all at Department of Chemistry, LMU Munich) for EDX, NMR, and ICP-OES measurements, respectively. The authors acknowledge funding support from the Deutsche Forschungsgemeinschaft (DFG, German Research Foundation) under Germany's Excellence Strategy-EXC 2089/1-390776260 (e-Conversion).
L. G. B. and B. V. L. acknowledge financial support by the German Federal Ministry of Research and Education (BMBF), project 03XP0430B (FestBatt).

5.6. References

[1] J. B. Bates, N. J. Dudney, G. R. Gruzalski, R. A. Zuhr, A. Choudhury, C. F. Luck, J. D. Robertson, *Solid State Ionics* **1992**, *53–56*, 647–654, DOI 10.1016/0167-2738(92)90442-R.

[2] J. B. Bates, N. J. Dudney, G. R. Gruzalski, R. A. Zuhr, A. Choudhury, C. F. Luck, J. D. Robertson, *J. Power Sources* **1993**, *43*, 103–110, DOI 10.1016/0378-7753(93)80106-Y.

[3] J. B. Bates, G. R. Gruzalski, N. J. Dudney, C. F. Luck, X. Yu, *Solid State Ionics* **1994**, *70–71*, 619–628, DOI 10.1016/0167-2738(94)90383-2.

[4] J. B. Bates, N. J. Dudney, D. C. Lubben, G. R. Gruzalski, B. S. Kwak, X. Yu, R. A. Zuhr, *J. Power Sources* **1995**, *54*, 58–62, DOI 10.1016/0378-7753(94)02040-A.

[5] J. B. Bates, N. J. Dudney, B. Neudecker, A. Ueda, C. D. Evans, *Solid State Ionics* **2000**, *135*, 33–45, DOI 10.1016/S0167-2738(00)00327-1.

[6] Y. Hamon, A. Douard, F. Sabary, C. Marcel, P. Vinatier, B. Pecquenard, A. Levasseur, *Solid State Ionics* **2006**, *177*, 257–261, DOI 10.1016/j.ssi.2005.10.021.

[7] H. Y. Park, S. C. Nam, Y. C. Lim, K. G. Choi, K. C. Lee, G. B. Park, S. R. Lee, H. P. Kim, S. B. Cho, *J. Electroceram.* **2006**, *17*, 1023–1030, DOI 10.1007/s10832-006-8976-3.

[8] X. Yu, J. B. Bates, G. E. Jellison Jr., F. X. Hart, *J. Electrochem. Soc.* **1997**, *144*, 524–532, DOI 10.1149/1.1837443.

[9] V. Lacivita, N. Artrith, G. Ceder, *Chem. Mater.* **2018**, *30*, 7077–7090, DOI 10.1021/acs.chemmater.8b02812.

[10] E. G. Herbert, W. E. Tenhaeff, N. J. Dudney, G. M. Pharr, *Thin Solid Films* **2011**, *520*, 413–418, DOI 10.1016/j.tsf.2011.07.068.

[11] S. D. Jones, J. R. Akridge, F. K. Shokoohi, *Solid State Ionics* **1994**, *69*, 357–368, DOI 10.1016/0167-2738(94)90423-5.

[12] V. Lacivita, A. S. Westover, A. Kercher, N. D. Phillip, G. Yang, G. Veith, G. Ceder, N. J. Dudney, *J. Am. Chem. Soc.* **2018**, *140*, 11029–11038, DOI 10.1021/jacs.8b05192.

[13] M. A. T. Marple, T. A. Wynn, D. Cheng, R. Shimizu, H. E. Mason, Y. S. Meng, *Angew. Chem. Int. Ed.* **2020**, *59*, 22185–22193, *Angew. Chem.* **2020**, *132*, 22369–22377, DOI 10.1002/anie.202009501.

[14] M. A. Carrillo Solano, M. Dussauze, P. Vinatier, L. Croguennec, E. I. Kamitsos, R. Hausbrand, W. Jaegermann, *Ionics* **2016**, *22*, 471–481, DOI 10.1007/s11581-015-1573-1.

[15] B. C. Bunker, D. R. Tallant, C. A. Balfe, R. J. Kirkpatrick, G. L. Turner, M. R. Reidmeyer, *J. Am. Ceram. Soc.* **1987**, *70*, 675–681, DOI 10.1111/j.1151-2916.1987.tb05738.x.

[16] B. Fleutot, B. Pecquenard, H. Martinez, M. Letellier, A. Levasseur, *Solid State Ionics* **2011**, *186*, 29–36, DOI 10.1016/j.ssi.2011.01.006.

[17] B. Wang, B. C. Chakoumakos, B. C. Sales, B. S. Kwak, J. B. Bates, *J. Solid State Chem.* **1995**, *115*, 313–323, DOI 10.1006/jssc.1995.1140.

[18] K. Senevirathne, C. S. Day, M. D. Gross, A. Lachgar, N. A. Holzwarth, *Solid State Ionics* **2013**, *233*, 95–101, DOI 10.1016/j.ssi.2012.12.013.

[19] D. Baumann, W. Schnick, *Eur. J. Inorg. Chem.* **2015**, 617–621, DOI 10.1002/ejic.201403125.

[20] P. López-Aranguren, M. Reynaud, P. Głuchowski, A. Bustinza, M. Galceran, J. M. López Del Amo, M. Armand, M. Casas-Cabanas, *ACS Energy Lett.* **2021**, *6*, 445–450, DOI 10.1021/acsenergylett.0c02336.

[21] S. Schneider, L. G. Balzat, B. V. Lotsch, W. Schnick, *Chem. Eur. J.* **2023**, *29*, e202202984, DOI 10.1002/chem.202202984.

[22] S. Schneider, E.-M. Wendinger, V. Baran, A.-K. Hatz, B. V. Lotsch, M. Nentwig, O. Oeckler, T. Bräuniger, W. Schnick, *Chem. Eur. J.* **2023**, *29*, e202300174, DOI 10.1002/chem.202300174.

[23] H. Rabaâ, R. Hoffmann, N. Cruz Hernández, J. Fernandez Sanz, *J. Solid State Chem.* **2001**, *161*, 73–79, DOI 10.1006/jssc.2001.9269.

[24] N. D. Lepley, N. A. W. Holzwarth, *J. Electrochem. Soc.* **2012**, *159*, A538–A547, DOI 10.1149/2.jes113225.

[25] J. Li, W. Lai, *Solid State Ionics* **2020**, *351*, 115329, DOI 10.1016/j.ssi.2020.115329.

[26] G. L. Paraschiv, F. Muñoz, L. R. Jensen, R. M. Larsen, Y. Yue, M. M. Smedskjaer, *J. Am. Ceram. Soc.* **2018**, *101*, 5004–5019, DOI 10.1111/jace.15747.

[27] A. Kidari, C. Mercier, A. Leriche, B. Revel, M. J. Pomeroy, S. Hampshire, *Mater. Lett.* **2012**, *84*, 38–40, DOI 10.1016/j.matlet.2012.06.029.

[28] N. Mascaraque, J. L. G. Fierro, F. Muñoz, A. Durán, Y. Ito, Y. Hibi, R. Harada, A. Kato, A. Hayashi, M. Tatsumisago, *J. Mater. Res.* **2015**, *30*, 2940–2948, DOI 10.1557/jmr.2015.128.

[29] E.-M. Bertschler, R. Niklaus, W. Schnick, *Chem. Eur. J.* **2017**, *23*, 9592–9599, DOI 10.1002/chem.201700979.

[30] E.-M. Bertschler, C. Dietrich, J. Janek, W. Schnick, *Chem. Eur. J.* **2017**, *23*, 2185–2191, DOI 10.1002/chem.201605316.

[31] E.-M. Bertschler, C. Dietrich, T. Leichtweiß, J. Janek, W. Schnick, *Chem. Eur. J.* **2018**, *24*, 196–205, DOI 10.1002/chem.201704305.

[32] E.-M. Bertschler, R. Niklaus, W. Schnick, *Chem. Eur. J.* **2018**, *24*, 736–742, DOI 10.1002/chem.201704975.

[33] Y. A. Du, N. A. Holzwarth, *Phys. Rev. B* **2010**, *81*, 1–15, DOI 10.1103/PhysRevB.81.184106.

[34] Y. A. Du, N. A. Holzwarth, *Phys. Rev. B* **2008**, *78*, 1–13, DOI 10.1103/PhysRevB.78.174301.

[35] N. I. Ayu, E. Kartini, L. D. Prayogi, M. Faisal, Supardi, *Ionics* **2016**, *22*, 1051–1057, DOI 10.1007/s11581-016-1643-z.

[36] V. I. Voronin, E. A. Sherstobitova, V. A. Blatov, G. S. Shekhtman, *J. Solid State Chem.* **2014**, *211*, 170–175, DOI 10.1016/j.jssc.2013.12.015.

[37] B. Raguž, K. Wittich, R. Glaum, *Eur. J. Inorg. Chem.* **2019**, *2019*, 1688–1696, DOI 10.1002/ejic.201801100.

[38] T. Ben-Chaabane, L. Smiri-Dogguy, Y. Laligant, A. Le Bail, *Eur. J. Solid State Inorg. Chem.* **1998**, *35*, 255–264, DOI 10.1016/S0992-4361(98)80006-4.

[39] E.-M. Bertschler, PhD thesis, Ludwig-Maximilians-University Munich, München, **2017**.

[40] W. Schnick, J. Lücke, *Z. Anorg. Allg. Chem.* **1990**, *588*, 19–25, DOI 10.1002/zaac.19905880103.

[41] S. Horstmann, E. Irran, W. Schnick, *Z. Anorg. Allg. Chem.* **1998**, *624*, 620–628, DOI 10.1002/(SICI)1521-3749(199804)624:4<620::AID-ZAAC620>3.0.CO;2-K.

[42] D. Baumann, W. Schnick, *Inorg. Chem.* **2014**, *53*, 7977–7982, DOI 10.1021/ic500767f.

[43] J. R. Macdonald, W. B. Johnson in *Impedance Spectroscopy: Theory, Experiment, and Applications, Second Edition*, John Wiley & Sons, Inc., Hoboken, NJ, **2005**, pp. 1–26.

[44] G. J. Brug, A. L. van den Eeden, M. Sluyters-Rehbach, J. H. Sluyters, *J. Electroanal. Chem.* **1984**, *176*, 275–295, DOI 10.1016/S0022-0728(84)80324-1.

[45] J. T. S. Irvine, D. C. Sinclair, A. R. West, *Adv. Mater.* **1990**, *2*, 132–138, DOI 10.1002/adma.19900020304.

[46] S. Zhao, Z. Fu, Q. Qin, *Thin Solid Films* **2002**, *415*, 108–113, DOI 10.1016/S0040-6090(02)00543-6.

6. Please Mind the Gap: Highly Condensed P–N Networks in LiP_4N_7 and $Li_{3-x}P_6N_{11-x}(NH)_x$

Stefanie Schneider, Sebastian Klenk, Simon D. Kloß, and Wolfgang Schnick

Chem. Eur. J. **2023**, *29*, e202301986.
https://doi.org/10.1002/chem.202303251
DOI: 10.1002/chem.202303251

Reprinted (adapted) with permission from Chemistry – European Journal. Copyright 2023

The highly condensed lithium nitridophosphates LiP_4N_7 and $Li_{3-x}P_6N_{11-x}(NH)_x$ were prepared at pressures of 10 GPa in the multianvil press. Their structures were elucidated and their thermal stabilities and expansion coefficients were investigated. Synthesis of these materials closes a gap in the periodic table, as other alkali nitridophosphates like NaP_4N_7 or $Na_3P_6N_{11}$ have been known for decades.

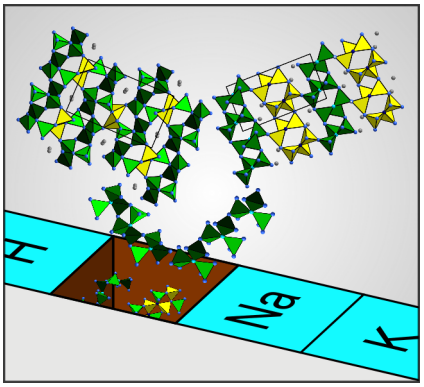

6.1. Abstract

Alkali nitridophosphates AP_4N_7 and $A_3P_6N_{11}$ (A = Na, K, Rb, Cs) have been known for decades. However, their Li homologues have remained elusive. In this work, the highly condensed lithium (imido)nitridophosphates LiP_4N_7 and $Li_{3-x}P_6N_{11-x}(NH)_x$ ($x = 1.66(3)$) were synthesized from $LiPN_2$ and P_3N_5 in the multianvil press at 10 GPa. They constitute the first lithium nitridophosphates with 3D networks exhibiting a degree of condensation larger than 0.5 and high thermal stability. LiP_4N_7 crystallizes in the orthorhombic space group $P2_12_12_1$ with $a = 4.5846(6)$ Å, $b = 8.0094(11)$ Å, and $c = 13.252(2)$ Å ($Z = 4$). $Li_{3-x}P_6N_{11-x}(NH)_x$ crystallizes in the triclinic space group $P\bar{1}$ with $Z = 2$, $a = 4.6911(11)$ Å, $b = 7.024(2)$ Å, $c = 12.736(3)$ Å, $\alpha = 87.726(11)$, $\beta = 80.279(11)$, and $\gamma = 70.551(12)°$. Both compounds are stable against hydrolysis in air.

6.2. Introduction

Although nitridophosphates have been thoroughly investigated over the past 30 years, the limits of this compound class have not yet been reached. Research in this field does not just continuously grow outward, there also remain surprising knowledge gaps to be filled.

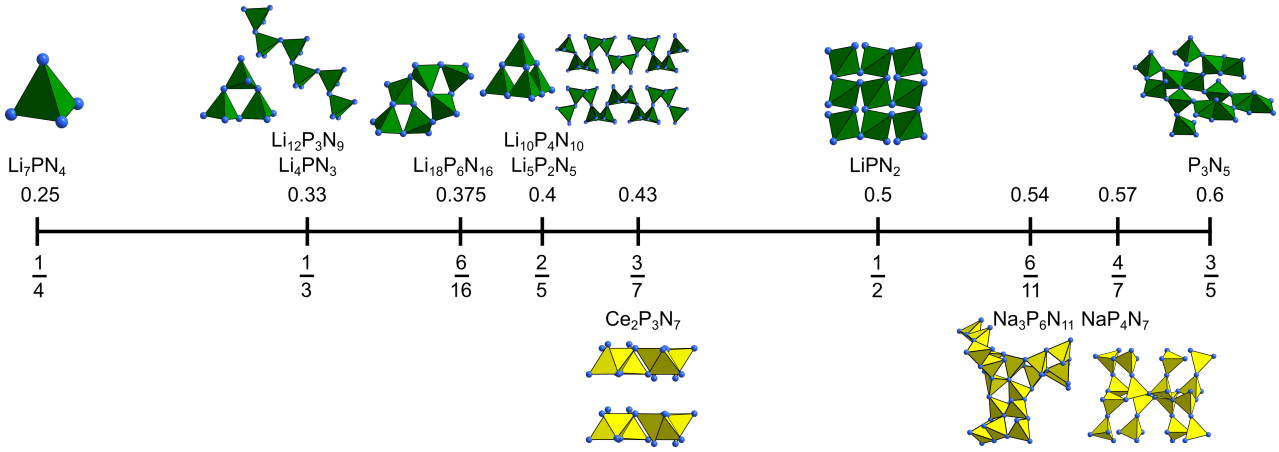

Figure 6.1.: Visualization of the degree of condensation κ. Shown are the structural motifs of Li_7PN_4,[1] $Li_{12}P_3N_9$,[2] Li_3PN_4,[2] $Li_{10}P_4N_{10}$,[3] $Li_5P_2N_5$,[4] $Ce_2P_3N_7$,[5] $LiPN_2$,[6] $Na_3P_6N_{11}$,[7] NaP_4N_7,[8] and P_3N_5[9] with their respective degrees of condensation κ. At $\kappa < 0.5$, motifs of several tetrahedra or layers occur, at $\kappa \geq 0.5$, 3D networks are observed. Lithium oxonitridophosphates are shown in green, other nitridophosphates in yellow.

One way to visualize where there are gaps in the field, is the degree of condensation κ (Figure 6.1). κ represents the quotient of the number of central atoms to vertex atoms in a tetrahedral network and was originally developed to describe Si–O networks.[10] Its lower and upper limits are the non-condensed tetrahedron ($\kappa = 0.25$) and the value of the binary compound. In the case of silicates this is SiO_2 with $\kappa = 0.5$. Since P–N compounds are formed from PN_4-tetrahedra similarly to SiO_4 in

silicates, κ can also be used to describe nitridophosphate structures. Due to $\kappa > 0.5$ in the upper limit P_3N_5, triply coordinated vertices can be found in nitridophosphates in contrast to silicates.
Comparing silicates and phosphates, some degrees of condensation appear repeatedly. There are several common degrees of condensation that can be observed in nitridophosphates and that occur throughout series of homologs. They are accompanied by structural motifs like non-condensed tetrahedra ($\kappa = 1/4$) in Li_7PN_4,[1] rings of three or chains of tetrahedra ($\kappa = 1/3$) in $Li_{12}P_3N_9$, Li_4PN_3 or AE_2PN_3 (AE = Mg, Ca),[2,11] adamantane-like supertetrahedra or layers in $Li_{10}P_4N_{10}$, $Li_5P_2N_5$ ($\kappa = 2/5$)[3,4,12] or $RE_2P_3N_7$ (RE = La, Ce, Pr; $\kappa = 3/7$).[5] In the range of highly condensed structures ($\kappa \geq 0.5$), motifs are connected to three-dimensional networks with N connecting two ($\kappa = 1/2$) or three ($\kappa = 6/11, 4/7$) tetrahedra. This is known from compounds like APN_2 (A = H, Li, Na),[6,13–16] AEP_2N_4 (AE = Be, Ca, Sr, Ba),[17–20] $A_3P_6N_{11}$ (A = Na, K, Rb, Cs),[21,22] and AP_4N_7 (A = H, Na, Ka, Rb, Cs).[7,8,23–26]
Notably, the two common κ of $6/11$ and $4/7$ have been described for all alkali metals except for Li. This seems surprising, since Li-containing solids play a major role in today's technologies, mainly as battery materials.[27–30] However, just this seems to have stunted research of highly condensed lithium nitridophosphates, as high conductivity is rather expected in compounds with a high Li content.[2,4,12,31]
Surprisingly, the single publication claiming synthesis of LiP_4N_7 stems from a period in which Li batteries have not played such a large role as yet.[32] In 1985, the compound was obtained as semi-amorphous powder from LiH and PNH_2 in NH_3 gas flow, but the structure could not be elucidated at the time. Theoretical calculations have simulated the structure with models of HP_4N_7 and NaP_4N_7.[33]
In this work, we present the synthesis and structural characterization of LiP_4N_7 and $Li_{3-x}P_6N_{11-x}(NH)_x$. They are the first representatives in the Li–P–N system with $\kappa > 0.5$, closing the obvious gaps in the series AP_4N_7 (A = H, Na, K, Rb, Cs), and $A_3P_6N_{11}$ (A = Na, K, Rb, Cs) phases.

6.3. Results and Discussion

6.3.1. Synthesis

LiP_4N_7 and $Li_{3-x}P_6N_{11-x}(NH)_x$ were obtained upon reaction of $LiPN_2$ and P_3N_5 at 10 GPa and 1150 °C, using a multianvil press with a modified Walker-type module. Single crystals were obtained of both phases. Optimization of synthesis procedures showed short reaction durations to promote formation of LiP_4N_7, whereas longer duration promotes formation of $Li_{3-x}P_6N_{11-x}(NH)_x$. Due to the close similarity in reaction conditions, no phase pure product could be obtained. Syntheses of these phases is very sensitive against small changes in reaction parameters and do not follow idealized reaction Equation (6.1) and Equation (6.2).

$$P_3N_5 + LiPN_2 \longrightarrow LiP_4N_7 \tag{6.1}$$

$$P_3N_5 + 3\,LiPN_2 \rightarrow Li_3P_6N_{11} \tag{6.2}$$

LiP_4N_7 was obtained as main phase from stoichiometric use of starting materials. However, formation of $LiPN_2$ and $Li_{3-x}P_6N_{11-x}(NH)_x$ side phases could not be omitted.
Instead of formation of $Li_3P_6N_{11}$, H was incorporated into the structure. Possibly, the H source was superficially hydrolyzed crucible material *h*BN. Stoichiometric use of starting materials according to Equation (6.2) in a dried *h*BN crucible did not yield $Li_{3-x}P_6N_{11-x}(NH)_x$, but $LiPN_2$ and LiP_4N_7. Formation of $LiPN_2$ and LiP_4N_7 side phases could not be omitted.

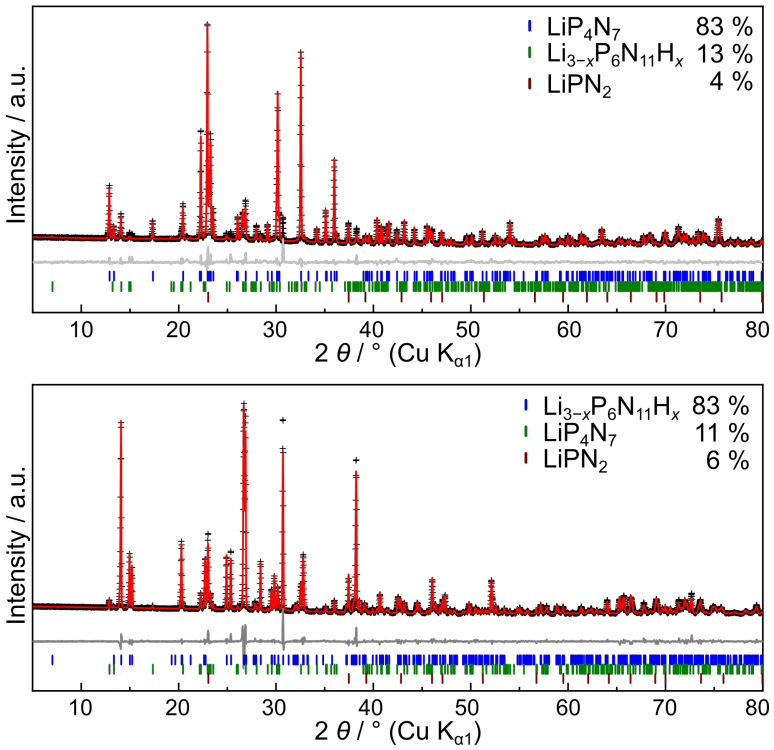

Figure 6.2.: Rietveld refinement of the samples with highest content of LiP_4N_7 (top) and $Li_{3-x}P_6N_{11-x}(NH)_x$ (bottom). Measured with Cu $K_{\alpha1}$ radiation. Measured intensities are shown with black crosses, calculated and residual intensities are shown as red and gray lines, respectively. Possible reflection positions are shown with markers according to the legends in the graphs.

Possibly, use of different precursors might enable more different reaction conditions following other synthesis strategies for nitrides like the azide route[8,22] or lithium nitride self-flux.[2,4,12,31] For example, HPN_2 could be used for targeted introduction of H.
Samples with the highest phase content of LiP_4N_7 and $Li_{3-x}P_6N_{11-x}(NH)_x$ were used for Rietveld refinement (Figures 6.2, D.1 and D.2 and Table D.8), to corroborate the structural models as obtained from single-crystal X-ray diffraction data.

6.3.2. Crystal Structure

The crystal structures of LiP_4N_7 and $Li_{3-x}P_6N_{11-x}(NH)_x$ were determined by single-crystal X-ray diffraction (scXRD). The structures were solved using direct methods and Li positions were determined by difference Fourier synthesis.

LiP_4N_7: LiP_4N_7 crystallizes in the orthorhombic space group $P2_12_12_1$ (no. 19) with $a = 4.5846(6)$, $b = 8.0094(11)$, $c = 13.252(2)$ Å, and $Z = 4$. Additional crystallographic data are listed in Table 6.1. The structure consists of four P positions that are tetrahedrally coordinated by N. All seven N positions connect at least two tetrahedra, with two N positions, N3 and N6, connecting three tetrahedra (Figure 6.3a). The sole Li position is embedded into this network (Figure 6.3e).
The network can be most easily explained by following the connectivity of N3 and N6, the two N positions connecting three tetrahedra to propeller-like motifs similar to those in β-HP_4N_7. N6 connects two instances of P4 tetrahedra and one additional P3 tetrahedron (Figure 6.3a). N6 occurs as two vertices of the P4 tetrahedron, resulting in a P4–N6–P4–N6 backbone with one P3 tetrahedron connected to each N6. These P3 tetrahedra share another vertex with one P4 tetrahedron. This leads to bands of propeller-like motifs that share both P4 tetrahedra and are additionally connected by one vertex. The resulting dreier-rings (Liebau nomenclature) are connected along [100] (Figure 6.3b).[10]

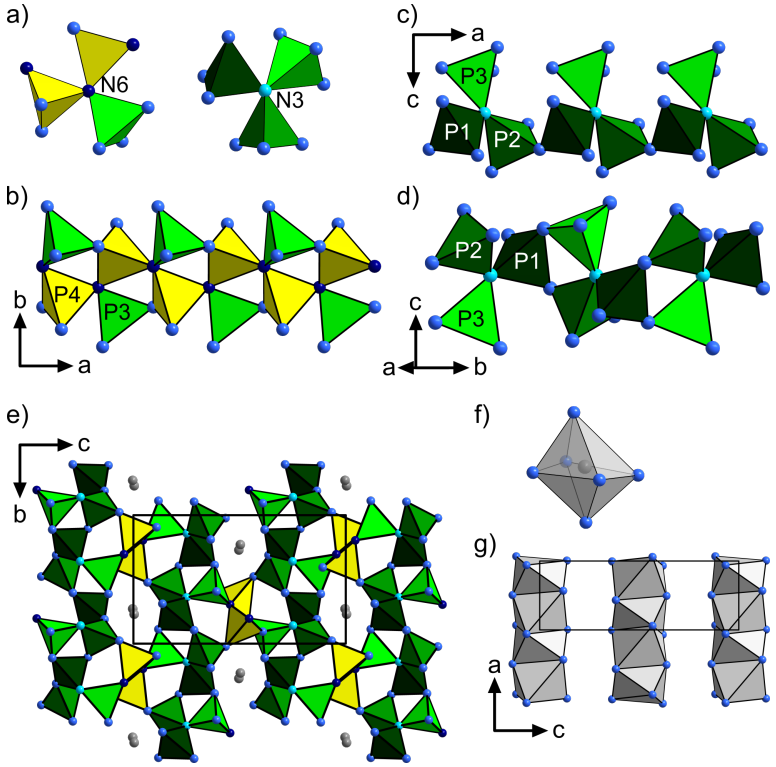

Figure 6.3.: Network structure of LiP_4N_7. a) Triply coordinated N6 (dark blue, left) and N3 (light blue, right). b) Connectivity of P4 tetrahedra (yellow) around N6 (dark blue). c) Connectivity of P1, P2, and P3 tetrahedra (dark green, green and bright green, respectively) around N3 (light blue) along [100]. d) Connectivity of P1, P2, and P3 bands along [010]. e) Network structure of LiP_4N_7 in and around the unit cell. Li cations are shown in gray. f) Coordination polyhedron around Li. g) Columns of LiN_6 octahedra along [100].

N3 connects P1, P2, and P3 tetrahedra. This triplet shares the N4 vertex with symmetrically identical tetrahedra along [100] (Figure 6.3c). These bands of triplets are in turn connected along [010] by N1 and N7 of the P1 tetrahedron, forming further dreier-rings (Figure 6.3d) and resulting in layers of triplets around N3 in the (001) plane. Along [001], these layers are connected by the

tetrahedra around P4–N6–P4–N6 backbone (Figure 6.3e). The network has the hitherto unknown topological point symbol $\{3^2.4.5^3.6^4\}\{3^2.4^2.5^2.6^4\}\{3^4.4^3.5^4.6^4\}\{3^4.4^4.5^5.6^2\}$, which was calculated using ToposPro.[34]

The single crystallographic Li position has a distorted octahedral coordination sphere which shares two opposite faces with symmetrically identical LiN_6 octahedra, forming strands along [100] (see Figure 6.3f+g). Possibly, Li is slightly mobile, both within the large coordination polyhedron, and along strands of face-sharing LiN_6 octahedra. This could explain its large displacement (0.129(9) $Å^2$). In principle, it is possible that instead of full occupancy of Li, H or O is incorporated into the structure. However, difference Fourier analysis did not show residual electron density at suitable distances to N to support presence of H. Furthermore, since no phase pure sample could be obtained, bulk methods like Fourier-transform infrared (FTIR) spectroscopy or nuclear magnetic resonance (NMR) spectroscopy cannot unequivocally prove presence of H. Thus, we have chosen to use the stoichiometric notation LiP_4N_7.

$Li_{3-x}P_6N_{11-x}(NH)_x$: $Li_{3-x}P_6N_{11-x}(NH)_x$ crystallizes in the triclinic space group $P\bar{1}$ (no. 2) with $a = 4.6911(11)$, $b = 7.024(2)$, $c = 12.736(3)$ Å, $\alpha = 87.726(11)$, $\beta = 80.279(11)$, $\gamma = 70.551(12)°$, and $Z = 2$. Crystallographic details are listed in Table 6.1. As in LiP_4N_7, vertex-sharing PN_4-tetrahedra constitute the 3D-network. All N atoms connect at least two tetrahedra, with N1 and N7 connecting three tetrahedra.

There are two crystallographically different propeller-like motifs, comparable to those in $BaP_6N_{10}NH$ (Figure 6.4a).[35] N1 is coordinated by three P atoms: P1, P2, and P3. This triplet of tetrahedra is connected to crystallographically identical motifs, forming bands of dreier-rings along [100] (Figure 6.4b). These bands are stacked along [010], connected by P2 and P3 tetrahedra. This leads to vierer-rings of P2 and P3 tetrahedra, with P1 tetrahedra protruding along [100] (Figure 6.4c). P1 and P3 form vierer-rings again, connecting these stacks to layers in the a,b-plane. The layers are connected along [001] to crystallographically different layers with the same constitution to form a three-dimensional network with large gaps containing Li-ions and H (Figure 6.4d). The point symbol for the net is $\{3^2.4^2.5^2.6^2.7.8\}\{3^2.4^2.5^2.6^4\}\{3^2.4^4.5^3.7\}$ and was calculated using ToposPro.[34] No network with this point symbol has been reported as yet.

Li positions were determined using difference Fourier synthesis and imply full and partial occupancy of Li1 and Li2, respectively. The distorted LiN_6 octahedra are connected by edges along [100] (Figure 6.4e–g). Possibly, more than one H per formula unit can be inserted in the structure, which is also corroborated by the presence of several resonances visible in NMR spectra. Since the position of H could not be determined unequivocally, its positions were constrained onto a singly bridging N atom with the largest possible distance to Li (N5) and an N position with remaining electron density at an appropriate distance to N (N4). The occupancy of the latter H position was constrained to partial occupancy of the Li2 position. With full and partial occupancies for H1 and H2, respectively, scXRD suggests an H content of $x = 1.66(3)$. However, for quantitative analysis of H content in the bulk, phase-pure samples are necessary. Thus, the notation indicating a phase-width was chosen: $Li_{3-x}P_6N_{11-x}(NH)_x$.

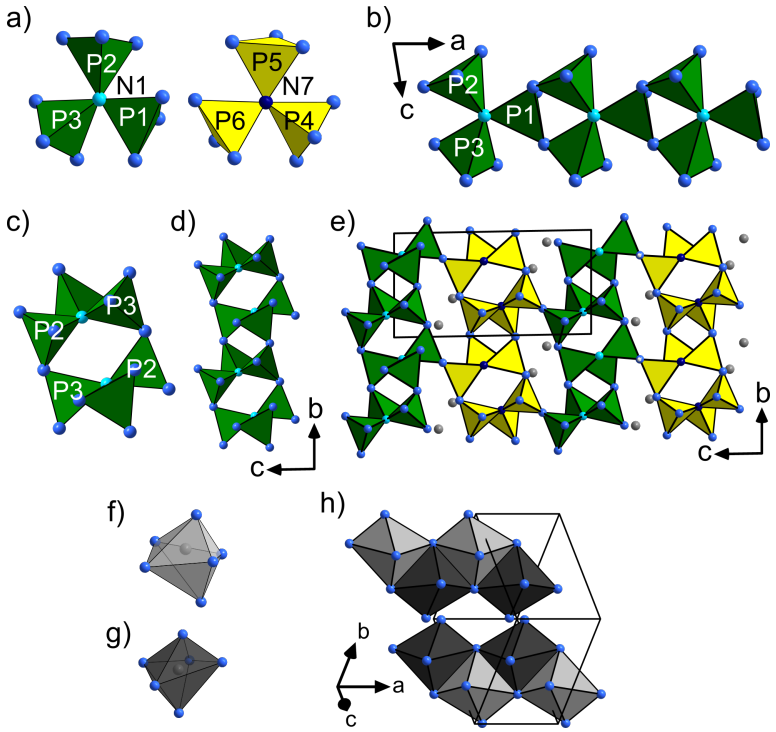

Figure 6.4.: Structure of $Li_{3-x}P_6N_{11-x}(NH)_x$. a) Propeller-like motifs around N1 (light blue, green tetrahedra, left) and N7 (dark blue, yellow tetrahedra, right). b) Propeller-like structure motifs are connected along [100] via two N (blue). c) Bands of propeller-motifs are connected to stacks with P1 tetrahedra protruding to each side, forming vierer-rings along [010]. d) Connection of stacks along [010] forming layers in the (001) plane. e) Layers of crystallographically different propeller motifs are connected along [001]. f) Distorted LiN_6 octahedron around Li1. g) Distorted LiN_6 octahedron around Li2. h) Edge-sharing LiN_6 octahedra connected along [100].

In other $A_3P_6N_{11}$ (A = Na, K), boiling in concentrated acids was found to replace metal positions with oxonium ions. Heating of the compounds with metal chlorides can replace ions, since cations are only coordinated weakly.[26] A similar mechanism could be conceivable for $Li_{3-x}P_6N_{11-x}(NH)_x$. Furthermore, by ion exchange, it might be possible to synthesize other highly condensed networks like a $Li_3P_6N_{11}$ phase with the structure type and network topology of $Na_3P_6N_{11}$ or $K_3P_6N_{11}$ or vice versa.

6.3.3. Nuclear Magnetic Resonance and Fourier-Transform Infrared Spectroscopy

Due to the low electron density of hydrogen, its presence in the structure cannot be confirmed unequivocally by XRD methods. Therefore, nuclear magnetic resonance (NMR) and Fourier-transform infrared (FTIR) spectroscopy were employed. However, since no phase pure samples were available, the informative value of these investigations has to be considered carefully.
^{31}P, coupled $^{31}P\{^1H\}$ and ^{7}Li NMR spectra of two samples with LiP_4N_7 and $Li_{3-x}P_6N_{11-x}(NH)_x$ as main P-containing phases were measured (Figures D.7–D.12). However, due to unavailability of phase pure samples, assignment of signals to crystallographic positions is not possible.

Table 6.1.: Crystallographic details on the refinement from single crystal data of LiP_4N_7 and $Li_{3-x}P_6N_{11-x}(NH)_x$.

Sum formula	LiP_4N_7	$Li_{1.34(3)}P_6N_{9.34(3)}(NH)_{1.66(3)}$
Formula weight / $g\,mol^{-1}$	228.89	354.82
Crystal system	Orthorhombic	Triclinic
Space group	$P212121$ (no. 19)	$P\bar{1}$ (no. 2)
Lattice parameters / Å, °	$a = 4.5823(9)$	$a = 4.6911(11)$
	$b = 8.0066(9)$	$b = 7.024(2)$
	$c = 13.2407(18)$	$c = 12.736(3)$
		$\alpha = 87.726(11)$
		$\beta = 80.279(11)$
		$\gamma = 70.551(12)$
Cell volume / $Å^3$	485.78(13)	390.0(2)
Formula units per unit cell Z	4	2
Density / $g\,cm^{-3}$	3.130	3.022
μ / mm^{-1}	1.465	1.375
Crystal size / mm^3	$0.04 \times 0.015 \times 0.015$	$0.03 \times 0.03 \times 0.02$
Radiation λ	Mo-K_α $\lambda = 0.710\,73$ Å	
Temperature / K	113(2)	111(2)
θ-range / °	$2.973 \leq \theta \leq 31.518$	$3.1 \leq \theta \leq 32.0$
Total no. of reflections	6132	7400
Independent reflections	1626	2693
Refined parameters	109	168
R_{int}; R_σ	0.0375; 0.0364	0.0428; 0.0558
$R1$ (all data); $R1$ ($F^2 > 2\sigma(F^2)$)	0.0302; 0.0271	0.0617; 0.0425
$wR2$ (all data); $wR2$ ($F^2 > 2\sigma(F^2)$)	0.0650; 0.0642	0.1043; 0.0983
Goodness of fit (χ^2)	1.159	1.032
$\Delta\rho_{max}; \Delta\rho_{min}$ / $e\,Å^{-3}$	0.494; −0.406	0.953; −1.111

^{31}P NMR spectra were compared in order to assign the resonances to the respective phases (Figure D.13a). ^{31}P resonances of LiP_4N_7 occur at −8.4 and −15.9 ppm, those of $Li_{3-x}P_6N_{11-x}(NH)_x$ 0.8 and −3.0 ppm. Possibly, the signal at −15.9 ppm contains portions of both LiP_4N_7 and $Li_{3-x}P_6N_{11-x}(NH)_x$.

The $^{31}P\{^1H\}$ coupled spectrum shows presence of H in the sample with $Li_{3-x}P_6N_{11-x}(NH)_x$ as main P-containing phase (Figure D.11). However, no quantitative information can be derived from the spectrum. In the $^{31}P\{^1H\}$ coupled spectrum of a sample consisting mainly of LiP_4N_7, there are also smaller signals. However, since the side phase contains H, its presence cannot be confirmed or excluded definitely.

^7Li spectra each show a single signal at −0.3 and −0.2 ppm. These signals are very similar and in the range of other chemical shifts for ^7Li.[2,4,12,31]

The FTIR spectrum of a sample consisting mainly of LiP_4N_7 (69 % LiP_4N_7, 19 % $Li_{3-x}P_6N_{11-x}(NH)_x$,

12 % $LiPN_2$) shows no significant absorption bands in the area around 2500–3500 cm^{-1}, in which N–H or O–H absorption bands would be expected (Figure 6.5, black line). The small signal at 3340 cm^{-1} can be explained by 19 % of H-containing side phase $Li_{3-x}P_6N_{11-x}(NH)_x$ or superficial hydrolysis, indicating that no significant amount of H is present in the sample. Increased noise in the area from 2400–1900 cm^{-1} is due to C–C bonds in the diamond window of the ATR unit. The spectrum shows three mayor groups of absorption bands, which is in accordance with literature.[32] However, comparison to literature is difficult, both because the IR spectrum from literature has low resolution and because no phase pure samples could be obtained.
The P–N vibration modes in the fingerprint area of $Li_{3-x}P_6N_{11-x}(NH)_x$ are very similar to those of LiP_4N_7 (Figure 6.5, gray line). However, absorption of N–H vibrational modes is visible at 3220 cm^{-1}, corroborating the presence of H.

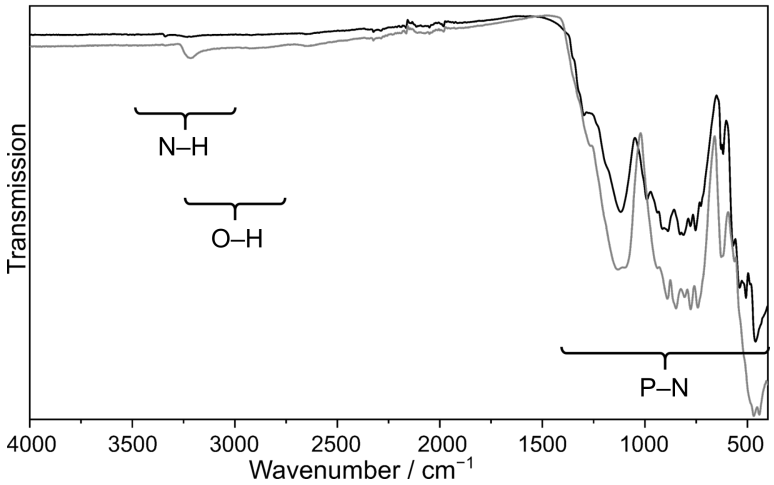

Figure 6.5.: FTIR spectrum of a sample with LiP_4N_7 as main phase (69 % LiP_4N_7, 19 % $Li_{3-x}P_6N_{11-x}(NH)_x$, 12 %$LiPN_2$, black line), and $Li_{3-x}P_6N_{11-x}(NH)_x$ (83 % $Li_{3-x}P_6N_{11-x}(NH)_x$, 11 % LiP_4N_7, 6 % $LiPN_2$, gray line). The spectrum was measured under Ar atmosphere with an ATR unit with a diamond window. Increased background in the area around 1900–2300 cm^{-1} results from C–C vibrations in the diamond window.

6.3.4. Thermal Stability

The thermal stability of LiP_4N_7 and $Li_{3-x}P_6N_{11-x}(NH)_x$ was investigated using variable-temperature XRD. For LiP_4N_7, no decomposition was observed up to 900 °C, solely a small thermal shift of lattice parameters is visible. Above 900 °C, additional reflections of low intensity appear that could not be assigned to known phases (Figure 6.6a). Thermal expansion coefficients were calculated using lattice parameters from Rietveld refinement at temperatures from room temperature up to 1000 °C. The expansion of the a and b lattice parameters is very similar with $\alpha_a = 4.42(5) \times 10^{-6}$ and $4.4(2) \times 10^{-6}\,K^{-1}$. This might be a result of the high connectivity along [100] and [010]. Along [001], the structure is more open, which is reflected in the larger thermal expansion along this direction ($\alpha_c = 8.5(2) \times 10^{-6}\,K^{-1}$). The volumetric expansion coefficient $\alpha_V = 17.5(4) \times 10^{-6}\,K^{-1}$ (Figure 6.6c), is in a range comparable to other nitridophosphates with $\kappa = 4/7$.[36]

At 800 °C, incipient decomposition of $Li_{3-x}P_6N_{11-x}(NH)_x$ is observed. Only Li_3P is visible in the diffraction pattern at 840 °C and above (Figure 6.6b). Li_3P can often be observed in lithium nitridophosphate syntheses at high temperatures and is a common decomposition product.[4,12]
The thermal expansion coefficient was calculated as described above (Figure 6.6d). Thermal expansion along [100] could not be reliably determined in the temperature range available (α_a = 0.2(3) × 10^{-6} K^{-1}). This might be due to the highly condensed dreier-rings along [100] that cannot be stretched as much as the more open features along [010] and [001]. Expansion along [010] and [001] are 9.2(5) × 10^{-6} and 16.9(4) × 10^{-6} K^{-1}, respectively. The volumetric expansion coefficient of α_V = 25.2(8) × 10^{-6} K^{-1} is comparable to other nitridophosphates with κ = 6/11 like $BaP_6N_{10}NH$ (α_V = 22.2 × 10^{-6} K^{-1}),[35] $Rb_3P_6N_{11}$ (α_V = 13.9 × 10^{-6} K^{-1}),[22] or $Cs_3P_6N_{11}$ (α_V = 13.0 × 10^{-6} K^{-1}).[22] The error margin in $Li_{3-x}P_6N_{11-x}(NH)_x$ is higher and deviation of values larger than in LiP_4N_7, since the determination of lattice parameters with Ag $K_{\alpha1}$ is less exact than with Mo $K_{\alpha1}$.

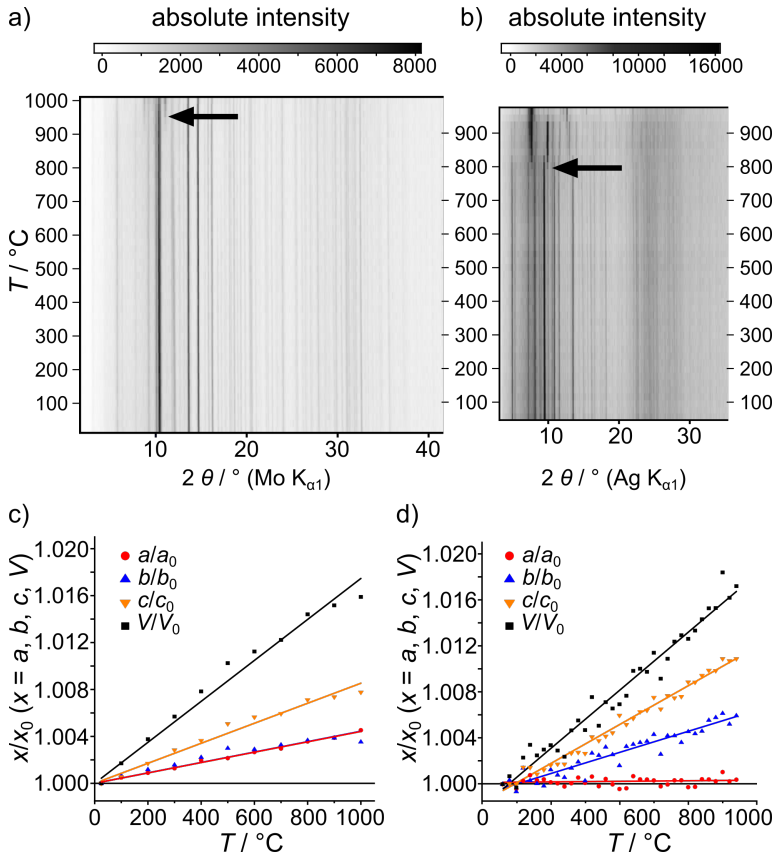

Figure 6.6.: Thermal stability measurements and thermal expansion. a) Variable temperature powder X-ray diffractograms of LiP_4N_7 measured from 40–1000 °C with Mo $K_{\alpha1}$ radiation. An arrow marks beginning decomposition. b) Variable temperature powder X-ray diffractogram of $Li_{3-x}P_6N_{11-x}(NH)_x$ measured from 60–900 °C with Ag $K_{\alpha1}$ radiation. An arrow marks beginning decomposition. c) Visualization of thermal expansion of LiP_4N_7 with linear fits of lattice parameters and volume. d) Visualization of thermal expansion of $Li_{3-x}P_6N_{11-x}(NH)_x$ with linear fits of lattice parameters and volume.

The high degree of condensation accounts for the high stability of the compounds. Both LiP_4N_7 and $Li_{3-x}P_6N_{11-x}(NH)_x$ are stable against hydrolysis and can be stored under ambient conditions indefinitely.
This is consistent with the general correlation of stability and the degree of condensation that can be found in other nitridophosphates and silicates. Whereas Li_7PN_4 is highly sensitive against air and moisture and can only be handled in inert conditions,[1] $Li_{10}P_4N_{10}$ can be washed with dry ethanol[12] and $LiPN_2$ is stable against acids and bases.[14] LiP_4N_7 and $Li_{3-x}P_6N_{11-x}(NH)_x$ were washed with concentrated acids without indication of decomposition.

6.4. Conclusion

The two highly condensed lithium (imido)nitridophosphates LiP_4N_7 and $Li_{3-x}P_6N_{11-x}(NH)_x$ were synthesized and characterized. Their structures were solved and refined from scXRD data. The high degree of condensation is realized by N atoms triply coordinated by P. In LiP_4N_7, one of these N atom positions occurs twice in one tetrahedron, resulting in a band of propeller-like motifs similar to those in β-HP_4N_7, sharing tetrahedra. The resulting highly condensed band of dreier-rings is connected to additional propeller-like motifs. $Li_{3-x}P_6N_{11-x}(NH)_x$ exhibits two triply by P coordinated N atom positions. Here, both form propeller-like motifs, which share corners to other propeller motifs. For more information on the H position in $Li_{3-x}P_6N_{11-x}(NH)_x$, neutron powder diffraction would be a helpful tool.
In comparison to other lithium nitridophosphates, both compounds show high thermal and chemical stability, which is likely due to their highly condensed network structure. Both compounds are stable against hydrolysis and can be stored at ambient conditions indefinitely. The degree of condensation is also expressed in the relatively low thermal expansion coefficient.
In further research, the questions of H content and positions, ionic conductivity, and potential synthesis at milder conditions will be addressed. Synthesis of these compounds fills the gap of nitridophosphates with the formula type AP_4N_7 (A = H, Na, K, Rb, Cs) and $A_3P_6N_{11}$ (A = Na, K, Rb, Cs).

6.5. Acknowledgements

The authors thank Dr. Lisa Gamperl, Christian Minke (both at Department of Chemistry of LMU), and Armin Schulz (MPI FKF Stuttgart) for SEM/EDX, NMR, and Raman measurements, respectively. Funding support from the Deutsche Forschungsgemeinschaft (DFG, German Research Foundation) under Germany's Excellence Strategy-EXC 2089/1-390776260 (e-Conversion) is gratefully acknowledged.

6.6. References

[1] W. Schnick, J. Luecke, *J. Solid State Chem.* **1990**, *87*, 101–106, DOI 10.1016/0022-4596(90)90070-E.

[2] E.-M. Bertschler, R. Niklaus, W. Schnick, *Chem. Eur. J.* **2017**, *23*, 9592–9599, DOI 10.1002/chem.201700979.

[3] W. Schnick, U. Berger, *Angew. Chem. Int. Ed.* **1991**, *30*, 830–831, *Angew. Chem.* **1991**, *103*, 857–858, DOI 10.1002/anie.199108301.

[4] E.-M. Bertschler, R. Niklaus, W. Schnick, *Chem. Eur. J.* **2018**, *24*, 736–742, DOI 10.1002/chem.201704975.

[5] S. D. Kloß, N. Weidmann, R. Niklaus, W. Schnick, *Inorg. Chem.* **2016**, *55*, 9400–9409, DOI 10.1021/acs.inorgchem.6b01611.

[6] W. Schnick, J. Lücke, *Z. Anorg. Allg. Chem.* **1990**, *588*, 19–25, DOI 10.1002/zaac.19905880103.

[7] J. Ronis, B. Bondars, A. A. Vitola, T. Millers, *Latv. PSR Zinat. Akad. Kim. Serija1* **1990**, *3*, 299–301.

[8] K. Landskron, E. Irran, W. Schnick, *Chem. Eur. J.* **1999**, *5*, 2548–2553, DOI 10.1002/(sici)1521-3765(19990903)5:9<2548::aid-chem2548>3.3.co;2-n.

[9] S. Horstmann, E. Irran, W. Schnick, *Z. Anorg. Allg. Chem.* **1998**, *624*, 620–628, DOI 10.1002/(SICI)1521-3749(199804)624:4<620::AID-ZAAC620>3.0.CO;2-K.

[10] F. Liebau, *Structural chemistry of silicates*, Springer, Berlin, Heidelberg, **1985**, DOI 10.1016/0025-5408(86)90097-8.

[11] V. Schultz-Coulon, W. Schnick, *Z. Anorg. Allg. Chem.* **1997**, *623*, 69–74, DOI 10.1002/zaac.19976230112.

[12] E.-M. Bertschler, C. Dietrich, T. Leichtweiß, J. Janek, W. Schnick, *Chem. Eur. J.* **2018**, *24*, 196–205, DOI 10.1002/chem.201704305.

[13] H. Jacobs, R. Nymwegen, S. Doyle, T. Wroblewski, W. Kockelmann, *Z. Anorg. Allg. Chem.* **1997**, *623*, 1467–1474, DOI 10.1002/zaac.19976230923.

[14] P. Eckerlin, C. Langereis, I. Maak, A. Rabenau, *Angew. Chem.* **1960**, *7*, 19561.

[15] R. Marchand, P. L'Haridon, Y. Laurent, *J. Solid State Chem.* **1982**, *43*, 126–130, DOI 10.1016/0022-4596(82)90221-3.

[16] K. Landskron, S. Schmid, W. Schnick, *Z. Anorg. Allg. Chem.* **2001**, *627*, 2469–2472, DOI 10.1002/1521-3749(200111)627:11<2469::aid-zaac2469>3.0.co;2-4.

[17] F. J. Pucher, S. Rebecca Römer, F. W. Karau, W. G. Schnick, *Chem. Eur. J.* **2010**, *16*, 7208–7214, DOI 10.1002/chem.201000153.

[18] F. J. Pucher, A. Marchuk, P. J. Schmidt, D. Wiechert, W. Schnick, *Chem. Eur. J.* **2015**, *21*, 6443–6448, DOI 10.1002/chem.201500047.

[19] F. W. Karau, L. Seyfarth, O. Oeckler, J. Senker, K. Landskron, W. Schnick, *Chem. Eur. J.* **2007**, *13*, 6841–6852, DOI 10.1002/chem.200700216.

[20] F. W. Karau, W. Schnick, *J. Solid State Chem.* **2005**, *178*, 135–141, DOI 10.1016/j.jssc.2004.10.034.

[21] H. Jacobs, R. Nymwegen, *Z. Anorg. Allg. Chem.* **1997**, *623*, 429–433, DOI 10.1002/zaac.19976230168.

[22] K. Landskron, W. Schnick, *J. Solid State Chem.* **2001**, *156*, 390–393, DOI 10.1006/jssc.2000.9010.

[23] S. Horstmann, E. Irran, W. Schnick, *Angew. Chem. Int. Ed.* **1997**, *36*, 1992–1994, *Angew. Chem.* **1997**, *109*, 2085–2087, DOI 10.1002/anie.199719921.

[24] D. Baumann, W. Schnick, *Inorg. Chem.* **2014**, *53*, 7977–7982, DOI 10.1021/ic500767f.

[25] D. Baumann, W. Schnick, *Angew. Chem. Int. Ed.* **2014**, *53*, 14490–14493, *Angew. Chem.* **2014**, *126*, 14718–14721, DOI 10.1002/anie.201406086.

[26] A. A. Vitola, J. Ronis, T. Millers, *B. Acad. Sci. USSR. Ch.* **1990**, *1*, 35–39.

[27] M. Park, X. Zhang, M. Chung, G. B. Less, A. M. Sastry, *J. Power Sources* **2010**, *195*, 7904–7929, DOI 10.1016/j.jpowsour.2010.06.060.

[28] T. H. Kim, J. S. Park, S. K. Chang, S. Choi, J. H. Ryu, H. K. Song, *Adv. Energy Mater.* **2012**, *2*, 860–872, DOI 10.1002/aenm.201200028.

[29] N. Boaretto, I. Garbayo, S. Valiyaveettil-SobhanRaj, A. Quintela, C. Li, M. Casas-Cabanas, F. Aguesse, *J. Power Sources* **2021**, *502*, 1–34, DOI 10.1016/j.jpowsour.2021.229919.

[30] J. Li, J. Fleetwood, W. B. Hawley, W. Kays, *Chem. Rev.* **2022**, *122*, 903–956, DOI 10.1021/acs.chemrev.1c00565.

[31] E.-M. Bertschler, C. Dietrich, J. Janek, W. Schnick, *Chem. Eur. J.* **2017**, *23*, 2185–2191, DOI 10.1002/chem.201605316.

[32] A. Vitola, V. Avotins, I. Lange, G. Smilškalne, T. Millers, *Latv. J. Chem.* **1985**, *3*, 288–292.

[33] Y. A. Du, N. A. Holzwarth, *Phys. Rev. B* **2010**, *81*, 1–15, DOI 10.1103/PhysRevB.81.184106.

[34] V. A. Blatov, A. P. Shevchenko, *Topos Pro v. 5.1.5.7*, TOPOS Expert, **1989–2016**.

[35] S. Wendl, L. Eisenburger, M. Zipkat, D. Günther, J. P. Wright, P. J. Schmidt, O. Oeckler, W. Schnick, *Chem. Eur. J.* **2020**, *26*, 5010–5016, DOI 10.1002/chem.201905082.

[36] S. Wendl, L. Eisenburger, P. Strobel, D. Günther, J. P. Wright, P. J. Schmidt, O. Oeckler, W. Schnick, *Chem. Eur. J.* **2020**, *26*, 7292–7298, DOI 10.1002/chem.202001129.

7. Summary

In this work, an overview is given over the hitherto known crystalline lithium oxonitridophosphates and nitridophosphates. In the first part (Chapters 3–5), the synthesis and characterization of two novel lithium oxonitridophosphates, $Li_{5+x}P_2O_{6-x}N_{1+x}$ and $Li_{8+x}P_3O_{10-x}N_{1+x}$ and one lithium oxonitridophosphate oxide, $Li_{27-x}[P_4O_{7+x}N_{9-x}]O_3$ is presented. It was found that excess of lithium species is invaluable for the formation of lithium oxonitridophosphates, as has been observed for lithium nitridophosphates with low degrees of condensation. This method yields single-crystals of reasonable sizes, enabling single-crystal X-ray diffraction (scXRD) for structural investigation. Magic angle spinning nuclear magnetic resonance (MAS-NMR) spectroscopy was an inestimable tool for the characterization of the local P atom environment. With this method, $[PO_3N]^{4-}$, $[PO_2N_2]^{5-}$, and $[PON_3]^{6-}$ could be distinguished and the data base for ^{31}P resonances in non-condensed lithium oxonitridophosphates could be expanded further. Additionally, the hitherto not reported motifs $[P_2O_6N]^{5-}$ and $[P_2O_5N_2]^{6-}$ could be identified and the chemical shifts of both PO_3N and PO_2N_2 within these motifs could be elucidated. All the lithium oxonitridophosphates synthesized exhibit significant disorder, which makes structural characterization challenging. Satisfying characterization can only be accomplished by synopsis of several methods. Further methods used for determination of crystal structures were powder X-ray diffraction (PXRD) and neutron powder diffraction (NPD). Fourier-transform infrared (FTIR) spectroscopy and elemental analyses energy-dispersive X-ray (EDX), inductively coupled plasma optical emission spectroscopy (ICP-OES), and CHNS combustion analysis were used to exclude presence of other elements. Temperature-dependent PXRD was used to determine thermal stabilities. Ionic conductivities and activation energies of lithium oxonitridophosphates were calculated from impedance measurements. Since amorphous lithium oxonitridophosphate (a-LiPON) is a widely used solid electrolyte, ionic conductivities of crystalline phases can give interesting information on conductivity processes.

In the second part covered by Chapter 6, one lithium nitridophosphate, LiP_4N_7 and one lithium imidonitridophosphate, $Li_{3-x}P_6N_{11-x}(NH)_x$ are presented and characterized. Prior to this thesis, there were no known highly condensed lithium nitridophosphates with $\kappa > 0.5$. Their syntheses, structures and characterization, and thermal stabilities and thermal expansion coefficients are reported and contextualized. A synthesis strategy for highly condensed lithium nitridophosphates from $LiPN_2$ and P_3N_5 was developed, which yielded single-crystals of appropriate sizes. Before this work, no highly condensed lithium nitridophosphates were known with $\kappa > 0.5$. The synthesis of $Li_{3-x}P_6N_{11-x}(NH)_x$ and LiP_4N_7 shows that there are additional lithium nitride structures to be found in this area. For lithium nitridophosphates, thermal expansion coefficients were calculated from variable-temperature PXRD data. Highly condensed networks exhibit high rigidity, enabling possible application as hard

materials. In the following, individual summaries of the chapters provide more detailed information on the particular publications.

3 Structure Determination of the Crystalline LiPON Model Structure $Li_{5+x}P_2O_{6-x}N_{1+x}$ with $x \approx 0.9$

4 Comprehensive Investigation of Anion Species in Crystalline Li^+ ion Conductor $Li_{27-x}[P_4O_{7+x}N_{9-x}]O_3$ ($x \approx 1.9(3)$)

5 Finding Order in Disorder – The Highly Disordered Lithium Oxonitridophosphate Double Salt $Li_{8+x}P_3O_{10-x}N_{1+x}$ ($x = 1.4(5)$)

6 Please Mind the Gap: Highly Condensed P–N Networks in LiP_4N_7 and $Li_{3-x}P_6N_{11-x}(NH)_x$

7.1. Structure Determination of the Crystalline LiPON Model Structure $Li_{5+x}P_2O_{6-x}N_{1+x}$ with $x \approx 0.9$

Stefanie Schneider, Lucas G. Balzat, Bettina V. Lotsch, and Wolfgang Schnick

Published in: *Chem. Eur. J.* **2023**, *29*, e202202984.
Access via: DOI: 10.1002/chem.202202984
Reprinted at: Chapter 3, Supporting Information in appendix A

The crystalline lithium oxonitridophosphate $Li_{5+x}P_2O_{6-x}N_{1+x}$ was synthesized from P_3N_5, Li_3N, and Li_2O at 800 °C in a Ta crucible within a quartz ampoule under Ar atmosphere. Instead of reaction according to Equation (7.1), Li_3N had to be added as starting material to realize a Li_3N flux.

$$2\ P_3N_5 + (18-3x)\ Li_2O \longrightarrow 3\ Li_{5+x}P_2O_{6-x}N_{1+x} + (7-3x)\ Li_3N \tag{7.1}$$

The structure, consisting of pairs of corner-sharing tetrahedra, was elucidated from a combination of single-crystal and powder X-ray diffraction data. The compound crystallizes in the monoclinic space group $P2_1/c$ (no. 14) with $a = 15.130\,87(11)$ Å, $b = 9.706\,82(9)$ Å, $c = 8.886\,81(7)$ Å, $\beta = 106.8653(8)°$ and $Z = 8$.

Deconvolution of ^{31}P resonances in MAS-NMR spectra showed the presence of both $[P_2O_6N]^{5-}$ and $[P_2O_7N_2]^{6-}$ units (6(4) and 94(4) %, respectively), resulting in the sum formula $Li_{5+x}P_2O_{6-x}N_{1+x}$ with $x \approx 0.9$.

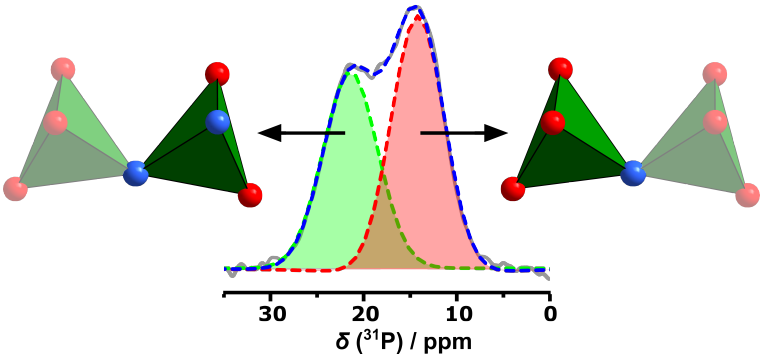

Figure 7.1.: Diphosphate structure motifs with ^{31}P NMR spectrum of $Li_{5+x}P_2O_{6-x}N_{1+x}$. O and N atoms are shown in red and blue, respectively.

To corroborate the composition and to exclude the possibility of other elements being present, FTIR spectroscopy and elemental analyses (EDX spectroscopy, CHNS, and ICP-OES) were carried out. Furthermore, thermal stability was elucidated by variable-temperature PXRD. The compound begins to decompose at 640 °C. Ionic conductivity was calculated from impedance measurements. The total ionic conductivity of $Li_{5+x}P_2O_{6-x}N_{1+x}$ amounts to $\sigma_{tot} = 4.6 \times 10^{-8}$ S cm^{-1} at 25 °C with a corresponding activation energy $E_a = 0.52(1)$ eV.

7.2. Comprehensive Investigation of Anion Species in Crystalline Li^+ ion Conductor $Li_{27-x}[P_4O_{7+x}N_{9-x}]O_3$ ($x \approx 1.9(3)$)

Stefanie Schneider, Eva-Maria Wendinger, Volodymyr Baran, Anna-Katharina Hatz, Bettina V. Lotsch, Markus Nentwig, Oliver Oeckler, Thomas Bräuniger, and Wolfgang Schnick

Published in: *Chem. Eur. J.* **2023**, *29*, e202300174.
Access via: DOI: 10.1002/chem.202300174
Reprinted at: Chapter 4, Supporting Information in appendix B

$Li_{27-x}[P_4O_{7+x}N_{9-x}]O_3$ was synthesized from P_3N_5, Li_3N, and Li_2O in an ampoule synthesis at 800 °C (Equation (7.2)). Li_3N was used in excess for Li_3N flux conditions.

$$(7-3x)\ Li_3N + 4\ P_3N_5 + (30+x)\ Li_2O \longrightarrow 3\ Li_{27-x}[P_4O_{7+x}N_{9-x}]O_3 \tag{7.2}$$

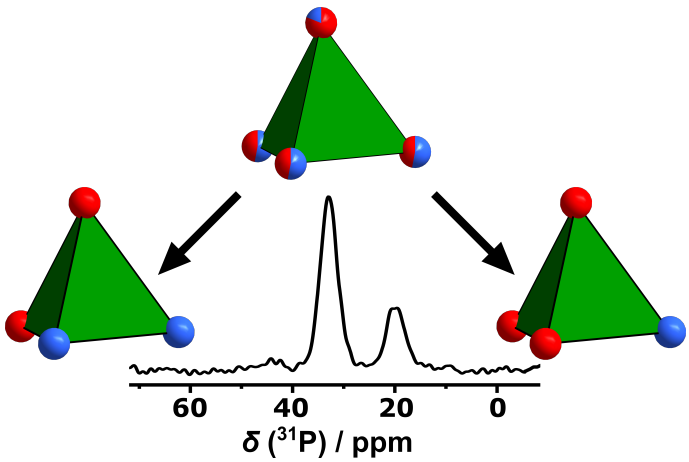

Figure 7.2.: Mixed occupancy of P(O,N) as $[PO_2N_2]^{5-}$ and $[PO_3N]^{4-}$ and the corresponding ^{31}P NMR spectrum.

$Li_{27-x}[P_4O_{7+x}N_{9-x}]O_3$ crystallizes in the cubic space group $I\bar{4}3d$ with $a = 12.0106(14)$ Å and $Z = 4$. The apparent contradiction of two ^{31}P NMR signals at one crystallographic P position could be resolved by neutron diffraction, which showed mixed occupancy of O and N atom positions. The resulting structure consists of $[PO_2N_2]^{5-}$ and $[PO_3N]^{4-}$ tetrahedra, as well as oxide ions, that are encompassed by Li atoms. With the mixed occupancy of O and N positions, the resulting partial occupancy of Li positions of 92.9(12) % leads to the sum formula $Li_{27-x}[P_4O_{7+x}N_{9-x}]O_3$ with $x = 1.9(3)$. FTIR, EDX(SEM), ICP, and CHNS measurements were performed to exclude possible presence of other elements and structural features such as amine groups. $Li_{27-x}[P_4O_{7+x}N_{9-x}]O_3$ is a predominantly ionic conductor ($\tau_i = 0.991$) with a bulk ionic conductivity of $\sigma_{bulk} = 6.6 \times 10^{-8}\,S\,cm^{-1}$ at room temperature and an activation energy of $E_a = 0.46(2)$ eV.

7.3. Finding Order in Disorder – The Highly Disordered Lithium Oxonitridophosphate Double Salt $Li_{8+x}P_3O_{10-x}N_{1+x}$ ($x = 1.4(5)$)

Stefanie Schneider, Sandra T. Kreiner, Lucas G. Balzat, Bettina V. Lotsch, and Wolfgang Schnick

Published in: *Chem. Eur. J.* **2023**, *29*, e202301986.
Access via: DOI: 10.1002/chem.202301986
Reprinted at: Chapter 5, Supporting Information in appendix C

$Li_{8+x}P_3O_{10-x}N_{1+x}$, a lithium oxonitridophosphate double salt, was synthesized in an ampoule synthesis under Ar from P_3N_5 and Li_2O at 800 °C. The structure is formed over a wide variety of starting material ratios.

This compound constitutes the first oxonitridophosphate double salt with two distinct phosphate motifs, single tetrahedra and pairs of tetrahedra connected by a shared vertex. The structure crystallizes in the triclinic space group $P\bar{1}$ with $a = 5.125(2)$, $b = 9.888(5)$, $c = 10.217(5)$ Å, $\alpha = 70.30(2)$, $\beta = 76.65(2)$, $\gamma = 77.89(2)°$, and $Z = 2$. Using MAS-NMR, $[PO_2N_2]^{5-}$, $[PO_3N]^{4-}$, $[P_2O_6N]^{5-}$, and $[PO_5N_2]^{6-}$ were identified. O and N atom positions of the single tetrahedra exhibit mixed occupancy. $P_2(O,N)_7$ is highly disordered. There are two orientation of this motif that show an occupancy of 31.5(8) and 68.5(8) %. The two partial structures can be transformed into each other by rotation around the P2–O5 bond and bending of the P–N–P bridging angle. $Li_{8+x}P_3O_{10-x}N_{1+x}$ is an ionic conductor with a total conductivity $\sigma_{tot} = 1.2 \times 10^{-7}$ S cm^{-1} at room temperature and an activation energy $E_a = 0.47(2)$ eV. The compound is stable up to 720 °C.

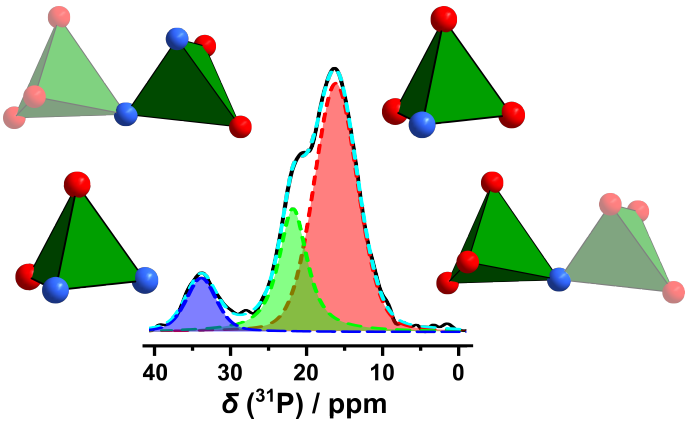

Figure 7.3.: ^{31}P NMR spectrum with structural motifs corresponding to the respective signals.

7.4. Please Mind the Gap: Highly Condensed P–N Networks in LiP_4N_7 and $Li_{3-x}P_6N_{11-x}(NH)_x$

Stefanie Schneider, Sebastian Klenk, Simon D. Kloß, and Wolfgang Schnick

Published in: *Chem. Eur. J.* **2023**, e202303251.
Access via: DOI: 10.1002/chem.202303251
Reprinted at: Chapter 5, Supporting Information in appendix C

The highly condensed lithium (imido)nitridophosphates LiP_4N_7 and $Li_{3-x}P_6N_{11-x}(NH)_x$ were synthesized using a multianvil press. The synthesis from P_3N_5 and $LiPN_2$ was executed at 10 GPa and 1150 °C in the multianvil press. For LiP_4N_7, the temperature was held for 15 min and for $Li_{3-x}P_6N_{11-x}(NH)_x$, 60 min. Their high degrees of condensation ($\kappa_{LiP_4N_7} = 0.57$ and $\kappa_{Li_{3-x}P_6N_{11-x}(NH)_x} = 0.54$) are realized by triply coordinated N atoms similar to β-HP_4N_7.

LiP_4N_7 crystallizes in the orthorhombic space group $P2_12_12_1$ (no. 19) with $a = 4.5846(6)$, $b = 8.0094(11)$, $c = 13.252(2)$ Å, and $Z = 4$. Its structure is highly condensed due to motifs of propeller-like triplets that overlap into bands of *dreier*-rings. $Li_{3-x}P_6N_{11-x}(NH)_x$ exhibits a triclinic structure in the space group $P\bar{1}$ (no. 2) with $a = 4.6911(11)$, $b = 7.024(2)$, $c = 12.736(3)$ Å, $\alpha = 87.726(11)$, $\beta = 80.279(11)$, $\gamma = 70.551(12)°$, and $Z = 2$. There is no evidence for presence of H in LiP_4N_7. However, presence of H in $Li_{3-x}P_6N_{11-x}(NH)_x$ was proven by MAS-NMR and FTIR spectroscopy. Presence of other elements was excluded by EDX spectroscopy and CHNS combustion analysis. The thermal stability was measured by variable-temperature PXRD. LiP_4N_7 and $Li_{3-x}P_6N_{11-x}(NH)_x$ are stable against decomposition up to 900 and 800 °C, respectively. Their volumetric expansion coefficients are 17.5(4) and 25.2(8) $\times 10^{-6}\,K^{-1}$ for LiP_4N_7 and $Li_{3-x}P_6N_{11-x}(NH)_x$, respectively, which is comparable to other structures with $\kappa = 0.57$ and $\kappa = 0.54$.

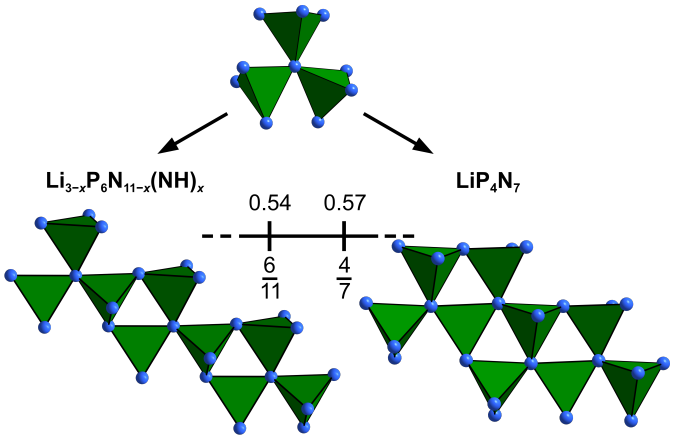

Figure 7.4.: Structural motifs of LiP_4N_7 and $Li_{3-x}P_6N_{11-x}(NH)_x$, composed of threefold vertex-sharing tetrahedra.

8. Discussion and Outlook

8.1. Lithium oxonitridophosphates

8.1.1. Structural motifs

In this thesis, the synthesis and in-depth characterization of lithium oxonitridophosphates with hitherto unknown structural motifs was achieved. Up until the start of this work, only four crystalline lithium oxonitridophosphates were reported in literature, $Li_{2.88}PO_{3.73}N_{0.14}$, $Li_{3.6}PO_{3.4}N_{0.6}$, Li_2PO_2N, and $Li_{14}(PON_3)_2O$.[1–4] These compounds exhibit solely two distinct structural motifs: non-condensed and infinite chains of $P(O,N)_4$ tetrahedra. A phase diagram of the Li–P–O–N system with crystalline and amorphous phases is given in Figure 8.1.

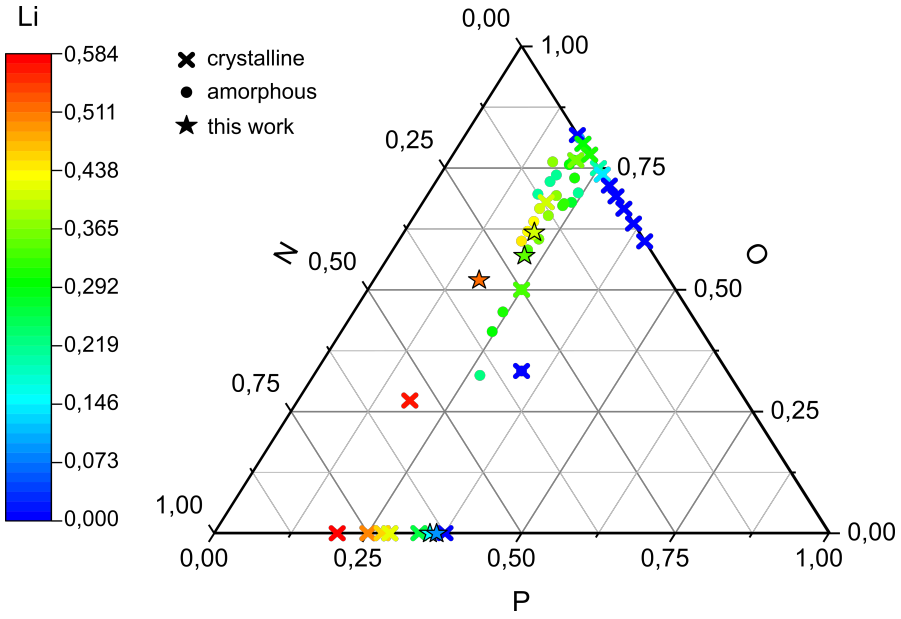

Figure 8.1.: Quasi-ternary phase diagram of Li–P–O–N. Lithium-content is indicated by coloring. Crystalline phases are marked with crosses, amorphous phases with circles.[1–39]

In both $Li_{2.88}PO_{3.73}N_{0.14}$ and $Li_{3.6}PO_{3.4}N_{0.6}$, the P atom is coordinated mostly by O atoms, with a mixed occupancy of O atom positions with a small fraction of N and, in the case of $Li_{2.88}PO_{3.73}N_{0.14}$, vacancies at O atom positions. They are obtained from oxophosphates that were reacted with small amounts of N-containing reactants (N_2-containing atmosphere and Li_3N).[1,4] The double salt $Li_{14}(PON_3)_2O$ contains defined non-condensed PON_3 tetrahedra with O^{2-} as second anionic species.

Its synthesis was accomplished by stoichiometrically precise reaction of $PO(NH_2)_3$ with $LiNH_2$.[3] Another product of stoichiometric addition with N-containing starting materials is Li_2PO_2N. It was obtained from Li_2O, P_2O_5, and P_3N_5. The structure consists of infinite chains of corner-sharing tetrahedra with a P–N–P backbone and O atoms at apical positions.[2]

In order to obtain further lithium oxonitridophosphate phases, a synthesis strategy of lithium nitridophosphates was applied in this work. Li_3N was used in excess to create a flux. With P_3N_5 and Li_2O as phosphorus and oxygen sources, the ratio of starting materials was varied to obtain hitherto not reported structural motifs. By variation of P_3N_5, Li_3N, and Li_2O ratios in ampoule syntheses, it was possible to obtain three additional crystalline lithium oxonitriophosphates: $Li_{5+x}P_2O_{6-x}N_{1+x}$ ($x \approx 0.9$), $Li_{27-x}[P_4O_{7+x}N_{9-x}]O_3$ ($x = 1.9(3)$), and $Li_{8+x}P_3O_{10-x}N_{1+x}$ ($x = 1.4(5)$). The compounds $Li_{5+x}P_2O_{6-x}N_{1+x}$ and $Li_{8+x}P_3O_{10-x}N_{1+x}$ exhibit pairs of corner-sharing tetrahedra, a structural motif hitherto unobserved in lithium oxonitridophosphates. Partially due to various forms of disorder, they all contain more than one anionic species. Figure 8.2 shows the structural motifs including the diphosphate motif first observed in $Li_{5+x}P_2O_{6-x}N_{1+x}$.

$Li_{5+x}P_2O_{6-x}N_{1+x}$ comprises pairs of tetrahedra, connected by a shared N atom. This $[P_2O_6N]^{5-}$ motif is found in two crystallographically independent sites in the structure. A large fraction of these pairs of tetrahedra (ca. 90 %) exhibit not only one, but two incorporated N atoms, resulting in $[P_2O_5N_2]^{6-}$. This diphosphate motif has so far only been observed as in lithium phosphate $Li_4P_2O_7$ and was observed by NMR and IR in amorphous lithium oxonitridophosphates (a-LiPON) with a bridging N atom.[40,41]

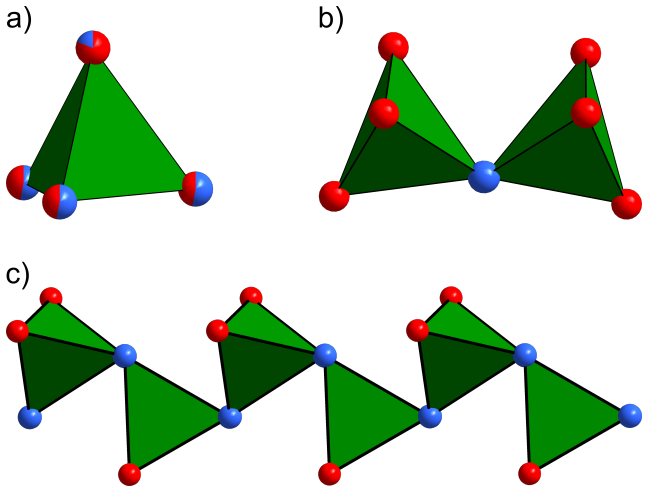

Figure 8.2.: Structural motifs in lithium oxonitridophosphates. O atoms are shown in red, N atoms in blue. a) Non-condensed tetrahedra (here with mixed occupancy of vertices). b) Diphosphate motif obtained with $Li_{5+x}P_2O_{6-x}N_{1+x}$. c) Infinite chains of tetrahedra with P–N–P backbone.

$Li_{27-x}[P_4O_{7+x}N_{9-x}]O_3$ exhibits non-condensed $P(O,N)_4$ tetrahedra and O^{2-} anions. Although only one crystallographic P atom position was observed in single-crystal X-ray data, solid-state magic angle spinning nuclear magnetic resonance (MAS NMR) spectroscopy showed presence of $[PO_3N]^{4-}$

and $[PO_2N_2]^{5-}$ tetrahedra. The statistically mixed occupancy of O/N positions was verified using neutron powder diffraction data. Due to the presence of both $P(O,N)_4$ tetrahedra and oxide anions, $Li_{27-x}[P_4O_{7+x}N_{9-x}]O_3$ is a lithium oxonitridophosphate oxide like $Li_{14}(PON_3)_2O$. However, whereas in the related double salt $Li_{14}(PON_3)_2O$ there are defined $[PON_3]^{6-}$ tetrahedra, $Li_{27-x}[P_4O_{7+x}N_{9-x}]O_3$ exhibits mixed occupancy on O/N positions within the tetrahedra comparable to $Li_{2.88}PO_{3.73}N_{0.14}$ or $Li_{3.6}PO_{3.4}N_{0.6}$.[3,4] The lithium oxonitride double salts known so far contain various anionic species within the same motif realized through mixed occupancy of O/N positions. In contrast, $Li_{8+x}P_3O_{10-x}N_{1+x}$ exhibits two different large anions, both of which show mixed occupancy of O/N positions. The first motif, a non-condensed $P(O,N)_4$ tetrahedron, occurs as $[PO_3N]^{4-}$ or $[PO_2N_2]^{5-}$. The second motif consists of two tetrahedra connected by a bridging N atom and occurs as $[P_2O_6N]^{5-}$, but also as $[P_2O_5N_2]^{6-}$. In addition to mixed occupancy of apical O/N positions, these pairs of tetrahedra are severely disordered. The disorder in all these newly found structures requires a multitude of analytical methods for thorough characterization, as no one method can give all the details needed.

8.1.2. Solid-State Magic Angle Spinning Nuclear Magnetic Resonance Spectroscopy

One method to corroborate and complement X-ray diffraction (XRD) methods is solid-state magic angle spinning nuclear magnetic resonance (ssMAS NMR) spectroscopy. Since the amount of O and N around the central atom create distinctly different environments for P atoms, different types of $P(O,N)_4$ tetrahedra can be distinguished. In lithium oxonitridopohsphates, the ^{31}P NMR resonance of non-condensed tetrahedra is shifted by +10 ppm for each O substituted by N.[42] With the data available on non-condensed tetrahedra, the types of $P(O,N)_4$ were identified in $Li_{27-x}[P_4O_{7+x}N_{9-x}]O_3$ and $Li_{8+x}P_3O_{10-x}N_{1+x}$.

Since no experimental analytic data for ^{31}P NMR resonances of pairs of corner-sharing tetrahedra existed before this work, theoretical calculations and comparisons with corner-sharing tetrahedra in Li_2PO_2N were consulted to deduce the $P_2(O,N)_7$ species present.[42] From $Li_{5+x}P_2O_{6-x}N_{1+x}$ and $Li_{8+x}P_3O_{10-x}N_{1+x}$, we were able to find the ^{31}P chemical shifts of the $[PO_3N]^{4-}$ and $[PO_2N_2]^{5-}$ partial motifs within these pairs of corner-sharing tetrahedra: 14–16 ppm for $[PO_3N]^{4-}$ and around 21 ppm for $[PO_2N_2]^{5-}$.

In comparison to $Li_4P_2O_7$, in which ^{31}P resonances occur between −2.9 and −6.6 ppm depending on the polymorph,[40] the ^{31}P resonances in $Li_{5+x}P_2O_{6-x}N_{1+x}$ and $Li_{8+x}P_3O_{10-x}N_{1+x}$ occur noticeably shifted towards high field. It seems surprising that introduction of the bridging N results in such a strong shift (ca. +20 ppm) while insertion of another apical N atom leads to a shift of only 5–7 ppm. It could be useful to synthesize compounds with higher N contents in the $P_2(O,N)_7$ motif to enable comparison of a complete series of ^{31}P NMR shifts up to $[P_2N_7]^{11-}$. The data obtained on the newly synthesized compounds corroborates *ab initio* molecular dynamics (AIMD) calculations and can be a reference point for further investigation of anion species within a-LiPON.[42]

8.1.3. Neutron Powder Diffraction

Neutron powder diffraction was used to complement X-ray diffraction (XRD), as it allows for unequivocal differentiation between oxygen and nitrogen. Additionally, it is elemental in refinement of (underoccupied) Li and H atom positions. Especially in cases where XRD and NMR spectroscopy seemingly contradict each other, like in the case of $Li_{27-x}[P_4O_{7+x}N_{9-x}]O_3$, neutron diffraction can be very helpful. Although only one crystallographic P position was found by single-crystal XRD (scXRD), NMR showed—seemingly contradictory—two ^{31}P signals. Since the scattering contrast of O and N is much higher in neutron diffraction than in XRD, the two elements can be distinguished and ordering that would be invisible in XRD, could be observed. In the case of $Li_{27-x}[P_4O_{7+x}N_{9-x}]O_3$, neutron diffraction corroborated mixed occupancy of O and N and their respective ratios were determined. The seemingly contradictory results from XRD and NMR could be accomodated with a single crystallographic P atom position that exists in different environments due to mixed occupancy of the coordinating atoms.

Additionally, presence of H could be refuted, since no additional suitable core density was observed. As incorporation of H is an ubiquitous possibility and detection of H atom positions notoriously difficult with XRD methods, neutron diffraction is a decisive method.

Furthermore, Li atom positions can easily be found and their occupancy refined reliably. In the case of $Li_{27-x}[P_4O_{7+x}N_{9-x}]O_3$, due to the good quality of scXRD data, Li positions were known. Full occupancy would not have led to charge neutrality, however, neutron diffraction showed partial occupancy of Li positions, corroborating the determined occupancy of O and N positions. This partial occupancy is thought to have significant influence on the Li^+ ion conductivity of $Li_{27-x}[P_4O_{7+x}N_{9-x}]O_3$.

8.1.4. Ionic conductivity

Since a-LiPON is known as solid electrolyte[43,44] with an ionic conductivity in the range of $10^{-6}\,S\,cm^{-1}$,[43,45,46] impedance measurements were performed for all lithium oxonitridophosphates synthesized in this work. The conductivities of $Li_{5+x}P_2O_{6-x}N_{1+x}$, $Li_{27-x}[P_4O_{7+x}N_{9-x}]O_3$, and $Li_{8+x}P_3O_{10-x}N_{1+x}$ are 2.2×10^{-7}, 6.6×10^{-8} and $1.2 \times 10^{-7}\,S\,cm^{-1}$ at 25 °C, respectively. Their activation energies are between 0.46(2) and 0.52(1) eV. These conductivities, although moderate in comparison to other compound classes like lithium super ionic conductors ($Li_{2+2x}Zn_{1-x}GeO_4$, LiSICON), garnet-type Li^+ conductors (e.g. $Li_{6.65}Ga_{0.15}La_3Zr_{1.90}Sc_{0.10}O_{12}$[47]), or perowskite-type Li^+ conductors, (e.g., $[(La_{0.5}Li_{0.5})_{0.5}M_{0.5}]TiO_3$[48]) are well within the range of other lithium oxonitridophosphates (Table 8.1).

Amorphous LiPON exhibits the largest Li^+ ion conductivity of the lithium oxonitridophosphates, which might be solely due to its amorphous structure. Disorder was found to be very beneficial for high ionic conductivity, as the activation energy for jumps of Li^+ from one position to a neighboring position is reduced. Introduction of disorder in the form of mixed occupancies of O and N positions or vacancies at Li positions is thought to likelyhood of jumps to other positions as activation energy is reduced.[49,50]

While not amorphous, crystalline lithium oxonitridophosphates exhibit significant disorder, considering among other things their mixed occupancy of O and N positions. In the lithium oxonitridophosphates synthesized in this work, mixed occupancy of O/N positions within tetrahedra and pairs of tetrahedra are found in $Li_{27-x}[P_4O_{7+x}N_{9-x}]O_3$ and $Li_{5+x}P_2O_{6-x}N_{1+x}$, respectively. In $Li_{8+x}P_3O_{10-x}N_{1+x}$, both the tetrahedron and the $P_2O_{6-x}N_{1+x}$ motif exhibit mixed occupancy, but also the $P_2O_{6-x}N_{1+x}$ motif itself is disordered. Thus, instead of eleven environments for the eleven Li positions detected, twenty different environments are observed.
Although Li^+ ion conduction processes are not fully understood in crystalline lithium oxonitridophosphates, they provide valuable model structures for investigation of conductivity of a-LiPON. With a variety of different crystalline unit cells as starting points, conductivity in a-LiPON might be simulated in a combined synthetic and theoretical approach, in which first, an a-LiPON thin film is generated and analyzed using methods like ssNMR. The structural motifs observed by NMR can then be built together by combination of crystalline unit cells containing the respective motif. The compounds synthesized in this work contain all structural motifs that have so far been observed in NMR studies of a-LiPON.

Table 8.1.: Ionic conductivities and activation energies of lithium oxonitridophosphates and other solid electrolytes at room temperature. Compounds from this work are highlighted.

Compound	σ_{tot} / S cm^{-1}	E_a / eV	Ref
$Li_{2.88}PO_{3.73}N_{0.14}$	1×10^{-13}	0.97	[1]
$Li_{3.6}PO_{3.4}N_{0.6}$	5.6×10^{-8}	0.55	[4]
$\mathbf{Li_{27-x}[P_4O_{7+x}N_{9-x}]O_3}$	6.6×10^{-8}	0.46	[37]
$\mathbf{Li_{5+x}P_2O_{6-x}N_{1+x}}$	4.6×10^{-8}	0.52	[36]
$\mathbf{Li_{8+x}P_3O_{10-x}N_{1+x}}$	1.2×10^{-7}	0.47	[38]
Li_2PO_2N	8.8×10^{-7} [a]	0.57	[2]
a-LiPON	1.6×10^{-6}	0.58	[46]
LiSICON	4×10^{-5}	0.44	[51]

[a] at 80 °C.

Additionally, conduction mechanisms within crystalline LiPON should be investigated further. Theoretical calculations suggest that condensation of tetrahedra by N atoms increases conductivity, as the overall coulombic attraction of the motif and Li should decrease.[49] For example, the altogether six negative charges of two $[PO_4]^{3-}$ anions is reduced to five in the condensed $[P_2O_6N]^{5-}$. Thus, counter-intuitively, the conductivity increases with the degree of condensation. However, once a critical degree of condensation is reached, so that Li^+ jumps are hindered, this effect should subside. Once phase pure samples become available, impedance measurements should be repeated to review the results obtained in simulations. Additionally, the influence of Li_2O as side phase can then be identified.
In the future, targeted synthesis of further crystalline lithium oxonitridophosphates should be carried on in order to obtain more different structural motifs in an ordered environment to enable direct

study of the influence of structural motifs on the conductivity. Possibly, targeted introduction of disorder into crystalline structures could be achieved to create quasi-amorphous phases that exhibit larger conductivities.

8.1.5. Applicability and mass production

Obviously, there are many unknown factors regarding possible applicability of crystalline lithium oxonitridophosphates in all-solid-state batteries, giving future research a wide range of starting points in this field. Synthesis of unknown crystalline lithium oxonitridophosphates is a time and work intensive project and hitherto, their conductivities are modest. The compounds presented in this work need reaction times of 30–90 h and conductivities are in the range of 10^{-7}–10^{-8} S cm^{-1} at room temperature. However, the compounds presented in this work have not been optimized for conductivity. Thus, both synthesis and conductivities need to be tuned in order to use crystalline lithium oxonitridophosphates in batteries. Regarding synthesis, the hot isostatic press (HIP) can be a valuable tool to accelerate LiPON research, as several ratios of starting materials can be reacted simultaneously. We found that reactions under N_2 pressures in the range of 150–200 MPa, lithium oxonitridophosphates can be produced. Although preliminary experiments did not yield phase pure samples, we are confident that future studies can solve this problem. Using the HIP to synthesize lithium oxonitridophosphates can reduce reaction times from several days to only five hours. According to literature, synthesis from red phosphorus in the HIP might be an option to eliminate the time-consuming step of P_3N_5 synthesis.[52] Thus, if synthesis in the HIP is found to be scalable, it might be a method for mass production of crystalline lithium nitridophosphates.
Conductivities of both known and formerly unknown compounds synthesized with a new method must be investigated, since microstructure of compounds can be influenced significantly by preparation methods.[53] In order to tune ionic conductivity, various parameters need to be investigated, like influence of tempering on the availability of vacancies for Li jumps or the effect of different N_2 pressures on crystallinity. Additionally, if available, phase pure compounds should be thoroughly investigated regarding their ionic conductivities, since the purity of samples might have a significant influence.
Furthermore, in order for crystalline lithium oxonitridophosphates to be applicable in all-solid-state batteries, their stability against reaction with elemental Li must be investigated. If reaction takes place, formation of a stable solid electrolyte interface (SEI) is possible.

8.1.6. Possible higher degrees of condensation in LiPON

One more field of future research will be to extended the structural chemistry of lithium oxonitrides. So far, only structures with very low degrees of condensation have been synthesized and investigated ($\kappa < 0.3$). However, looking at the structurally related compound class of lithium nitridophoshpates, more degrees of condensation should be available with lithium oxonitridophosphates, too. In the Li–P–N system, there are five different known degrees of condensation with seven structures in the

range of $0.25 \leq \kappa \leq 0.5$. All exhibit distinct structural motifs that contain apical N atom positions, which could in principle also be occupied by O atoms. Thus, these structures could also be available for lithium oxonitridophosphates.

In comparison to alkaline earth or mixed cation oxonitridophosphates, there are several compounds known with degrees of condensation of up to $\kappa = 0.5$. For example, the compounds $Sr_3P_6O_6N_8$, $LiPr_2P_4N_7O_3$, $MgSrP_3N_5O_2$, $CaMg_2P_6O_3N_{10}$, and SrP_3N_5O exhibit κ of 0.375, 0.4, 0.429, 0.46 and 0.5, respectively.[54–59] All of these compounds were synthesized in the multianvil press. Preliminary experiments with different ratios of PON, Li_3N, Li_2O, and P_4O_{10} have only yielded $LiPN_2$, Li_2PO_2N, or Li_3PO_4. Possibly, synthesis of oxonitridophosphates with higher κ requires higher pressures than applied so far. However, there are many possibilities left to synthesize lithium oxonitridophosphates with similar κ, like the azide route with LiN_3 and PON. If there are oxo-imidonitridophosphates available like $H_3P_8O_8N_9$,[60] they might be used with lithium hydride in a metathesis reaction. With the help of increased pressure, otherwise too unstable compounds become available as starting materials, as their decomposition is hindered up to higher temperatures. Altogether, considering that various degrees of condensation occur again and again in different compound classes, it is quite likely that lithium oxonitridophosphates with $\kappa > 0.3$ can be synthesized.

8.2. Synthesis of highly condensed lithium nitridophosphates

Although the structural diversity of known lithium nitridophosphates is considerable, no structures known with $\kappa > 0.5$ were published. Within this work, we show that such a degree of condensation can be achieved (Figure 8.3). The span of known structural motifs in low κ spans from non-condensed tetrahedra over various constellations like condensed *dreier*- and *vierer*-rings in $Li_{18}P_6N_{10}$ or T2 supertetrahedra in $Li_{10}P_4N_{10}$ up to the crystobalite-analogue three-dimensional network in $LiPN_2$. Other nitridophosphates exhibit highly condensed structures. This also holds true for homologues of lithium, for example $A_3P_6N_{11}$ (A = Na, K, Rb, Cs) or AP_4N_7 (A = H, Na, K, Rb, Cs).

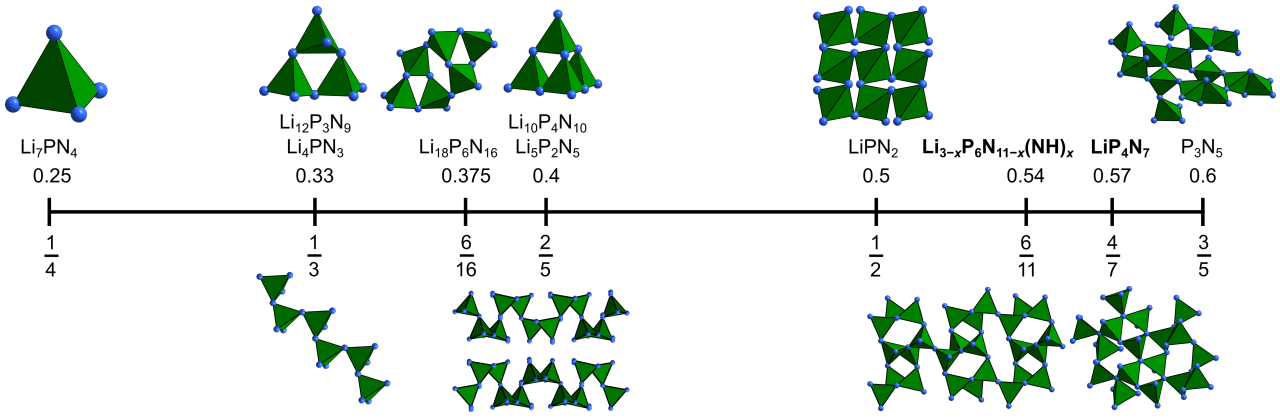

Figure 8.3.: Structural motifs observed in lithium nitridophosphates since this work.[6–9,39,61,62]

With LiP_4N_7 ($\kappa = 0.57$) and $Li_{3-x}P_6N_{11-x}(NH)_x$ ($\kappa = 0.54$), the first representatives of lithium (imido)nitridophosphates with $\kappa > 0.5$ were synthesized and characterized. They can be produced by reaction of P_3N_5 and $LiPN_2$ in the multianvil press at 10 GPa and 1150 °C and exhibit networks of connected tetrahedra. The high degree of condensation is realized by triply coordinated N-atoms that form propeller-like motifs analogous to those in β-HP_4N_7.
A third highly condensed lithium nitridophosphate, $Li_2P_8N_{14}$, was also obtained. Here, the synthesis employs P_3N_5 and $LiPN_2$ at pressures of 4–6 GPa and temperatures of 1150 °C (Equation (8.1)). Ion exchange starting from SrP_8N_{14} and LiCl also yields this compound (Equation (8.2)).

$$2\,P_3N_5 + 2\,LiPN_2 \xrightarrow[1150\,^\circ C]{5\,GPa} Li_2P_8N_{14} \tag{8.1}$$

$$SrP_8N_{14} + 2\,LiCl \xrightarrow[1150\,^\circ C]{5\,GPa} Li_2P_8N_{14} + SrCl_2 \tag{8.2}$$

Due to low single-crystal quality, the structure could not be deduced unequivocally. However, indexing of a single crystal X-ray dataset yielded a monoclinic cell with lattice parameters $a = 8.5923(12)$, $b = 5.0741(8)$, $c = 23.691(4)$ Å, $\beta = 98.080(7)°$, and $Z = 8$. The thus derived structural model showed a layered structure similar to that of other MP_8N_{14} phases (M = Mg, Ca, Sr, Ba, Fe, Co, Ni).
With $Li_{3-x}P_6N_{11-x}(NH)_x$, the first lithium imidonitridophosphate was synthesized. The presence of hydrogen in the structure was proven by NMR and IR, however, quantitative determination of H content was not possible due to unavailability of phase pure samples. For its heavier homologue $K_3P_6N_{11}$, ion exchange properties have been observed.[63] For example, sodium can be introduced into the structure upon boiling in aqueous NaCl solutions or upon heating with NaCl. However, H_3O^+ incorporation has also been postulated.[63] Possibly, the $P_6N_{10}NH_x$ network can also incorporate other cations like Na^+ or H_3O^+, which would lead to new structures of these homologues. Similarly, it is likely that also Li^+ can be incorporated into the structure of $K_3P_6N_{11}$, leading to a compound with the generalized formula $K_{3-x}Li_xP_6N_{11}$. This might be a method to obtain phase pure samples of $Li_{3-x}P_6N_{11-x}(NH)_x$. Equally possible is the omission of NH, leading to $Li_3P_6N_{11}$. If no phase transition occurs upon ion exchange, new modifications of $Li_3P_6N_{11}$ are conceivable.
Mobile cations with large coordination polyhedra as they are found in LiP_4N_7 and $Li_{3-x}P_6N_{11-x}(NH)_x$ might also make these compounds interesting candidates for lithium ion conductivity. In contrast to other lithium (oxo)nitridophosphates, the thermal expansion of these highly condensed structures is very low, which is an advantageous property for use as solid electrolyte. Furthermore, LiP_4N_7 and $Li_{3-x}P_6N_{11-x}(NH)_x$ are thermally stable up to 900 and 800 °C, respectively, and chemically stable against even concentrated acids like hydrochloric acid. Their chemical stability against metallic Li or formation of SEIs must be tested.

8.3. Final remarks

The results of this work show the complexity and difficulty of investigating a chemical system as intricate and multifaceted as that of lithium (oxo)nitridophosphates. Although the main compounds of this thesis have been synthesized and characterized with the greatest care, many questions remain open and a plethora of side phases with unknown properties is yet to be retrieved as main compounds. We are confident that these systems will stimulate future research as current studies have only just started to scratch the surface.

8.4. References

[1] B. Wang, B. C. Chakoumakos, B. C. Sales, B. S. Kwak, J. B. Bates, *J. Solid State Chem.* **1995**, *115*, 313–323, DOI 10.1006/jssc.1995.1140.

[2] K. Senevirathne, C. S. Day, M. D. Gross, A. Lachgar, N. A. Holzwarth, *Solid State Ionics* **2013**, *233*, 95–101, DOI 10.1016/j.ssi.2012.12.013.

[3] D. Baumann, W. Schnick, *Eur. J. Inorg. Chem.* **2015**, 617–621, DOI 10.1002/ejic.201403125.

[4] P. López-Aranguren, M. Reynaud, P. Głuchowski, A. Bustinza, M. Galceran, J. M. López Del Amo, M. Armand, M. Casas-Cabanas, *ACS Energy Lett.* **2021**, *6*, 445–450, DOI 10.1021/acsenergylett.0c02336.

[5] W. Schnick, J. Luecke, *J. Solid State Chem.* **1990**, *87*, 101–106, DOI 10.1016/0022-4596(90)90070-E.

[6] E.-M. Bertschler, R. Niklaus, W. Schnick, *Chem. Eur. J.* **2017**, *23*, 9592–9599, DOI 10.1002/chem.201700979.

[7] E.-M. Bertschler, C. Dietrich, J. Janek, W. Schnick, *Chem. Eur. J.* **2017**, *23*, 2185–2191, DOI 10.1002/chem.201605316.

[8] W. Schnick, U. Berger, *Angew. Chem. Int. Ed.* **1991**, *30*, 830–831, *Angew. Chem.* **1991**, *103*, 857–858, DOI 10.1002/anie.199108301.

[9] E.-M. Bertschler, R. Niklaus, W. Schnick, *Chem. Eur. J.* **2018**, *24*, 736–742, DOI 10.1002/chem.201704975.

[10] W. Schnick, J. Lücke, *Z. Anorg. Allg. Chem.* **1990**, *588*, 19–25, DOI 10.1002/zaac.19905880103.

[11] S. Horstmann, E. Irran, W. Schnick, *Angew. Chem. Int. Ed.* **1997**, *36*, 1873–1875, *Angew. Chem.* **1997**, *109*, 1938–1940. DOI 10.1002/anie.199718731.

[12] L. Boukbir, R. Marchand, Y. Laurent, P. Bacher, G. Roult, *Ann. Chim. Fr.* **1989**, *14*, 475–481, DOI 10.1002/chin.199030021.

[13] G. Han, A. Vasylenko, A. R. Neale, B. B. Duff, R. Chen, M. S. Dyer, Y. Dang, L. M. Daniels, M. Zanella, C. M. Robertson, L. J. Kershaw Cook, A. L. Hansen, M. Knapp, L. J. Hardwick, F. Blanc, J. B. Claridge, M. J. Rosseinsky, *J. Am. Chem. Soc.* **2021**, *143*, 18216–18232, DOI 10.1021/jacs.1c07874.

[14] N. I. Ayu, E. Kartini, L. D. Prayogi, M. Faisal, Supardi, *Ionics* **2016**, *22*, 1051–1057, DOI 10.1007/s11581-016-1643-z.

[15] T. Ben-Chaabane, L. Smiri-Dogguy, Y. Laligant, A. Le Bail, *Eur. J. Solid State Inorg. Chem.* **1998**, *35*, 255–264, DOI 10.1016/S0992-4361(98)80006-4.

[16] E. V. Murashova, N. N. Chudinova, *Crystallogr. Reports* **2001**, *46*, 942–947, DOI 10.1134/1.1420823.

[17] V. I. Voronin, E. A. Sherstobitova, V. A. Blatov, G. S. Shekhtman, *J. Solid State Chem.* **2014**, *211*, 170–175, DOI 10.1016/j.jssc.2013.12.015.

[18] E. H. Arbib, B. Elouadi, J. P. Chaminade, J. Darriet, *J. Solid State Chem.* **1996**, *127*, 350–353, DOI 10.1524/ncrs.2006.221.14.261.

[19] M. Jansen, *Z. Naturforsch.* **1997**, *52 b*, 707–710, DOI 10.1515/znb-1997-0607.

[20] A. Dimitrov, B. Ziemer, W.-D. Hunnius, M. Meisel, *Angew. Chem. Int. Ed.* **2003**, *42*, 2484–2486, *Angew. Chem.* **2003**, *115*, 2537–2661, DOI 10.1002/anie.200351135.

[21] M. Jansen, M. Moebs, *Inorg. Chem.* **1984**, *3*, 4486–4488, DOI 10.1021/ic00194a017.

[22] M. H. Möbs, M. Jansen, *Z. Anorg. Allg. Chem.* **1984**, *514*, 39–48, DOI 10.1002/zaac.19845140705.

[23] B. Beagley, D. W. J. Cruickshank, T. G. Hewitt, K. H. Jost, *T. Faraday Soc.* **1968**, *65*, 1219–12305, DOI 10.1039/TF9696501219.

[24] B. Lüer, M. Jansen, *Z. Krist.-New Cryst. St.* **1991**, *197*, 247–248, DOI 10.1524/zkri.1991.197.3-4.247.

[25] R. Chen, W. Qu, X. Guo, L. Li, F. Wu, *Mater. Horiz.* **2016**, *3*, 487–516, DOI 10.1039/C6MH00218H.

[26] A. Manthiram, X. Yu, S. Wang, *Nat. Rev. Mater.* **2017**, *2*, 1–16, DOI 10.1038/natrevmats.2016.103.

[27] Y. Hamon, A. Douard, F. Sabary, C. Marcel, P. Vinatier, B. Pecquenard, A. Levasseur, *Solid State Ionics* **2006**, *177*, 257–261, DOI 10.1016/j.ssi.2005.10.021.

[28] A. S. Westover, N. J. Dudney, R. L. Sacci, S. Kalnaus, *ACS Energy Lett.* **2019**, *4*, 651–655, DOI 10.1021/acsenergylett.8b02542.

[29] K. I. Chung, W. S. Kim, Y. K. Choi, *J. Electroanal. Chem.* **2004**, *566*, 263–267, DOI 10.1016/j.jelechem.2003.11.035.

[30] A. Schwöbel, R. Hausbrand, W. Jaegermann, *Solid State Ionics* **2015**, *273*, 51–54, DOI 10.1016/j.ssi.2014.10.017.

[31] Z. A. Grady, C. J. Wilkinson, C. A. Randall, J. C. Mauro, *Front. Energy Res.* **2020**, *8*, 1–23, DOI 10.3389/fenrg.2020.00218.

[32] B. B. Owens, *J. Power Sources* **2000**, *90*, 2–8, DOI 10.1016/S0378-7753(00)00436-5.

[33] A. C. Kozen, A. J. Pearse, C. F. Lin, M. Noked, G. W. Rubloff, *Chem. Mater.* **2015**, *27*, 5324–5331, DOI 10.1021/acs.chemmater.5b01654.

[34] Q. Zhao, S. Stalin, C. Z. Zhao, L. A. Archer, *Nat. Rev. Mater.* **2020**, *5*, 229–252, DOI 10.1038/s41578-019-0165-5.

[35] A. Thißen, D. Ensling, M. Liberatore, Q. H. Wu, F. J. Madrigal, M. S. Bhuvaneswari, R. Hunger, W. Jaegermann, *Ionics* **2009**, *15*, 393–403, DOI 10.1007/s11581-009-0339-z.

[36] S. Schneider, L. G. Balzat, B. V. Lotsch, W. Schnick, *Chem. Eur. J.* **2023**, *29*, e202202984, DOI 10.1002/chem.202202984.

[37] S. Schneider, E.-M. Wendinger, V. Baran, A.-K. Hatz, B. V. Lotsch, M. Nentwig, O. Oeckler, T. Bräuniger, W. Schnick, *Chem. Eur. J.* **2023**, *29*, e202300174, DOI 10.1002/chem.202300174.

[38] S. Schneider, S. T. Kreiner, L. G. Balzat, B. V. Lotsch, W. Schnick, *Chem. Eur. J.* **2023**, *29*, e202301986, DOI 10.1002/chem.202301986.

[39] S. Schneider, S. Klenk, S. D. Kloß, W. Schnick, *Chem. Eur. J.* **2023**, e202303251, DOI 10.1002/chem.202303251.

[40] B. Raguž, K. Wittich, R. Glaum, *Eur. J. Inorg. Chem.* **2019**, *2019*, 1688–1696, DOI 10.1002/ejic.201801100.

[41] V. Lacivita, A. S. Westover, A. Kercher, N. D. Phillip, G. Yang, G. Veith, G. Ceder, N. J. Dudney, *J. Am. Chem. Soc.* **2018**, *140*, 11029–11038, DOI 10.1021/jacs.8b05192.

[42] M. A. T. Marple, T. A. Wynn, D. Cheng, R. Shimizu, H. E. Mason, Y. S. Meng, *Angew. Chem. Int. Ed.* **2020**, *59*, 22185–22193, *Angew. Chem.* **2020**, *132*, 22369–22377, DOI 10.1002/anie.202009501.

[43] X. Yu, J. B. Bates, G. E. Jellison Jr., F. X. Hart, *J. Electrochem. Soc.* **1997**, *144*, 524–532, DOI 10.1149/1.1837443.

[44] P. Knauth, *Solid State Ionics* **2009**, *180*, 911–916, DOI 10.1016/j.ssi.2009.03.022.

[45] J. B. Bates, N. J. Dudney, G. R. Gruzalski, R. A. Zuhr, A. Choudhury, C. F. Luck, J. D. Robertson, *Solid State Ionics* **1992**, *53–56*, 647–654, DOI 10.1016/0167-2738(92)90442-R.

[46] S. Zhao, Z. Fu, Q. Qin, *Thin Solid Films* **2002**, *415*, 108–113, DOI 10.1016/S0040-6090(02)00543-6.

[47] L. Buannic, B. Orayech, J. M. López Del Amo, J. Carrasco, N. A. Katcho, F. Aguesse, W. Manalastas, W. Zhang, J. Kilner, A. Llordés, *Chem. Mater.* **2017**, *29*, 1769–1778, DOI 10.1021/acs.chemmater.6b05369.

[48] Y. Inaguma, L. Chen, M. Itoh, T. Nakamura, *Solid State Ionics* **1994**, *70-71*, 196–202, DOI 10.1016/0167-2738(94)90309-3.

[49] V. Lacivita, N. Artrith, G. Ceder, *Chem. Mater.* **2018**, *30*, 7077–7090, DOI 10.1021/acs.chemmater.8b02812.

[50] J. Li, W. Lai, *Solid State Ionics* **2020**, *351*, 115329, DOI 10.1016/j.ssi.2020.115329.

[51] J. Kuwano, A. R. West, *MRS Bull.* **1980**, *15*, 1661–1667.

[52] S. Wendl, S. Mardazad, P. Strobel, P. J. Schmidt, W. Schnick, *Angew. Chem. Int. Ed.* **2020**, *59*, 18240–18243, *Angew. Chem.* **2020**, *132*, 18397–18400, DOI 10.1002/anie.202008570.

[53] A. Banik, T. Famprikis, M. Ghidiu, S. Ohno, M. A. Kraft, W. G. Zeier, *Chem. Sci.* **2021**, *12*, 6238–6263, DOI 10.1039/d0sc06553f.

[54] S. J. Sedlmaier, J. Schmedt Auf Der Günne, W. Schnick, *Dalt. Trans.* **2009**, 4081–4084, DOI 10.1039/b905136h.

[55] S. D. Kloß, W. Schnick, *Inorg. Chem.* **2018**, *57*, 4189–4195, DOI 10.1021/acs.inorgchem.8b00455.

[56] F. J. Pucher, W. Schnick, *Z. Anorg. Allg. Chem.* **2014**, *640*, 2708–2713, DOI 10.1002/zaac.201400330.

[57] R. M. Pritzl, N. Prinz, P. Strobel, P. J. Schmidt, D. Johrendt, W. Schnick, *Chem. Eur. J.* **2023**, DOI 10.1002/chem.202301218.

[58] A. Marchuk, L. Neudert, O. Oeckler, W. Schnick, *Eur. J. Inorg. Chem.* **2014**, 3427–3434, DOI 10.1002/ejic.201402302.

[59] S. J. Sedlmaier, E. Mugnaioli, O. Oeckler, U. Kolb, W. Schnick, *Chem. Eur. J.* **2011**, *17*, 11258–11265, DOI 10.1002/chem.201101545.

[60] S. J. Sedlmaier, V. R. Celinski, J. Schmedt Auf Der Günne, W. Schnick, *Chem. Eur. J.* **2012**, *18*, 4358–4366, DOI 10.1002/chem.201103010.

[61] W. Schnick, J. Luecke, *Solid State Ionics* **1990**, *38*, 271–273, DOI 10.1016/0167-2738(90)90432-Q.

[62] E.-M. Bertschler, C. Dietrich, T. Leichtweiß, J. Janek, W. Schnick, *Chem. Eur. J.* **2018**, *24*, 196–205, DOI 10.1002/chem.201704305.

[63] A. A. Vitola, J. Ronis, T. Millers, *B. Acad. Sci. USSR. Ch.* **1990**, *1*, 35–39.

A. Supporting Information for Chapter 3 ($Li_{5+x}P_2O_{6-x}N_{1+x}$)

Stefanie Schneider, Lucas G. Balzat, Bettina V. Lotsch, and Wolfgang Schnick

Chem. Eur. J. **2023**, *29*, e202202984.

Reprinted (adapted) with permission from Chemistry – European Journal. Copyright 2022

Abstract Non-crystalline lithium oxonitridophosphate (LiPON) is used as solid electrolyte in all-solid-state batteries. Crystalline lithium oxonitridophosphates are important model structures to retrieve analytical information that can be used to understand amorphous phases better. The new crystalline lithium oxonitridophosphate $Li_{5+x}P_2O_{6-x}N_{1+x}$ was synthesized as off-white powder by ampoule synthesis at 700–800 °C under Ar atmosphere. It crystallizes in the monoclinic space group $P2_1/c$ with $a = 15.130\,87(11)$ Å, $b = 9.706\,82(9)$ Å, $c = 8.886\,81(7)$ Å, and $\beta = 106.8653(8)°$. Two $P(O,N)_4$ tetrahedra connected by an N atom form the structural motif $[P_2O_{6-x}N_{1+x}]^{(5+x)-}$. The structure was elucidated from X-ray diffraction data and the model corroborated by NMR and infrared spectroscopy, and elemental analyses. Measurements of ionic conductivity show a total ionic conductivity of 6.8×10^{-7} S cm^{-1} at 75 °C with an activation energy of 0.52 ± 0.01 eV.

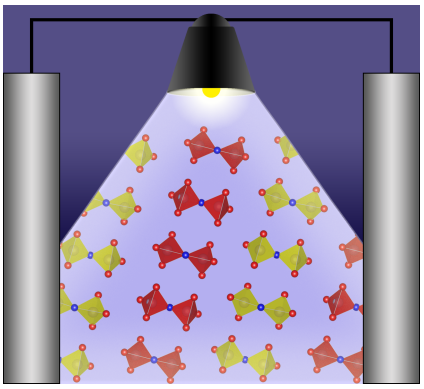

A.1. Experimental Procedures

Synthesis of P3N5:[1] P_4S_{10} (Acros Organics, > 99.8 %) was transferred to a dry quartz tube in argon counterflow. The starting material was saturated with a stream of ammonia (Air liquide, 99.999 %) (4 h) at room temperature, heated with a rate of 5 K min^{-1} in a constant flow of ammonia and held at 850 °C for 4 h. After cooling down (5 K min^{-1}), the orange product was removed from the tube, washed with water, ethanol, and acetone, and dried. The obtained product was analyzed using powder X-ray diffraction. Presence of hydrogen in the sample was ruled out using infrared spectroscopy and elemental analysis CHNS. The obtained P_3N_5 was used for synthesis of the title compound.

Synthesis of $Li_{5+x}P_2O_{6-x}N_{1+x}$: P_3N_5, Li_3N (Rockwood, 99.999 %), and Li_2O (Alfa Aesar, 99.5 %) were combined and ground in an agate mortar in inert atmosphere using an argon-filled glovebox (Unilab, MBraun, Garching, O_2 < 1 ppm, H_2O < 1 ppm). The mixture was transferred to a Ta crucible within a silica tube with a long funnel in argon counterflow. Silica ampoules were sealed off using a vacuum line with argon and an oxyhydrogen burner (all gasses: Air Liquide, 99.999 %). Ampoules were heated at 5 K min^{-1} to 800 °C and held for 90 h. The samples were cooled to room temperature at a rate of 5 K min^{-1}.

Powder X-ray diffraction: Samples were sealed into glass capillaries (diameter 0.5 mm, wall thickness 0.01 mm, Hilgenberg GmbH). Data was collected using a Stoe STADI P diffractometer with Cu $K_{\alpha1}$ radiation (λ = 1.5406 Å), Ge(111) monochromator and Mythen 1 K detector in Debye-Scherrer geometry. Structure solution and Rietveld refinement was performed using the TOPAS-Academic software package.[2] After extraction of intensities using a Pawley fit, the structure was solved using a charge flipping algorithm.[3–5] A shifted-Chebyshev function was used for the background and peak shapes were refined using the fundamental parameters approach.[6,7]

Single-crystal X-ray diffraction: Single crystals were selected under dried paraffin oil and sealed into oil-filled glass capillaries (diameter 0.1 mm, wall thickness 0.01 mm, Hilgenberg GmbH). Data was acquired using a D8 Venture diffractometer (Bruker, Billerica MA, USA), with Mo K_α radiation (λ = 0.710 73 Å) from a rotating anode. Cell parameters were determined and precession images were generated using the APEX3 program package.[8] Deposition Number(s) 2191662 contain(s) the supplementary crystallographic data for this paper. These data are provided free of charge by the joint Cambridge Crystallographic Data Centre and Fachinformationszentrum Karlsruhe Access Structures service.

Temperature-dependent X-ray diffraction: A Stoe STADI P diffractometer using Mo $K_{\alpha1}$ radiation (λ = 0.710 73 Å) and a Ge(111) monochromator in Debye-Scherrer geometry, equipped with a graphite furnace and an imaging plate position sensitive detector was used to take temperature-dependent powder X-ray data. The sample was sealed into a glass capillary (diameter 0.3 mm, wall

thickness 0.01 mm, Hilgenberg GmbH) and closed with a clog of vacuum grease (Leybonol, LVO 810 Lithelen). Measurements were taken every 20 K starting at room temperature up to 1000 °C, with a heating rate of 5 K/min.

Solid-state magic angle spinning (MAS) NMR methods: NMR spectra were collected on ^{6}Li, ^{7}Li, and ^{31}P with a DSX AVANCE spectrometer (Bruker) with a magnetic field of 11.7 T. The $Li_{5+x}P_2O_{6-x}N_{1+x}$ sample was filled into a rotor with a diameter of 2.5 mm, which was mounted on a commercial MAS probe (Bruker) and spun with a rotation frequency of 25 kHz. The obtained data was analyzed using device-specific software.[9]

Fourier-transform infrared (FTIR) spectroscopy: FTIR measurements were performed on a woodpecker cell with a window of CsBr using a Vertex-80V-FTIR spectrometer by Bruker. Data was collected at room temperature under static vacuum (ca. 5 mbar) in the range of400–4000 cm^{-1} Data was acquired using OPUS 6.5[10] and illustrated using Origin.[11]

Elemental analysis: Energy-dispersive X-ray spectroscopy (EDX): EDX measurements were performed at a Dualbeam Helios Nanolab G3 UC (FEI) scanning electron microscope featuring an EDX detector (X-Max 80 SDD, Oxford instruments). The samples were positioned on adhesive carbon pads. A conductive carbon film was applied using a high-vacuum sputter coater (BAL-TEC MED 020, BalTec A). Multiple particles were targeted using an accelerating voltage of 20 kV.
Inductively coupled plasma optical emission spectrometry (ICP OES): Elemental analysis was conducted at a Varian Vista RL with a 40 MHz RF generator, and a VistaChip CCD detector.
Mass spectrometry: CHNS spectrometry was performed using a Vario MICRO Cube device (Elementar, Langenselbold, Germany).

Ionic conductivity measurements: Electrochemical impedance spectroscopy (EIS) was performed using an Ivium compactstat.h potentiostat (24 bit instrument) in a two-electrode setup with a RHD Instruments Microcell HC cell stand loaded with a RHD Instruments TSC battery cell. Before EIS measurements were carried out, all samples were thoroughly ground in an agate mortar and subsequently compacted into pills with a thickness of about 0.3 mm and a diameter of 5 mm using uniaxial cold-pressing ($p \approx 2$ t). To ensure good contact during EIS, all pills were sputtered with ruthenium metal using a Quorum Q150 GB sputter coater. All samples were measured in the frequency range of 1 MHz–0.1 Hz and an excitation voltage of 100 mV. Temperature-dependent data was gathered from 25–75 °C in 5 °C steps and an equilibration time of 1 h. All samples were prepared and measured in an argon-filled glovebox (MB200, MBraun, Garching, $O_2 < 0.1$ ppm, $H_2O < 1$ ppm). Data analysis and fitting procedures were carried out with the software RelaxIS3 (RHD instruments, Darmstadt).

A.2. Results and Discussion

A.2.1. Structure determination, additional crystallographic data, and Rietveld refinement

The crystal structure of $Li_{5+x}P_2O_{6-x}N_{1+x}$ was determined with complementary analysis of single-crystal and powder X-ray diffraction (scXRD and PXRD). Due to small crystallite size, no data set with sufficient quality could be acquired from scXRD. However, the monoclinic P crystal system and cell parameters could be determined from scXRD and were used for structure solution from powder data. Since the space group type $P2_1/c$ can be determined unambiguously in the reciprocal lattice, this space group was assumed. To eliminate the possibility of overlooked or pseudo symmetry, the structure was solved in all eight possible monoclinic P space group types, as well as in $P\bar{1}$ and results were compared.

Structure solution in $P\bar{1}$ yielded a sensible model, which was subjected to the ADDSYM routine in Platon.[12] Due to the weaker scattering, Li positions could not be definitely located. Thus, using the model including Li atomic positions, no higher symmetry could be found. Upon removal of Li positions, ADDSYM resulted in the space group P21/c.

With the cell parameters obtained from scXRD data, Pawley fits were executed in all eight monoclinic P space group types ($P2$, $P2_1$, Pm, Pc, $P2/m$, $P2_1/m$, $P2/c$, $P2_1/c$) using TOPAS 6.[3–5] Peak broadening effects and side phases were fitted during Pawley fitting. Structures were solved using charge flipping.[6,7] Models were compared and those with plausible structural motifs ($P2_1$ and $P2_1/c$) were refined.

The Platon routine "expand to $P1$" was used to enable comparison of the structures with the COMPSTRU routine at the Bilbao Crystallographic Server. This yielded no compatible normalizer of the structures, which is probably due to Li atomic positions, which could not be localized unambiguously. Reintroduction of the $P2_1$ model into the ADDSYM routine yielded the space group type $P2_1/c$ if no Li positions were considered. Li atomic positions were found using difference electron density maps generated with TOPAS 6.

Refinement of the $P2_1$ model yielded improbably long and short P–N and P–O distances, respectively, whereas atomic distances in the $P2_1/c$ model were plausible and well within the range of other known P–N/O distances in LiPON phases.[13–16] Values for refinement quality criteria were much lower for $P2_1/c$ than for $P2_1$. With all these indications toward $P2_1/c$ we are confident this is the correct space group.

Deposition Number CSD 2191662 https://www.ccdc.cam.ac.uk/services/structures?id=doi:10.1002/-chem.202202984 contains the supplementary crystallographic data for this paper. These data are provided free of charge by the joint Cambridge Crystallographic Data Centre and Fachinformationszentrum Karlsruhe http://www.ccdc.cam.ac.uk/structures.

Table A.1.: Wyckoff positions, atomic coordinates, and equivalent displacement parameters (in $Å^2$) of $Li_{5+x}P_2O_{6-x}N_{1+x}$ obtained from powder X-ray diffraction at room temperature. Standard deviations in parentheses.

Atom	Wyckoff position	x	y	z	U_{eq}
P1	4e	0.2990(5)	0.2000(7)	0.0205(9)	0.0038
P2	4e	0.0948(4)	0.2808(8)	0.4305(8)	0.0038
P3	4e	0.7955(4)	0.3019(7)	0.0196(9)	0.0038
P4	4e	0.5908(4)	0.2167(8)	0.4369(9)	0.0038
N1	4e	0.2017(10)	0.2047(17)	0.474(2)	0.0038
N2	4e	0.3095(9)	0.7861(17)	0.026(2)	0.0038
O1	4e	0.3053(9)	0.3992(14)	0.3768(19)	0.0114
O2	4e	0.3813(7)	0.3187(12)	0.0714(14)	0.0114
O3	4e	0.3065(10)	0.1027(16)	0.1751(18)	0.0114
O4	4e	0.0749(9)	0.3872(17)	0.2943(15)	0.0114
O5	4e	0.0945(7)	0.1304(13)	0.0928(13)	0.0114
O6	4e	0.022(1)	0.1555(15)	0.4151(18)	0.0114
O7	4e	0.1385(7)	0.6816(12)	0.4525(14)	0.0114
O8	4e	0.7957(10)	0.3968(14)	0.1688(18)	0.0114
O9	4e	0.1999(10)	0.6120(14)	0.1221(17)	0.0114
O10	4e	0.5764(7)	0.3831(13)	0.0712(14)	0.0114
O11	4e	0.5285(10)	0.3420(14)	0.4113(19)	0.0114
O12	4e	0.5697(10)	0.1155(16)	0.2801(16)	0.0114
Li1	4e	0.3924(19)	0.254(3)	0.314(4)	0.0038
Li2	4e	0.0056(18)	0.270(3)	0.122(4)	0.0038
Li3	4e	0.1146(19)	0.783(3)	0.162(3)	0.0038
Li4	4e	0.283(2)	0.468(4)	0.144(4)	0.0038
Li5	4e	0.577(2)	0.006(4)	0.122(4)	0.0038
Li6	4e	0.0391(16)	0.540(3)	0.389(3)	0.0038
Li7	4e	0.226(2)	0.542(4)	0.340(4)	0.0038
Li8	4e	0.6281(16)	0.451(3)	0.369(3)	0.0038
Li9	4e	0.1971(18)	0.249(3)	0.236(4)	0.0038
Li10	4e	0.085(2)	0.484(4)	0.091(4)	0.0038

Table A.2.: Selected interatomic distances [Å] occurring in $Li_{5+x}P_2O_{6-x}N_{1+x}$ obtained from powder X-ray diffraction at room temperature. Standard deviations are given in parentheses.

P1–	N1	1.686(17)	O1–	Li7	1.80(4)	O6–	Li2	2.06(4)
	O1	1.624(18)		Li5	2.06(4)		Li10	2.08(4)
	O2	1.660(13)		Li4	2.11(4)		Li10	2.31(4)
	O3	1.644(18)		Li1	2.11(4)		Li3	2.33(3)
P2–	N1	1.717(16)		Li9	2.28(3)		Li2	2.78(4)
	O4	1.553(16)		Li8	2.63(3)	O7–	Li6	1.99(3)
	O5	1.681(14)	O2–	Li1	2.20(4)		Li3	2.03(3)
	O6	1.620(17)		Li4	2.30(4)		Li2	2.26(3)
P3–	N2	1.745(15)		Li1	2.45(4)		Li7	2.31(4)
	O7	1.510(13)	O3–	Li8	1.88(3)		Li3	2.69(3)
	O8	1.614(18)		Li1	2.11(3)	O8–	Li3	2.03(3)
	O9	1.530(17)		Li9	2.36(4)	O9–	Li4	1.85(4)
P4–	N2	1.597(15)	O4–	Li6	1.86(3)		Li7	1.98(4)
	O10	1.600(15)		Li2	1.95(3)		Li10	2.09(4)
	O11	1.515(16)		Li10	2.08(4)		Li3	2.19(3)
	O12	1.659(16)		Li9	2.46(3)	O10–	Li8	2.62(3)
N1–	Li9	2.14(4)		Li7	2.67(4)	O11–	Li8	1.96(3)
	Li4	2.35(4)	O5–	Li2	1.98(3)		Li1	2.16(3)
	Li9	2.39(4)		Li9	2.05(3)		Li5	2.21(4)
N2–	Li8	1.95(3)		Li6	2.25(3)		Li5	2.33(4)
	Li7	2.43(4)		Li6	2.42(30)	O12–	Li5	1.79(4)

Table A.3.: Selected interatomic angles [°] occurring in $Li_{5+x}P_2O_{6-x}N_{1+x}$ obtained from powder Xray diffraction at room temperature. Standard deviations are given in parentheses.

P1	–N1–	P2	121.2(10)	O7	–P3–	O8	117.61(8)
P4	–N2–	P3	125.7(10)	O7		O9	111.8(8)
O1	–P1–	O2	114.5(8)	O7		N2	100.0(8)
O1		O3	108.1(9)	O8		O9	112.0(9)
O1		N1	112.3(9)	O8		N2	104.8(9)
O2		O3	107.9(8)	O9		N2	109.4(9)
O2		N1	102.6(8)	O10	–P4–	O11	112.6(8)
O3		N1	111.3(9)	O10		O12	103.5(8)
O4	–P2–	O5	106.2(7)	O10		N2	115.2(8)
O4		O6	117.4(9)	O11		O12	112.9(9)
O4		N1	114.7(9)	O11		N2	101.6(9)
O5		N1	105.3(8)	O12		N2	111.3(9)
O5		O6	106.6(8)	O6		N1	105.6(9)

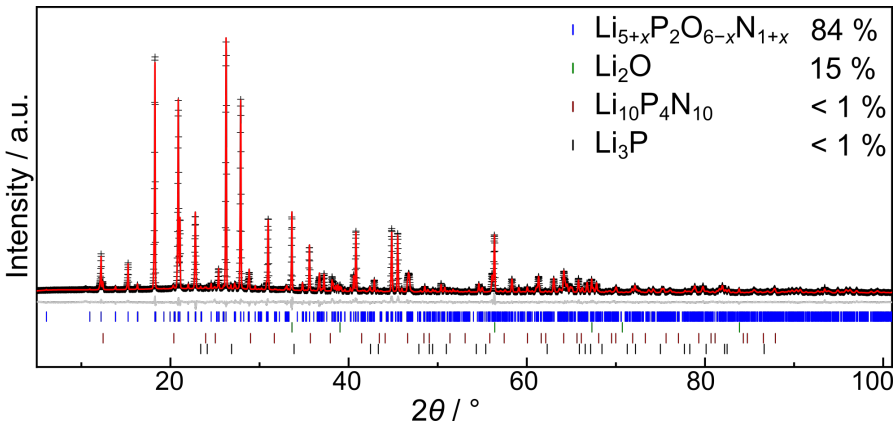

Figure A.1.: Rietveld refinement for $Li_{5+x}P_2O_{6-x}N_{1+x}$ with observed (black crosses, Cu-$K_{\alpha 1}$), and calculated (red) intensities. The difference profile is shown in gray. Positions of Bragg reflections for $Li_{5+x}P_2O_{6-x}N_{1+x}$, Li_2O, $Li_{10}P_4N_{10}$, and Li_3P are shown with blue, green, brown and black vertical bars, respectively.

A.2.2. NMR

The value for x was calculated from the area ratio of the fitted peaks in the ^{31}P NMR spectrum. With an initial relative error of 2 % of the areas, an overall relative error of 4 % results in the quotient, yielding $x = 0.94(4)$ for this sample. The phase width indicated by x is estimated to be much larger, but could not be assessed in detail. The synthesis is very sensitive and changes in parameters result in side phases like $Li_{10}P_4N_{10}$, leading to overlapping NMR signals that cannot be deconvoluted. The ^{6}Li NMR spectrum shows a single broad signal with a peak at 1.15 ppm. A shoulder at 1.8 ppm is visible. Mobility of Li^+ ions leads to exposition to the same environment. Thus, with increasing mobility the signals move closer together and narrow. High mobility would lead to a single sharp signal.[17,18] The environments the ions are exposed to vary and the mobility is low, which leads to a strong overlap of the signals. In the ^{7}Li NMR spectrum, a single broad signal with a full width at half maximum (FWHM) of 5 ppm is visible. Additional signals are not visible when compared to noise levels.

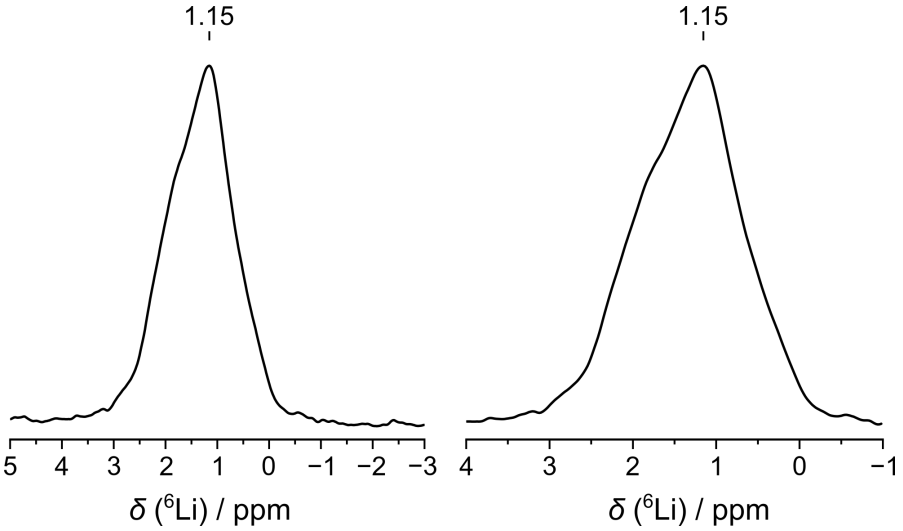

Figure A.2.: ^{6}Li measurement (left) with close-up (right). The broad signals point towards very low mobility of Li^+ ions.

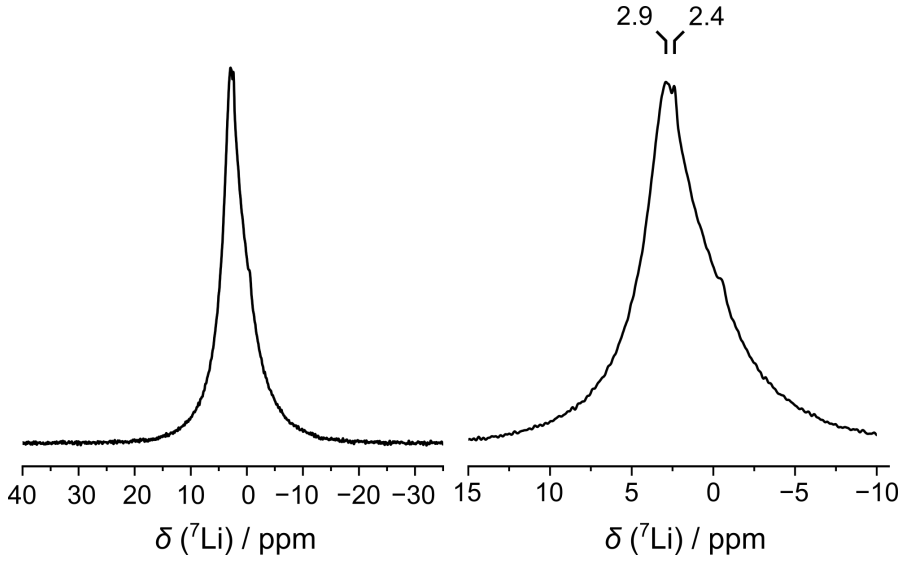

Figure A.3.: ^{7}Li measurement (left) with close-up (right). The broad signals point towards very low mobility of Li^{+} ions.

A.2.3. Additional information on electron-dispersive X-ray diffraction (EDX) measurements

EDX measurements were taken to confirm that no other elements besides Li, P, O, and N are present in the sample. However, light elements cannot (Li) or not reliably (O, N) be detected. Furthermore, the sample is prone to hydrolysis, which confounds O values. At 30 % of the mass in the sample used for EDX measurements, Li_2O constituted a molar fraction of 75 % of the sample. P, O, and N were measured and their values compared (Table A.4). The content of O in the sample is lower (40(2) instead of 67 %), whereas the content of N is much higher (38(2) instead of 11 %) than expected. These values suggest that large amounts of N are incorporated additionally to the bridging atom. The observed ratio, normalized to P and balanced with Li, results in the sum formula $Li_{7.4}P_2O_{3.6}N_{3.4}$. Additional incorporation, as suggested by EDX values, is corroborated by NMR signals showing more than one signal. However, NMR shift suggests only one additional N per dimer, which can only result in a maximum of $x = 1$. Thus, this EDX measurement must be seen as only a gross approximation.

Table A.4.: EDX (SEM) measurements of $Li_{5+x}P_2O_{6-x}N_{1+x}$ (in atom-%).

Point	P	O	N
1	21	40	39
2	20	42	38
3	22	41	37
4	24	38	38
5	18	43	39
6	23	36	41
7	25	38	37
8	22	38	39
9	19	41	39
10	25	39	36
11	24	39	37
12	20	41	38
average	22(2)	40(2)	38(2)
calculated	22	67	11
relative difference / %	−1	−41	+249

A.2.4. Additional information on elemental analysis (ICP-OES)

Inductively coupled plasma optical emission spectroscopy (ICP-OES) was performed. Since the sample is prone to hydrolysis, no absolute values can be obtained. Furthermore, the measurements had to be taken on samples which consisted of $Li_{5+x}P_2O_{6-x}N_{1+x}$, Li_2O, and $Li_{10}P_4N_{10}$. Respective percentages were determined with Rietveld refinements using TOPAS 6 and are listed in Table Table A.7.[2,6,7] These percentages were considered in the calculation of expected Li : P ratios for $x = 0$ and $x = 0.9$ as listed below and compared to measured values. The calculated Li : P ratio for $x = 0$ deviates by 26(3) % from the expected value, whereas with $x = 0.9$, as determined with NMR, a deviation of 18(3) % results (Table A.5).

Table A.5.: Respective percentages for $Li_{5+x}P_2O_{6-x}N_{1+x}$, Li_2O, and $Li_{10}P_4N_{10}$ in the samples for ICP-OES measurements. Expected and measured Li : P ratios are calculated for respective compositions.

Sample	$Li_{5+x}P_2O_{6-x}N_{1+x}$	Li_2O	$Li_{10}P_4N_{10}$	Li : P ratio		
				calc. $x = 0$	measured	calc. $x = 0.9$
1	74	16	10	0.85	1.096	0.94
2	70	20	10	0.94	1.306	1.03

A.2.5. Additional information on elemental analysis (CHNS)

Elemental analysis was conducted on a sample which consists to 70 % of the mass of $Li_{5+x}P_2O_{6-x}N_{1+x}$ and 30 % of Li_2O. With these values, an expected value of 6.8 % for $Li_{5+x}P_2O_{6-x}N_{1+x}$ $x = 0$ results. With $x = 0.9$ as determined with NMR, an expected value of 12.6 % results. The measured value of 13.05 % corresponds to $x = 0.97$, which is within the error margin of the result obtained from NMR. However, as the measured percentage of H in the sample is 1.24 %, the sample probably hydrolyzed during the weighing of the sample, confounding the measurement. The elevated value for N, however, indicates that more than one N per formula unit was incorporated in the structure. NMR values are considered much more reliable than the CHNS values obtained.

Table A.6.: Elemental analysis (CHNS) of $Li_{5+x}P_2O_{6-x}N_{1+x}$ (in wt-%).

element	measured	expected $x = 0/x = 0.9$
C	0	0
H	1.24	0
N	13.05	6.8 / 12.6
S	0	0

A.2.6. Additional information on electrochemical impedance spectroscopy (EIS)

Since no phase pure samples of $Li_{5+x}P_2O_{6-x}N_{1+x}$ are available, the EIS data of two different exemplar samples of $Li_{5+x}P_2O_{6-x}N_{1+x}$ are shown here. The phase compositions of the two samples were obtained through Rietveld refinements and are listed in Table A.7. All samples of $Li_{5+x}P_2O_{6-x}N_{1+x}$ contained varying amounts of Li_2O, and $Li_{10}P_4N_{10}$ as minor side phases. The temperature-dependent EIS spectra of sample 1 and 2 are shown in Figures A.4 and A.5. All spectra were fitted with an R1/CPE1-R2/CPE2-CPE3 model. The total activation energy for both samples was calculated by fitting the temperature dependent data to a linear Arrhenius type behavior. The Arrhenius plots are shown in Figure A.6. The bulk (R1) and total (R1+R2) ionic conductivities at 25 °C and 75 °C, and the activation energies of both samples are shown in Table A.8. The capacities of CPE1 and CPE2 at 25 °C and 75 °C of both samples were calculated using the Brug formula and are listed in Table A.9.[19]

Table A.7.: Phase compositions obtained from Rietveld refinement of two different samples of $Li_{5+x}P_2O_{6-x}N_{1+x}$ used for EIS measurements.

Phase	Phase content Sample 1 / wt-%	Phase content Sample 2 / wt-%
$Li_{5+x}P_2O_{6-x}N_{1+x}$	75	75
Li_2O	16	11
$Li_{10}P_4N_{10}$	9	14

Table A.8.: Bulk and total ionic conductivities at 25 °C and 75 °C and activation energies of two different samples of $Li_{5+x}P_2O_{6-x}N_{1+x}$.

Sample	25 °C		75 °C		E_a / eV
	σ_{bulk} S cm^{-1}	σ_{total} S cm^{-1}	σ_{bulk} S cm^{-1}	σ_{total} S cm^{-1}	
1	2.2×10^{-7}	4.6×10^{-8}	1.4×10^{-6}	6.8×10^{-7}	0.52
2	2.6×10^{-7}	2.7×10^{-8}	1.2×10^{-6}	4.1×10^{-7}	0.52

Table A.9.: Capacities of CPE1 and CPE2 at 25 °C and 75 °C of two different samples of $Li_{5+x}P_2O_{6-x}N_{1+x}$.

Sample	25 °C		75 °C	
	C_{CPE1} / F	C_{CPE2} / F	C_{CPE1} / F	C_{CPE2} / F
1	3.7×10^{-11}	7.1×10^{-11}	2.9×10^{-11}	1.1×10^{-10}
2	3.7×10^{-11}	5.9×10^{-11}	3.2×10^{-11}	9.1×10^{-11}

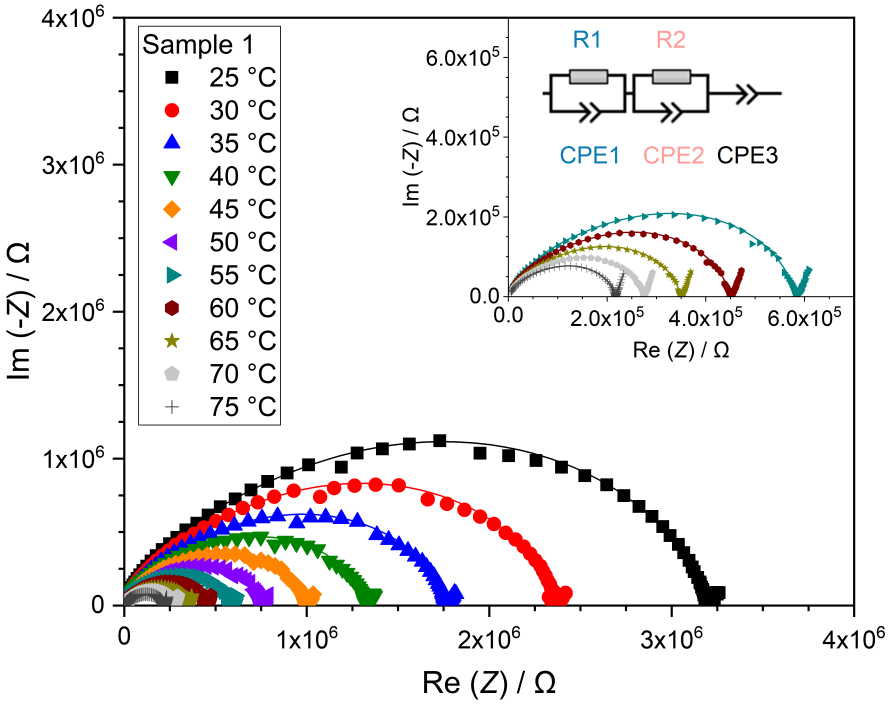

Figure A.4.: Nyquist plot of temperature-dependent EIS measurements of Sample 1 of $Li_{5+x}P_2O_{6-x}N_{1+x}$ from 25–75 °C. The inset shows an enlarged portion of the Nyquist plot up to $7.0 \times 10^5\,\Omega$. All spectra were modelled with a R1/CPE1-R2/CPE2-CPE3 model.

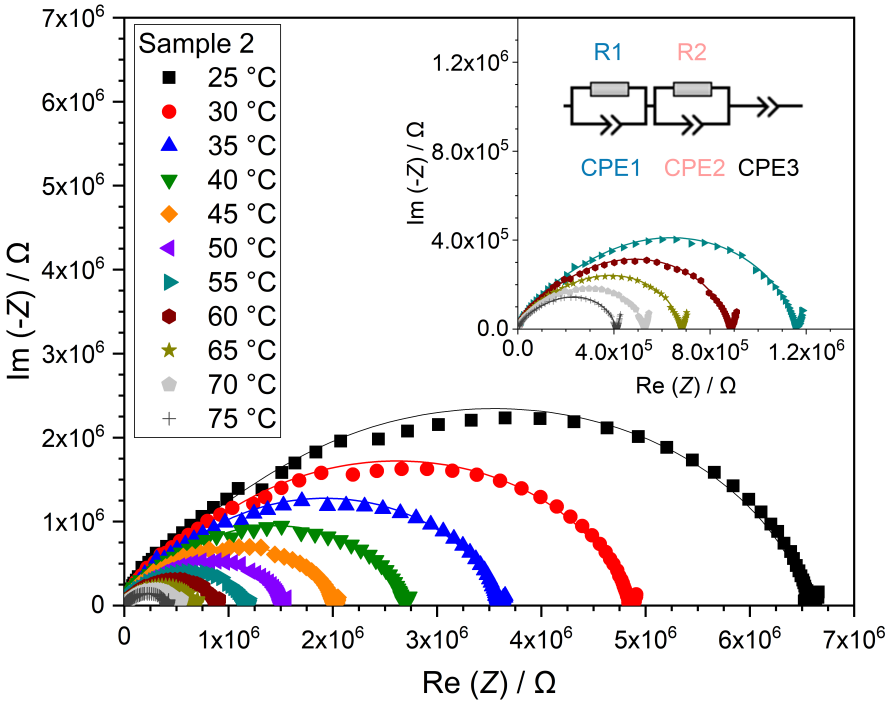

Figure A.5.: Nyquist plot of temperature-dependent EIS measurements of Sample 2 of $Li_{5+x}P_2O_{6-x}N_{1+x}$ from 25–75 °C. The inset shows an enlarged portion of the Nyquist plot up to $1.4 \times 10^6\,\Omega$. All spectra were modelled with a R1/CPE1-R2/CPE2-CPE3 model.

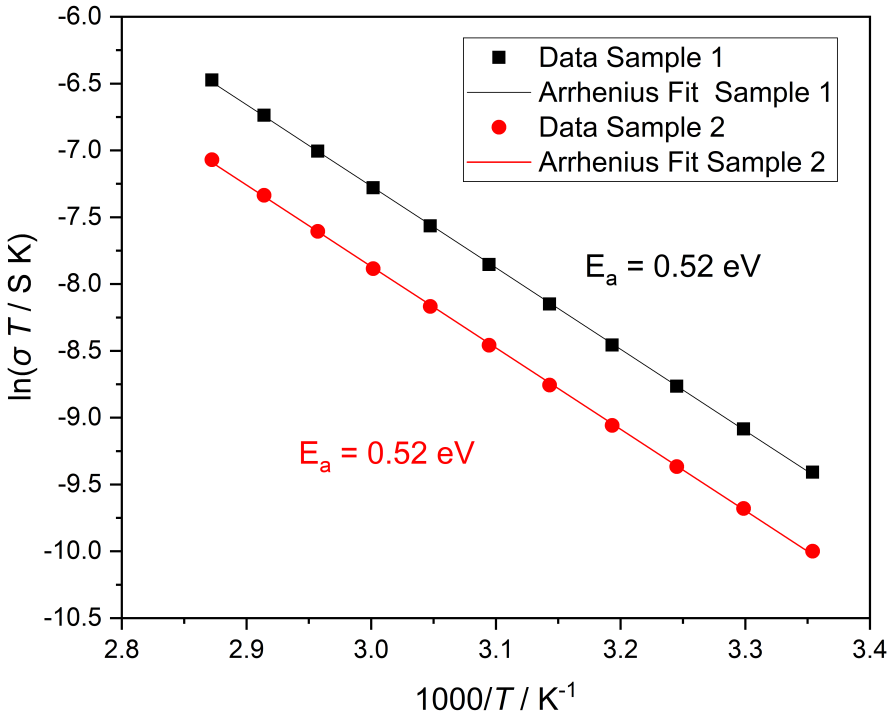

Figure A.6.: Arrhenius plots and total activation energies of Sample 1 and Sample 2 of $Li_{5+x}P_2O_{6-x}N_{1+x}$. This is a corrected version of the figure according to a submitted corrigendum.

A.3. Author Contributions

Stefanie Schneider Conceptualization: Equal; Formal analysis: Lead; Investigation:Lead; Validation: Equal; Visualization: Lead; Writing – original draft: Lead; Writing – review & editing: Lead
Lucas G. Balzat Formal analysis: Supporting; Investigation: Supporting; Validation: Supporting; Visualization: Supporting; Writing – original draft: Supporting; Writing – review & editing: Supporting
Bettina V. Lotsch Conceptualization: Supporting; Funding acquisition: Equal; Methodology: Supporting; Project administration: Supporting; Resources: Equal; Supervision: Equal; Writing – original draft: Supporting; Writing – review & editing: Supporting
Wolfgang Schnick Conceptualization: Equal; Funding acquisition: Equal; Project administration: Lead; Resources: Equal; Supervision: Lead; Validation: Equal; Writing – original draft: Supporting; Writing – review & editing: Supporting

A.4. References

[1] A. Stock, B. Hoffmann, *Ber. Dtsch. Chem. Ges.* **1903**, *36*, 314–319, DOI 10.1002/cber.19030360170.

[2] A. A. Coelho, *TOPAS Academic version 6*, Coelho Software, Brisbane, Australia, **2016**.

[3] G. Oszlányi, A. Sütő, *Acta Crystallogr. A* **2004**, *60*, 134–141, DOI 10.1107/S0108767303027569.

[4] G. Oszlányi, A. Sütő, *Acta Crystallogr. A* **2008**, *64*, 123–134, DOI 10.1107/S0108767307046028.

[5] A. A. Coelho, *Acta Crystallogr. A* **2007**, *63*, 400–406, DOI 10.1107/S0108767307036112.

[6] R. W. Cheary, A. A. Coelho, *J. Appl. Crystallogr.* **1992**, *25*, 109–121, DOI 10.1107/S0021889891010804.

[7] R. W. Cheary, A. A. Coelho, J. P. Cline, *J. Res. Natl. Inst. Stan.* **2004**, *109*, 1–25, DOI 10.6028/jres.109.002.

[8] Bruker, *APEX3 v2018.1-0*, **2018**.

[9] Bruker, *Topspin v.3.0 pl 3*, Bruker Biospin GmbH, Germany, **2010**.

[10] Bruker, *OPUS 6.5*, Bruker Optik GmbH, Ettlingen, Germany, **2007**.

[11] *Origin Pro 2018G*, Origin Lab Corporation, Northampton, USA, **2018**.

[12] A. L. Spek, *Acta Crystallogr. D* **2009**, *65*, 148–155, DOI 10.1107/S090744490804362X.

[13] B. Wang, B. C. Chakoumakos, B. C. Sales, B. S. Kwak, J. B. Bates, *J. Solid State Chem.* **1995**, *115*, 313–323, DOI 10.1006/jssc.1995.1140.

[14] D. Baumann, W. Schnick, *Eur. J. Inorg. Chem.* **2015**, 617–621, DOI 10.1002/ejic.201403125.

[15] K. Senevirathne, C. S. Day, M. D. Gross, A. Lachgar, N. A. Holzwarth, *Solid State Ionics* **2013**, *233*, 95–101, DOI 10.1016/j.ssi.2012.12.013.

[16] P. López-Aranguren, M. Reynaud, P. Głuchowski, A. Bustinza, M. Galceran, J. M. López Del Amo, M. Armand, M. Casas-Cabanas, *ACS Energy Lett.* **2021**, *6*, 445–450, DOI 10.1021/acsenergylett.0c02336.

[17] R. Böhmer, K. R. Jeffrey, M. Vogel, *Prog. Nucl. Magn. Reson. Spectrosc.* **2007**, *50*, 87–174, DOI 10.1016/j.pnmrs.2006.12.001.

[18] A. Kuhn, V. Duppel, B. V. Lotsch, *Energy Environ. Sci.* **2013**, *6*, 3548–3552, DOI 10.1039/c3ee41728j.

[19] G. J. Brug, A. L. van den Eeden, M. Sluyters-Rehbach, J. H. Sluyters, *J. Electroanal. Chem.* **1984**, *176*, 275–295, DOI 10.1016/S0022-0728(84)80324-1.

B. Supporting Information for Chapter 4 ($Li_{27-x}[P_4O_{7+x}N_{9-x}]O_3$)

Stefanie Schneider, Eva-Maria Wendinger, Volodymyr Baran, Anna-Katharina Hatz, Bettina V. Lotsch, Markus Nentwig, Oliver Oeckler, Thomas Bräuniger, and Wolfgang Schnick

Chem. Eur. J. **2023**, *29*, e202300174.

Reprinted (adapted) with permission from Chemistry – European Journal. Copyright 2023

Abstract The Li^+ ion conductor $Li_{27-x}[P_4O_{7+x}N_{9-x}]O_3$ ($x \approx 1.9(3)$) has been synthesized from P_3N_5, Li_3N and Li_2O in a Ta ampoule at 800 °C under Ar atmosphere. The cubic compound crystallizes in space group $I\bar{4}3d$ with $a = 12.0106(14)$ Å and $Z = 4$. It contains both non-condensed $[PO_2N_2]^{5-}$ and $[PO_3N]^{4-}$ tetrahedra as well as O^{2-} ions, surrounded by Li^+ ions. Charge neutrality is achieved by partial occupancy of Li positions, which was refined with neutron powder diffraction data. Measurements of the partial ionic and electronic conductivity show a total ionic conductivity of 6.6×10^{-8} S cm^{-1} with an activation energy of 0.46(2) eV and a bulk ionic conductivity of 4×10^{-6} S cm^{-1} at 25 °C, which is close to the ionic conductivity of amorphous lithium nitridophosphate. This makes $Li_{27-x}[P_4O_{7+x}N_{9-x}]O_3$ an interesting candidate for investigation of structural factors affecting ionic conductivity in lithium oxonitridophosphates.

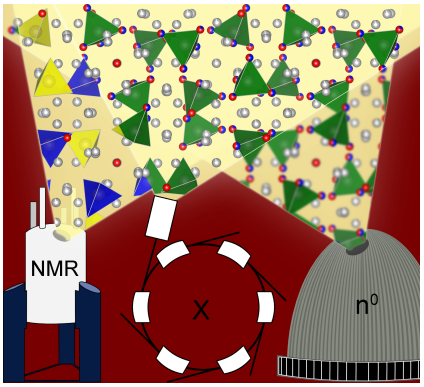

B.1. Experimental Procedures

Synthesis of P_3N_5: P_3N_5 was synthesized according to literature.[1] P_4S_{10} (Acros Organic, > 99.8 %) was placed in a dry silica glass tube within a silica glass tube. After saturation with NH_3 (Air Liquide, 99.999 %) for 4 h, the starting material was heated to 800 °C with a rate of 300 K h^{-1}, kept at this temperature for 4 h and cooled with a rate of 300 K h^{-1} in NH_3 gas flow. The orange product was then washed with H_2O, EtOH, and acetone, and dried.

Synthesis of $Li_{27-x}[P_4O_{7+x}N_{9-x}]O_3$: All work was performed under Ar atmosphere in a glovebox (Unilab, MBraun, Garching, O_2 < 1 ppm, H_2O < 1 ppm). P_3N_5 (34.7 mg, 0.213 mmol), Li_3N (Rockwood Lithium, 99.99 %, 11.1 mg, 0.320 mmol), and Li_2O (Alfa Aesar, 99.5 %, 54.1 mg, 1.81 mmol) were added together in a molar 2 : 4 : 17 ratio and ground thoroughly in an agate mortar. The mixture was transferred to a dry Ta crucible placed in a silica tube under Ar counterflow. The ampoule was sealed using an oxyhydrogen burner (all gasses: Air Liquide, 99.999 %). The silica ampoule was heated with a rate of 300 K h^{-1}, held at 800 °C for 90 h and cooled to room temperature with a rate of 300 K h^{-1}. The light gray product was washed with EtOH (5 mL) under Ar atmosphere.

Single-crystal X-ray diffraction: Single-crystal X-ray diffraction data were obtained using synchrotron radiation with a wavelength of λ = 0.2947 Å at ESRF beamline ID11. Semiempirical absorption correction was performed with SADABS.[2] The structure was solved with SHELXS using direct methods and refined with SHELXL.[3] Deposition Number(s) 2204799, 2204800 contain(s) the supplementary crystallographic data for this paper. These data are provided free of charge by the joint Cambridge Crystallographic Data Centre and Fachinformationszentrum Karlsruhe Access Structures service.

Powder X-ray diffraction: The product was sealed into a glass capillary ($\oslash$ = 0.5 mm, wall thickness 0.1 mm, Hilgenberg GmbH) and investigated using a Stoe STADI P diffractometer with Cu $K_{\alpha1}$ radiation (λ = 1.5406 Å), Ge(111) monochromator and a Mythen 1 K detector in parafocusing Debye–Scherrer geometry. Rietveld refinements were performed using TOPAS 6.[4–6]
For temperature-dependent powder X-ray data, Mo $K_{\alpha1}$ radiation (λ = 0.709 30 Å) with a Ge(111) monochromator was used to record data with a Stoe STADI P and an image plate position sensitive detector. Patterns were recorded in steps of 20 K, starting from room temperature up to 1000 °C with a heating rate of 15 K min^{-1}.

Solid-state magic angle spinning (MAS) NMR methods: NMR data for ^1H, ^6Li, ^7Li, and ^{31}P were obtained using a DSX Advance spectrometer (Bruker). The sample was packed into a rotor ($\oslash$ = 2.5 mm), mounted on a commercial MAS probe (Bruker) and spun with a frequency of 25 kHz. The obtained data was analyzed using device-specific software.[7]

Neutron powder diffraction: The product was packed in a vanadium container ($\oslash = 3\,\mathrm{mm}$) with an indium seal to protect the sample against humidity in the atmosphere. Neutron powder diffraction data has been collected at the instrument SPODI at the neutron source FRM II (Garching b. München, Germany) within a Rapid Access Program.[8] The measurement was performed in Debye-Scherrer geometry with an incident neutron beam having a rectangular cross section of $40 \times 20\,\mathrm{mm}$ at the sample position. Monochromatic neutrons with a wavelength of 1.548 32(4) Å were chosen from the 551 reflection of a vertically focused composite Ge monochromator. High resolution neutron powder diffraction data were collected over a 2θ range from 1.0–151.9° using a detector consisting from 80 position-sensitive ^{3}He counting tubes covering an angular range of $2\theta = 160°$ and an effective height of 300 mm was used. The obtained data were analyzed and Rietveld refinements were performed using the program package TOPASAcademic.[4]

Fourier-transform infrared (FTIR) spectroscopy: FTIR measurements were performed at a Bruker FTIR Alpha II compact spectrometer equipped with a diamond ATR unit. The powder was measured under Ar atmosphere. The spectrum was measured from 400–4000 cm^{-1}.

Elemental analysis: Energy-dispersive X-ray (EDX) spectra were taken at a Dualbeam Helios Nanolab G3 UC (FEI) scanning electron microscope (SEM) featuring an EDX detector (X-Max 80 SDD, Oxford instruments). The sample was placed onto an adhesive carbon pad and coated with a conducting carbon film using a high-vacuum sputter coater (BAL-TEC MED 020, Bal Tec A).
Inductively coupled plasma optical emission spectroscopy (ICPOES): A Varian Vista RL with a 40 MHz RF generator was used with a VistaChip CCD detector to measure ICP-OES.
Combustion spectroscopy: A Vario MICRO Cube device (Elementar, Langenselbold, Germany) was used to measure the weight percentages of C, H, N, and S.

Determination of partial ionic and electronic conductivity: Electrochemical impedance spectroscopy and potentiostatic polarization measurements were performed with an Ivium compactstat.h (24 bit instrument) in a two-electrode setup using an rhd instruments Microcell HC cell stand loaded with rhd instruments TSC Battery cells. The samples were ground thoroughly and compacted to a pellet of about 0.5–1.0 mm thickness and 5 mm in diameter by uniaxial cold pressing (1000 MPa). The pellets showed relative densities of $80 \pm 5\,\%$. The pellets were sputtered with ruthenium as ion-blocking electrodes on both sides. The spectra were recorded in a frequency range of 1 MHz–0.01 Hz and an AC voltage of 100 mV was applied. Each sample was measured for several temperature cycles between −5 and 85 °C with 5 °C steps inside a glovebox under argon atmosphere. Analysis of the impedance spectra was carried out with the RelaxIS3 software from rhd instruments. Linearity, stability and causality were checked by the Kramers–Kronig relation before fitting the data. The samples were subsequently used for potentiostatic polarization measurements to extract the electronic partial conductivity at 25 °C. For these a voltage of 0.25, 0.50, 0.75 and 1.00 V was applied for 5–10 h each and the drop in resulting current measured. The resistance was calculated from the current measured at a steady state after several hours.

B.2. Results and Discussion

B.2.1. Additional crystallographic data (single-crystal X-ray diffraction)

Single-crystal data were acquired at beamline ID11 of the ESRF in Grenoble from a crystal chosen from a heterogeneous sample. When refined from single-crystal data, occupations of O1/N1 and O2/N2 converge toward ≈ 20 % N and ≈ 50 % N, respectively. However, as X-ray diffraction is not sufficient to discriminate O and N, mixed occupations of O/N positions and site occupancies of Li positions were refined using neutron data.

Table B.1.: Wyckoff positions, atomic coordinates, and equivalent displacement parameters (in $Å^2$) of $Li_{27-x}[P_4O_{7+x}N_{9-x}]O_3$ obtained from single-crystal X-ray diffraction at room temperature. Standard deviations in parentheses.

Atom	Wyckoff position	*s.o.f.*	x	y	z	U_{eq}
P1	16c		0.84138(2)	= x	= x	0.00906(10)
N1 / O1	16c	0.19 / 0.81	0.91884(8)	= x	= x	0.0168(3)
N2 / O2	48e	0.53 / 0.47	0.89934(9)	0.83399(10)	0.72212(8)	0.0192(2)
O3	12a		1/8	0	3/4	0.0149(3)
Li1	12b	0.929	5/8	0	3/4	0.0178(9)
Li2	48e	0.929	0.7957(3)	0.7527(3)	0.6075(3)	0.0263(6)
Li3	48e	0.929	0.9443(3)	0.6425(3)	0.8001(4)	0.0384(8)

Table B.2.: Anisotropic displacement parameters (in $Å^2$) of $Li_{27-x}[P_4O_{7+x}N_{9-x}]O_3$ as obtained from single-crystal X-ray diffraction at room temperature, standard deviations in parentheses.

Atom	U_{11}	U_{22}	U_{33}	U_{12}	U_{13}	U_{23}
P1	0.00906(10)	$= U11$	$= U11$	0.00005(8)	$= U12$	$= U12$
N1 / O1	0.0168(3)	$= U11$	$= U11$	−0.0035(3)	$= U12$	$= U12$
N2 / O2	0.0204(4)	0.0254(5)	0.0118(3)	−0.0002(4)	0.0049(3)	−0.0013(3)
O3	0.0134(7)	0.0157(4)	0.0157(4)	0	0	0
Li1	0.016(2)	0.0185(13)	0.0185(13)	0	0	0
Li2	0.0263(13)	0.0268(13)	0.0259(13)	−0.0030(11)	0.0036(11)	0.0009(11)
Li3	0.0309(17)	0.042(2)	0.0428(19)	−0.0133(14)	0.0125(14)	−0.0191(16)

Table B.3.: Selected interatomic distances (in Å) occurring in $Li_{27-x}[P_4O_{7+x}N_{9-x}]O_3$ obtained from single-crystal X-ray diffraction at room temperature, standard deviations in parentheses.

P1–	N2/O2	(3×)	1.5951(10)	Li1–	Li2	(4×)	2.4630(36)
	N1/O1		1.6114(10)		Li3	(4×)	2.5568(40)
O/N1–	Li2	(3×)	1.970(4)	Li2–	Li3		2.3108(57)
	Li3	(3×)	2.298(4)		Li3		2.3399(51)
O/N2–	Li1		1.9596(11)		Li3		2.4363(51)
	Li3		2.023(4)		Li3		2.4474(52)
	Li2		2.097(4)		Li1		2.4630(36)
	Li3		2.118(4)		Li2		2.8059(51)
	Li2		2.132(4)		Li2	(2×)	2.9013(51)
	Li3		2.541(4)	Li3–	Li2		2.3108(57)
O3–	Li3	(4×)	1.996(4)		Li2		2.3399(51)
	Li2	(4×)	2.031(4)		Li2		2.4363(60)
					Li2		2.4474(52)
					Li1		2.5568(45)
					Li3		2.9083(51)

Table B.4.: Selected interatomic angles (in °) occurring in $Li_{27-x}[P_4O_{7+x}N_{9-x}]O_3$ obtained from single-crystal X-ray diffraction at room temperature, standard deviations in parentheses.

N2/O2	–P1–	N2/O2	(3×)	111.48(6)
N2/O2		N1/O1	(3×)	107.38(5)

B.2.2. Additional crystallographic data (X-ray data Rietveld refinement)

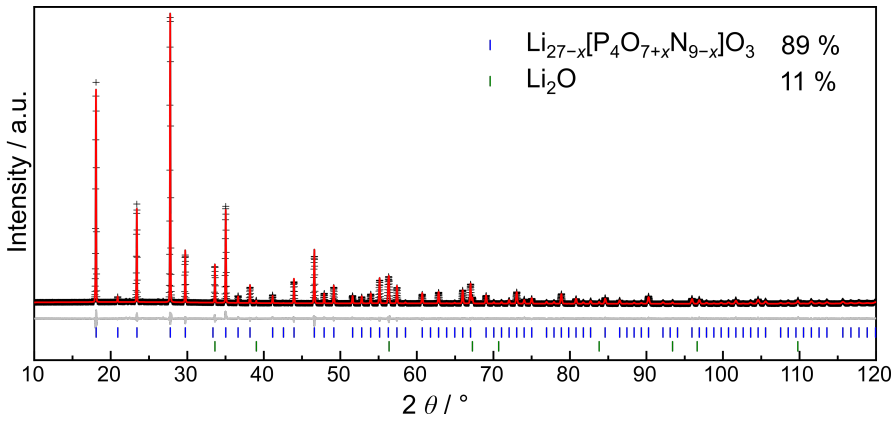

Figure B.1.: Rietveld refinement for $Li_{27-x}[P_4O_{7+x}N_{9-x}]O_3$ with observed (black crosses, Cu-$K_{\alpha 1}$ radiation), and calculated (red) intensities. The difference profile is shown in gray. Positions of Bragg reflections for $Li_{27-x}[P_4O_{7+x}N_{9-x}]O_3$ and Li_2O are shown with blue and green markers, respectively.

Table B.5.: Crystallographic data on the Rietveld refinement for $Li_{27-x}[P_4O_{7+x}N_{9-x}]O_3$ from powder X-ray diffraction data.

Formula	$Li_{27-x}[P_4O_{7+x}N_{9-x}]O_3$
Formula weight / $g\,mol^{-1}$	587.8
Crystal system; space group	cubic; $I\bar{4}3d$ (no. 220)
Lattice parameter / Å	12.0036(2)
Cell volume / $Å^3$	1729.54(7)
Formula units per unit cell	4
Density / $g\,cm^{-3}$	2.25772(9)
μ / mm^{-1}	0.5463(2)
Radiation	Cu-$K_{\alpha 1}$ ($\lambda = 1.540\,596$ Å)
2θ-range / °	$5 \leq 2\theta \leq 120$
Data points	7705
Total number of reflections	129
Refined parameters	40
Background function	shifted Chebyshev
Number of background parameters	12
Goodness of fit	3.298
R_p; R_{wp}	0.0515; 0.0717
R_{exp}; R_{Bragg}	0.0217; 0.0250

B.2.3. Additional crystallographic data (neutron data Rietveld refinement)

Rietveld refinement on neutron powder diffraction data can reveal the occupation of O/N positions. Free refinement of Li positions points to partial occupancy, but with respect to the data quality and the presence of side phases, free refinement of O/N and Li site occupancies requires too many parameters. Instead, for the sake of charge neutrality, site occupancies of Li positions was calculated as a function of O/N occupancy.[9] TOPAS 6 was used to perform Rietveld refinements.[4] O/N positions were constrained to full occupancy, vacancies are not considered.

$occ\ N-3$	$occN1$	0.19248‘_0.02711	(1)
$occ\ O-2$	$=1-occN1;$	: 0.80752‘_0.02711	(2)
$occ\ N-3$	$occN2$	0.52651‘_0.02559	(3)
$occ\ O-2$	$=1-occN2;$	: 0.47349‘_0.02559	(4)

The charge of each atomic position, excluding Li, is then defined using the *prm* instruction. As the occupation of O3 is 1 within the error margin, occupation of these positions was fixed to 1. The full charge of the positions is then calculated by multiplication of their occupation by their charge and their Wyckoff multiplicity (compare Table B.1).
To calculate the total anionic charge of both $[PO_2N_2]^{5-}$, $[PO_3N]^{4-}$, and O^{2-}, the defined parameters are added:

$$
\begin{aligned}
&prm\ chargeP1 && = occP1 * 5 * 16; && : 80 && (5)\\
&prm\ chargeN1 && = occN1 * -3 * 16; && : -9.23897\text{`}\_1.30143 && (6)\\
&prm\ chargeO1 && = (1 - occN1) * -2 * 16; && : -25.84069\text{`}\_0.86762 && (7)\\
&prm\ chargeN2 && = occN2 * -3 * 48; && : -75.81690\text{`}\_3.68512 && (8)\\
&prm\ chargeO2 && = (1 - occN2) * -2 * 48; && : -45.45540\text{`}\_2.45675 && (9)\\
&prm\ chargeO3 && = occO3 * -2 * 12; && : -24 && (10)
\end{aligned}
$$

$$
\begin{aligned}
&prm\ charge\_anion = chargeP1 + chargeN1 + chargeO1 + chargeN2 + && (11)\\
&chargeO2 + chargeO3; && : -100.35196\text{`}\_1.30273
\end{aligned}
$$

Since Li exhibits a charge of +1, the occupation of Li can then be calculated by division of the anionic charge by the overall amount of Li in a unit cell:

$$
\begin{aligned}
&prm\ occLi1 && = (charge\_anion/108) * -1; && : 0.92918\text{`}\_0.01206 && (12)\\
&prm\ occLi2 && = (charge\_anion/108) * -1; && : 0.92918\text{`}\_0.01206 && (13)\\
&prm\ occLi3 && = (charge\_anion/108) * -1; && : 0.92918\text{`}\_0.01206 && (14)
\end{aligned}
$$

The calculated occupation of Li positions was inserted within the site section. Due to data quality, the occupation of all Li positions was assumed the same, as their respective environments are similar.

$$
\begin{aligned}
&occ\ Li + 1 && = occLi1; && : 0.92918\text{`}\_0.01206 && (15)\\
&occ\ Li + 1 && = occLi2; && : 0.92918\text{`}\_0.01206 && (16)\\
&occ\ Li + 1 && = occLi3; && : 0.92918\text{`}\_0.01206 && (17)
\end{aligned}
$$

This calculation results in estimated standard deviations of about 1 % in Li positions and 3 % in O/N positions. Thus, charges are also subject to error intervals.

Deposition Numbers CSD 2204799-2204800 contain the supplementary crystallographic data for this paper. These data are provided free of charge by the joint Cambridge Crystallographic Data Centre and Fachinformationszentrum Karlsruhe http://www.ccdc.cam.ac.uk/structures.

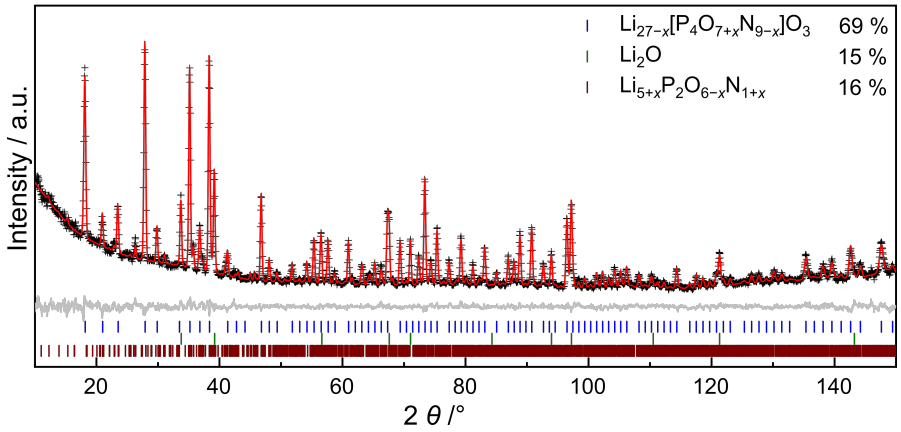

Figure B.2.: Rietveld refinement for $Li_{27-x}[P_4O_{7+x}N_{9-x}]O_3$ neutron data with observed (black, $\lambda = 1.5484$ Å), and calculated (red) intensities. The difference profile is shown in gray. Positions of Bragg reflections for $Li_{27-x}[P_4O_{7+x}N_{9-x}]O_3$, Li_2O, and $Li_{5+x}P_2O_{6-x}N_{1+x}$ are shown with blue, green, and brown markers, respectively.

Table B.6.: Rietveld refinement for $Li_{27-x}[P_4O_{7+x}N_{9-x}]O_3$ neutron powder diffraction data.

Formula	$Li_{27-x}[P_4O_{7+x}N_{9-x}]O_3$
Formula weight / g mol^{-1}	587.8
Crystal system; space group	cubic; $I4\bar{3}d$ (no. 220)
Lattice parameter / Å	12.0119(2)
Cell volume / Å^3	1733.15(10)
Formula units per unit cell	4
Density / g cm^{-3}	2.25(2)
Diffractometer	MLZ neutron powder diffractometer SPODI
Radiation	neutron ($\lambda = 1.5484$ Å)
Monochromator	Ge(551)
2θ-range / °	$9 \leq 2\theta \leq 151.9$
Data points	3020
Total number of reflections	173
Refined parameters	73
Background function	shifted Chebyshev
Number of background parameters	12
Goodness of fit	1.334
R_p; R_{wp}	0.0239; 0.0285
R_{exp}; R_{Bragg}	0.0214; 0.0148

B.2.4. NMR spectroscopy

In ^{31}P magic angle spinning (MAS) NMR spectra, two signals are visible at 33.0 and 19.6 ppm (Figure B.3) that result from $[PO_2N_2]^{5-}$ and $[PO_3N]^{4-}$. There are no further signals from possible P-containing side phases like Li_3P (−274.5 ppm). The weak signal at 44 ppm (see main paper) might

point to presence of $[PON_3]^{6-}$, but the signal was too small to be deconvoluted. The signals were integrated and fitted with Lorentzian functions (Figure B.4).

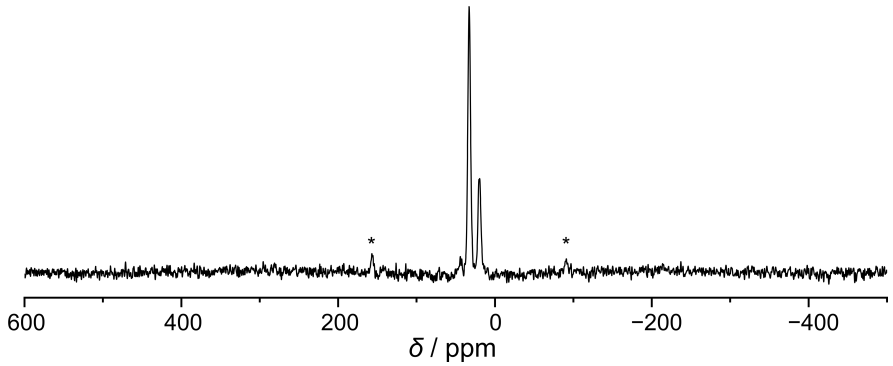

Figure B.3.: ^{31}P MAS NMR spectrum measured from 600 to −400 ppm with two signals at 33.0 and 19.6 ppm that result from $[PO_3N]^{4-}$ and $[PO_2N_2]^{5-}$ units. Asterisks mark rotational side bands. No P-containing side phases are visible.

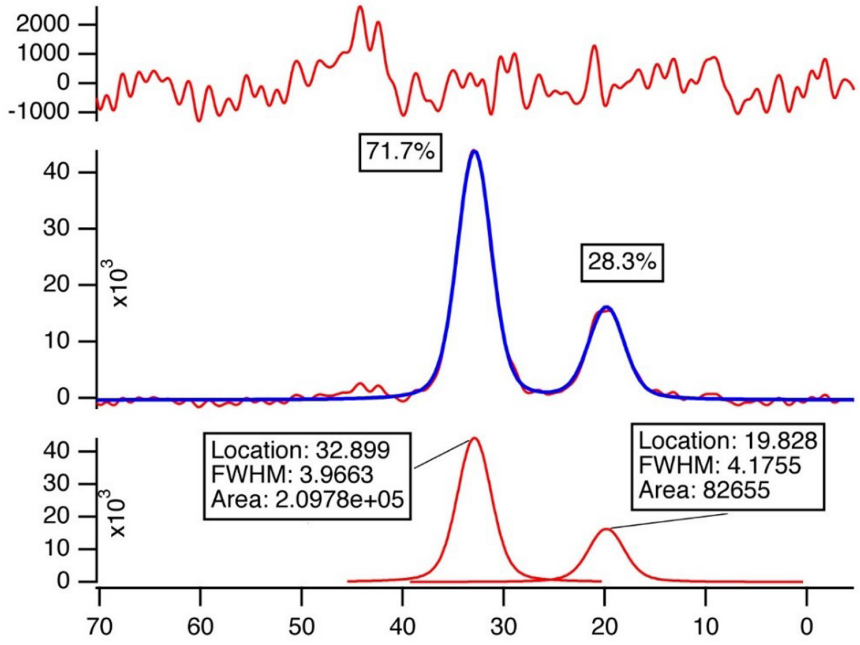

Figure B.4.: ^{31}P MAS NMR measurement with fitted Lorentzian functions (middle). The curve on the top shows the difference between measured (red curve in the middle) and fitted (blue curve in the middle). The bottom curves are the fitted functions with further details annotated.

Table B.7.: Chemical shifts and ratio of intensities from ^{31}P MAS NMR fitting in Figure B.4.

Sample	Chemical shifts / ppm	Percentage
1	32.90, 19.83	71.7 : 28.3
2	33.03, 19.96	72.2 : 27.8
Average	32.96, 19.90	72.0 : 28.0

^6Li and ^7Li MAS NMR spectra measured at 25 kHz exhibit a single Li signal with FWHMs of 0.8 ppm and 3.5 ppm, respectively. The signal shows shoulders, which is due to three Li positions with strongly overlapping signals.[10,11]

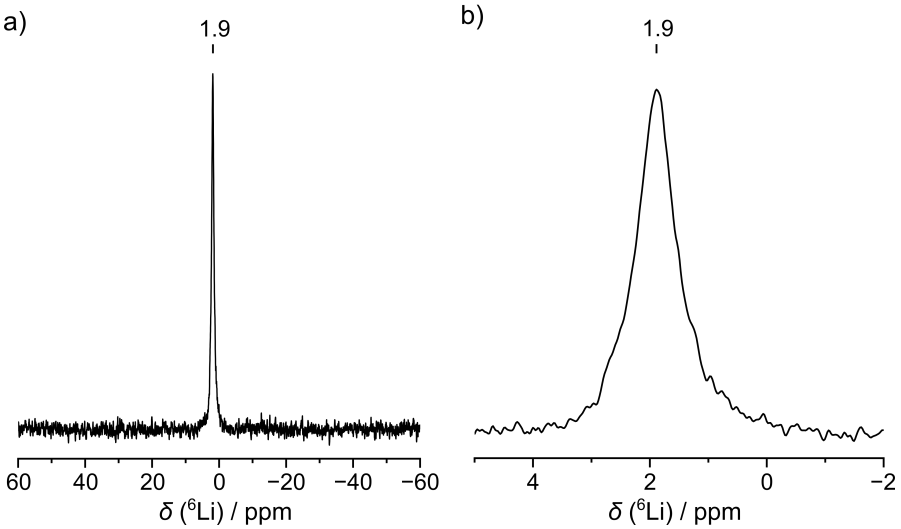

Figure B.5.: ^6Li MAS NMR measurement. a) Only one signal is visible in the spectrum. b) Enlarged section showing asymmetry of the signal with shoulders.

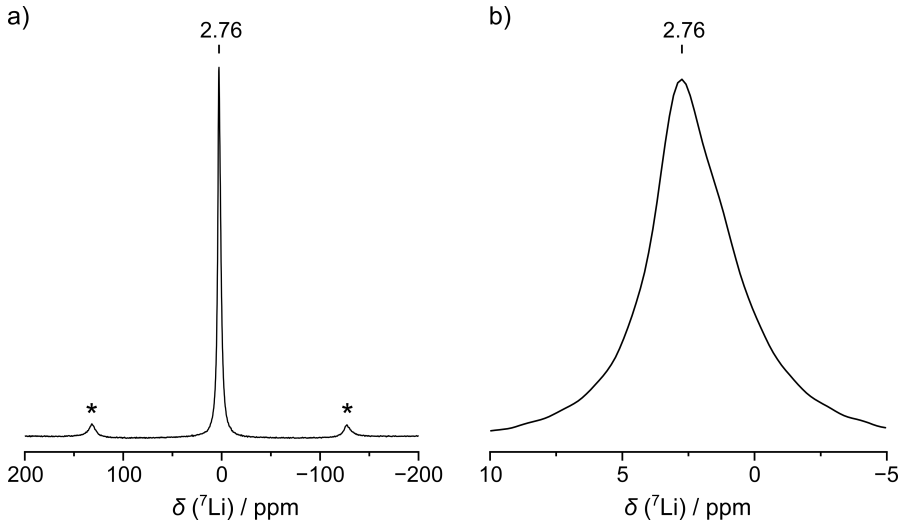

Figure B.6.: ^{7}Li MAS NMR measurement. a) Only one signal is visible in the spectrum. b) Closeup of the signal. The single signal is asymmetric with due to three Li positions with strongly overlapping signals.

Additional information on 2D NMR

In order to confirm that both signals result from one phase, a ^{31}P–^{31}P 2D double-quantum (DQ) single-quantum (SQ) correlation MAS NMR experiment using the Post-C7 sequence[12] was performed (Figure S7). The spectrum was obtained under a MAS rate of 20 kHz, (rotor ⌀ = 2.5 mm) acquiring 64 scans for each slice with a repetition delay of 120 s with a Post-C7 sequence.[13,14] Both abscissa and ordinate show the chemical shift in ppm. Autocorrelation peaks are visible along the diagonal dashed line. However, the autocorrelation signal of the smaller peak at 19.6 ppm is very weak. Cross correlation peaks should be visible at intersection points of the signals. An agglomeration of small signals is visible at the intersection of the large F2 (SQ) signal at 33 ppm and the small F1 (DQ) signal at 19.6 ppm. These signals rise only slightly above the background visible throughout the spectrum. However, these weak signals are almost as strong as the autocorrelation peak of the signal at 19.6 ppm. This agglomeration of intensities indicates that both signals are present within the same phase. The cross correlation of the small F2(SQ) signal (19.6 ppm) with the large F1(DQ) signal (33 ppm) is not visible. The intensity of correlation signals depends on the proximity of the correlated atoms. Thus, the larger the distance, the weaker is the signal. Other nitridophosphates like $Sn_6[P_{12}N_{24}]$, $CaH_4P_6N_{12}$ and $MgH_4P_6N_{12}$ analyzed with this method consist of corner-sharing tetrahedra and distances between P atoms in these compounds are 2.93 Å and 2.83–3.02 Å, and 2.78–3.01 Å, respectively.[15,16] In contrast, the shortest P–P distances in $Li_{27-x}[P_4O_{7+x}N_{9-x}]O_3$ within discrete tetrahedra are 4.40 Å and reach the detection limits of this method.

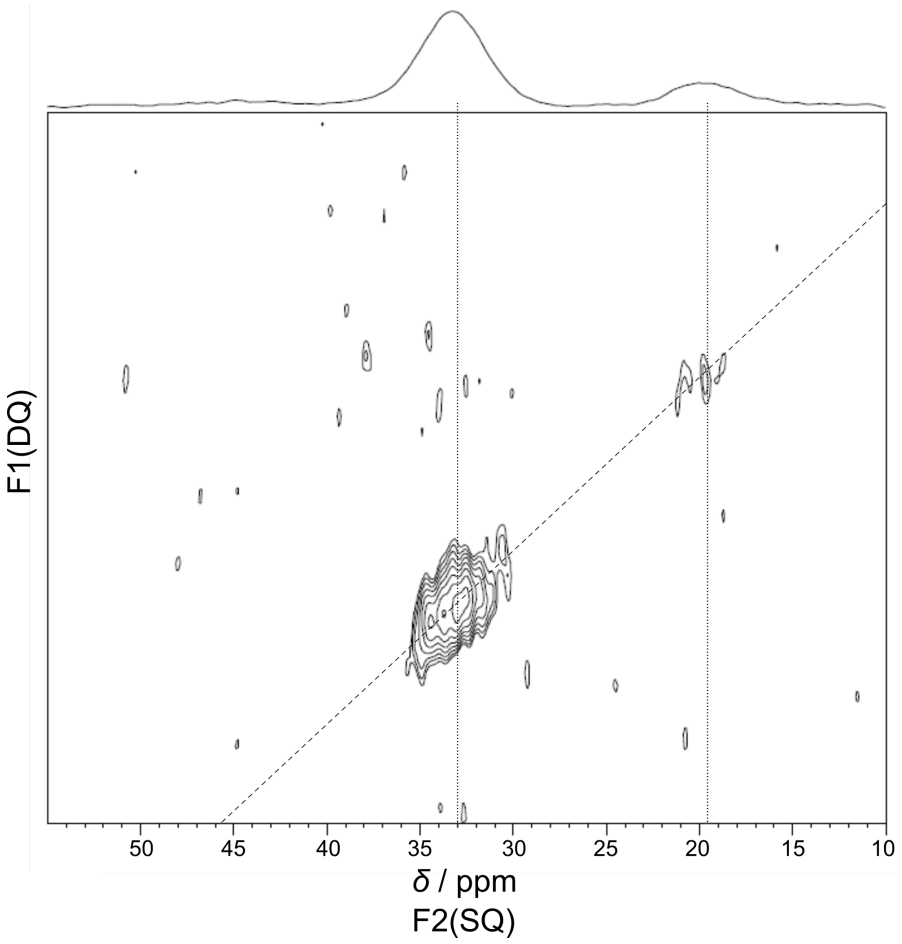

Figure B.7.: ^{31}P–^{31}P double-quantum (DQ) single-quantum (SQ) correlation MAS NMR spectrum of $Li_{27-x}[P_4O_{7+x}N_{9-x}]O_3$. Along the diagonal dashed line, autocorrelation peaks produced by isochronous spins are visible. Non-isochronous spins give rise to off-diagonal peaks. At the expected positions, agglomerations of weak signals might indicate that both signals are present in the same phase.

B.2.5. Details on scanning electron microscopy (EDX/SEM)

EDX shows a higher amount of O and a smaller amount of N than expected in the samples. The higher amount of O can be explained by superficial hydrolysis of the sample, as the probe is exposed to air for a short time when inserted into the SEM

Table B.8.: SEM-EDX results of $Li_{27-x}[P_4O_{7+x}N_{9-x}]O_3$ (in atom-%).

Point	P	O	N
1	18	60	22
2	20	61	19
3	21	59	20
4	15	61	24
5	17	63	21
6	21	59	20
7	19	60	21
8	20	58	22
9	28	54	17
10	19	66	15
average	19(3)	61(3)	20(2)
calculated (at $x = 1.9$)	17.4	51.7	30.9

B.2.6. Details on elemental analysis (ICP-OES)

Inductively-coupled plasma optical emission spectroscopy (ICP-OES) was performed on a sample consisting of $Li_{27-x}[P_4O_{7+x}N_{9-x}]O_3$, Li_2O, $Li_{5+x}P_2O_{6-x}N_{1+x}$, and $Li_{10}P_4N_{10}$. Weight percentages of the phases were determined with Rietveld refinement using TOPAS 6 and are given in Table B.9.[4–6] Expected Li:P ratios for $x = 0$ and $x = 1.9$ are given in consideration of phase ratios and compared to measured values. Due to side phases, obtaining unambiguous data is complicated, as the expected Li:P ratios lie close together, with measured values in between. The measured values differ by 3–10 % from the calculated value for $x = 0$ (2–15 % for $x = 1.9$). As can be seen in Table B.9, samples with higher amount of side phases yield wider error margins.

Table B.9.: Respective percentages for $Li_{27-x}[P_4O_{7+x}N_{9-x}]O_3$, $Li_{5+x}P_2O_{6-x}N_{1+x}$, Li_2O, and $Li_{10}P_4N_{10}$. Expected and measured Li:P ratios are calculated for $x = 0$ and $x = 1.9$

No.	$Li_{27-x}[P_4O_{7+x}N_{9-x}]O_3$	$Li_{5+x}P_2O_{6-x}N_{1+x}$	Li_2O	$Li_{10}P_4N_{10}$	Li : P ratio		
					calc $x = 0$	measured	calc $x = 1.9$
1	72	9	19	0	1.89	1.83(4)	1.79
2	72	9	19	0	1.89	1.85(3)	1.79
3	62	15	18	5	1.66	1.86(7)	1.59

B.2.7. Temperature dependent X-ray powder diffraction

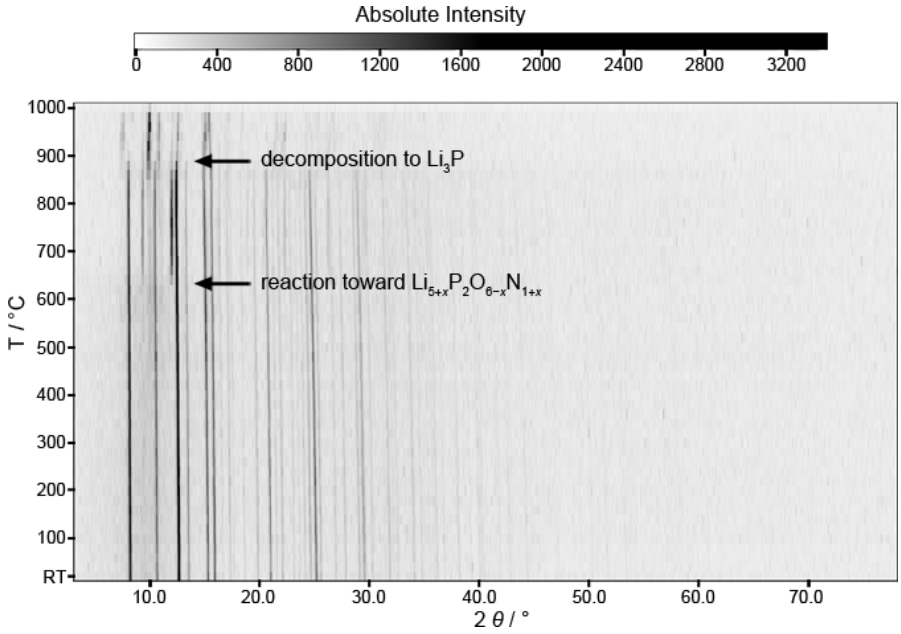

Figure B.8.: Temperature-dependent X-ray diffraction data for $Li_{27-x}[P_4O_{7+x}N_{9-x}]O_3$ (Mo-$K_{\alpha 1}$-radiation, $\lambda = 0.709\,30$ Å).

B.2.8. Additional information on EIS

Since only small quantities of the product with only 11 % Li_2O were available, the measurements were repeated with another sample containing 65 % $Li_{27-x}[P_4O_{7+x}N_{9-x}]O_3$, 18 % $Li_{5+x}P_2O_{6-x}N_{1+x}$, and 16 % Li_2O to demonstrate reproducibility. The fractions of the different phases were obtained from Rietveld refinements of the sample. The impedance spectra are similar to those of the sample with only 11 % Li_2O (Figure 4.6) and show bulk and grain boundary processes, but the grain boundary resistance is less pronounced as depicted in Figure B.9a. This suggests that the other side phase leads to a slightly better contact or less resistive grain boundaries between the $Li_{27-x}[P_4O_{7+x}N_{9-x}]O_3$ particles. Overall, the average total conductivity is slightly higher with $1.4 \times 10^{-7}\,S\,cm^{-1}$, but the bulk conductivity of $1 \times 10^{-6}\,S\,cm^{-1}$ is comparable to the value of the sample with 11 % Li_2O. To obtain a consistent fit over the whole temperature range, the capacitance value of the high frequency semicircle was refined at low temperatures and kept constant for the other temperatures. This leads to a better deconvolution of the activation energies resulting in averaged values of three samples as listed in Table B.10 of 0.35(4) eV and 0.40(2) eV for the bulk and grain boundary process, respectively. The averaged activation energy of the total process is 0.39(3) eV. The activation energy is lower than the activation energy of the sample with only 11 % Li_2O, which is consistent with the less pronounced influence of the grain boundaries in this sample.

An average electronic conductivity of $9 \times 10^{-10}\,S\,cm^{-1}$ of $Li_{27-x}[P_4O_{7+x}N_{9-x}]O_3$ was obtained by potentiostatic polarization measurements leading to a transference number $\tau_i = \sigma_{ion}/(\sigma_{ion} + \sigma_{eon})$ of

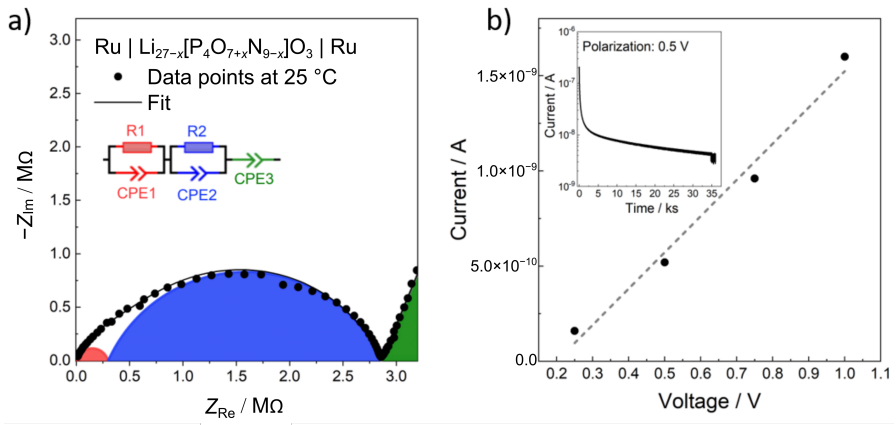

Figure B.9.: a) Representative spectrum of sample containing 65 % $Li_{27-x}[P_4O_{7+x}N_{9-x}]O_3$, 18 % $Li_{5+x}P_2O_{6-x}N_{1+x}$, and 16 % Li_2O. The spectrum is similar to the sample with only 11 % Li_2O and shows a bulk (red) and a grain boundary (blue) process, but the grain boundary resistance is less pronounced. b) I–V curve for the determination of the partial electronic conductivity of $Li_{27-x}[P_4O_{7+x}N_{9-x}]O_3$ at 25 °C ($\sigma_{eon} = 4 \times 10^{-10}\,S\,cm^{-1}$). The inset shows representative data for the DC polarization experiment at 0.5 V.

Table B.10.: Activation energies of non-phase pure $Li_{27-x}[P_4O_{7+x}N_{9-x}]O_3$ as obtained from measurements of the sample containing 65 % $Li_{27-x}[P_4O_{7+x}N_{9-x}]O_3$, 18 % $Li_{5+x}P_2O_{6-x}N_{1+x}$, and 16 % Li_2O.

Sample $Li_{27-x}[P_4O_{7+x}N_{9-x}]O_3$ with 18 % $Li_{5+x}P_2O_{6-x}N_{1+x}$ and 16 % Li_2O	E_a bulk / eV	E_a grain boundary / eV	E_a R_{tot} / eV
A	0.38	0.39	0.39
B	0.29	0.39	0.35
C	0.36	0.43	0.42
Average	0.35	0.40	0.39
Standard deviation	0.04	0.02	0.03

0.991, making $Li_{27-x}[P_4O_{7+x}N_{9-x}]O_3$ a mainly ionic conductor. A representative I-V and polarization curve is depicted in Figure B.9b.

B.3. Author Contributions

Stefanie Schneider: Conceptualization: Equal; Data curation: Lead; Formal analysis: Lead; Investigation: Lead; Validation: Equal; Visualization: Lead; Writing – original draft: Lead; Writing – review & editing: Lead

Eva-Maria Wendinger: Conceptualization: Supporting; Investigation: Supporting; Methodology: Supporting; Writing – review & editing: Supporting

Volodymyr Baran: Investigation: Supporting; Methodology: Supporting

Anna-Katharina Hatz: Formal analysis: Supporting; Investigation: Supporting; Methodology: Supporting; Writing – review & editing:Supporting

Bettina V. Lotsch: Conceptualization: Supporting; Funding acquisition: Supporting; Methodology: Supporting; Project administration: Supporting; Resources: Supporting; Supervision: Supporting; Writing – review & editing:Supporting

Markus Nentwig: Formal analysis: Supporting; Investigation: Supporting; Writing – original draft:Supporting; Writing – review & editing: Supporting

Oliver Oeckler: Conceptualization: Supporting; Funding acquisition: Supporting; Investigation: Supporting; Project administration: Supporting; Supervision: Supporting; Validation: Supporting; Writing – review & editing: Supporting

Thomas Bräuniger: Conceptualization: Supporting; Formal analysis: Supporting; Investigation: Supporting; Methodology: Supporting; Validation: Supporting; Writing – review & editing: Supporting

Wolfgang Schnick: Conceptualization: Lead; Funding acquisition: Lead; Methodology: Equal; Project administration: Lead; Resources: Lead; Supervision: Lead; Validation: Equal; Writing – original draft: Supporting; Writing – review & editing: Supporting

B.4. References

[1] A. Stock, B. Hoffmann, *Ber. Dtsch. Chem. Ges.* **1903**, *36*, 314–319, DOI 10.1002/cber.19030360170.

[2] Bruker, *SADABS*, Bruker AXS Inc., Madison, WI, USA, **2009**.

[3] G. M. Sheldrick, *Acta Crystallogr. C* **2015**, *71*, 3–8, DOI 10.1107/S2053229614024218.

[4] A. A. Coelho, *TOPAS Academic version 6*, Coelho Software, Brisbane, Australia, **2016**.

[5] R. W. Cheary, A. A. Coelho, *J. Appl. Crystallogr.* **1992**, *25*, 109–121, DOI 10.1107/S0021889891010804.

[6] R. W. Cheary, A. A. Coelho, J. P. Cline, *J. Res. Natl. Inst. Stan.* **2004**, *109*, 1–25, DOI 10.6028/jres.109.002.

[7] Bruker, *Topspin v.3.0 pl 3*, Bruker Biospin GmbH, Germany, **2010**.

[8] M. Hoelzel, A. Senyshyn, O. Dolotko, *J. large-scale Res. Facil. JLSRF* **2015**, *1*, 18–21, DOI 10.17815/jlsrf-1-24.

[9] P. S. Whitfield, I. J. Davidson, L. D. Mitchell, S. A. Wilson, S. J. Mills, *Mater. Sci. Forum* **2010**, *651*, 11–25, DOI 10.4028/www.scientific.net/MSF.651.11.

[10] R. Böhmer, K. R. Jeffrey, M. Vogel, *Prog. Nucl. Magn. Reson. Spectrosc.* **2007**, *50*, 87–174, DOI 10.1016/j.pnmrs.2006.12.001.

[11] A. Kuhn, V. Duppel, B. V. Lotsch, *Energy Environ. Sci.* **2013**, *6*, 3548–3552, DOI 10.1039/c3ee41728j.

[12] M. Hohwy, H. J. Jakobsen, M. Edén, M. H. Levitt, N. C. Nielsen, *J. Chem. Phys.* **1998**, *108*, 2686–2694, DOI 10.1063/1.475661.

[13] Y. Ishii, *J. Chem. Phys.* **2001**, *114*, 8473–8483, DOI 10.1063/1.1359445.

[14] M. Carravetta, M. Eden, O. G. Johannessen, H. Luthman, P. J. Verdegem, J. Lugtenburg, A. Sebald, M. H. Levitt, *J. Am. Chem. Soc.* **2001**, *123*, 10628–10638, DOI 10.1021/ja016027f.

[15] F. J. Pucher, C. F. von Schirnding, F. Hummel, V. R. Celinski, J. Schmedt auf der Günne, B. Gerke, R. Pöttgen, W. Schnick, *Eur. J. Inorg. Chem.* **2015**, *2015*, 382–388, DOI 10.1002/ejic.201403040.

[16] A. Marchuk, V. R. Celinski, J. Schmedt auf der Günne, W. Schnick, *Chem. Eur. J.* **2015**, *21*, 5836–5842, DOI 10.1002/chem.201406240.

C. Supporting Information for Chapter 5 ($Li_{8+x}P_3O_{10-x}N_{1+x}$)

Stefanie Schneider, Sandra T. Kreiner, Lucas G. Balzat, Bettina V. Lotsch, and Wolfgang Schnick

Chem. Eur. J. **2023**, *29*, e202301986.

Reprinted (adapted) with permission from Chemistry – European Journal. Copyright 2023

Abstract The crystalline lithium oxonitridophosphate $Li_{8+x}P_3O_{10-x}N_{1+x}$ was obtained in an ampoule synthesis from P_3N_5 and Li_2O. The compound crystallizes in the triclinic space group $P\bar{1}$ with $a = 5.125(2)$, $b = 9.888(5)$, $c = 10.217(5)$ Å, $\alpha = 70.30(2)$, $\beta = 76.65(2)$, $\gamma = 77.89(2)°$. $Li_{8+x}P_3O_{10-x}N_{1+x}$ is a double salt, the structure of which contains distinctive complex anion species, namely non-condensed $P(O,N)_4$ tetrahedra, and $P(O,N)_7$ double tetrahedra connected by one N atom. Additionally, there is mixed occupation of O/N positions, which enables further anionic species by variation of O/N occupancies. To characterize these motifs in detail, complementary analytical methods were applied. The double tetrahedron exhibits significant disorder in single-crystal X-ray diffraction. Furthermore, the title compound is a Li^+ ion conductor with a total ionic conductivity of 1.2×10^{-7} S cm^{-1} at 25 °C, and a corresponding total activation energy of 0.47(2) eV.

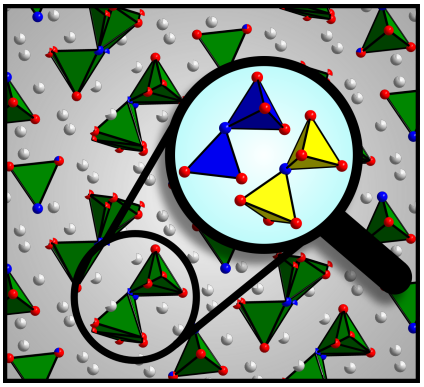

C.1. Experimental Procedures

Synthesis of P_3N_5:[1] P_4S_{10} (Acros Organics, > 99.8 %) was placed into a dried silica tube within a silica reaction tube in Ar (Air Liquide, 99.999 %) counterflow. After saturation with NH_3 (Air Liquide, 99.999 %) over 4 h, the starting material was heated to 850 °C at 5 K min^{-1} and held for 4 h before cooling at −5 K min^{-1}. The orange product was removed and washed with diluted hydrochloric acid, water, and acetone.

Synthesis of $Li_{8+x}P_3O_{10-x}N_{1+x}$: P_3N_5, and Li_2O (molar ratio 1 : 9) were ground together in an argon-filled glovebox (Unilab, MBraun, Garching, O_2 < 1 ppm, H_2O < 1 ppm), transferred in Ar counterflow into a Ta crucible within a silica tube and sealed into a silica ampoule under Ar. The mixture was heated to 800 °C at a rate of 5 K min^{-1}, held for 90 h and cooled at a rate of 5 K min^{-1}. The air-sensitive product was obtained as off-white powder under Ar.

Single-crystal X-ray diffraction: Single crystals were chosen under dried paraffin oil and irradiated with Mo-K_α radiation (λ = 0.710 73 Å) from a rotating anode in a D8 Venture (Bruker, Billerica MA, USA). Absorption correction was performed with SADABS and integration was performed with the APEX 3 program package.[2,3] The structure was solved with SHELXT and refined with SHELXL.[4] Deposition Number CSD 2246044 contains the supplementary crystallographic data for this paper. These data are provided free of charge by the joint Cambridge Crystallographic Data Centre and Fachinformationszentrum Karlsruhe http://www.ccdc.cam.ac.uk/structures.

X-ray powder diffraction: Glass capillaries (diameter 0.5 mm, wall thickness 0.01 mm, Hilgenberg GmbH) filled to ca. 1.5 cm, sealed off and mounted on a Stoe STADI P diffractometer. The sample was irradiated with Cu-$K_{\alpha1}$ radiation (λ = 1.5406 Å) through a Ge(111) monochromator. Data was obtained with a Mythen 1K detector in Debye-Scherrer geometry.

Temperature-dependent powder X-ray diffraction data was obtained on a Stoe StadiP equipped with a graphite furnace and an imaging plate position sensitive detector. The sample was irradiated with Ag-$K_{\alpha1}$ radiation (λ = 0.559 407 5 Å) with a Ge(111) monochromator. The sample was filled into a quartz glass capillary (diameter 0.4 mm, wall thickness 0.01 mm, Hilgenberg GmbH) and closed with a clog of vacuum grease (Leybonol, LVO 810 Lithelen). Measurements were taken from 60–960 °C in steps of 20 K, with a heating rate of 5 K min^{-1}.

Solid-state magic angle spinning (MAS) NMR methods: A DSX AVANCE spectrometer (Bruker) with a magnetic field of 11.7 T was used to collect NMR spectra of ^{6}Li, ^{7}Li, and ^{31}P. $Li_{8+x}P_3O_{10-x}N_{1+x}$ was filled into a rotor (⌀ = 2.5 mm), which was then spun with a rotation frequency of 20 kHz on a commercial MAS probe (Bruker). The spectra were analyzed using device-specific software.[5]

Fourier-transform Infrared (FTIR) spectroscopy: FTIR data was obtained using a Bruker FTIR Alpha II compact spectrometer with a diamond ATR unit under Ar atmosphere. The spectrum was measured from 400–4000 cm^{-1}.
Energy-dispersive X-ray spectroscopy (EDX): A scanning electron microscope (Dualbeam Helios Nanolab G3 UC (FEI)) equipped with an EDX detector (X-Max 80 SDD, Oxford Instruments) was used for EDX measurements. The samples were positioned on adhesive carbon pads and coated with a conductive carbon film using a high-vacuum sputter coater (safematic CCU-010). Using an accelerating voltage of 20 kV, multiple particles were targeted.
Inductively coupled plasma optical emission spectrometry (ICP-OES): ICP-OES was conducted at a Varian Vista RL with a 40 MHz RF generator, and a CCD detector (VistaChip)
Mass spectrometry: CHNS spectrometry was performed on a Vario MICRO Cube device (Elementar, Langenselbold, Germany).

Electrochemical measurements: Before the measurements, the samples were thoroughly ground in an agate mortar and then compacted into pellets of approximately 0.3–0.7 mm thickness and 5 mm in diameter using uniaxial cold-pressing ($p \approx 2$ t). The pellets were then sputtered with platinum metal using a Quorum 150 GB sputter coater to achieve an ion-blocking measurement setup and to ensure good contact during measurements. The ionic conductivity was determined via EIS, which was carried out in a two-electrode setup using an Ivium compactstat.h potentiostat (24 bit instrument) with a RHD Instruments Microcell HC cell stand loaded with a RHD Instruments TSC SW Closed measuring cell. All samples were measured in the frequency range of 1 MHz–0.1 Hz with an excitation voltage of 100 mV. The applied pressure in the measuring cells was about 700 kPa.
The activation energy was determined by fitting temperature dependent data to a linear Arrhenius-type behaviour. Temperature-dependent data were collected between 25–75 °C in 5 K steps and an equilibration time of 1 h was used. Data analysis and fitting procedures of EIS data were carried out using the software RelaxIS 3 (RHD Instruments, Darmstadt). After EIS measurements, the pellets were kept in the same measurement cells and were subsequently used for the determination of the electronic conductivity. The electronic conductivity was determined via potentiostatic polarization measurements at 25 °C. Voltages of 0.25, 0.50, 0.75, 1.00 and 1.25 V were applied for 16 h each with the drop of the resulting current measured. The resistance was extracted using Ohm's law from the current measured at a steady state after 16 h. Sample preparation and electrochemical measurements were carried out in an argon-filled glovebox (MB200, MBraun, Garching, $O_2 < 0.1$ ppm, $H_2O < 0.1$ ppm).

C.2. Results and Discussion

C.2.1. Additional crystallographic data (single-crystal X-ray diffraction)

Single-crystal data was acquired with Mo-K_α radiation. Absorption correction and integration of the data was performed with SADABS and the APEX3 program package, respectively.[2,3] The structure was solved using SHELXT and refined with SHELXL.[4] The occupancy of O and N at ligand positions were refined in accordance with NMR data, with all non-condensed tetrahedra comprising at least one N and additional partial occupancy with N at one further position. The diphosphate unit is heavily disordered. This prevents unequivocal assignment of O and N positions. However, as occupancy of bridging positions with N is energetically favorable,[6–8] they were assumed to be completely occupied by N. Li positions were assigned from maxima in the difference Fourier maps located in suitable distances to neighboring atoms that are within a range known from other lithium (oxo)nitridophosphates. If site occupancies of the Li atom positions are freely refined, all Li positions show occupancies less than one. Therefore, the combined charge of the Li atoms was restrained using occupancy restraints to match the negative charge of the P(O,N) anion motifs. Li coordination by O/N is displayed in Figure C.1.
Supplementary details on the crystal structure investigation is provided by the joint deposition service by the Cambridge Crystallographic Centre / FIZ Karlsruhe on quoting the depository number CSD 2246044.

Table C.1.: Wyckoff positions, atomic coordinates, and equivalent displacement parameters (in Å^2) of $Li_{8+x}P_3O_{10-x}N_{1+x}$ obtained from single-crystal X-ray diffraction at room temperature. Standard deviations in parentheses.

Atom	Wyckoff position	*s.o.f.*	x	y	z	U_{eq}
P001	2i	1	0.18846(13)	0.17331(7)	0.06938(7)	0.00784(14)
P002	2i	1	0.39094(14)	0.51253(8)	0.29228(7)	0.01176(15)
P03A	2i	0.315	0.324(4)	0.2315(16)	0.4723(18)	0.0123(18)
O001	2i	1	0.1515(5)	0.1450(2)	0.9307(2)	0.0171(4)
N002	2i	1	0.9925(4)	0.3170(2)	0.0829(2)	0.0084(4)
O003	2i	1	0.4924(4)	0.1956(3)	0.0484(3)	0.0265(6)
O004	2i	0.77	0.1321(6)	0.0331(3)	0.1964(2)	0.0229(6)
N004	2i	0.23	0.1321(6)	0.0331(3)	0.1964(2)	0.0229(6)
O005	2i	1	0.2279(5)	0.6661(3)	0.2904(3)	0.0267(5)
O06A	2i	0.315	0.351(3)	0.470(2)	0.164(2)	0.013(3)
O07A	2i	0.315	0.2914(12)	0.4630(8)	0.7450(9)	0.0116(16)
N08A	2i	0.315	0.351(3)	0.3898(14)	0.4386(12)	0.044(3)
O09A	2i	0.315	0.070(2)	0.1955(15)	0.4427(11)	0.029(2)
O10A	2i	0.315	0.568(3)	0.1845(19)	0.3625(19)	0.036(4)
O11A	2i	0.315	0.370(4)	0.133(2)	0.6265(18)	0.052(4)
P03B	2i	0.685	0.3116(17)	0.2102(7)	0.4675(7)	0.0083(6)
O06B	2i	0.685	0.4148(14)	0.4844(11)	0.1455(10)	0.0116(11)
O07B	2i	0.685	0.6747(7)	0.4745(5)	0.3320(5)	0.0233(10)
N08B	2i	0.685	0.1987(8)	0.3884(4)	0.4064(4)	0.0183(10)
O09B	2i	0.685	0.0614(9)	0.1345(6)	0.4830(5)	0.0208(9)
O10B	2i	0.685	0.5344(15)	0.1584(7)	0.3568(8)	0.0124(9)
O11B	2i	0.685	0.3987(10)	0.1816(4)	0.6148(5)	0.0113(7)
Li01	2i	0.886	0.606(1)	0.2838(6)	0.1678(5)	0.0097(9)
Li02	2i	0.830	0.8893(12)	0.0637(7)	0.3777(7)	0.0172(12)
Li03	2i	0.674	0.1320(16)	0.4164(10)	0.6084(8)	0.0199(16)
Li04	2i	0.793	0.0003(13)	0.3704(8)	0.2539(8)	0.0198(14)
Li05	2i	0.719	0.2642(14)	0.7033(10)	0.4726(9)	0.0231(17)
Li06	2i	0.930	0.0297(14)	0.1488(7)	0.7472(8)	0.0293(16)
Li07	2i	0.837	0.7348(15)	0.5382(9)	0.0125(8)	0.0265(16)
Li08	2i	0.860	0.1787(18)	0.6859(7)	0.0898(8)	0.0280(16)
Li09	2i	0.837	0.3952(18)	0.0175(9)	0.3219(12)	0.041(2)
Li10	2i	0.957	0.786(2)	0.0557(11)	0.0084(16)	0.071(4)
Li11	2i	0.909	0.471(2)	0.2114(14)	0.7842(9)	0.062(3)

Table C.2.: Anisotropic displacement parameters (in $Å^2$) of $Li_{8+x}P_3O_{10-x}N_{1+x}$ as obtained from single-crystal X-ray diffraction at room temperature, standard deviations in parentheses.

Atom	U_{11}	U_{22}	U_{33}	U_{23}	U_{13}	U_{12}
P001	0.0076(3)	0.0089(3)	0.0077(3)	−0.0020(2)	−0.0013(2)	−0.0030(2)
P002	0.0094(3)	0.0178(3)	0.0100(3)	0.0018(2)	−0.0031(2)	−0.0082(2)
P03A	0.0086(19)	0.024(5)	0.0099(17)	0.000(3)	−0.0024(13)	−0.013(3)
O001	0.0243(11)	0.0176(10)	0.0129(9)	−0.0034(8)	−0.0042(8)	−0.0082(8)
N002	0.0060(8)	0.0082(9)	0.0126(9)	0.0001(7)	−0.0007(7)	−0.0064(7)
O003	0.0098(9)	0.0327(13)	0.0476(16)	−0.0013(9)	−0.0032(9)	−0.0280(12)
O004	0.0378(15)	0.0145(11)	0.0156(11)	−0.0118(10)	−0.0076(10)	0.0030(8)
N004	0.0378(15)	0.0145(11)	0.0156(11)	−0.0118(10)	−0.0076(10)	0.0030(8)
O005	0.0221(12)	0.0328(13)	0.0318(14)	0.0049(10)	−0.0087(10)	−0.0210(11)
O06A	0.008(6)	0.021(6)	0.016(7)	−0.001(4)	−0.003(4)	−0.014(5)
O07A	0.006(2)	0.012(3)	0.019(4)	−0.003(2)	−0.001(2)	−0.007(3)
N08A	0.077(8)	0.049(6)	0.021(5)	−0.048(5)	0.008(5)	−0.017(4)
O09A	0.026(4)	0.047(7)	0.022(5)	−0.025(5)	−0.002(4)	−0.009(4)
O10A	0.021(6)	0.045(8)	0.015(5)	0.024(5)	0.006(4)	0.002(5)
O11A	0.042(7)	0.078(13)	0.035(7)	−0.019(8)	0.003(5)	−0.016(9)
P03B	0.0105(10)	0.0091(11)	0.0063(11)	−0.0021(7)	−0.0008(7)	−0.0037(8)
O06B	0.015(3)	0.0123(19)	0.009(2)	−0.002(2)	−0.001(2)	−0.0052(15)
O07B	0.0139(15)	0.034(2)	0.031(2)	0.0072(14)	−0.0110(15)	−0.022(2)
N08B	0.0156(17)	0.0193(18)	0.0080(15)	0.0056(14)	0.0041(12)	0.0022(12)
O09B	0.0136(16)	0.031(2)	0.023(2)	−0.0083(17)	−0.0017(15)	−0.0116(17)
O10B	0.0099(17)	0.0185(19)	0.0121(18)	−0.0054(14)	−0.0011(12)	−0.0073(14)
O11B	0.0094(15)	0.0144(16)	0.0114(15)	−0.0037(12)	−0.0048(11)	−0.0022(13)
Li01	0.009(2)	0.012(2)	0.009(2)	−0.0011(18)	−0.0001(17)	−0.0046(18)
Li02	0.009(2)	0.025(3)	0.020(3)	0.001(2)	−0.003(2)	−0.012(3)
Li03	0.016(3)	0.045(5)	0.009(3)	−0.020(3)	0.003(2)	−0.015(3)
Li04	0.014(3)	0.032(4)	0.024(3)	0.014(2)	−0.014(2)	−0.024(3)
Li05	0.007(3)	0.051(5)	0.023(4)	−0.004(3)	−0.003(3)	−0.026(3)
Li06	0.024(3)	0.012(3)	0.038(4)	−0.003(2)	0.013(3)	−0.003(2)
Li07	0.025(3)	0.042(4)	0.020(3)	−0.030(3)	0.005(3)	−0.011(3)
Li08	0.050(5)	0.017(3)	0.020(3)	0.009(3)	−0.018(3)	−0.010(3)
Li09	0.035(4)	0.027(4)	0.071(6)	−0.001(3)	−0.044(5)	−0.007(4)
Li10	0.032(5)	0.034(5)	0.130(11)	−0.009(4)	0.002(5)	−0.012(6)
Li11	0.070(7)	0.107(9)	0.025(4)	−0.075(7)	0.008(4)	−0.014(5)

Table C.4.: Selected interatomic distances (in Å) occurring in $Li_{8+x}P_3O_{10-x}N_{1+x}$ obtained from single-crystal X-ray diffraction at room temperature, standard deviations in parentheses.

P001–	O004/N004	1.572(2)	O07A–	O07B	0.828(8)
	O003	1.575(2)		Li04	1.980(10)
	N002	1.586(2)		Li03	1.986(14)
	O001	1.592(3)		Li11	2.39(2)
P002–	O07B	1.537(4)		Li07	2.446(13)
	O005	1.568(3)	N08A–	N08B	0.92(2)
	O06A	1.57(2)		Li03	1.90(2)
	N08A	1.578(11)		Li05	2.25(2)
	O06B	1.589(11)	O09A–	O09B	0.609(13)
	O07A	1.634(7)		Li05	1.966(13)
	N08B	1.688(4)		Li02	2.09(2)
P03A–	P03B	0.25(2)		Li04	2.156(12)
	N08A	1.51(2)	O10A–	O10B	0.36(2)
	O09A	1.54(3)		Li02	1.82(2)
	O10A	1.58 (2)		Li01	1.88(2)
	O11A	1.59(2)		Li09	2.22(2)
P03B–	P03A	0.25 (2)	O11A–	O11B	0.50(2)
	O10B	1.547(10)		Li09	1.72(2)
	O09B	1.568(11)		Li06	1.90(2)
	O11B	1.59(10)		Li11	2.20(3)
	N08B	1.681(7)	O06B–	O06A	0.37(2)
O001–	Li10	1.850(10)		Li07	1.915(10)
	Li11	2.002(9)		Li01	1.982(11)
	Li06	2.095(9)		Li07	2.03(2)
	Li08	2.108(8)		Li08	2.074(11)
	Li10	2.110(11)		Li04	2.467(11)
N002–	Li04	2.000(10)	O07B–	O07A	0.828(8)
	Li01	2.018(5)		Li03	1.920(12)
	Li07	2.055(9)		Li04	1.923(8)
	Li08	2.155(10)		Li05	2.206(9)
	Li07	2.283(8)	N08B–	N08A	0.92(2)
O003–	Li10	1.889(11)		P002	1.688(4)
	Li01	1.961(8)		Li03	2.115(10)
	Li08	2.196(8)		Li04	2.118(10)
O004/N004–	Li06	1.990(8)		Li03	2.274(9)

Continued

	Li09	2.016(13)	O09B–	O09A	0.609(13)
	Li02	2.056(7)		Li02	1.905(11)
	Li10	2.45(2)		Li02	2.002(8)
O005–	P002	1.568(3)		Li05	2.140(10)
	Li06	1.997(7)		Li09	2.475(12)
	Li11	2.012(12)	O10B–	O10A	0.36(2)
	Li08	2.062(10)		Li09	1.86(2)
	Li05	2.070(11)		Li02	1.887(9)
	Li03	2.078(9)		Li01	1.911(8)
O06A–	O06B	0.37(2)	O11B–	O11A	0.50(2)
	Li07	1.98(2)		Li11	1.976(13)
	Li01	2.02(2)		Li09	1.999(9)
	Li08	2.08(2)		Li06	2.072(8)
	Li04	2.10(2)		Li05	2.123(10)
	Li07	2.27(2)		Li03	2.423(10)

Table C.5.: Selected interatomic angles (in degree) occurring in $Li_{8+x}P_3O_{10-x}N_{1+x}$ obtained from single-crystal X-ray diffraction at room temperature, standard deviations in parentheses. The left part of the table shows angles in the non-condensed tetrahedron and bridging angles between the pairs of $P_2(O,N)_7$. The right part of the table shows angles within $P_2(O,N)_7$.

O001	–P001–	N002	107.75(11)	O005	–P002–	O06A	110.1(7)
O001	–P001–	O003	107.13(14)	O005	–P002–	O07A	104.5(3)
O001	–P001–	O004/N004	107.35(12)	O005	–P002–	N08A	115.6(5)
N002	–P001–	O003	110.05(13)	O06A	–P002–	O07A	103.9(7)
N002	–P001–	O004/N004	114.84(14)	O06A	–P002–	N08A	114.3(8)
O003	–P001–	O004/N004	109.4(2)	N07A	–P002–	O08A	107.2(6)
				O005	–P002–	O06B	110.8(4)
P002	–N08A–	P03A	130.5(11)	O005	–P002–	O07B	118.2(2)
P002	–N08B–	P03B	124.3(3)	O005	–P002–	N08B	107.1(2)
				O06B	–P002–	O07B	108.2(3)
				O06B	–P002–	N08B	103.3(4)
				O07B	–P002–	N08B	108.2(2)
				N08A	–P03A–	O09A	118.1(14)
				N08A	–P03A–	O10A	100.7(13)
				N08A	–P03A–	O11A	114.8(13)
				O09A	–P03A–	O10A	105.7(14)
				O09A	–P03A–	O11A	108.3(14)
				O10A	–P03A–	O11A	108.2(14)
				O08B	–P03B–	N09B	104.1(5)
				O08B	–P03B–	N10B	111.4(5)
				O08B	–P03B–	N11B	107.7(5)
				O09B	–P03B–	O10B	106.0(6)
				O09B	–P03B–	O11B	112.2(5)
				O10B	–P03B–	O11B	115.0(5)

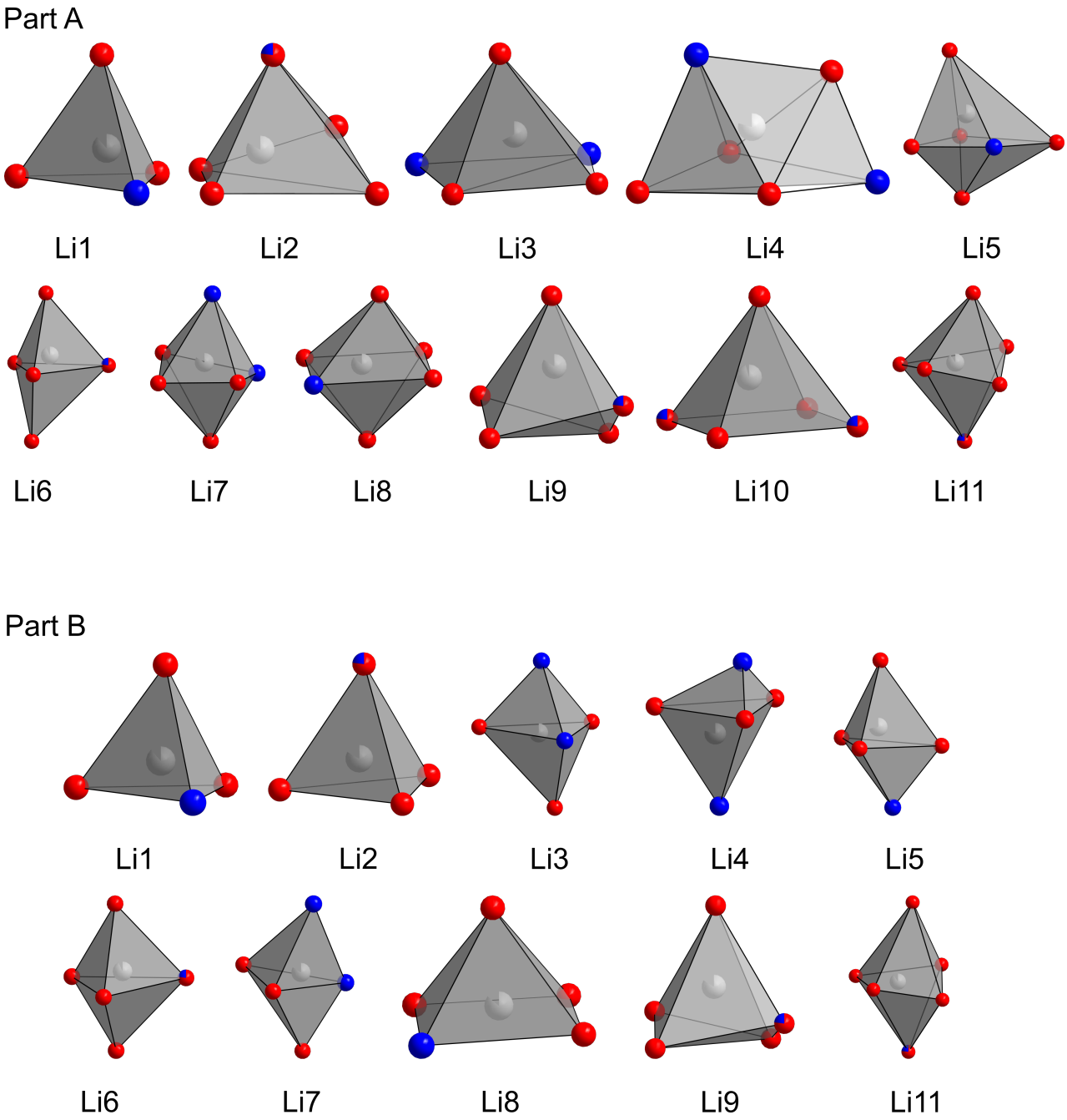

Figure C.1.: Coordination spheres of Li positions by O and N in the differently oriented diphosphate motifs. As Li10 is only coordinated by O and N from the phosphate motif, the coordination spheres are identical.

C.2.2. Rietveld refinement of $Li_{8+x}P_3O_{10-x}N_{1+x}$

Table C.6.: Crystallographic data on the Rietveld refinement of $Li_{8+x}P_3O_{10-x}N_{1+x}$.

Formula	$Li_{8+x}P_3O_{10-x}N_{1+x}$
Formula weight / $g\,mol^{-1}$	328.54
Crystal system; space group	Triclinic, $P\bar{1}$
Lattice parameters / Å, °	$a = 5.147\,47(12)$
	$b = 9.9265(3)$
	$c = 10.2595(3)$
	$\alpha = 70.2334(12)$
	$\beta = 76.5747(12)$
	$\gamma = 77.8033(12)$
Cell volume / $Å^3$	474.78(2)
Formula units per unit cell	2
Density / $g\,cm^{-3}$	$2.298\,14(10)$
μ / mm	0.6946(7)
Diffractometer	Stoe Stadi P
Radiation	Cu-$K_{\alpha 1}$ ($\lambda = 1.540\,596$ Å)
Detector	Mythen 1K
Monochromator	Ge(111)
2θ-range / °	$5 \leq 2\theta \leq 120$
Data points	7839
Total number of reflections	1481
Refined parameters	135
Background function	Shifted Chebyshev
Number of background parameters	12
Goodness of fit	1.3583
R_p; R_{wp}	0.0510; 0.0686
R_{exp}; R_{Bragg}	0.0505; 0.0246

C.2.3. Additional information on NMR

^{31}P magic angle spinning (MAS) NMR spectra were measured on a sample consisting of $Li_{8+x}P_3O_{10-x}N_{1+x}$, Li_2O, and $Li_{5+x}P_2O_{6-x}N_{1+x}$ (81, 13 and 7 percent, respectively). The signal at 33.7 ppm can be ascribed to $[PO_2N_2]^{5-}$. The signals at 21.8 ppm results from both $[PO_3N]^{4-}$ and the doubly by N coordinated P from $[P_2O_5N_2]^{6-}$, and the large signal at 16.3 ppm can be assigned to the singly by N coordinated P from both $[P_2O_5N_2]^{6-}$ and $[P_2O_6N]^{5-}$, respectively. The additional signal at −274.9 ppm is due to small amounts of residual Li_3P, which is known to be formed at elevated temperatures and prolonged reaction durations.[9–14]

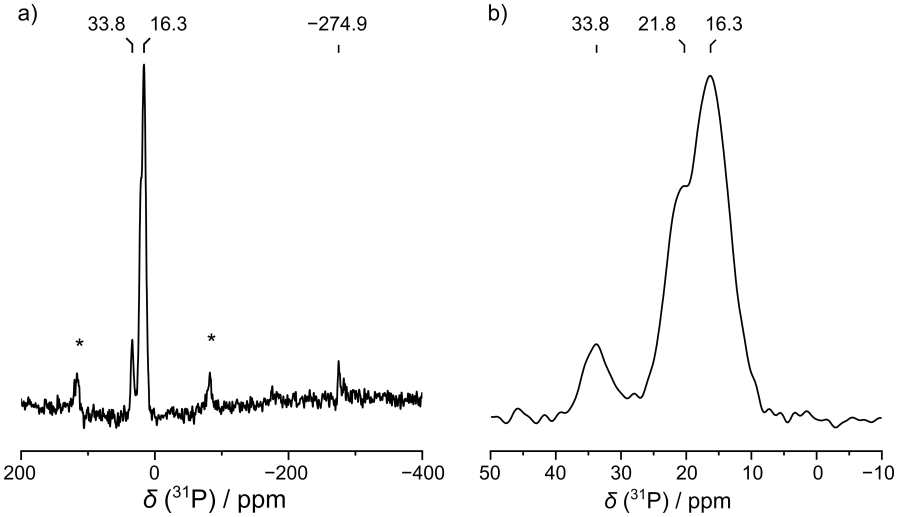

Figure C.2.: a) Full ^{31}P MAS NMR spectrum measured from 300 to −300 ppm. Two distinct signals at 33.7 and 16.2 ppm are visible that result from $[PO_2N_2]^{5-}$ and $[P_2O_6N]^{5-}$ units. The signal at −274.9 ppm results from small amounts of Li_3P. Asterisks mark rotational side bands. b) Close-up view of the ^{31}P signals of $Li_{8+x}P_3O_{10-x}N_{1+x}$. The signal at 16.3 ppm exhibits a shoulder at 21.8 ppm, resulting from $[PO_3N]^{4-}$ and $[P_2O_5N_2]^{6-}$ units.

^{6}Li and ^{7}Li MAS NMR spectra were measured at 20 kHz. The spectra exhibit a single Li signal with a FWHM of 1.2 ppm and 6.0 ppm for ^{6}Li and ^{7}Li, respectively. The signals show shoulders, which is probably due to the many crystallographically different Li positions that each have different environments. The width of the signals further point toward low conductivity, as large ionic conductivity would narrow the signals more.[15,16]

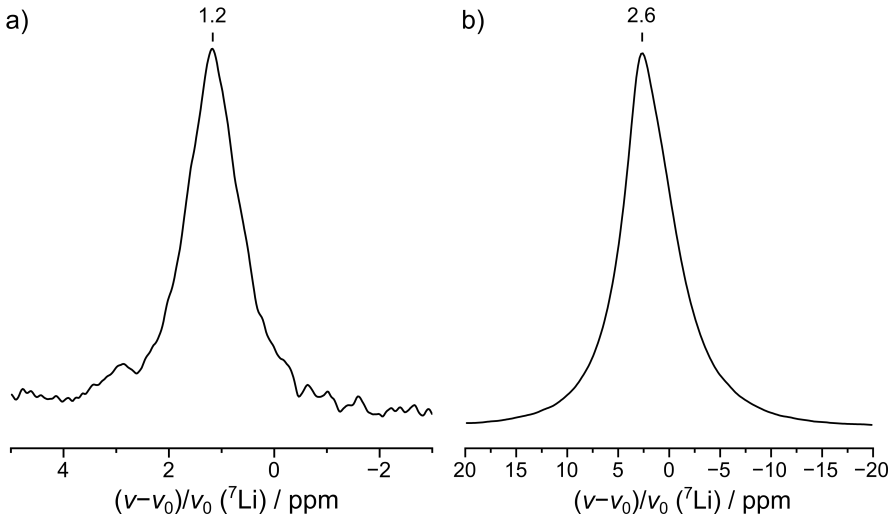

Figure C.3.: Li MAS NMR spectra. a) ^{6}Li MAS NMR spectrum. b) ^{7}Li MAS NMR spectrum. The spectra show only one signal each. The signals are relatively broad due to many different Li positions.

C.2.4. Additional information on energy-dispersive X-ray (EDX) spectroscopy (EDX)

Table C.7.: EDX (SEM) measurements of $Li_{8+x}P_3O_{10-x}N_{1+x}$ (in atom-%).

Point	P	O	N
1	16	59	25
2	27	47	26
3	18	57	25
4	45	14	40
5	21	54	26
6	21	51	28
7	18	55	27
8	19	56	25
9	19	56	25
10	14	60	27
11	14	60	26
average	21(9)	52(13)	27(4)
calculated ($x = 3$)	21.4	50	28.6
deviation (%, $x = 3$)	1.6	3.6	−5.1
calculated ($x = 1.4$)	21.4	61.4	17.1
deviation (%, $x = 1.4$)	1.6	15.3	57.9
average	19(3)	61(3)	20(2)
calculated (at x = 1.9)	17.4	51.7	30.9

C.2.5. Additional information on elemental analysis (ICP-OES)

Inductively-coupled plasma optical emission spectroscopy (ICP-OES) was performed on samples consisting of $Li_{8+x}P_3O_{10-x}N_{1+x}$, Li_2O, and $Li_{5+x}P_2O_{6-x}N_{1+x}$. Respective phase percentages (in wt-%) were obtained by Rietveld refinement using TOPAS 6,[17–19] Table C.8. The amount of N from average samples of $Li_{5+x}P_2O_{6-x}N_{1+x}$ ($x \approx 0.9$) was considered in the calculation of expected N-content.

Table C.8.: Respective percentages of $Li_{8+x}P_3O_{10-x}N_{1+x}$, Li_2O, and $Li_{5+x}P_2O_{6-x}N_{1+x}$ in the samples for ICP-OES measurements. Expected and measured Li : P ratios are calculated for respective compositions with an average $x = 0.9$ for $Li_{5+x}P_2O_{6-x}N_{1+x}$.

Sample	$Li_{8+x}P_3O_{10-x}N_{1+x}$	Li_2O	$Li_{5+x}P_2O_{6-x}N_{1+x}$	$Li_8P_3O_{10}N$	Li : P ratio measured	$Li_{11}P_3O_7N_4$
1	82	7	11	0.65	1.06	0.91
2	75	6	19	0.63	1.05	0.87
3	75	6	19	0.63	1.04	0.87
4	73	24	4	1.02	1.40	1.33

C.2.6. Additional information on elemental analysis CHNS

Elemental analysis was conducted on samples containing $Li_{8+x}P_3O_{10-x}N_{1+x}$ (75 and 73 %), Li_2O (6 and 24 %), $Li_{5+x}P_2O_{6-x}N_{1+x}$ (19 and 4 %, percentages were obtained from Rietveld refinement). The amount of N from average samples of $Li_{5+x}P_2O_{6-x}N_{1+x}$ ($x \approx 0.9$) was considered in the calculation of expected N-content. The absence of H shows that no hydrolysis has taken place to confound the measurement. The higher amount of N measured might be due to unknown N-containing side phases that are not visible in the Rietveld refinement.

Table C.9.: CHNS measurements of $Li_{8+x}P_3O_{10-x}N_{1+x}$ (in wt-%).

Sample	measured				expected N-content		
	C	H	N	S	$Li_8P_3O_{10}N$	$Li_{9.4}P_3O_{8.6}N_{2.4}$	$Li_{11}P_3O_7N_4$
1	0	0	17.57	0	5.65	10.05	14.85
2	0	0	14.24	0	3.68	7.95	12.63

C.2.7. Additional information on ionic and electronic conductivity measurements

Since only multi-phase samples in small quantities were available, several pellets with different phase compositions were measured. All samples contained Li_2O and $Li_{5+x}P_2O_{6-x}N_{1+x}$ as side phases. Li_2O only shows a negligible ionic conductivity ($10 \times 10^{-12}\,S\,cm^{-1}$ at 25 °C),[20] therefore the samples

containing Li_2O can be approximated as less dense pellets of $Li_{8+x}P_3O_{10-x}N_{1+x}$. On the other hand, the side phase $Li_{5+x}P_2O_{6-x}N_{1+x}$ is a lithium ion conductor ($10 \times 10^{-8}\,S\,cm^{-1}$ at 25 °C).[14] However, since only small quantities are present (max. 6 wt-%), the influence is expected to be minimal. To demonstrate reproducibility, Figure S4 shows exemplary EIS data of a pellet with the composition 81 wt-% $Li_{8+x}P_3O_{10-x}N_{1+x}$, 17 wt-% Li_2O and 2 wt-% $Li_{5+x}P_2O_{6-x}N_{1+x}$ (further denoted as Sample 2). The phase composition was determined through Rietveld refinement. Similar to the data in Figure 5.6, the data in Figure C.4 were fitted with two semicircles, represented by a resistor and CPE in parallel (R1/CPE1 and R2/CPE2). Polarization at the ion-blocking electrodes was modeled with an additional CPE (CPE3). The capacities of CPE1 and CPE2 were calculated using the Brug formula[21] and are 2.1×10^{-11} F and 2.7×10^{-11} F at 25 °C, respectively. Like the data presented in Figure 5.6, the capacities of the two semicircles are too similar to meaningfully assign different processes to the semicircles. Hence, in the following only the total conductivity and activation energy will be reported.[22] Using R1+R2, the total conductivity of sample 2 is $3.4 \times 10^{-8}\,S\,cm^{-1}$ at 25 °C and the total activation energy is 0.49(2) eV (see Figure C.4, inset). The total conductivity of sample 2 is slightly lower than the sample presented in Figure 5.6 ($1.2 \times 10^{-7}\,S\,cm^{-1}$), which might be due to the different phase compositions of the samples, where a larger amount of $Li_{5+x}P_2O_{6-x}N_{1+x}$ might lead to better contact between particles. A similar effect has been reported with a similar LiPON material.[23] The total activation energy of sample 2, however, is in good agreement with the data reported in Figure 5.6 and both are the same within the error margin (0.47(2) eV and 0.49(2) eV).

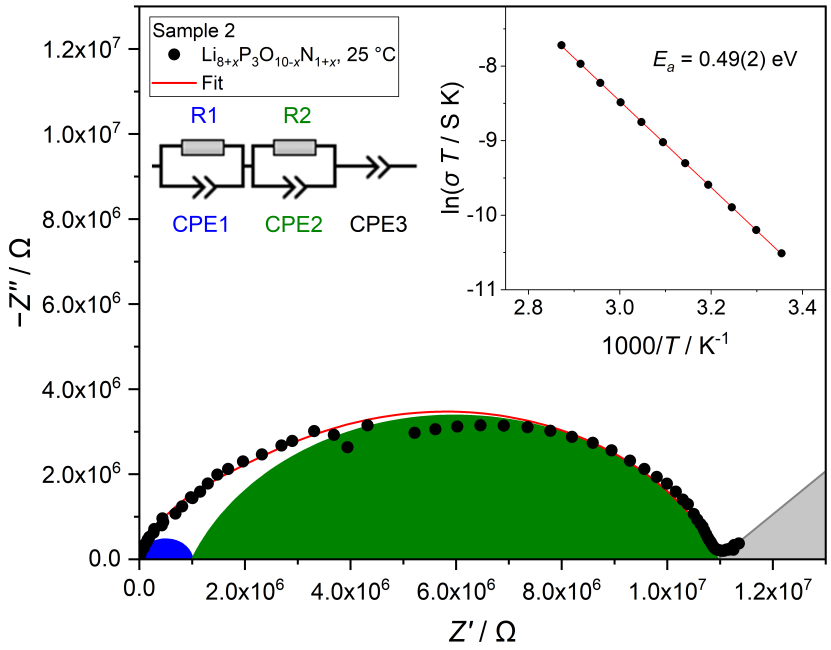

Figure C.4.: Impedance data of sample 2 containing 81 wt-% $Li_{8+x}P_3O_{10-x}N_{1+x}$, 17 wt-% Li_2O and 2 wt-% $Li_{5+x}P_2O_{6-x}N_{1+x}$at 25 °C. The data were fitted with two semicircles (R1/CPE1, blue, and R2/CPE2, green), and an additional CPE (CPE3) to model polarization, with each of the contributions highlighted. The inset shows temperature-dependant data gathered between 25–75 °C in 5 °C steps with 1 h of equilibration fitted to a linear Arrhenius model, leading to a total activation energy of 0.49(2) eV. This is a corrected version of the figure according to a submitted corrigendum.

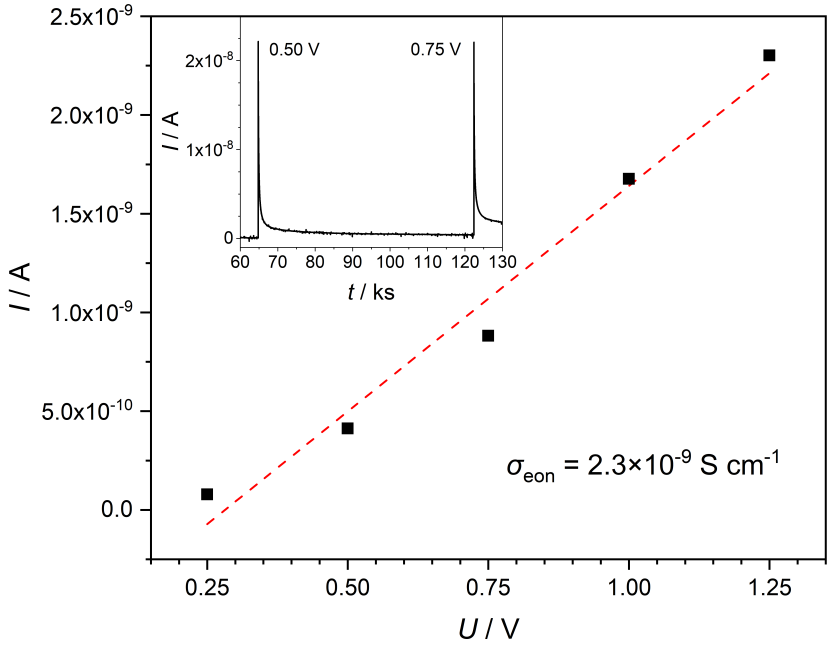

Figure C.5.: I/U-curve for the determination of the electrical conductivity of $Li_{8+x}P_3O_{10-x}N_{1+x}$. The electrical conductivity was extracted via potentiostatic polarization measurements, leading to an electric conductivity of $2.3 \times 10^{-9}\,S\,cm^{-1}$. The inset shows an excerpt of the polarization curve with current spikes after applying 0.50 and 0.75 V, respectively.

C.3. Author Contributions

Stefanie Schneider: Conceptualization: Lead; Formal analysis: Lead; Investigation: Lead; Validation: Equal; Visualization: Lead; Writing – original draft: Lead; Writing – review & editing: Equal
Sandra T. Kreiner: Formal analysis: Supporting; Investigation: Supporting; Writing – review & editing: Supporting
Lucas G. Balzat: Formal analysis: Supporting; Investigation: Supporting; Validation: Supporting; Visualization: Supporting; Writing – original draft: Supporting; Writing – review & editing: Supporting
Bettina V. Lotsch: Funding acquisition: Supporting; Methodology: Supporting; Project administration: Supporting; Resources: Supporting; Supervision: Supporting; Validation: Supporting; Writing – review & editing: Supporting
Wolfgang Schnick: Conceptualization: Lead; Funding acquisition: Lead; Project administration: Lead; Resources: Lead; Supervision: Lead; Validation: Equal; Writing – original draft: Supporting; Writing – review & editing: Supporting

C.4. References

[1] A. Stock, B. Hoffmann, *Ber. Dtsch. Chem. Ges.* **1903**, *36*, 314–319, DOI 10.1002/cber.19030360170.

[2] Bruker, *SADABS*, Bruker AXS Inc., Madison, WI, USA, **2009**.

[3] Bruker, *APEX3 v2018.1-0*, **2018**.

[4] G. M. Sheldrick, *Acta Crystallogr. C* **2015**, *71*, 3–8, DOI 10.1107/S2053229614024218.

[5] Bruker, *Topspin v.3.0 pl 3*, Bruker Biospin GmbH, Germany, **2010**.

[6] V. Lacivita, N. Artrith, G. Ceder, *Chem. Mater.* **2018**, *30*, 7077–7090, DOI 10.1021/acs.chemmater.8b02812.

[7] Y. A. Du, N. A. Holzwarth, *Phys. Rev. B* **2010**, *81*, 1–15, DOI 10.1103/PhysRevB.81.184106.

[8] Y. A. Du, N. A. Holzwarth, *Phys. Rev. B* **2008**, *78*, 1–13, DOI 10.1103/PhysRevB.78.174301.

[9] E.-M. Bertschler, R. Niklaus, W. Schnick, *Chem. Eur. J.* **2017**, *23*, 9592–9599, DOI 10.1002/chem.201700979.

[10] E.-M. Bertschler, T. Bräuniger, C. Dietrich, J. Janek, W. Schnick, *Angew. Chem. Int. Ed.* **2017**, *56*, 4806–4809, *Angew. Chem.* **2017**, *129*, 4884–4887, DOI 10.1002/anie.201701084.

[11] E.-M. Bertschler, R. Niklaus, W. Schnick, *Chem. Eur. J.* **2018**, *24*, 736–742, DOI 10.1002/chem.201704975.

[12] E.-M. Bertschler, C. Dietrich, T. Leichtweiß, J. Janek, W. Schnick, *Chem. Eur. J.* **2018**, *24*, 196–205, DOI 10.1002/chem.201704305.

[13] E.-M. Bertschler, C. Dietrich, J. Janek, W. Schnick, *Chem. Eur. J.* **2017**, *23*, 2185–2191, DOI 10.1002/chem.201605316.

[14] S. Schneider, L. G. Balzat, B. V. Lotsch, W. Schnick, *Chem. Eur. J.* **2023**, *29*, e202202984, DOI 10.1002/chem.202202984.

[15] R. Böhmer, K. R. Jeffrey, M. Vogel, *Prog. Nucl. Magn. Reson. Spectrosc.* **2007**, *50*, 87–174, DOI 10.1016/j.pnmrs.2006.12.001.

[16] A. Kuhn, V. Duppel, B. V. Lotsch, *Energy Environ. Sci.* **2013**, *6*, 3548–3552, DOI 10.1039/c3ee41728j.

[17] R. W. Cheary, A. A. Coelho, *J. Appl. Crystallogr.* **1992**, *25*, 109–121, DOI 10.1107/S0021889891010804.

[18] R. W. Cheary, A. A. Coelho, J. P. Cline, *J. Res. Natl. Inst. Stan.* **2004**, *109*, 1–25, DOI 10.6028/jres.109.002.

[19] A. A. Coelho, *TOPAS Academic version 6*, Coelho Software, Brisbane, Australia, **2016**.

[20] S. Lorger, R. Usiskin, J. Maier, *J. Electrochem. Soc.* **2019**, *166*, A2215–A2220, DOI 10.1149/2.1121910jes.

[21] G. J. Brug, A. L. van den Eeden, M. Sluyters-Rehbach, J. H. Sluyters, *J. Electroanal. Chem.* **1984**, *176*, 275–295, DOI 10.1016/S0022-0728(84)80324-1.

[22] J. T. S. Irvine, D. C. Sinclair, A. R. West, *Adv. Mater.* **1990**, *2*, 132–138, DOI 10.1002/adma.19900020304.

[23] S. Schneider, E.-M. Wendinger, V. Baran, A.-K. Hatz, B. V. Lotsch, M. Nentwig, O. Oeckler, T. Bräuniger, W. Schnick, *Chem. Eur. J.* **2023**, *29*, e202300174, DOI 10.1002/chem.202300174.

D. Supporting Information for Chapter 6 (LiP_4N_7 and $Li_{3-x}P_6N_{11-x}(NH)_x$)

Stefanie Schneider, Sebastian Klenk, Simon Kloß, and Wolfgang Schnick

Chem. Eur. J. **2023**, e202303251.

Reprinted (adapted) with permission from Chemistry – European Journal. Copyright 2023

Abstract Alkali nitridophosphates AP_4N_7 and $A_3P_6N_{11}$ (A = Na, K, Rb, Cs) have been known for decades. However, their Li homologues have remained elusive. In this work, the highly condensed lithium (imido)nitridophosphates LiP_4N_7 and $Li_{3-x}P_6N_{11-x}(NH)_x$ ($x = 1.66(3)$) were synthesized from $LiPN_2$and P_3N_5 in the multianvil press at 10 GPa. They constitute the first lithium nitridophosphates with 3D networks exhibiting a degree of condensation larger than 0.5 and high thermal stability. LiP_4N_7 crystallizes in the orthorhombic space group $P2_12_12_1$ with $a = 4.5846(6)$ Å, $b = 8.0094(11)$ Å, and $c = 13.252(2)$ Å ($Z = 4$). $Li_{3-x}P_6N_{11-x}(NH)_x$ crystallizes in the triclinic space group $P\bar{1}$ with $Z = 2$, $a = 4.6911(11)$ Å, $b = 7.024(2)$ Å, $c = 12.736(3)$ Å, $\alpha = 87.726(11)$, $\beta = 80.279(11)$, and $\gamma = 70.551(12)°$. Both compounds are stable against hydrolysis in air.

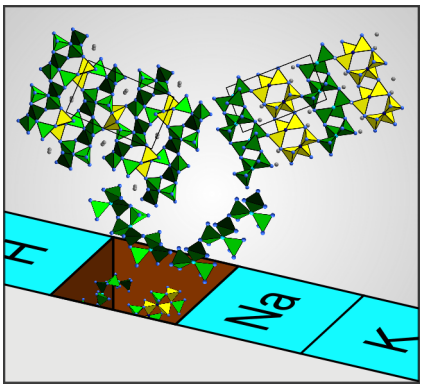

D.1. Experimental Procedures

Synthesis of P_3N_5: A dried silica tube was saturated with NH_3 for 4 h. P_4S_{10} (Sigma Aldrich, 99 %) was added and heated to 1125 K at 5 K min^{-1} in an NH_3 gas flow for 4 h following the procedure described by Stock et al.[1] The resulting powder was washed with water, ethanol, and acetone and dried under vacuum. Phase purity was confirmed by powder XRD, FTIR and CHNS combustion analysis.

Synthesis of $LiPN_2$: P_3N_5 and Li_3N (Rockwood Lithium, 94 %) in a molar ratio of 1 : 1.2 were ground in an agate mortar under inert atmosphere in an Ar-filled glovebox (Unilab, MBraun, Garching, $O_2 < 1$ ppm, $H_2O < 0.1$ ppm) and transferred to a Ta crucible within a silica tube in Ar atmosphere. The sealed silica tube was heated to 800 °C. The product was washed with diluted hydrochloric acid, water, and ethanol, and dried under vacuum.

High-pressure synthesis of LiP_4N_7 and $Li_{3-x}P_6N_{11-x}(NH)_x$: For high-pressure synthesis, a modified Walker-type multianvil press was used.[2,3] P_3N_5 and $LiPN_2$ were ground in a 1 : 1 ratio (1 : 3 for $Li_{3-x}P_6N_{11-x}(NH)_x$) and packed in a hexagonal boron nitride crucible (Henze, Kempten), which was closed with a *h*BN lid. The crucible was placed in the center of an MgO octahedron (doped with 5 % Cr_2O_3, edge length 18 mm, Ceramic Substrates & Components Ltd, Isle of Wight) using MgO spacers (Cesima Ceramics, Wust-Fischbach). Resistance heating using two graphite furnaces (Schunk Kohlenstofftechnik GmbH, Zolling) that were contacted to the anvils of the multianvil press by Mo discs ensured heating of the sample. A ZrO_2 tube (Cesima Ceramics, Wust-Fischbach) provides thermal insulation. The octahedron was placed between WC cubes (doped with 7 % Co, Hawedia, Marklkofen, Germany) with truncated edges (edge length 11 mm), and separated with pyrophillite gaskets (Ceramic Substrates & Components, Isle of Wight, UK). Additional details about the multianvil press and its experimental setup is given in literature.[3] The samples were first compressed to 10 GPa. For LiP_4N_7, the samples were then heated to 1150 °C over a period of 30 min, held for 15 min and cooled down over a period of 30 min. For $Li_{3-x}P_6N_{11-x}(NH)_x$, the temperature was raised to 1150 °C over 60 min, held for 60 min, and cooled down over 60 min. Eventually, the pressure was slowly decreased. The resulting gray product was isolated and washed with water.

Single crystal X-ray diffraction: A D8 Venture diffractometer (Bruker, Billerica MA, USA) was used with Mo K_α radiation from a rotating anode source to obtain scXRD data. Data was corrected for absorption with SADABS and integrated using the APEX3 program package.[4,5] ShelXT was used to solve the structure and ShelXL was used for refinement.[6] P and N atoms, as well as one Li position in $Li_{3-x}P_6N_{11-x}(NH)_x$were refined anisotropically. Li positions were found by difference fourier synthesis. Diamond3 was used for crystal structure visualization.[7]
Deposition Numbers CSD2290091 and CSD2290093 contain the supplementary crystallographic data for this paper. These data are provided free of charge by the joint Cambridge Crystallographic Data Centre and Fachinformationszentrum Karlsruhe http://www.ccdc.cam.ac.uk/structures.

Powder X-ray diffraction: The powder was sealed into a glass capillary (Ø = 0.5 mm, wall thickness 0.1 mm, Hilgenberg GmbH). A Stoe STADI P diffractometer (Stoe & Cie, Darmstadt, Germany) with Cu $K_{\alpha1}$ radiation ($\lambda = 1.5406$ Å), Ge(111) monochromator and a Mythen 1K detector (Dectris, Baden, Switzerland) in parafocusing Debye-Scherrer geometry was used to analyze the sample. The TOPAS 6 program package was used for Rietveld refinements.[8]

Variable-temperature XRD was performed on a Stoe STADI P diffractometer (Stoe & Cie, Darmstadt, Germany) with Mo $K_{\alpha1}$ radiation ($\lambda = 0.710\,73$ Å, for $Li_{3-x}P_6N_{11-x}(NH)_xAg$ $K_{\alpha1}$ radiation, $\lambda = 0.559\,407\,5$ Å). The diffractometer is equipped with a Ge(111) monochromator. A Mythen 1K detector (Dectris, Baden, Switzerland) in parafocusing Debye-Scherrer geometry was used for data acquisition. Rietveld refinement was performed with the TOPAS 6 program package.[8]

Solid-state magic angle spinning (MAS) nuclear magnetic resonance (NMR) spectroscopy: ^{31}P, ^{6}Li, and ^{7}Li spectra were measured using a DSX Avance spectrometer (Bruker) with a magnetic field of 11.7 T. The rotors containing the samples (⌀ = 2.5 mm) were spun with a rotation frequency of 20 kHz on a commercial MAS probe (Bruker). Topspin (Bruker) was used for analyzation of the spectra.[9]

Fourier-transform Infrared (FTIR) Spectroscopy: Measurement of FTIR spectra was performed on a Bruker FTIR Alpha II compact spectrometer with diamond ATR unit in Ar atmosphere. Data was obtained from 400–4000 cm^{-1} using the OPUS program package.[10]

Elemental analyses: Due to the presence of side phases in all samples, elemental analysis is difficult in the case of LiP_4N_7 and $Li_{3-x}P_6N_{11-x}(NH)_x$. Furthermore, Li, P, N, and H cannot be observed simultaneously with a single method. Li and H cannot be observed in energy-dispersive X-ray (EDX) spectroscopy, CHNS cannot measure P or Li. Thus, even the combination of methods offers only vague results. Thus, elemental analysis was only used to confirm that no additional elements are present in the samples.
Energy-dispersive X-ray spectroscopy (EDX): A scanning electron microscope (SEM) JSM-6500F (Jeol, Tokyo, Japan; maximum acceleration voltage 30 kV) was used to examine a carbon-coated sample. An energy dispersive spectrometer (Model 7418, Oxford Instruments, Abingdon, United Kingdom) was used for qualitative and semiquantitative elemental analysis. The obtained data was analyzed with INCA.[11]
Mass spectrometry (CHNS): CHNS spectrometry data was acquired using a Vario MICRO Cube device (Elementar, Langenselbold, Germany).

D.2. Additional crystallographic data:

The following Tables list additional information on atomic coordinates, displacement parameters, and geometric data for LiP_4N_7.

Table D.1.: Wyckoff positions and atomic coordinates of LiP_4N_7 obtained from single-crystal X-ray diffraction at 113 K, standard deviations in parentheses.

Atom	Wyckoff position	*s.o.f.*	x	y	z	U_{eq}
P1	4a	1	0.7436(2)	0.71699(7)	0.69761(5)	0.00669(10)
P2	4a	1	0.7529(2)	0.44308(7)	0.83382(4)	0.00653(10)
P3	4a	1	0.94169(14)	0.93048(7)	0.86785(4)	0.00535(10)
P4	4a	1	0.45031(13)	0.86751(7)	0.99306(4)	0.00532(10)
N1	4a	1	0.9320(5)	0.6120(2)	0.61782(14)	0.0073(3)
N2	4a	1	0.9402(5)	0.4779(2)	0.9335(2)	0.0082(3)
N3	4a	1	0.9928(4)	0.8593(2)	0.7493(2)	0.0065(3)
N4	4a	1	0.4943(4)	0.8116(2)	0.6367(2)	0.0079(3)
N5	4a	1	0.6099(4)	0.9068(3)	0.8913(2)	0.0077(3)
N6	4a	1	0.8885(4)	0.3044(2)	0.5446(2)	0.0066(3)
N7	4a	1	0.6150(5)	0.6049(2)	0.7853(2)	0.0084(3)
Li1	4a	1	0.767(7)	0.775(2)	0.4964(12)	0.129(9)

Table D.2.: Anisotropic displacement parameters (in $Å^2$) of LiP_4N_7 as obtained from single-crystal X-ray diffraction at 113 K, standard deviations in parentheses.

Atom	U_{11}	U_{22}	U_{33}	U_{23}	U_{13}	U_{12}
P1	0.0071(2)	0.0059(2)	0.0071(2)	−0.0008(2)	−0.0002(2)	0.0009(2)
P2	0.0073(2)	0.0065(2)	0.0058(2)	−0.0005(2)	0.0004(2)	−0.0011(2)
P3	0.0061(2)	0.0050(2)	0.0050(2)	0.0005(2)	0.0002(2)	−0.0002(2)
P4	0.0052(2)	0.0054(2)	0.0053(2)	0.0000(2)	0.0000(2)	0.0002(2)
N1	0.0085(7)	0.0056(6)	0.0077(7)	−0.0006(5)	0.0004(6)	0.0008(6)
N2	0.0092(7)	0.0089(7)	0.0065(7)	−0.0025(6)	−0.0013(6)	−0.0003(7)
N3	0.0069(7)	0.0068(7)	0.0059(6)	−0.0009(6)	0.0010(5)	−0.0015(6)
N4	0.0075(8)	0.0072(7)	0.0090(7)	0.0000(6)	−0.0004(6)	0.0027(6)
N5	0.0061(7)	0.0101(8)	0.0068(7)	0.0013(6)	0.0011(6)	0.0005(6)
N6	0.0059(7)	0.0061(7)	0.0079(7)	−0.0022(6)	−0.0006(6)	0.0012(5)
N7	0.0101(8)	0.0062(7)	0.0090(8)	0.0018(6)	0.0015(6)	0.0013(6)
Li1	0.29(3)	0.057(7)	0.046(6)	−0.007(6)	0.036(11)	0.030(13)

Table D.3.: Selected interatomic distances (in Å) and angles (in degree) occurring in LiP_4N_7 obtained from single-crystal X-ray diffraction at 113 K, standard deviations in parentheses.

P1–N7	1.582(2)	N7–P1–N4	112.05(10)	P3–N1–P1	127.02(12)
P1–N4	1.591(2)	N7–P1–N1	112.79(11)	P4–N2–P2	131.51(13)
P1–N1	1.604(2)	N7–P1–N3	108.96(9)	P3–N3–P2	123.53(12)
P1–N3	1.753(2)	N4–P1–N1	107.57(10)	P3–N3–P1	119.51(11)
P2–N7	1.579(2)	N4–P1–N3	110.90(10)	P2–N3–P1	116.15(10)
P2–N4	1.596(2)	N1–P1–N3	104.31(9)	P1–N4–P2	134.41(12)
P2–N2	1.600(2)	N7–P2–N4	110.92(9)	P3–N5–P4	130.55(13)
P2–N3	1.738(2)	N7–P2–N2	114.08(11)	P4–N6–P4	121.09(11)
P3–N5	1.564(2)	N7–P2–N3	109.12(10)	P4–N6–P3	123.14(10)
P3–N1	1.576(2)	N4–P2–N2	107.08(10)	P4–N6–P3	115.71(11)
P3–N3	1.688(2)	N4–P2–N3	112.14(10)	P2–N7–P1	128.00(12)
P3–N6	1.724(2)	N2–P2–N3	103.32(10)		
P4–N5	1.566(2)	N5–P3–N1	116.43(12)		
P4–N2	1.576(2)	N5–P3–N3	106.21(10)		
P4–N6	1.705(2)	N5–P3–N6	103.54(10)		
P4–N6	1.708(2)	N1–P3–N3	111.88(9)		
N1–Li1	2.20(2)	N1–P3–N6	107.05(9)		
N1–Li1	2.34(2)	N3–P3–N6	111.48(10)		
N2–Li1	2.31(2)	N5–P4–N2	112.81(11)		
N2–Li1	2.38(2)	N5–P4–N6	107.72(11)		
N4–Li1	2.16(2)	N5–P4–N6	103.48(10)		
N4–Li1	2.26(2)	N2–P4–N6	113.58(9)		
Li1–Li1	2.33(4)	N2–P4–N6	112.72(10)		
		N6–P4–N6	105.78(9)		

The following Tables list additional information on atomic coordinates, displacement parameters, and geometric data for $Li_{3-x}P_6N_{11-x}(NH)_x$.

Table D.4.: Wyckoff positions and atomic coordinates of $Li_{3-x}P_6N_{11-x}(NH)_x$ obtained from single-crystal X-ray diffraction at 113 K, standard deviations in parentheses.

Atom	Wyckoff position	*s.o.f.*	x	y	z	U_{eq}
P1	2i	1	0.8796(2)	0.28780(11)	0.06003(6)	0.0039(2)
P2	2i	1	0.4388(2)	0.11806(10)	0.15364(6)	0.0033(2)
P3	2i	1	0.5366(2)	0.72453(11)	0.07350(6)	0.0033(2)
P4	2i	1	0.7350(2)	0.20397(11)	0.43966(6)	0.0038(2)
P5	2i	1	0.1798(2)	0.22355(11)	0.57354(6)	0.0038(2)
P6	2i	1	0.2022(2)	0.38263(11)	0.34379(6)	0.0036(2)
N1	2i	1	0.2691(5)	0.2121(4)	0.0411(2)	0.0043(4)
N2	2i	1	0.2357(5)	0.6894(4)	0.0514(2)	0.0055(4)
N3	2i	1	0.7793(5)	0.1261(4)	0.1337(2)	0.0050(4)
N4	2i	1	0.7619(5)	0.5153(3)	0.1171(2)	0.0049(4)
H2	2i	0.66(3)	0.827363	0.524529	0.176907	0.006
N5	2i	1	0.2042(5)	0.2520(4)	0.2469(2)	0.0049(4)
H1	2i	1	0.017209	0.254194	0.243715	0.006
N6	2i	1	0.5387(5)	0.1154(4)	0.8316(2)	0.0047(4)
N7	2i	1	0.0330(5)	0.2828(4)	0.4553(2)	0.0040(4)
N8	2i	1	0.1405(6)	0.0139(4)	0.6156(2)	0.0071(4)
N9	2i	1	0.5260(6)	0.2214(4)	0.5534(2)	0.0084(5)
N10	2i	1	0.5411(5)	0.3733(4)	0.3634(2)	0.0047(4)
N11	2i	1	0.0101(5)	0.6166(4)	0.3316(2)	0.0052(4)
Li1	2i	1	0.015(2)	0.8896(11)	0.2254(5)	0.0232(14)
Li2	2i	0.34(3)	0.550(4)	0.640(3)	0.295(2)	0.019(6)

Table D.5.: Anisotropic displacement parameters (in $Å^2$) of $Li_{3-x}P_6N_{11-x}(NH)_x$as obtained from single-crystal X-ray diffraction at 113 K, standard deviations in parentheses.

Atom	U_{11}	U_{22}	U_{33}	U_{23}	U_{13}	U_{12}
P1	0.0031(3)	0.0041(3)	0.0048(3)	0.0007(2)	−0.0011(2)	−0.0014(2)
P2	0.0033(3)	0.0032(3)	0.0037(3)	−0.0004(2)	−0.0010(2)	−0.0012(2)
P3	0.0031(3)	0.0031(3)	0.0039(3)	−0.0002(2)	−0.0007(2)	−0.0012(2)
P4	0.0029(3)	0.0036(3)	0.0049(3)	−0.0004(2)	0.0000(2)	−0.0013(2)
P5	0.0033(3)	0.0031(3)	0.0043(3)	−0.0004(2)	0.0000(2)	−0.0007(2)
P6	0.0040(3)	0.0030(3)	0.0036(3)	−0.0002(2)	−0.0002(2)	−0.0011(2)
N1	0.0048(10)	0.0047(10)	0.0040(11)	0.0008(8)	−0.0012(8)	−0.0021(8)
N2	0.0044(10)	0.0084(10)	0.0038(10)	−0.0007(8)	−0.0008(8)	−0.0021(8)
N3	0.0053(11)	0.0040(10)	0.0058(11)	−0.0002(8)	−0.0011(8)	−0.0018(8)
N4	0.0061(11)	0.0036(10)	0.0048(11)	−0.0005(8)	−0.0023(8)	−0.0007(8)
N5	0.0039(10)	0.0061(10)	0.0053(10)	−0.0029(8)	0.0005(8)	−0.0025(8)
N6	0.0036(10)	0.0043(10)	0.0053(11)	−0.0017(8)	−0.0005(8)	−0.0002(8)
N7	0.0045(10)	0.0053(10)	0.0030(10)	0.0018(8)	-0.0004(8)	−0.0031(8)
N8	0.0120(12)	0.0037(10)	0.0060(11)	−0.0001(8)	−0.0004(9)	−0.0034(9)
N9	0.0038(11)	0.0164(12)	0.0047(11)	−0.0001(9)	−0.0007(8)	−0.0032(9)
N10	0.0026(10)	0.0058(10)	0.0061(11)	0.0008(8)	−0.0016(8)	−0.0017(8)
N11	0.0064(11)	0.0043(10)	0.0037(10)	−0.0008(8)	−0.0007(8)	−0.0002(8)
Li1	0.019(3)	0.026(3)	0.015(3)	0.011(3)	0.005(2)	−0.001(3)

Table D.6.: Selected interatomic distances (in Å) occurring in $Li_{3-x}P_6N_{11-x}(NH)_x$ obtained from single-crystal X-ray diffraction at 113 K, standard deviations in parentheses.

P1–N3	1.586(3)	P6–N5	1.564(3)
P1–N2	1.586(3)	P6–N11	1.606(3)
P1–N4	1.660(2)	P6–N10	1.630(3)
P1–N1	1.701(2)	P6–N7	1.747(3)
P2–N5	1.570(2)	H2–Li2	1.83(2)
P2–N3	1.594(3)	H2–H1	2.0308(5)
P2–N6	1.613(3)	H2–N5	2.393(2)
P2–N1	1.757(3)	H2–N11	2.465(3)
P3–N2	1.582(3)	H1–N3	2.306(3)
P3–N6	1.597(3)	H1–N10	2.391(2)
P3–N4	1.639(2)	Li1–N6	2.088(8)
P3–N1	1.711(3)	Li1–N8	2.091(7)
P4–N9	1.590(3)	Li1–N3	2.098(7)
P4–N8	1.591(3)	Li1–N11	2.306(8)
P4–N10	1.635(3)	Li2–H2	1.83(2)
P4–N7	1.709(3)	Li2–N10	2.04(2)
P5–N9	1.596(3)	Li2–N9	2.12(2)
P5–N8	1.604(3)	Li2–N11	2.24(2)
P5–N11	1.610(3)	Li2–N6	2.29(2)
P5–N7	1.739(3)	Li2–N4	2.39(2)

Table D.7.: Selected interatomic angles (in °) occurring in $Li_{3-x}P_6N_{11-x}(NH)_x$ obtained from single-crystal X-ray diffraction at 113 K, standard deviations in parentheses.

N3–P1–N2	113.01(14)	N9–P5–N7	108.84(14)
N3–P1–N4	113.11(13)	N8–P5–N11	104.33(14)
N3–P1–N1	107.04(13)	N8–P5–N7	108.80(13)
N2–P1–N4	108.01(13)	N11–P5–N7	112.70(13)
N2–P1–N1	110.03(13)	N5–P6–N11	111.78(14)
N4–P1–N1	105.35(13)	N5–P6–N10	114.47(14)
N5–P2–N3	117.77(14)	N5–P6–N7	105.43(13)
N5–P2–N6	110.47(14)	N11–P6–N10	106.71(14)
N5–P2–N1	102.83(13)	N11–P6–N7	110.45(13)
N3–P2–N6	107.63(14)	N10–P6–N7	107.96(13)
N3–P2–N1	108.67(13)	P1–N1–P3	119.4(2)
N6–P2–N1	109.19(13)	P1–N1–P2	115.8(2)
N2–P3–N6	111.22(14)	P3–N1–P2	123.4(2)
N2–P3–N4	109.22(14)	P3–N2–P1	125.8(2)
N2–P3–N1	110.69(13)	P1–N3–P2	123.1(2)
N6–P3–N4	104.36(13)	P3–N4–P1	126.68(13)
N6–P3–N1	112.98(13)	P6–N5–P2	139.2(2)
N4–P3–N1	108.09(13)	P3–N6–P2	125.1(2)
N9–P4–N8	115.48(14)	P4–N7–P5	117.6(2)
N9–P4–N10	107.76(14)	P4–N7–P6	117.0(2)
N9–P4–N7	107.03(14)	P5–N7–P6	124.8(2)
N8–P4–N10	111.08(14)	P4–N8–P5	130.6(2)
N8–P4–N7	110.47(14)	P4–N9–P5	125.0(2)
N10–P4–N7	104.37(13)	P6–N10–P4	121.7(2)
N9–P5–N8	113.97(15)	P6–N11–P5	126.8(2)
N9–P5–N11	108.23(14)		

Deposition Numbers CSD2290091 and CSD2290093 contain the supplementary crystallographic data for this paper. These data are provided free of charge by the joint Cambridge Crystallographic Data Centre and Fachinformationszentrum Karlsruhe http://www.ccdc.cam.ac.uk/structures.

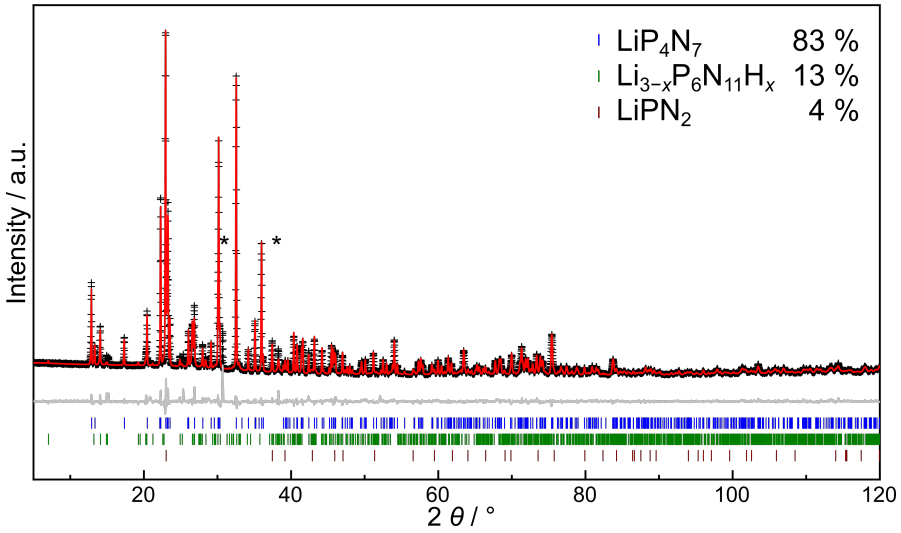

Figure D.1.: Rietveld plot of a sample with LiP_4N_7 as main phase. Observed intensities are shown with black crosses, calculated intensities and difference plot are shown in red and gray lines, respectively. Potential reflection positions of LiP_4N_7, $Li_{3-x}P_6N_{11-x}(NH)_x$, and $LiPN_2$ are shown in blue, green, and brown markers, respectively. Reflections of unknown phases are marked with asterisks.

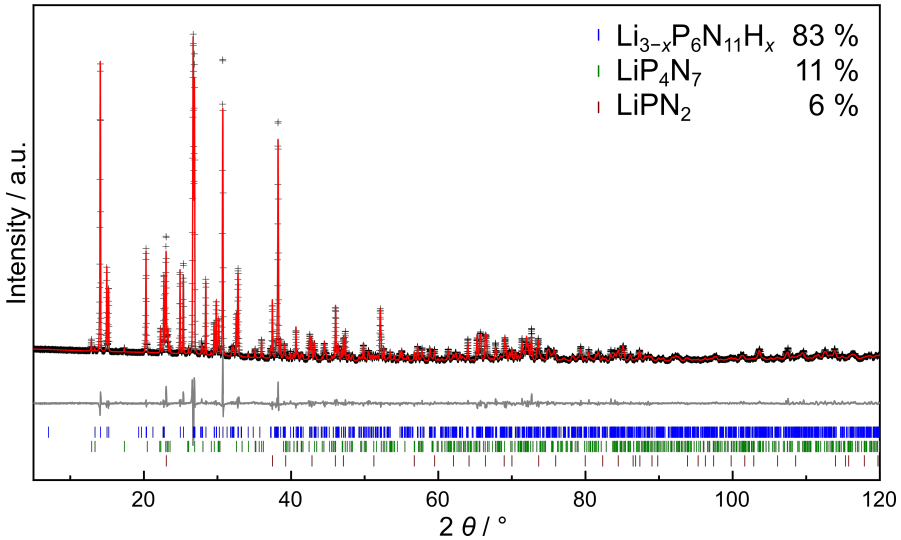

Figure D.2.: Rietveld plot of a sample with $Li_{3-x}P_6N_{11-x}(NH)_x$ as main phase. Observed intensities are shown with black crosses, calculated intensities and difference plot are shown in red and gray lines, respectively. Potential reflection positions of $Li_{3-x}P_6N_{11-x}(NH)_x$, LiP_4N_7, and $LiPN_2$ are shown in blue, green, and brown markers, respectively.

Table D.8.: Additional crystallographic data on the Rietveld refinements of LiP_4N_7 and $Li_{3-x}P_6N_{11-x}(NH)_x$.

Formula	LiP_4N_7	lipn
Formula weight / $g\,mol^{-1}$	228.89	354.82
Crystal system; space group	Orthorhombic, $P2_12_12_1$ (no.19)	Triclinic, $P\bar{1}$ (no. 2)
Lattice parameters / Å, °	$a = 4.589\,88(13)$	$a = 4.7018(2)$
	$b = 8.0153(3)$	$b = 7.0318(2)$
	$c = 13.2511(4)$	$c = 12.7580(4)$
		$\alpha = 87.5397(9)$
		$\beta = 79.5379(9)$
		$\gamma = 70.4475(13)$
Cell volume / $Å^3$	487.50(3)	390.80(2)
Formula units per unit cell	4	2
Density / $g\,cm^{-3}$	3.1185(2)	2.9819(2)
μ / mm	137.103(7)	128.713(8)
Diffractometer	Stoe Stadi P	
Radiation	Cu-$K_{\alpha1}$ ($\lambda = 1.540\,596$ Å)	
Detector	Mythen 1K	
Monochromator	Ge(111)	
2θ-range / °	$5 \leq 2\theta \leq 120$	
Data points	7839	7705
Total number of reflections	465	1177
Refined parameters	98	110
Background function	Shifted Chebyshev	
Number of background parameters	12	12
Goodness of fit	2.7665	2.7575
R_p; R_{wp}	0.0518; 0.0804	0.0558; 0.0766
R_{exp}; R_{Bragg}	0.0291; 0.0251	0.0278; 0.0348

D.3. Variable-temperature Powder X-ray diffraction

Variable-temperature powder X-ray diffraction showed no decomposition of a sample with 79 % LiP_4N_7, 17 % $Li_{3-x}P_6N_{11-x}(NH)_x$, and 4 % $LiPN_2$ (Figure D.3). The thermal expansion of the material was calculated using lattice parameters as obtained from Rietveld refinement (Figure D.4).

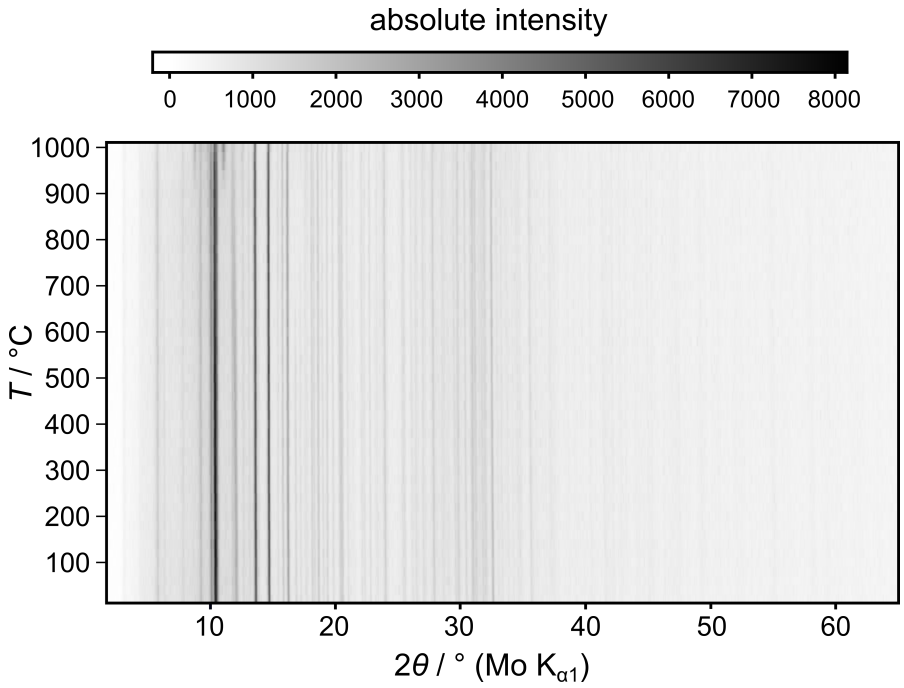

Figure D.3.: X-ray powder diffractogram of LiP_4N_7 at temperatures from 25–1000 °C, measured with Mo $K_{\alpha 1}$ ($\lambda = 0.709\,300$ Å) radiation.

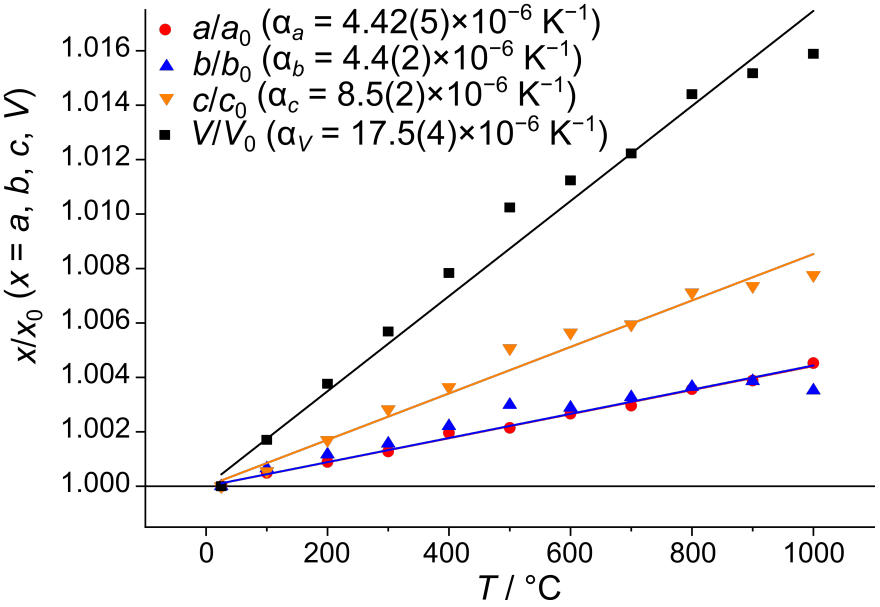

Figure D.4.: Thermal expansion of LiP_4N_7 at temperatures from 25–1000 °C.

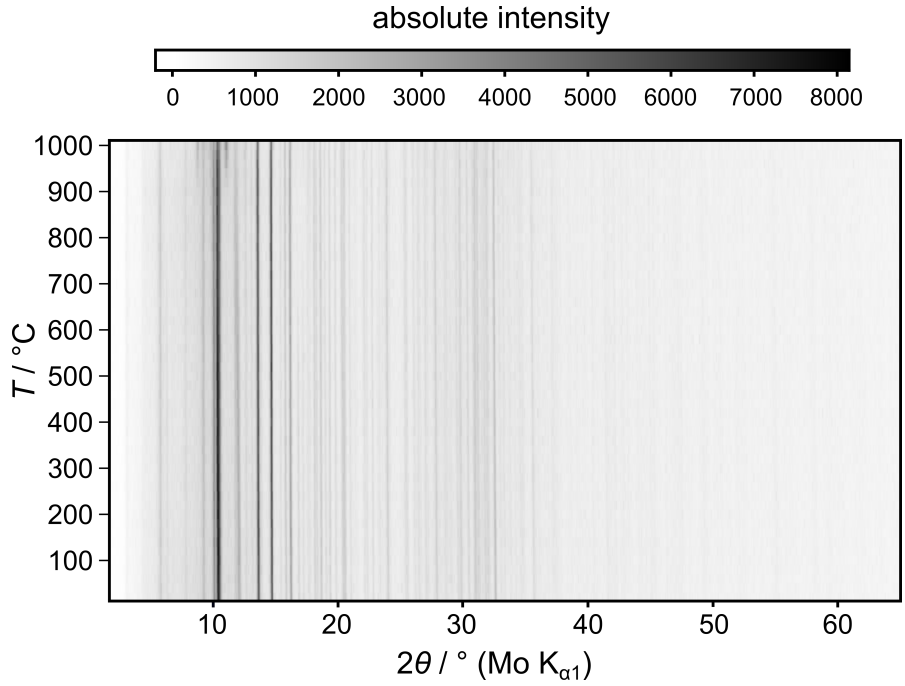

Figure D.5.: X-ray powder diffractogram of $Li_{3-x}P_6N_{11-x}(NH)_x$ at temperatures from 60–960 °C, measured with Ag $K_{\alpha 1}$ ($\lambda = 0.559\,407\,5$ Å) radiation.

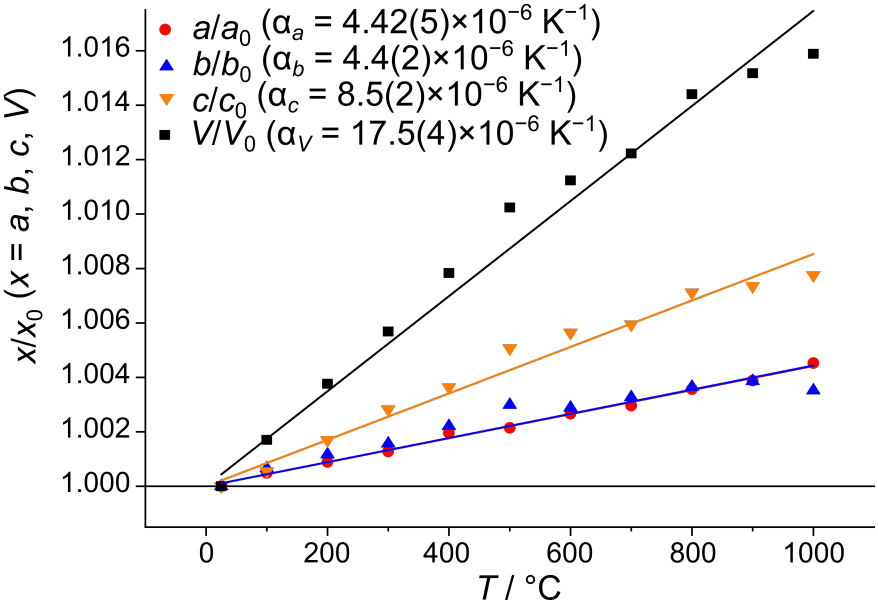

Figure D.6.: Thermal expansion of $Li_{3-x}P_6N_{11-x}(NH)_x$ at temperatures from 60–7400 °C.

D.4. Detailed information on nuclear magnetic resonance (NMR) spectroscopy

For further characterization of the samples, ^{31}P, and ^{7}Li NMR spectra were recorded. Since no phase pure samples were available, a sample with LiP_4N_7 (69 wt-%), $Li_{3-x}P_6N_{11-x}(NH)_x$ (19 wt-%), and $LiPN_2$ (12 wt-%) was used for LiP_4N_7 and a sample with $Li_{3-x}P_6N_{11-x}(NH)_x$ (30 wt-%), LiP_4N_7 (14 wt-%), $LiPN_2$ (3 wt-%), and *c*BN (53 wt-%) was used for the $Li_{3-x}P_6N_{11-x}(NH)_x$ spectrum. All ^{31}P spectra were compared and the intensities of ^{31}P signals correlated with the respective structures. $^{31}P\{^{1}H\}$ coupled spectra were used to investigate the presence of H.

In the sample consisting mainly of LiP_4N_7, four ^{31}P NMR signals occur at 5.4, −0.9, −8.4 and −15.9 ppm. The singal at −0.9 ppm is broad and partially superimposed on the resonance at −8.4 ppm. Furthermore, the signal at −15.9 ppm exhibits a shoulder toward more negative chemical shifts, indicating additional superimposed signals (Figure D.7). The broad signal at −0.9 ppm might result from $Li_{3-x}P_6N_{11-x}(NH)_x$, since direct comparison of ^{31}P spectra shows large signals of the mainly $Li_{3-x}P_6N_{11-x}(NH)_x$ containing phase in this area (Figure D.13a). The single ^{31}P signal of $LiPN_2$ occurs at 5.2 ppm (Figure D.13b), also explaining the sharp signal around 5.4 ppm in the spectrum of mainly LiP_4N_7. Thus, only the two signals at −8.4 and −15.9 ppm are likely to result from LiP_4N_7. Assignment to distinct P atom positions is not possible.

The $_{31}P\{_{1}H\}$ coupled spectrum shows two large signals at −0.9 and −16.0 ppm (Figure D.8). However, since the main signal is at −0.9 ppm, it might result from the $Li_{3-x}P_6N_{11-x}(NH)_x$ side phase rather than from LiP_4N_7. The signal at −16.0 ppm is slightly smaller and might result from an underlying signal as discussed above. However, since it is smaller than the signal attributed to the side phase with 19 wt-%, presence of H cannot be determined unequivocally.

The ^{7}Li NMR spectrum shows a single signal at −0.3 ppm (Figure D.9), as would be expected in LiP_4N_7 with one crystallographic Li position. The signal occurs within the range of known lithium nitridophosphates.[12–15] The ^{31}P spectrum of a sample containing $Li_{3-x}P_6N_{11-x}(NH)_x$ as main P-containing phase (30 wt-% $Li_{3-x}P_6N_{11-x}(NH)_x$, 14 wt-% LiP_4N_7, 3 wt-% $LiPN_2$, 53 wt-% *c*BN) shows four distinct signals at 0.8, −3.0, −7.7 and −16.0 ppm (Figure D.10). Due to the large *c*BN content, the spectrum shows low resolution. Direct comparison of the spectrum with that of the sample with mainly LiP_4N_7 (Figure D.13a) shows that the signals at −7.7 ppm in the spectrum with mainly $Li_{3-x}P_6N_{11-x}(NH)_x$ is in fact at the same position as the signal at −8.4 ppm in the spectrum with mainly LiP_4N_7. Thus, the signals at −7.7 ppm and at −16.0 ppm are assigned to LiP_4N_7. Only the two signals at 0.8 and −3.0 ppm remain from $Li_{3-x}P_6N_{11-x}(NH)_x$. Possibly, since the signal at −16 ppm is still the strongest signal, $Li_{3-x}P_6N_{11-x}(NH)_x$ might also exhibit a resonance with this chemical shift. Assignment of the signals to the respective P atom positions of $Li_{3-x}P_6N_{11-x}(NH)_x$was not possible.

The ^{1}H-coupled ^{31}P spectrum shows four signals at 0.8, −2.9, −7.4 and −16.8 ppm (Figure D.11). A slight shift in peak position is due to low resolution of the spectrum. However, at least two of the signals result from $Li_{3-x}P_6N_{11-x}(NH)_x$. Additionally, since the signal at −16.0 ppm might result partially from $Li_{3-x}P_6N_{11-x}(NH)_x$, there are possibly additional resonances. Although phase-pure

samples are necessary for quantitative analysis, H is present in $Li_{3-x}P_6N_{11-x}(NH)_x$.
The 7Li NMR spectrum shows a single broad peak at −0.2 ppm (Figure D.12). Since there are two Li positions in $Li_{3-x}P_6N_{11-x}(NH)_x$, this indicates similar chemical environment or slight mobility. The chemical shift of both samples is in the range of other known ^{7}Li shifts for lithium nitridophosphates.[12–15]

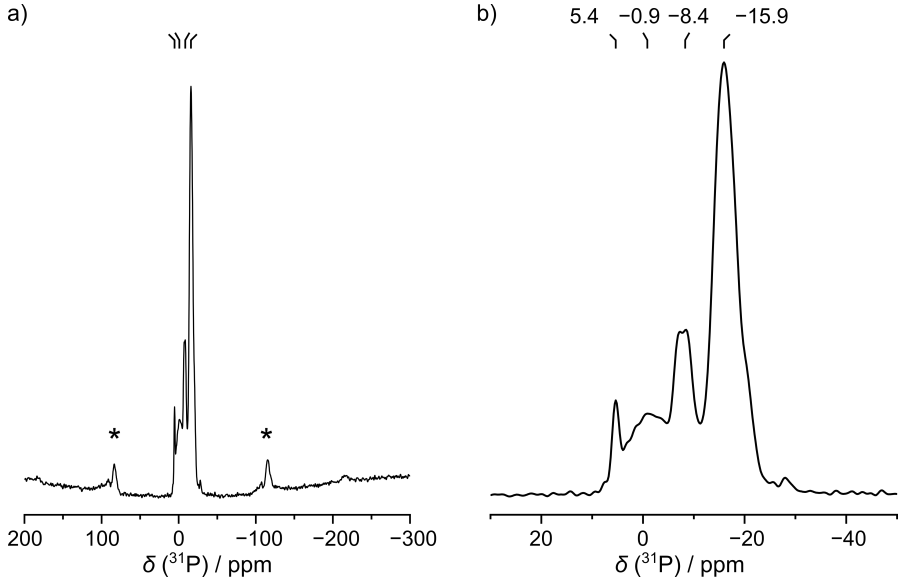

Figure D.7.: ^{31}P NMR spectrum of a sample consisting of LiP_4N_7 (69 wt-%), $Li_{3-x}P_6N_{11-x}(NH)_x$ (19 wt-%), and $LiPN_2$ (12 wt-%), measured at a spinning frequency of 20 kHz. a) Full spectrum. No Li_3P is visible (−273 ppm). Rotational side bands are marked with asterisks. b) Close-up of the spectrum showing four distinct signals.

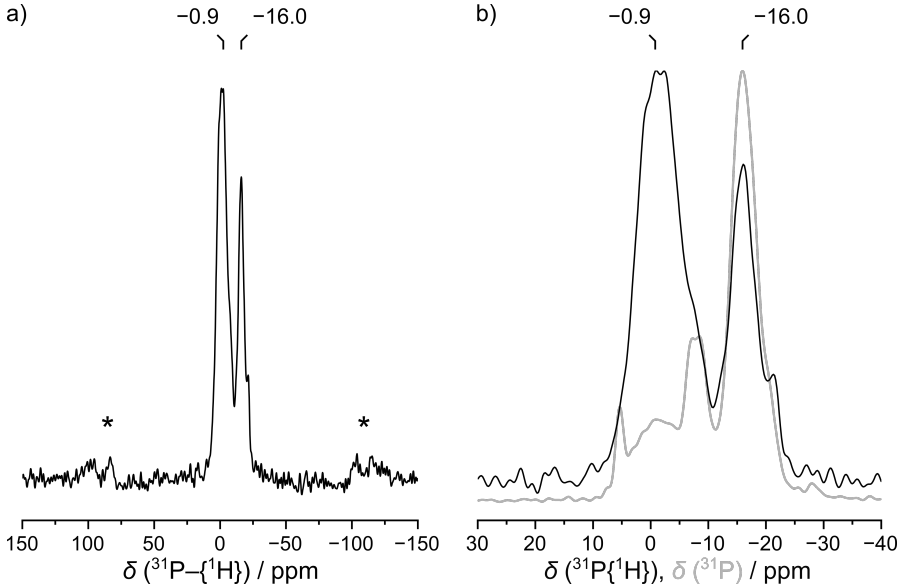

Figure D.8.: $^{31}P\{^1H\}$ coupled NMR spectrum of a sample consisting of LiP_4N_7 (69 wt-%), $Li_{3-x}P_6N_{11-x}(NH)_x$ (19 wt-%), and $LiPN_2$ (12 wt-%), measured at a spinning frequency of 20 kHz. a) Full spectrum. Rotational side bands are marked with asterisks. b) Close-up of the spectrum. The coupled signal is shown as black line, the decoupled measurement of ^{31}P is shown in a gray line. The spectra were normalized to their largest peaks.

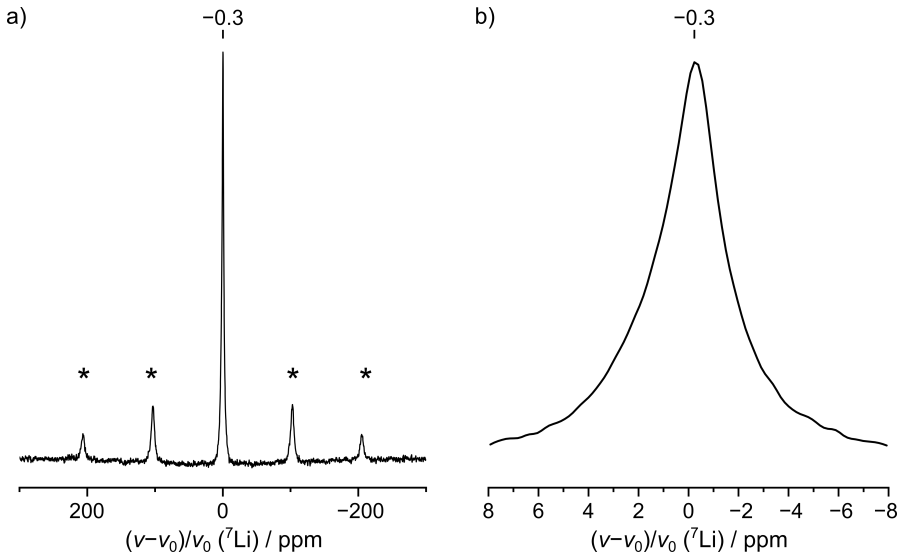

Figure D.9.: ^7Li NMR spectrum of a sample consisting of LiP_4N_7 (69 wt-%), $Li_{3-x}P_6N_{11-x}(NH)_x$ (19 wt-%), and $LiPN_2$ (12 wt-%), measured at a spinning frequency of 20 kHz. a) full spectrum. Rotational side bands are marked with asterisks. b) close-up of the spectrum showing one signal with shoulders towards higher ppm.

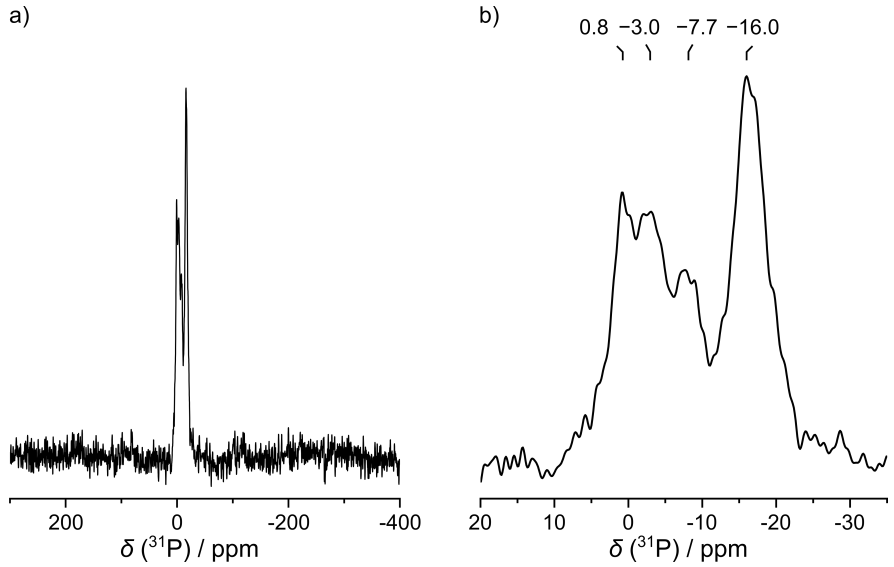

Figure D.10.: ^{31}P NMR spectrum of a sample consisting of $Li_{3-x}P_6N_{11-x}(NH)_x$(30 wt-%), LiP_4N_7 (14 wt-%), $LiPN_2$ (3 wt-%), and *c*BN (53 wt-%), measured at a spinning frequency of 20 kHz. a) full spectrum. No Li_3P is visible (−273 ppm). b) Close-up of the spectrum showing four distinct signals.

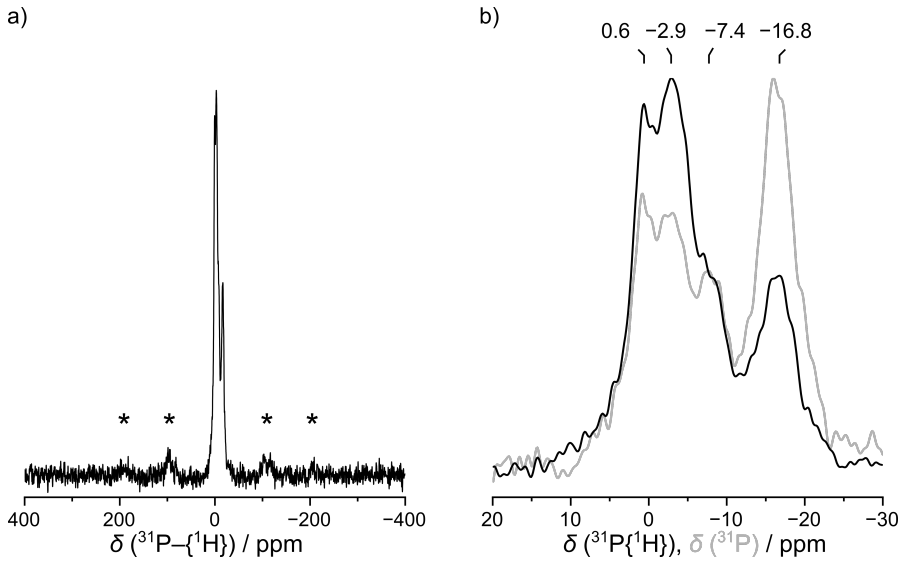

Figure D.11.: $^{31}P\{^1H\}$ coupled NMR spectrum of a sample consisting of $Li_{3-x}P_6N_{11-x}(NH)_x$ (30 wt-%), LiP_4N_7 (14 wt-%), $LiPN_2$ (3 wt-%), and *c*BN (53 wt-%), measured at a spinning frequency of 20 kHz. a) full spectrum. Rotational side bands are marked with asterisks. b) close-up of the spectrum. The coupled signal is shown as black line, the direct measurement of 31P is shown in a gray line.

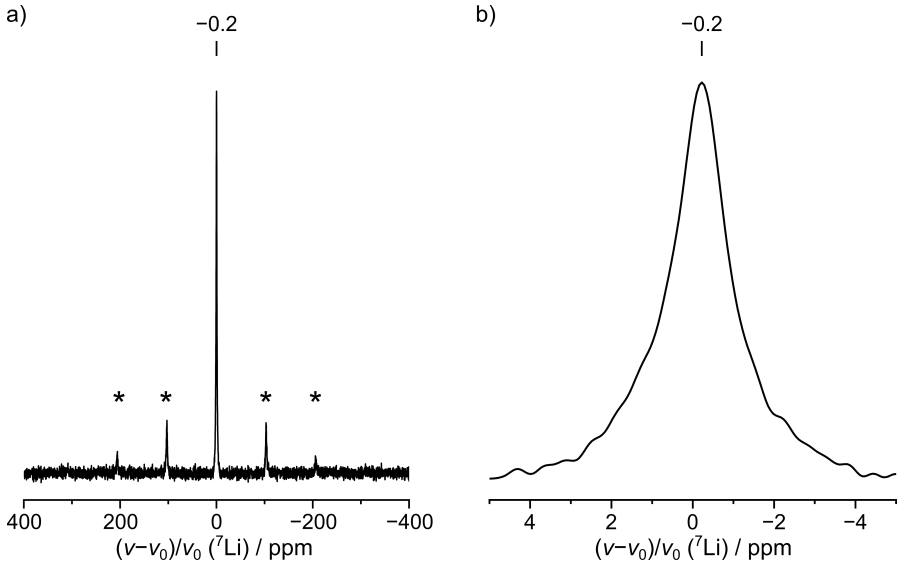

Figure D.12.: 7Li NMR spectrum of a sample consisting of $Li_{3-x}P_6N_{11-x}(NH)_x$ (30 wt-%), LiP_4N_7 (14 wt-%), $LiPN_2$ (3 wt-%), and *c*BN (53 wt-%), measured at a spinning frequency of 20 kHz. a) full spectrum. Rotational side bands are marked with asterisks. b) close-up of the spectrum showing four distinct signals.

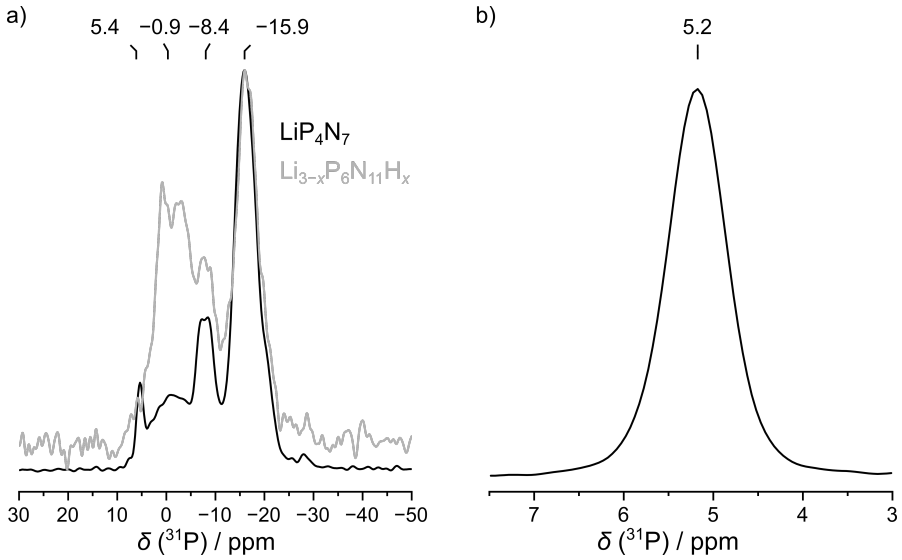

Figure D.13.: a) Comparison of the normalized ^{31}P NMR spectra of LiP_4N_7 (black line) and $Li_{3-x}P_6N_{11-x}(NH)_x$ (gray line). b) ^{31}P NMR spectrum of $LiPN_2$. Both measured with a spinning frequency of 20 kHz.

D.5. Raman spectroscopy

Raman spectra were measured at an incident laser wavelength of 632 nm. The used spectrometer was a Jobin Yvon Typ V 010 LabRam single grating spectrometer with a double super razor edge filter and a Peltier-cooled CCD camera (Jobin Yvon). The samples were measured in glass capillaries as used for PXRD.

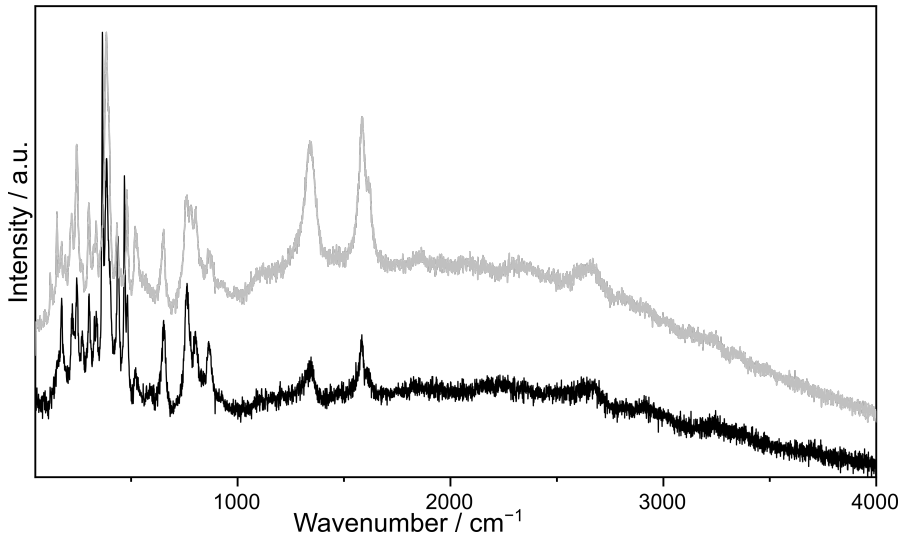

Figure D.14.: Raman spectra of a sample consisting mainly of LiP_4N_7 (83 wt-%, 13 wt-% $Li_{3-x}P_6N_{11-x}(NH)_x$, 4 wt-% $LiPN_2$, black line), and mainly of $Li_{3-x}P_6N_{11-x}(NH)_x$ (83 wt-%, 11 wt-% LiP_4N_7, 6 wt-% $LiPN_2$, gray line) measured from 50–4000 cm^{-1} at 632.817 nm.

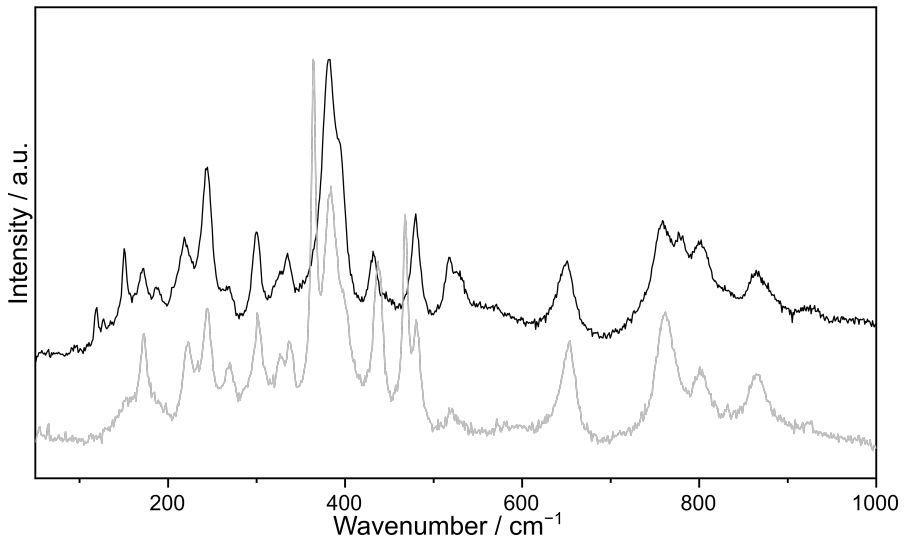

Figure D.15.: Raman spectra of a sample consisting mainly of LiP_4N_7 (83 wt-%, 13 wt-% $Li_{3-x}P_6N_{11-x}(NH)_x$, 4 wt-% $LiPN_2$, black line), and mainly of $Li_{3-x}P_6N_{11-x}(NH)_x$ (83 wt-%, 11 wt-% LiP_4N_7, 6 wt-% $LiPN_2$, gray line) measured from 50–1000 cm^{-1} at 632.817 nm.

D.6. Additional Details on Elemental Analysis

D.6.1. Scanning Electron Microscopy (SEM) and Energy-Dispersive X-ray (EDX) Spectroscopy

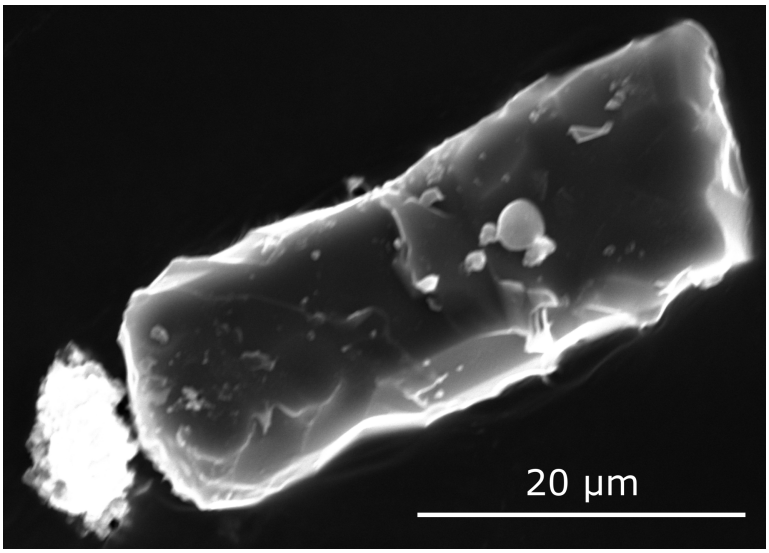

Figure D.16.: SEM image of a LiP_4N_7 crystal.

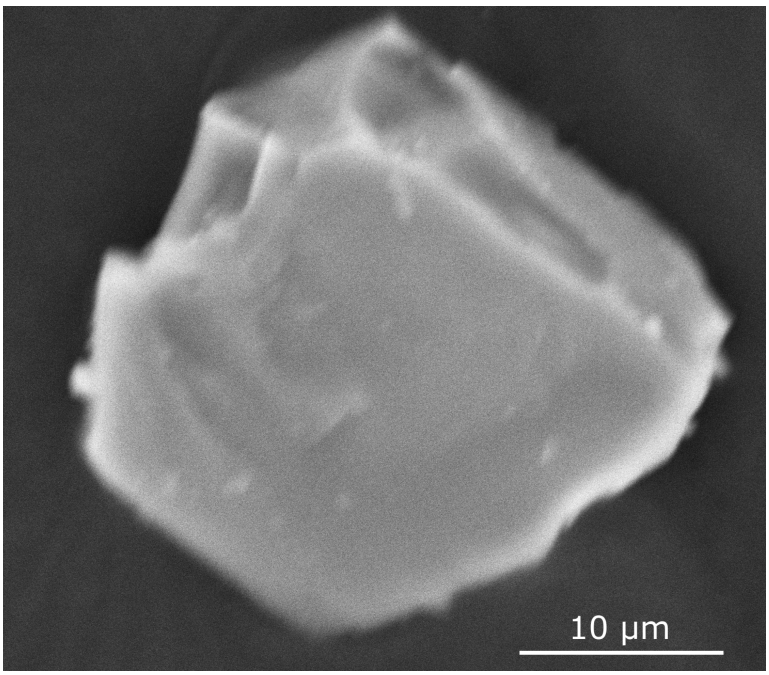

Figure D.17.: SEM image of a $Li_{3-x}P_6N_{11-x}(NH)_x$ crystal.

Energy-Dispersive X-ray (EDX) spectra were acquired on single-crystals (Figures D.16 and D.17) of LiP_4N_7 and $Li_{3-x}P_6N_{11-x}(NH)_x$. Since light elements like H and Li cannot be detected with the setup,

Table D.9.: EDX measurements on samples of mostly LiP_4N_7.

Sample	Point	P	O	N
1 (single crystal)	1	37	4	59
	2	39	4	57
	3	40	3	57
	4	39	3	58
	5	37	2	60
2 (powder)	1	39	4	57
	2	29	7	65
	3	48	7	45
	4	28	22	51
	5	29	15	56
	6	30	5	65
3 (powder)	1	32	9	60
	2	21	23	56
	3	43	13	44
	4	30	7	64
	5	29	15	56
	6	37	11	52
	7	35	9	56
Average (at-%)		35(7)	9(6)	57(6)
Calculated (at-%)		36.4	0	63.6
Deviation (%)		5	–	11

Table D.10.: EDX measurements on a single crystal of $Li_{3-x}P_6N_{11-x}(NH)_x$.

Sample	Point	P	O	N
1 (single crystal)	1	42	2	56
	2	46	3	51
	3	43	2	55
	4	45	3	52
	5	44	2	53
Average (at-%)		44(2)	2.4(5)	53(2)
Calculated (at-%)		35.3	0	64.7
Deviation (%)		−25	–	17

the atomic percentage of P and N in the sample were considered. No other elements were found using EDX spectroscopy. Since EDX is a surface method, O can result from superficial adherence of O_2.

D.7. Author Contributions

Stefanie Schneider: Conceptualization: Lead; Formal analysis: Lead; Investigation: Lead; Validation: Equal; Visualization: Lead; Writing – original draft: Lead; Writing – review & editing: Equal
Sebastian Klenk: Investigation: Supporting; Writing – review & editing: Supporting
Simon D. Kloß: Formal analysis: Supporting; Investigation: Supporting; Writing – original draft: Supporting; Writing – review & editing: Supporting
Wolfgang Schnick: Conceptualization: Equal; Funding acquisition: Lead; Project administration: Lead; Resources: Lead; Supervision: Lead; Validation: Equal; Writing – original draft: Supporting; Writing – review & editing: Supporting)

D.8. References

[1] A. Stock, B. Hoffmann, *Ber. Dtsch. Chem. Ges.* **1903**, *36*, 314–319, DOI 10.1002/cber.19030360170.

[2] D. Walker, *Am. Mineral.* **1991**, *76*, 1092–1100.

[3] H. Huppertz, *Z. Kristallogr.* **2004**, *219*, 330–338, DOI 10.1524/zkri.219.6.330.34633.

[4] Bruker, *SADABS*, Bruker AXS Inc., Madison, WI, USA, **2009**.

[5] Bruker, *APEX3 v2018.1-0*, **2018**.

[6] G. M. Sheldrick, *Acta Crystallogr. C* **2015**, *71*, 3–8, DOI 10.1107/S2053229614024218.

[7] K. Brandenburg, *Diamond Version 3.2k*, Crystal Impact GbR, Bonn, Germany, **2014**.

[8] A. A. Coelho, *TOPAS Academic version 6*, Coelho Software, Brisbane, Australia, **2016**.

[9] Bruker, *Topspin v.3.0 pl 3*, Bruker Biospin GmbH, Germany, **2010**.

[10] Bruker, *OPUS 6.5*, Bruker Optik GmbH, Ettlingen, Germany, **2007**.

[11] *INCA Version 4.02*, Oxford Instruments, Analytical Limited, Abingdon, United Kingdom.

[12] E.-M. Bertschler, R. Niklaus, W. Schnick, *Chem. Eur. J.* **2017**, *23*, 9592–9599, DOI 10.1002/chem.201700979.

[13] E.-M. Bertschler, C. Dietrich, J. Janek, W. Schnick, *Chem. Eur. J.* **2017**, *23*, 2185–2191, DOI 10.1002/chem.201605316.

[14] E.-M. Bertschler, C. Dietrich, T. Leichtweiß, J. Janek, W. Schnick, *Chem. Eur. J.* **2018**, *24*, 196–205, DOI 10.1002/chem.201704305.

[15] E.-M. Bertschler, R. Niklaus, W. Schnick, *Chem. Eur. J.* **2018**, *24*, 736–742, DOI 10.1002/chem.201704975.

E. Miscellaneous

E.1. List of Publications in this Thesis

In the following section, all publications in this thesis are listed in chronological order, including their titles, authors, and authors' contributions.

E.1.1. Structure Determination of the Crystalline LiPON Model Structure $Li_{5+x}P_2O_{6-x}N_{1+x}$ with $x \approx 0.9$

Stefanie Schneider, Lucas G. Balzat, Bettina V. Lotsch, and Wolfgang Schnick

Chem. Eur. J. **2023**, *29*, e202202984.
https://doi.org/10.1002/chem.202202984
DOI: 10.1002/chem.202202984

Stefanie Schneider performed synthesis, formal analysis and data evaluation in the group of Wolfgang Schnick and wrote the major part of the manuscript. Conductivity measurements and writing of the corresponding section in the manuscript were done by Lucas G. Balzat in the group of Bettina V. Lotsch. Wolfgang Schnick supervised the project. All authors were involved in the discussion of the results and revision of the manuscript.

E.1.2. Comprehensive Investigation of Anion Species in Crystalline Li^+ ion Conductor $Li_{27-x}[P_4O_{7+x}N_{9-x}]O_3$ ($x \approx 1.9(3)$)

Stefanie Schneider, Eva-Maria Wendinger, Volodymyr Baran, Anna-Katharina Hatz, Bettina V. Lotsch, Markus Nentwig, Oliver Oeckler, Thomas Bräuniger, and Wolfgang Schnick

Chem. Eur. J. **2023**, *29*, e202300174.
https://doi.org/10.1002/chem.202300174
DOI: 10.1002/chem.202300174

Synthesis and formal analysis was performed by Stefanie Schneider. Eva-Maria Wendinger performed preliminary work in the course of her Master's thesis supervised by Wolfgang Schnick and obtained single crystals. Single crystal X-Ray diffraction data was obtained at the ID11 beamline at the ESRF in Grenoble and the data interpreted by Markus Nentwig and Oliver Oeckler. Volodymyr Baran obtained and formally analyzed neutron powder diffraction data, which was interpreted by Stefanie Schneider. Ionic and electronic conductivity measurements were conducted and formally analyzed by Anna-Katharina Hatz in the group of Bettina V. Lotsch and contextualized by Stefanie Schneider. ^{31}P–^{31}P 2D double-quantum (DQ) single-quantum (SQ) correlation MAS NMR measurements were conducted by Thomas Bräuniger. The manuscript was written mainly by Stefanie Schneider. Wolfgang Schnick supervised the project. All authors contributed to the discussion of the results and revision of the manuscript.

E.1.3. Finding Order in Disorder – The Highly Disordered Lithium Oxonitridophosphate Double Salt $Li_{8+x}P_3O_{10-x}N_{1+x}$ ($x = 1.4(5)$)

Stefanie Schneider, Sandra T. Kreiner, Lucas G. Balzat, Bettina V. Lotsch, and Wolfgang Schnick

Chem. Eur. J. **2023**, *29*, e202301986.
https://doi.org/10.1002/chem.202301986
DOI: 10.1002/chem.202301986

Stefanie Schneider and Sandra T. Kreiner performed synthesis and formal analysis in the course of Sandra T. Kreiner's Bachelor's thesis that was supervised by Stefanie Schneider and Wolfgang Schnick. Data interpretation and structural elucidation were done by Stefanie Schneider. Stefanie Schneider wrote the major part of the manuscript. Lucas G. Balzat contributed ionic and electronic conductivity measurements and the writing of the corresponding section in the group of Bettina Lotsch. Wolfgang Schnick supervised the project. All authors contributed to the discussion of the results and revision of the manuscript.

E.1.4. Please Mind the Gap: Highly Condensed P–N Networks in LiP_4N_7 and $Li_{3-x}P_6N_{11-x}(NH)_x$

Stefanie Schneider, Sebastian Klenk, Simon D. Kloß, and Wolfgang Schnick

Chem. Eur. J. **2023**, *29*, e202301986.
https://doi.org/10.1002/chem.202301986
DOI: 10.1002/chem.202301986

Synthesis and formal analysis were done by Stefanie Schneider and Sebastian Klenk in the course of his Bachelor's thesis under the supervision of Stefanie Schneider and Wolfgang Schnick. Simon Kloß contributed preliminary work, resulting in a single crystal and single crystal X-Ray diffraction data. Data interpretation were performed by Stefanie Schneider. Lucas G. Balzat performed ionic and electronic measurements. Writing of the manuscript was mainly done by Stefanie Schneider, the section on ionic and electronic conductivity was written by Lucas G. Balzat. Wolfgang Schnick supervised the project. All authors contributed to the discussion and revision of the manuscript.

E.2. Funding

The research presented in this work was funded by the Deutsche Forschungsgemeinschaft (DFG, German Research Foundation, Germany's Excellence Strategy-EXC 2089/1-390776260 – e-conversion), the German Federal Ministry of Research and Education (BMBF, project 03XP0177B – FestBatt), the European Synchrotron Radiation Facility (ESRF, CH-6412), the Forschungs-Neutronenquelle Heinz Maier-Leibnitz (FRM II, proposal no. 16528), and the Ludwig-Maximilians Universität München (LMU). Travel awards by the Gesellschaft Deutscher Chemiker e.V. are gratefully acknowledged.

E.3. Conference Contributions and Presentations

Synthesis and Crystal Structure of LiP_4N_7 and $Li_3P_6N_{11}$
Stefanie Schneider, Wolfgang Schnick
Poster, 21st Conference on Inorganic Chemistry, **2022**

Fehlern und deren Fortpflanzung
Stefanie Schneider, Wolfgang Schnick
Talk, Seminar Schnick Group, **2022**

Lithium oxonitridophosphate(oxide)s
Stefanie Schneider, Wolfgang Schnick
Talk, Seminar Schnick Group, **2021**

Illuminatio structurarum de LiPONe neutronibus – Von Neutronen und LiPON
Stefanie Schneider, Wolfgang Schnick
Talk, Seminar Schnick Group, **2020**

Lithium-(oxo)nitridophosphates
Stefanie Schneider, Wolfgang Schnick
Talk, Cooperation Meeting, **2020**

LiP_4N_7 – eine hochkondensierte LiPN-Phase
Stefanie Schneider, Wolfgang Schnick
Talk, 4. Obergurgl-Seminar Festkörperchemie, **2019**, Austria

Lithium-(oxo)nitridophosphates
Stefanie Schneider, Wolfgang Schnick
Talk, Cooperation Meeting, **2020**, Germany

$Li_{27}P_4N_9O_{10}$ – ein kristallines LiPON mit isolierten $P(O,N)_4$-Tetraedern
Stefanie Schneider, Wolfgang Schnick
Talk, 3. Obergurgl-Seminar Festkörperchemie, **2018**, Austria

Untersuchung der Synthese neuer Lithium-Oxonitridophosphate
Stefanie Schneider, Wolfgang Schnick
Talk, Seminar Schnick Group, **2018**, Germany

E.4. Deposited Crystal Structures

The crystal structures reported in this thesis are available as Crystallographic Information Files (CIFs) free of charge at the joint Cambridge Crystallographic Data Centre and Fachinformationszentrum Karlsruhe Access Structures service. The data can be downloaded using the respective reference number.

Table E.1.: List of deposited crystal structures and corresponding CSD numbers from this work.

Compound	data source	CSD
$Li_{5+x}P_2O_{6-x}N_{1+x}$	X-Ray powder diffraction	2191662
$Li_{27-x}[P_4O_{7+x}N_{9-x}]O_3$	X-Ray single-crystal diffraction	2204799
$Li_{27-x}[P_4O_{7+x}N_{9-x}]O_3$	neutron powder diffraction	2204800
$Li_{8+x}P_3O_{10-x}N_{1+x}$	X-Ray single-crystal diffraction	2246044
LiP_4N_7	X-Ray single-crystal diffraction	2290091
$Li_{3-x}P_6N_{11-x}(NH)_x$	X-Ray single-crystal diffraction	2290093